Spectroscopic, Electrochemical and Structural Investigation of Platinum(IV) Complexes with Nitrogen-Rich Chelate Ligands

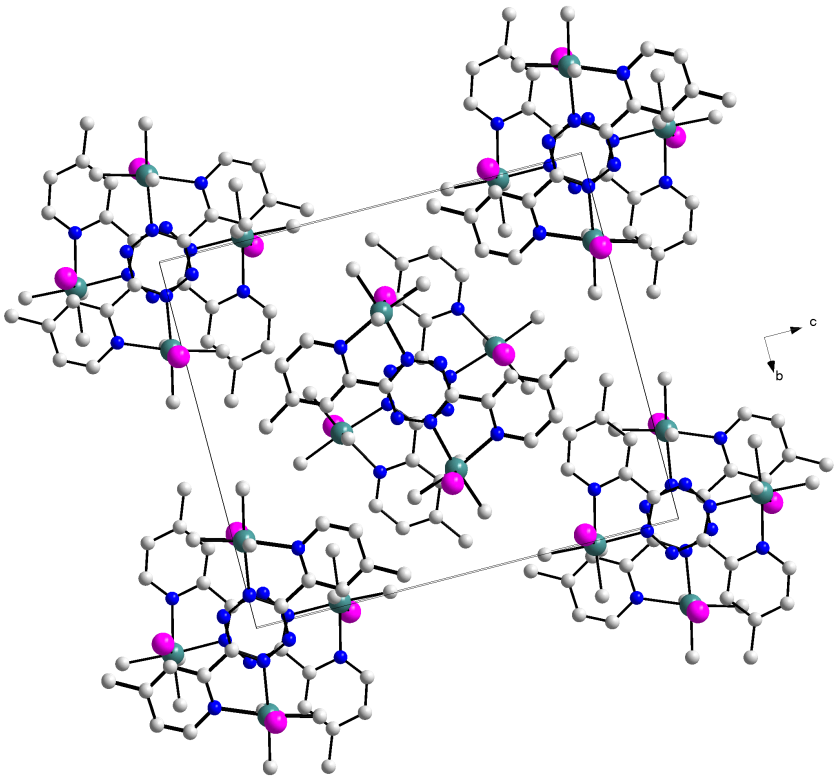

Cüneyt KAVAKLI

Spectroscopic, Electrochemical and Structural Investigation of Platinum(IV) Complexes with Nitrogen-Rich Chelate Ligands

Von der Fakultät Chemie der Universität Stuttgart
zur Erlangung der Würde eines
Doktors der Naturwissenschaften
(Dr. rer. nat.)
genehmigte Abhandlung

vorgelegt von

Cüneyt KAVAKLI
aus Eskisehir-Türkei

Hauptberichter:	Prof. Dr. W. Kaim
Mitberichter:	Prof. Dr. D. Gudat
Tag der mündlichen Prüfung:	18.09.2009

INSTITUT FÜR ANORGANISCHE CHEMIE DER UNIVERSITÄT STUTTGART

2009

TO MY PARENTS, MY WIFE AND MY DAUGHTER

Science is the most reliable guide for civilization, for life, for success in the world. Searching a guide other than the science is carelessness, ignorance and heresy.

M. Kemal Atatürk

Acknowledgements

This work was completed from July 2005 to July 2009 at the Institute of Inorganic Chemistry, University of Stuttgart.

It was possible to complete this work and writing of this thesis only with the help of various people. I would like to acknowledge all of them here.

First I would like to express my sincere gratitude to Prof. W. Kaim for providing me the opportunity of working in his group, for all his ideas, valuable critism and supports throughout in this study.

I would like to extend my gratitude to Dr. E. Bulak for all her discussions, unceasing supports, guiding me about Germany and precise assistance especially in the progress of writing this thesis.

Next I would like to thank Dr. B. Schwederski, for spending her time to help me about any kind of bureaucratic problems, German linguistics and providing her car whenever I needed particularly during my early days in Germany. I would also like to thank her for all EPR measurements and their simulations.

I would also like to thank,

Prof D. Gudat for the valuable discussions about NMR spectra and for ^{195}Pt-NMR measurement,

Dr. A. Gabrielsson and Dr. M. Sieger, for always helping me especially about electrochemistry and spectroelectrochemistry,

Dr. B. Sarkar for his fruitful scientific guidance and EPR measurements,

Mr. J. Fiedler from the Heyrovský Institute of Physical Chemistry in Prague, Czech Republic, for spectroelectrochemical measurements,

Dr. S. Záliš , Heyrovský Institute of Physical Chemistry in Prague, Czech Republic, Prof. T. Varnali, Bogazici University, Istanbul Turkey and Mr. O. Sarper, Universität Stuttgart for the DFT calculations,

Priv. Doz. Dr. M. Niemeyer, Dr. F. Lissner, Dr. I. Hartenbach and Mr. D. Bubrin from University of Stuttgart and by Prof. Cheng-Yong Su from Sun Yat-Sen University, China for X-Ray structural determinations,

Mrs. B. Förtsch for elemental analyses, Mrs. K. Török for NMR measurements,

Mr. J. Schnödt for the translation of the summary,

All the past and present members of the group of Prof. Kaim, especially Orkan Sarper for his invaluable friendship, help and supports.

The last but not the least, I would like to thank to my family for their all kind of supports and my wife Konstantina Dimadi for her endless encouragement during this work, being nearby whenever I needed help and making me feel like the luckiest man in this world.

CONTENTS

CHAPTER 1

Introduction

The molecules that have at least one direct metal-to-carbon interaction are termed as organometallic compounds. This definition would include metal alkyl compounds such as diethylzinc ($Zn(C_2H_5)_2$) as well as metal carbonyls such as $Ni(CO)_4$ which behave much like organic compounds in terms of their volatility, solubility in non-polar organic solvents, and general properties.[1]

The start of organometallic chemistry is pronounced with the synthesis of a platinum compound, $K[(C_2H_4)PtCl_3].H_2O$, by W. C. Zeise in 1827 whereas, studies of A. Werner who was awarded the Nobel Prize in 1913 are accepted as the beginning of metal-complex, or, in other words, coordination chemistry.[2,3]

As a pure metal, platinum is silvery-white in appearance, lustrous, ductile, and malleable.[4] It does not oxidize visibly when heated in air.[5] Platinum is insoluble in hydrochloric and nitric acid but dissolves in aqua regia to form hexachloroplatinic acid, H_2PtCl_6.[6,7] The most abundant isotope of platinum is ^{195}Pt (I = 1/2), comprising 33.83%. The most common oxidation states are 0, +2 and +4 although compounds in other oxidation states (+1, +3, etc) are also known. The predominant geometry for the +2 oxidation state is square planar, and for the +4 oxidation state is octahedral.[8,9]

Platinum is one of the rarer metals on earth. The largest platinum reserves are in South Africa and Russia.

Platinum has applications in many different areas, but the largest amount produced is used in the car industry. Another common use of platinum is as catalyst for chemical reactions; it has been employed in this area since 1800's.[10] One of the most important uses of platinum is the production of anti-cancer drugs. As a precious metal, large amounts of platinum are also consumed in jewellery. Some other fieldsthat platinum is used for are electronics, laboratory equipment, spark plugs, turbine engines and oxgen sensors.[11]

There is abundant archeological evidence that platinum was worked by the Indians of Equator and Colombia, many hundreds of years before the Spanish explorers in South America re-discovered the source of platinum in the Choco region (of Colombia) in 1550. The Incas prized platinum more than other precious metals, recognizing its rarity, and the fact that it never tarnishes; they sometimes alloyed it with silver and gold. [12]

European scientist met with the first actual platinum sample to be subjected to scientific investigation when it was brought in 1741 by Charles Wood.[10] Soon after it started to attract scientists. In 1817, a new property of platinum was introduced by Sir Humphry Davy to the Royal Society, that, it was a major catalyst, being capable of promoting a chemical reaction without undergoing any change itself.[10] One of the most important platinum complexes, *cis*-[$Pt(NH_3)_2Cl_2$] (cis-platin) was synthesized by Michele Peyronne (known as Peyronne's Chloride) in 1845; however, the importance of this complex as an anti-cancer agent was not known until 1969 when it was discovered by Prof. B. Rosenberg. [13-15]

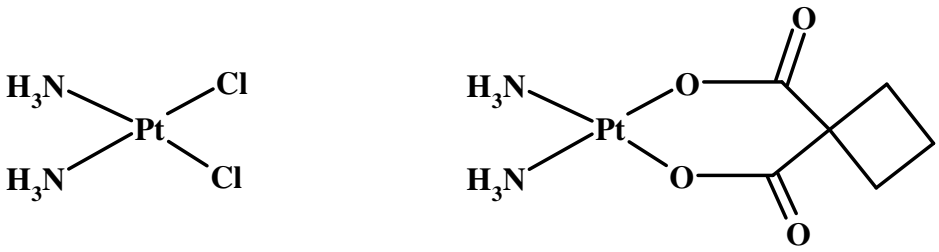

Fig. 1.1: *Cisplatin: cis-diamminedichloroplatinum(II) (left), Carboplatin: (1,1-cyclobutanedicarboxylato)-diammineplatinum(II) (right)*

Prof. Rosenberg and his co-workers were investigating the effect of an electric field on the growth processes in *Eschericha coli* bacteria.[13,16] They observed that cell division was inhibited but that cell growth was not affected illustrated by the formation of long filamentous rods.[13] Later, they discovered that the bacterial elongation they were observing was caused by electrolysis product, *cis*-diamminedichloroplatinum(II), generated from the platinum electrodes they were using. This accidental discovery prompted scientists to perform a series of investigations and studies into the effects of platinum compounds and cell division. Today, *cis*-platin is used in the treatment of various cancers, including small cell lung cancer, ovarian cancer and germ cell tumors. However, the *trans* isomer of it has no efficiency as a chemotherapeutic agent like *cis* isomer; It has been suggested that

trans isomers are inactive because they are more reactive than *cis*-derivatives; thus they are expected to react more rapidly with body constituents, reducing their selectivity.[17] Furthermore, it is thought that the *cis* isomer is active because of its chelating ability with biological molecules, such lesions are not possible with *trans* isomer.[13] Later in 1989, another platinum(II) complex carboplatin (1,1-cyclobutanedicarboxylato)-diammineplatinum(II)) was reported to be active also in cancer therapy [13] (Fig. 1.1, right).

Organoplatinum(II) complexes play a crucial role in catalytic processes to synthesize important organic compounds. A significant development in this area was presented by Periana, Taube et. al. in 1998 for the oxidative conversion of methane to methanol through a C-H bond activation at greater than 70% one pass yield based on methane using dichloro-(η^2 -{2,2´-bipyrimidyl})platinum(II), [(bpym)$PtCl_2$] as a catalyst.[18]

While platinum(II) compounds have proven their potential in biological applications such as in cancer therapy and in industrial applications as homogeneous catalysts, Pt^{IV} chemistry has also drawn enormous attention over the last two decades (Shilov process),[19,20] Puddephatt, Goldberg, et. al. have demonstrated experimentally that five-coordinate cationic Pt^{IV} complexes are involved as key intermediates along the reaction coordinates for Pt^{II}/Pt^{IV}-mediated C-X (X = halide, OR, etc) bond-breaking or -making processes.[21] Remarkably, such coordinative unsaturated platinum(IV) species were found to be isolable by applying bulky anionic N,N-chelating ligands.[21-24] Moreover, platinum(IV) complexes such as CHIP (*cis*-dichloro-*trans*-dihydroxo-bis-isopropylamineplatinum(IV))[25] and JM216 (*cis*-dichloro-*trans*-diacetato-aminecyclohexylmineplatinum(IV))[26] have been subject of several clinical trials for the cancer treatment, where the latter is particularly interesting in that it has axial acetate ligands which increase its lipophilicity and allow it to be administered orally.[27]

The fac-trialkylplatinum(IV) and its halides, $[R_3PtX]$, share a formal correspondence with *fac*-tricarbonylrhenium(I) and its halides, $[(OC)_3ReX]$, in terms of chemical and configurational stability and with respect to the qualitative electronic structure ($5d^6$ configuration).[28] Whereas the [*fac*-$Re(CO)_3]^+$ group exhibits low-energy metal-to-ligand charge transfer (MLCT) absorptions and metal-based oxidation which is often

accompanied by CO dissociation[29-31], the oxidation of [*fac*-$PtMe_3$]$^+$-containing complexes may primarily involve the formally carbanionic organic ligands.[32] Thus, a comparison of these two systems with the same chelate ligands is noteworthy.

Methylplatinum compounds are of interest due to their stability in both +II and +IV oxidation states of the metal.[33] They are capable of single electron transfer reactivity because of the electron rich metal carbon σ-bond which can interact with low lying π* acceptor orbitals. In contrast to the alkyl compounds of the electropositive main group elements, some of the "late" transition metals form metal alkyl bonds with diminished polarity and reactivity especially when high metal oxidation states compensate for the basicity of one or more alkyl ligands.[28] Intense low-energy absorptions due to charge transfer in the excited state[29b,34] (sometimes specified as single bond-to-ligand charge transfer, SBLCT) and even radical formation[35] can be observed as a consequence.[28] while methylplatinum (II) complexes have been studied with respect to Shilov-type C-H bond activation, multiply methylated Pt^{IV} systems are often obtained as stable products of methylation or oxidative addition reactions and vice versa, as starting materials for reductive elimination processes.[20b,36] $[PtMe_3I]_4$, known as the first trimethylplatinum(IV)-halide complex was first synthesized by Pope and Peachey[37] in 1907, and its structural feature was determined long time after through the end of 1960's.[38,39] Later in 1975 Baldwin and Kaska developed the synthetic route of this very stable compound.[40] Related Cl and Br tetramers can also be synthesized by following the same route.

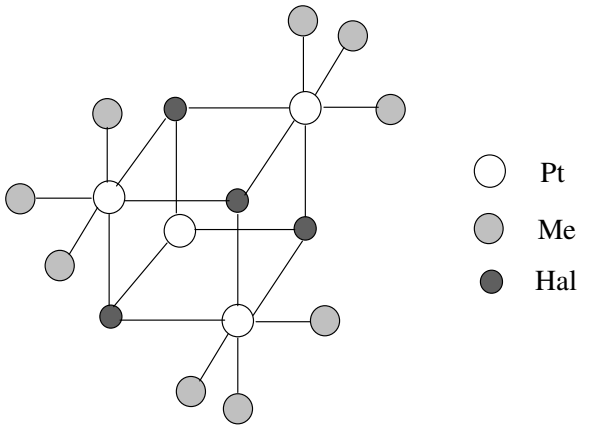

Fig. 1.2: *Molecular structure of $[PtMe_3X]_4$ (X: halogen)*[38]

Throughout this doctoral work several chelating α-diimine complexes of $[Pt(CH_3)_3X]_4$ (X: Cl, Br, I) were synthesized, characterized and electrochemically investigated.

Chapter 2 deals with the syntheses, characterization, structural and electrochemical investigations of 3,6-bis(2-pyridyl)-1,2,4,5-tetrazine (bptz) and 3,6-bis(2-(4-methylpyridyl))-1,2,4,5-tetrazine (bmptz) compounds with organometallic $[Pt(CH_3)_3X]_4$ (X: Cl, Br, I) fragments. Results found in the TD-DFT calculations of *fac*-$Pt(CH_3)_3Cl$(bptz) and *fac*-$Pt(CH_3)_3Br$(bptz) are also presented. In the last part of the chapter, spectroscopic and electrochemical properties of previously synthesized and structurally characterized $Pt(abpy)Me_3Br$[41] (abpy: 2,2´-azobispyridine) will be presented and compared with reported $Re(CO)_3X(abpy)$ (X: Cl, Br, I)[42] complexes.

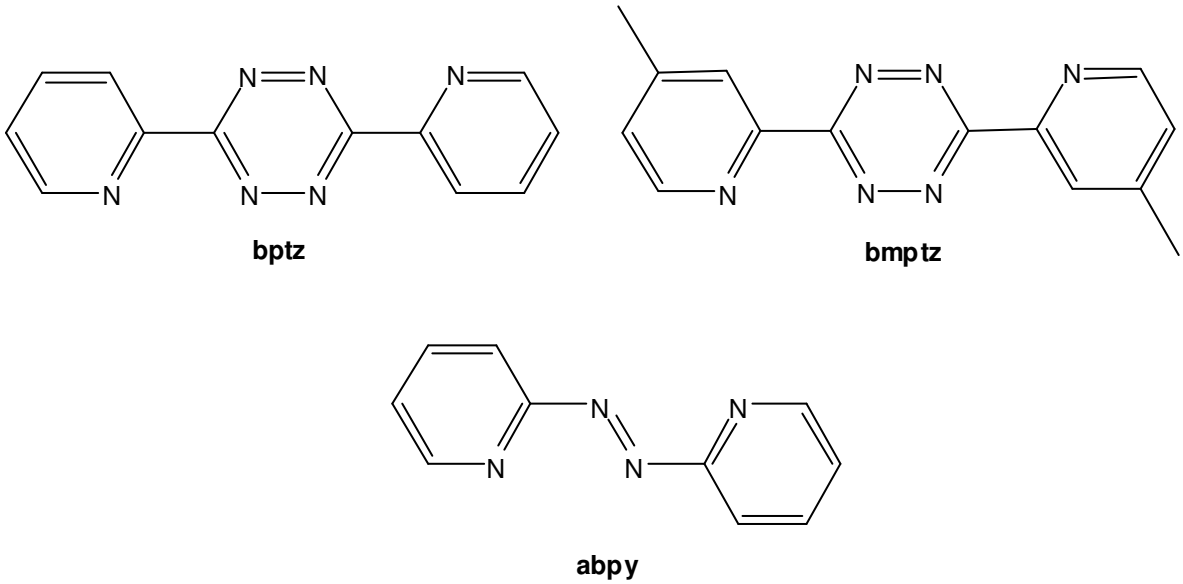

Fig. 1.3: *The ligands bptz, bmptz and abpy*

In chapter 3, complexes of the $[PtMe_3I]_4$ precursor with imidazole containing bis(1-methylimidazol-2-yl)glyoxal (big), bis-(1-methyl-2-imidazolyl)ketone (bik) and the products resulting from the reaction of the same precursor with two newly synthesized ligands 2,3-bis(1-methylimidazol-2-yl)quinoxaline (bmiq) and 2,3-bis(1-methylimidazol-2-yl)7,8-dimethylquinoxaline (dibmiq) ligands are described. The X-ray structural investigation as well as the electrochemical properties of *fac*-$Pt(CH_3)_3I$(big) and *fac*-$Pt(CH_3)_3I$(bik) are presented. Furthermore the results of the DFT calculations for these two well characterized compounds and the possible

products of the reaction of $[PtMe_3I]_4$ with bmiq are shown and compared with those experimental results.

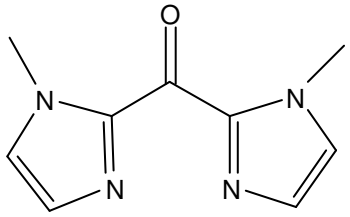

bik

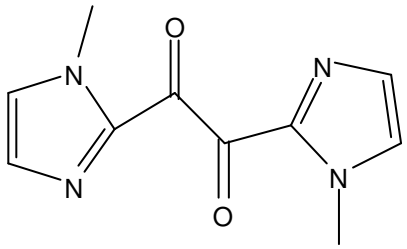

big

Fig. 1.4: *The ligands bik and big*

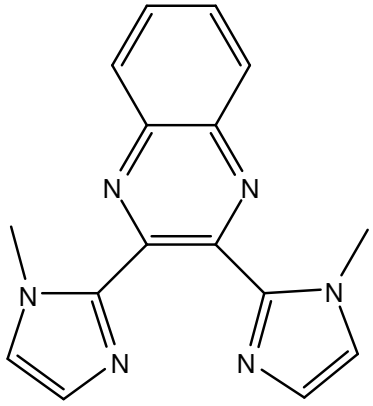

bmiq

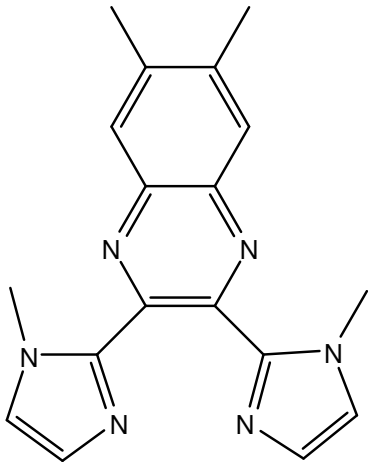

dibmiq

Fig. 1.5: *The ligands bmiq and dibmiq*

Chapter 4 deals with the rectangular complex $[\{Pt(CH_3)_3\}_4(\mu\text{–bp})_2(\mu\text{–bpym})_2](OTf)_4$ (bp: 4,4´-bipyridine, bpym: 2,2´-bipyrimidine). Molecular rectangles are taking attention especially due to their potential electron reservoir properties and size selective hosting capabilities against small molecules due to their cavities. In this chapter, the synthesis, analytical characterization and the electrochemical properties of the compound are presented. The data found are compared with those of the similar, previously synthesized $[Re_4(CO)_{12}(\mu\text{-bp})_2(\mu\text{-bpym})_2](OTf)_4$[43] complex.

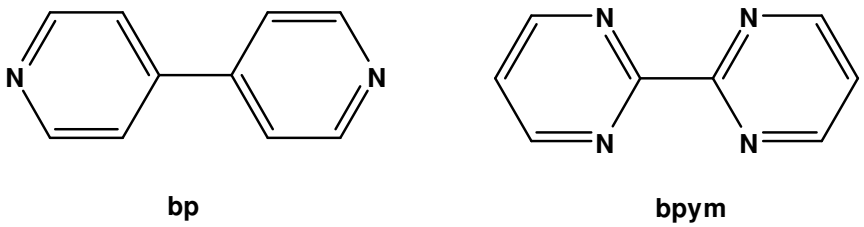

bp **bpym**

Fig. 1.6: *The ligands used in chapter 4*

Finally in chapter 5, the reaction between [Pt$(CH_3)_3$bpy](OTf) and the TCNX ligands (TCNX: TCNB, 1,2,4,5-tetracyanobenzene; TCNE, tetracyanoethene; and TCNQ, 7,7,8,8-tetracyano-*p*-quinodimethane) are described. The results of the reactions are discussed and supported by analytical analyses and cyclic voltammetry techniques.

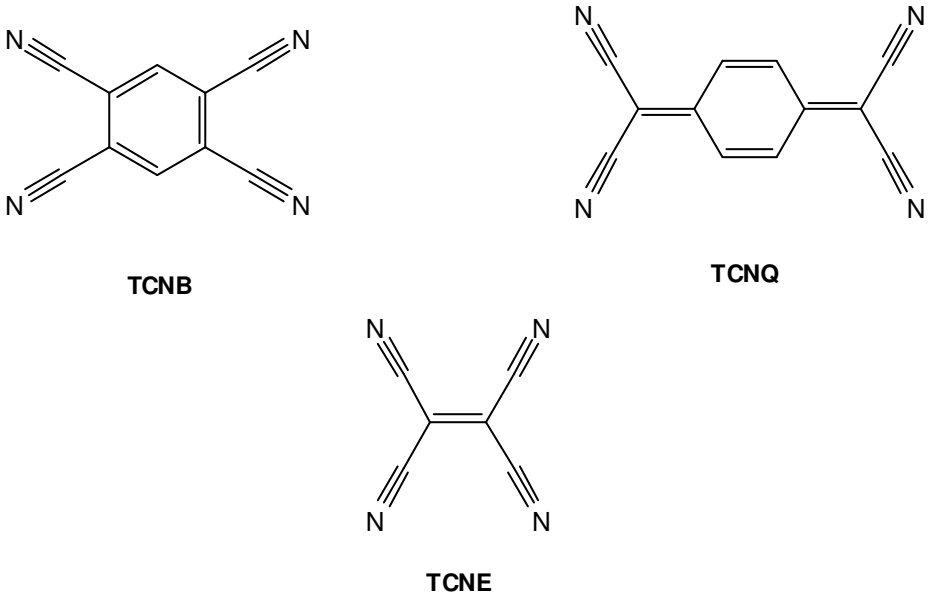

TCNB **TCNQ**

TCNE

Fig. 1.7: *TCNX ligands*

CHAPTER 2

Pt^{IV} Complexes of Tetrazine Containing Ligands

2.1 Introduction

Ligands which can serve as molecular bridges between metal centers and also contain a delocalized π system have received considerable attention in recent years[44]. Among these ligands 1,2,4,5-tetrazines and their 3,6-disubstituted derivatives have become increasingly popular for their potential use as electron propagating components.[45,46]

The insertion of four electronegative nitrogen atoms in a benzoid six-membered ring to form 1,2,4,5-tetrazines gives them interesting properties. In addition to the capacity of very efficient metal-metal bridging, these systems are distinguished by a very low lying π* orbital localized at the nitrogen atoms[47] which is responsible for facile reduction (electron transfer and hydrogenation)[48] and low-energy electronic transitions observable in absorption and emission.[49] Typically, the low-energy transitions of 1,2,4,5-tetrazines are of internal π–π^* or n-π^* character[49], however, it is also possible to observe intense metal-to-ligand charge transfer (MLCT, d-π^*) transitions at rather long wavelengths in the presence of electron rich metals coordinated via the N lone pairs. [45,50]

Tetrazines tend to display well-resolved EPR hyperfine structure in the radical complexes because the spin is virtually localized at the four nitrogen centers (a_u as spin bearing singly occupied MO).[45] Thus the first partially resolved EPR spectrum of a Ru-bpy type radical complex was observed for $\{(\mu\text{-bptz})[Ru(bpy)_2]_2\}^{\bullet+}$.[51] However, there are some instances where the metal-hyperfine structure in such complexes is difficult to obtain under normal X band EPR conditions because of line broadening, low abundance of the spin bearing metal isotope (e.g. Fe, Ru or Os) or overlapping of lines. In such cases, resolution of the g-anisotropy (Δg) by carrying out measurements at higher frequencies (95 GHz and above) provides a most sensitive

EPR parameter to investigate the electronic structure and in particular to estimate the amount of spin on the metals.[52]

Two degenerate Kekulé structures can be drawn for the 1,2,4,5-tetrazines. The parent compound (R=H in Fig. 2.1.1) was first synthesized by Hantzsch and Lehmann in 1900.[53]

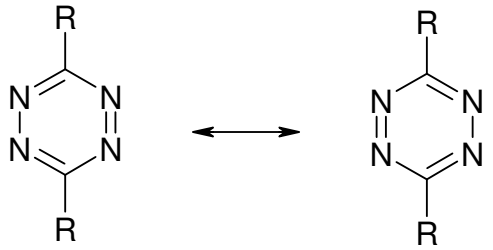

Fig. 2.1.1: *Kekulé structures for 1,2,4,5-tetrazines[52]*

The parent 1,2,4,5-tetrazine has not been used frequently in coordination chemistry owing to difficulties in preparation and handling (m.p. 99 ^{0}C, subl).[45] Of the easier accessible 3,6-disubstituted tetrazines, especially the bis-(2-pyridyl) derivatives 3,6-bis(2-pyridyl)-1,2,4,5-tetrazine (bptz)[50] and 3,6-bis(2-(4-methylpyridyl))-1,2,4,5-tetrazine (bmptz)[52,54] have been used. Both ligands are known to form stable radical complexes.[55]

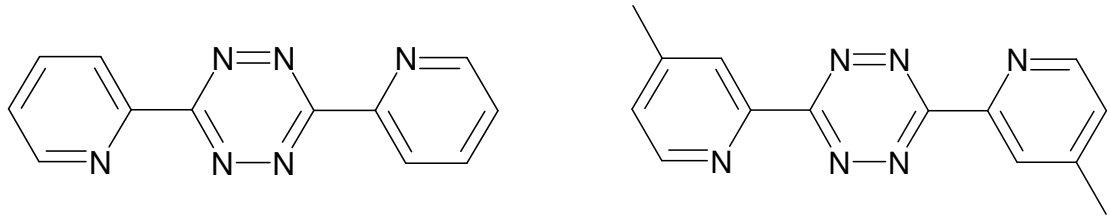

1 **2**

Fig. 2.1.2: *The ligands bptz (left) and bmptz (right)*

Bridging ligands involving the azo-group –N=N– as coordinating π-acceptor function can yield dinuclear complexes with unusual electronic and structural features.[56] Among these azo-containing ligands, 2,2´-azobispyridine (abpy)[57] is the most eminent in coordination chemistry,[56] first referred to by Baldwin, Lever and Parish.[58]

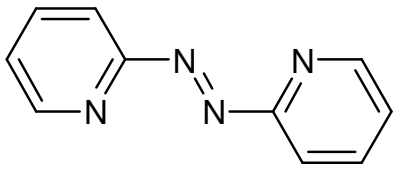

3

Fig. 2.1.3: *The ligand abpy*

Formally derived from the ubiquitous 2,2-bipyridine (bpy), its ability to bridge two metal centers at a distance of about 5 Å via edge-sharing of two five-membered chelate rings (S-frame configuration), the small size of its π-system and the low lying π^* orbital make the abpy very special ligand suitable for studying metal-metal interaction across an unsaturated bis-chelating molecular bridge.[56] Such ligands have become important for studies of intramolecular electron transfer[59], magnetic coupling[60] and mixed-valence chemistry.[61]

In this chapter, the syntheses, characterization, structural and spectroelectrochemical investigations of the [$PtMe_3X$] (X: Cl, Br, I) complexes of bptz and bmptz ligands will be discussed. Additionally, the last section of the chapter is devoted to the spectroscopic and electrochemical properties of previously synthesized and structurally characterized Pt(abpy)Me_3Br[41] and its comparison with reported $Re(CO)_3X$(abpy) (X: Cl, Br, I).[42]

2.2 Syntheses

[$PtMe_3X]_4$

The precursors $[PtMe_3X]_4$ (X: Cl, I) were synthesized by a modification of the route explained in the literature.[62] MeLi was added dropwise into a suspension of K_2PtX_6 (X: Cl, I) in dry and degassed diethylether (DEE) in an ice bath under argon atmosphere. The yellow K_2PtCl_6 and the black K_2PtI_6 suspensions both became white after stirring for one day.

$$K_2PtX_6 + 3MeLi \xrightarrow[1\ day]{DEE} 1/4[PtMe_3X]_4 + 3LiX + 2KX$$

Fig. 2.2.1: *General reaction scheme for the synthesis of* $[PtMe_3X]_4$ *(X: Cl, I)*

Although the reaction stoichiometry requires a 1:3 mole ratio of K_2PtX_6 to MeLi, an at least 6 fold excess of MeLi is needed for a good yield. Similar results were also reported by Clegg and Hall [63], although their synthesis differs somewhat from the one presented here. On the following day, 10% of HCl was slowly added to the suspension in ice bath in order to destroy the excess of MeLi. The colour of the solution became black having two phases. With the help of a seperatory funnel, the organic phase was separated from the inorganic phase, evaporated under vacuum, and the solid was washed several times with ethyl acetate.

$[PtMe_3Br]_4$ was obtained by a halogen exchange reaction. The $[PtMe_3Cl]_4$ was dissolved in CH_2Cl_2 (DCM) and reacted with 4 equivalent of NaBr solution in methanol for three days.

$$1/4[PtMe_3Cl]_4 + 4\ NaBr \xrightarrow[3\ days,\ RT]{DCM/Methanol} 1/4[PtMe_3Br]_4 + 4NaCl$$

Fig. 2.2.2: *Reaction scheme for the synthesis of* $[PtMe_3Br]_4$

After removal of the solvents, the residue was treated with CH_2Cl_2 and stirred. The mixture was filtered and CH_2Cl_2 was again added to the solid. After stirring and filtering, the filtrates were combined and the solvent removed. The colourless residue was washed with methanol to remove any NaCl remained.

fac-Pt(CH$_3$)$_3$X(bptz), _fac_-Pt(CH$_3$)$_3$I(bmptz), _anti_-[(μ-bmptz){_fac_-PtXMe$_3$}$_2$]

Mononuclear *fac*-Pt$(CH_3)_3$X(bptz) complexes were prepared by reacting $[PtMe_3X]_4$ (X: Cl, Br, I) with bptz in 1:1 ratio at room temperature in benzene. Similarly, equal moles of bmptz and $[PtMe_3I]_4$ were mixed in CH_2Cl_2 at room temperature to produce *fac*-Pt$(CH_3)_3$I(bmptz).

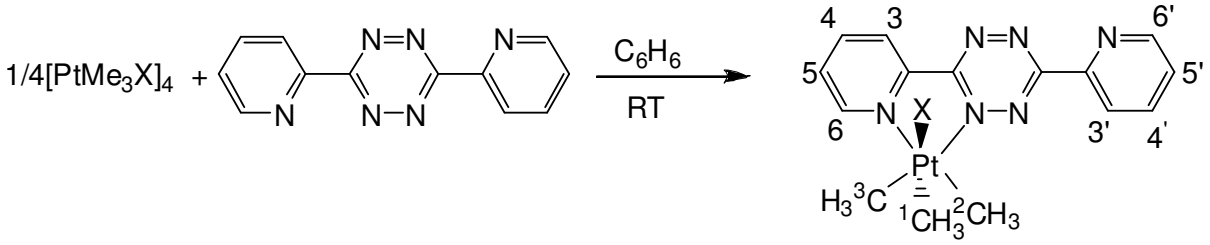

4a-c

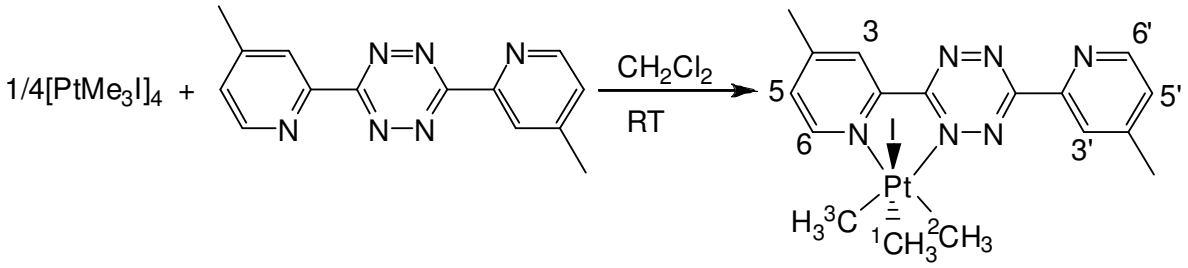

5

Fig. 2.2.3: *Reaction schemes for the synthesis of fac-Pt$(CH_3)_3$X(bptz) (X: Cl (**4a**), Br (**4b**), I (**4c**)) (top) and fac-Pt$(CH_3)_3$I(bmptz) (bottom)*

To obtain dinuclear bmptz complexes, the molar ratio of the Pt^{IV} precursor to the bmptz was doubled and the reaction was performed at room temperature in benzene.

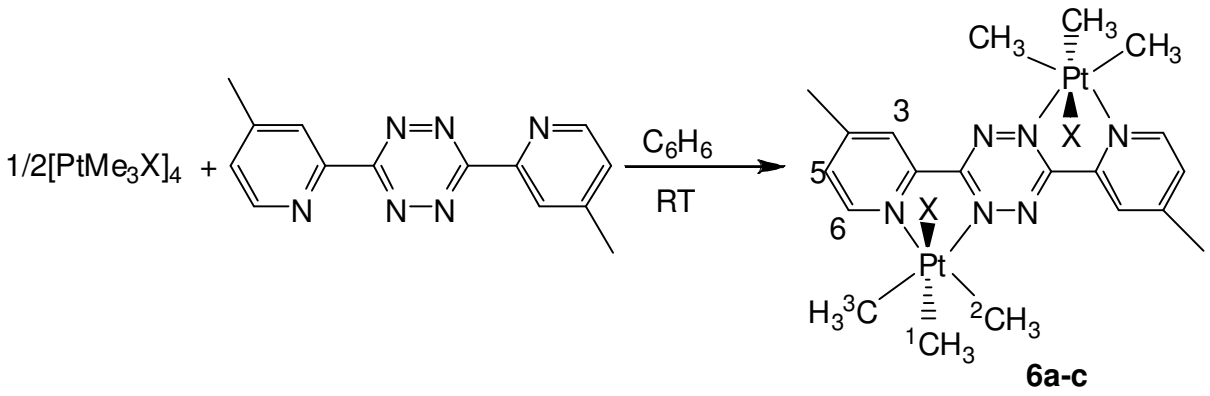

Fig. 2.2.4: *Reaction scheme for the synthesis of anti-[(μ-bmptz){fac-Pt(CH$_3$)$_3$X}$_2$] [X: Cl (**6a**), Br (**6b**), I (**6c**)]*

The pure products were obtained after washing with benzene several times and precipitating in dichloromethane/hexane mixture. It was not possible to obtain dinuclear bptz complexes, even when a fourfold excess of platinumtrimethylhalide was used. None of the complexes are light or air sensitive.

2.3 Characterization

^{1}H-NMR Spectroscopy

The complexes were characterized by ^{1}H-NMR, elemental analyses and mass spectroscopy. The details of CHN analysis and mass spectroscopy are given in chapter 6. The ^{1}H-NMR data of the complexes are summarized in Table 2.3.1 and 2.3.2.

The comparison of the NMR spectra of the free ligand and of related metal complexes shows clear evidence for the coordination of the metal-complex fragments to the chelating N atoms of the free ligand to form five-membered rings. For this reason, ^{1}H-NMR spectra can be used as an analytical method to judge the purity of the synthesized complexes.

Through the coordination of the metal center to the free bmptz or bptz ligands, the ^{1}H-NMR signals of the pyridine rings in the aromatic region exhibit downfield shifts. The different halogens have little different influence on these chemical shifts of the signals. The H^6 and H^3 signals in the spectrum of complex **4c** are overlapping. The expected ^{195}Pt satellites as a result of Pt-H couplings can be well identified, especially in the binuclear bmptz complexes. For the bptz complexes, these satellites could not be discriminated well because of the low signal-to-noise ratio of the spectra.

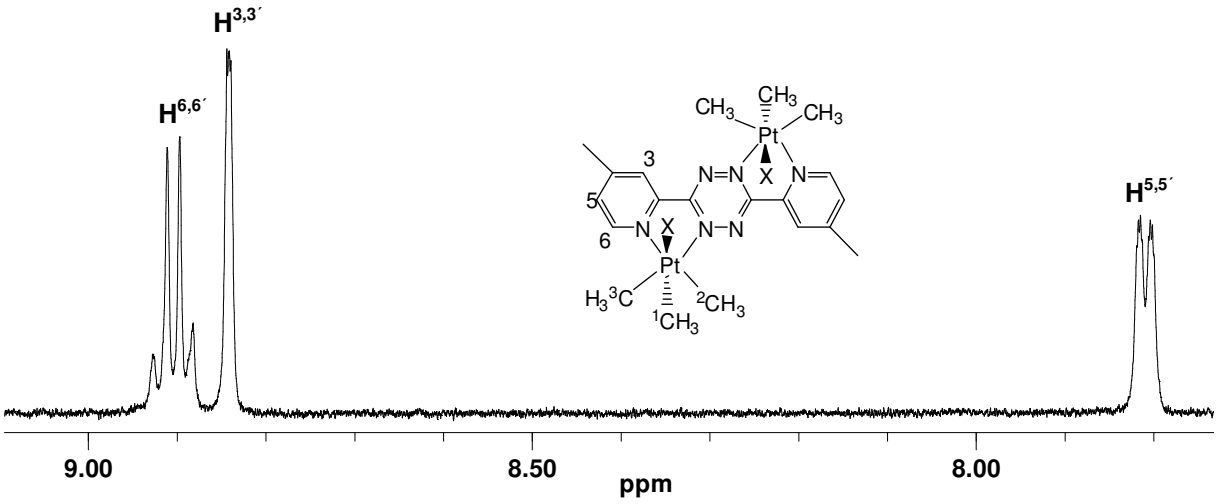

Fig. 2.3.1: *^{1}H-NMR spectrum (aromatic region) of **6b** measured in $CDCl_3$*

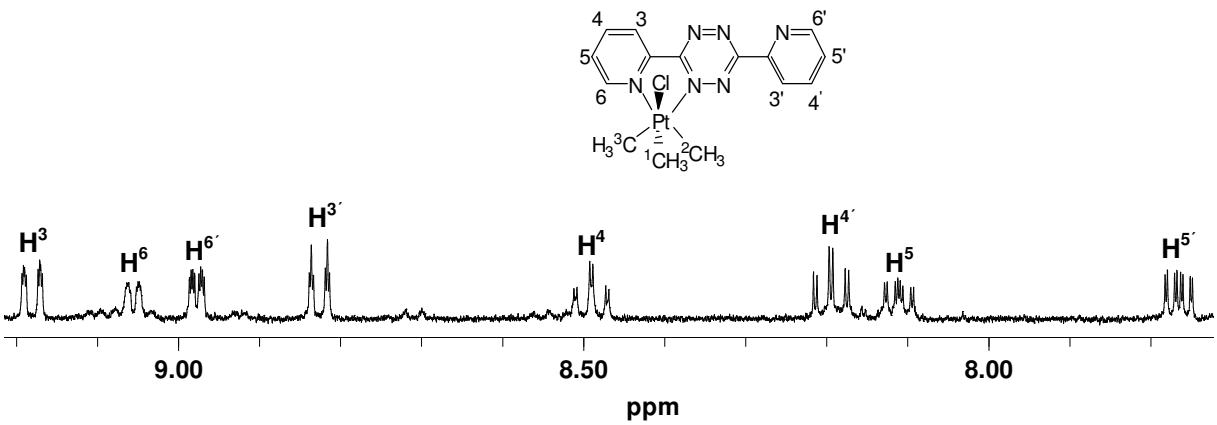

Fig. 2.3.2: *^{1}H-NMR spectrum (aromatic region) of **4a** measured in CD_3NO_2*

Eight different aromatic proton signals are observed for the mononuclear **4a, 4b** and **4c** complexes, whereas this number is six for **5** and three for dinuclear **6a, 6b** and **6c**. The existence of only one set of signals in the H-NMR spectra of dinuclear bmptz complexes points to the formation of exclusively one isomer, and its identity as the anti isomer was confirmed by X-ray crystallography mentioned in part 2.4.

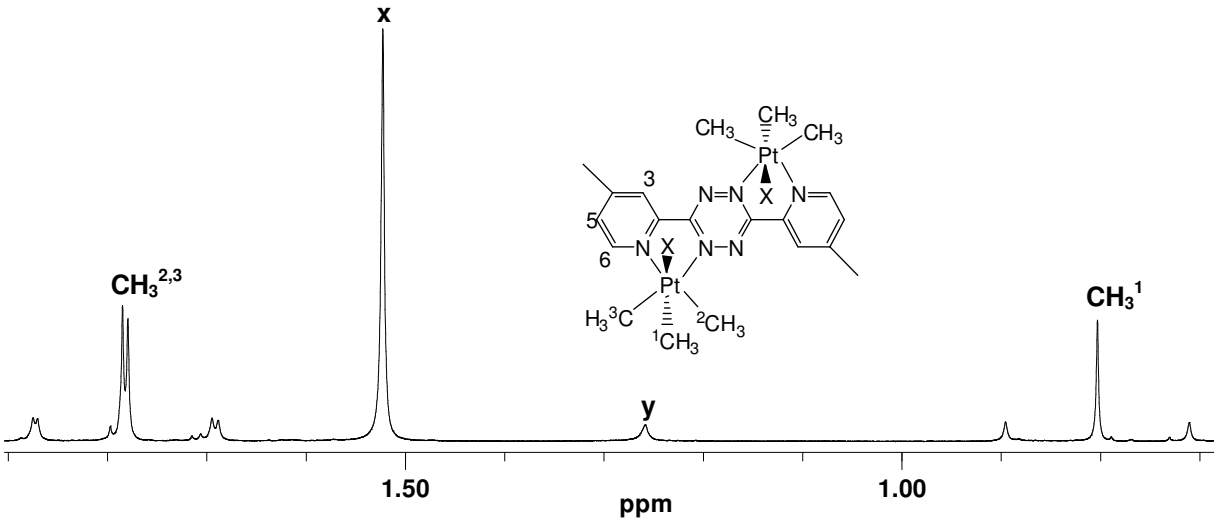

Fig. 2.3.3: *^{1}H-NMR spectra (aliphatic region) of **6b** measured in $CDCl_3$ (x: Water impurity, y: Solvent (hexane) peak)*

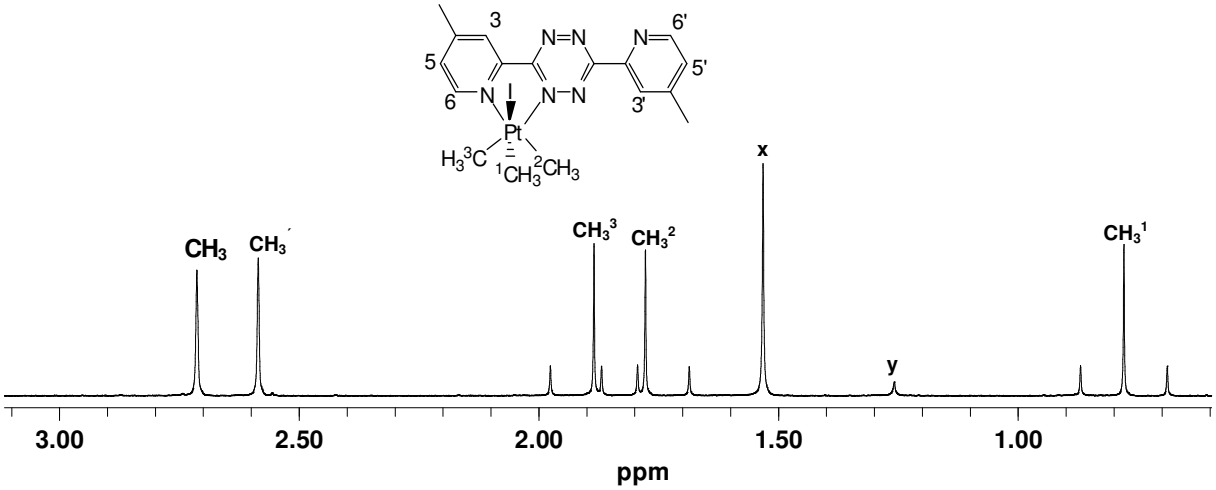

Fig. 2.3.4: *^{1}H-NMR spectra (aliphatic region) of **5** measured in $CDCl_3$. (x: Water impurity, y: Solvent (hexane) peak)*

The existence of two different singlets at 2.71 ppm and 2.59 ppm belonging to the methyl groups on the coordinated and the uncoordinated pyridine rings is proof for the formation of the mononuclear complex **5**. The corresponding methyl groups of the free bmptz ligand give one singlet at 2.55 ppm in the ^{1}H-NMR spectrum in $CDCl_3$.

Another point worth to discuss in the ^{1}H-NMR analyses of the complexes are the methyl signals accompanied by Pt-CH_3 couplings in the aliphatic region. Three well separated peaks with ^{195}Pt satellites are observed for the mononuclear complexes **4a-c** and **5** whereas the equatorial methyls give very close signals to each other in the case of dinuclear bmptz complexes (Fig. 2.3.3 and Fig. 2.3.4). The intensities of the platinum satellites are consistent with the natural abundance of ^{195}Pt (^{195}Pt: I = ½, 33.8% nat. abundance) for all complexes.

Table 2.3.1: *^{1}H-NMR spectroscopic data [a] (aromatic region) of ligands and their Pt^{IV} complexes in $CDCl_3$*

	δ [ppm]			
Complexes	**$H^{6,6´}$**	**$H^{5,5´}$**	**$H^{4,4´}$**	**$H^{3,3´}$**
1[b]	8.94	7.73	8.11	8.61
2	8.83	7.39	-	8.57
4a[c]	9.05/8.97	8.11/7.76	8.49/8.19	9.18/8.82
4b[c]	9.08/8.97	8.11/7.76	8.48/8.19	9.18/8.82
4c	9.12/9.04	7.93/7.66	8.30/8.07	9.12/8.78
5	8.92/8.88	7.71/7.47	-	8.91/8.57
6a	8.89	7.81	-	8.83
6b	8.90	7.81	-	8.84
6c	8.95	7.80	-	8.85

[a] Measurements were carried out in $CDCl_3$ unless stated otherwise. [b] In DMSO-d_6. [c] *In CD_3NO_2.*

Table 2.3.2: *^{1}H-NMR spectroscopic data [a] (aliphatic region) of ligands and their Pt^{IV} complexes in $CDCl_3$*

δ [ppm]				J [Hz]		
Complexes	**$^{1}CH_3$**	**$^{2}CH_3$**	**$^{3}CH_3$**	**Pt-$^{1}CH_3$**	**Pt-$^{2}CH_3$**	**Pt-$^{3}CH_3$**
4a[b]	0.58	1.42	1.51	75.10	72.25	72.04
4b[b]	0.68	1.51	1.59	74.92	72.71	72.36
4c	0.80	1.80	1.91	72.19	73.10	73.01
5	0.78	1.77	1.88	72.39	73.22	72.78
6a	0.71	1.70	1.71	74.49	72.38	71.85
6b	0.80	1.78	1.79	74.06	72.78	72.11
6c	0.91	1.89	1.90	71.87	73.60	72.75

[a] Measurements were carried out in $CDCl_3$ unless stated otherwise. [b] *In CD_3NO_2.*

2.4 Crystal Structures

***fac*-Pt(CH$_3$)$_3$Cl(bptz) (4a), *fac*-Pt(CH$_3$)$_3$Br(bptz) (4b) and *fac*-Pt(CH$_3$)$_3$I(bptz) (4c)**

X-ray quality crystals of **4a** and **4b** were obtained by slow evaporation of their nitromethane solutions while those of **4c** are grown by diffusion of hexane into nitromethane solution of the complex at -20 ^{0}C. All complexes show an expected [64c] *fac*-arrangement of the three methyl groups around the central platinum atom. X-Ray structures obtained for the samples are illustrated in Figs. 2.4.1-2.4.3, selected bond lengths and angles as well as some DFT-calculated values are summarized in Table 2.4.1. Crystallographic data and parameters are given in Chapter 6.4.1-6.4.3.

There are a number of bptz containing complexes in the literature; however, only a few of them were crystallographically investigated. This is presumably due to the low solubility of bptz containing complexes.

The complexes **4a-c** crystallize in the monoclinic $P2_1/c$ space group. Each of them has four molecules in their unit cell. The axial C1 atom of the complex **4c** had to be calculated isotropically, as it did not give a positive definition of the anisotropy. Fig. 2.4.1 illustrates the molecular structure of the complex **4a**.

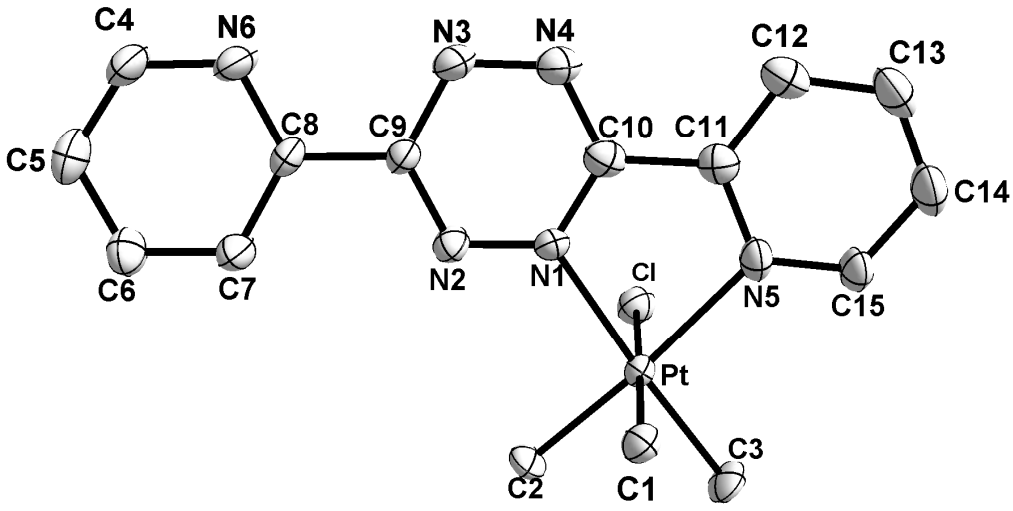

Fig. 2.4.1: *Molecular structure of **4a** in the crystal*

Table 2.4.1: *Selected bond lengths (Å) and the angles (^{0}) of the complexes*

Bond Lengths	**4a**	**4a** [1)]	**4b**	**4b** [1)]	**4c**
Pt-C1	2.117(7)	2.092	2.150(5)	2.094	2.257(13)
Pt-C2	2.041(7)	2.062	2.039(5)	2.066	2.035(16)
Pt-C3	2.042(7)	2.066	2.041(5)	2.069	2.069(18)
Pt-X[2)]	2.466(2)	2.461	2.5916(6)	2.615	2.7633(14)
Pt-N1	2.146(5)	2.123	2.147(4)	2.119	2.128(14)
Pt-N5	2.190(7)	2.199	2.185(4)	2.197	2.187(14)
N1-N2	1.319(7)	1.319	1.310(5)	1.318	1.38(2)
N4-N3	1.324(9)	1.321	1.315(6)	1.320	1.36(2)
N5-C11	1.384(9)	1.354	1.333(7)	1.340	1.32(2)
N5-C15	1.321(9)	1.339	1.338(7)	1.355	1.35(2)
C11-C10	1.463(10)	1.466	1.459(7)	1.465	1.46(2)
C9-C8	1.475(9)	1.462	1.479(7)	1.484	1.46(3)
N6-C4	1.341(10)	1.335	1.328(7)	1.334	1.33(3)
N6-C8	1.353(8)	1.344	1.340(6)	1.345	1.34(2)
N1-C10	1.342(9)	1.364	1.345(7)	1.363	1.39(2)
N2-C9	1.326(8)	1.345	1.350(6)	1.347	1.31(2)
Angles					
N1 - Pt - N5	76.6(2)	76.7	75.91(15)	76.9	75.3(6)
N1 - Pt - C1	89.2(2)	93.3	89.26(17)	96.3	89.0(6)
N1 - Pt - C2	98.3(3)	97.7	97.60(18)	95.9	98.2(6)
N1 - Pt - C3	176.4(3)	174.1	175.31(19)	173.4	174.5(7)
N1 - Pt – X[2)]	90.47(17)	89.9	90.59(11)	87.4	90.2(4)
C2 - Pt - C3	85.2(3)	88.2	86.9(2)	90.4	87.2(8)
N2 - N1 - Pt	124.2(4)	126.4	124.1(3)	126.3	124.2(11)
Pt - N1- C10	115.8(5)	115.6	115.7(3)	115.3	117.9(11)
Pt - N5- C11	114.2(5)	114.2	114.9(3)	114.1	115.7(12)
Pt - N5- C15	127.0(5)	126.7	125.5(4)	127.1	127.7(13)

*[1)] From DFT calculations. [2)] X: Cl (**4a**), Br (**4b**), I (**4c**)*

The complexes have an octahedral structural configuration around the platinum(IV) metal center. The N1-Pt-N5 bite angles were found at 76.6^0, 75.9^0, and 75.3^0, respectively, from **4a** to **4c**. The same angle for two crystallographically different but structurally similar $Pt(bpym)Cl_2$ molecules was reported to be 78.7^0 and 80.8^0 in the literature.[41]

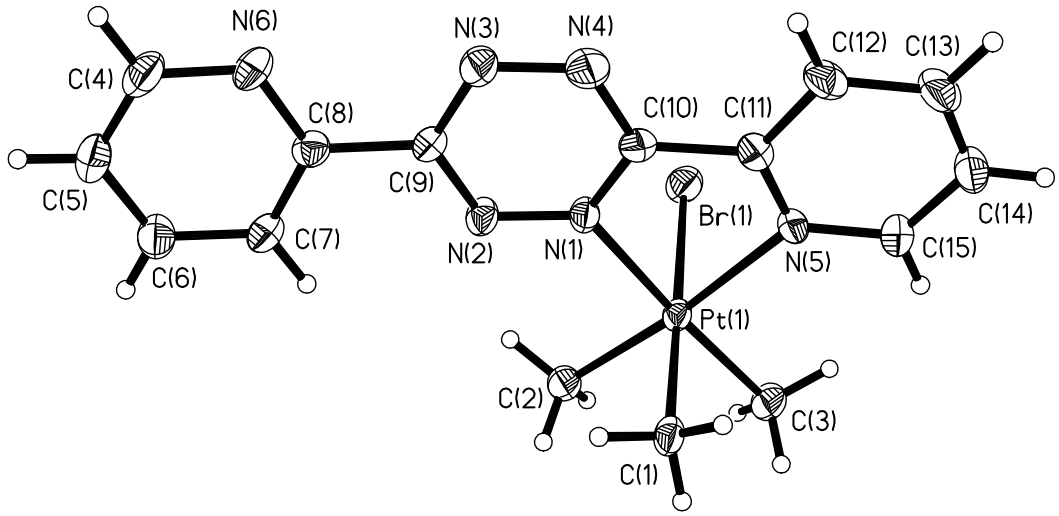

Fig. 2.4.2: *Molecular structure of* ***4b*** *in the crystal*

The N4–C10–C11–C12 torsional angle of the molecule **4a** at 0.16^0 indicates co-planarity whereas the N3–C9–C8–N6 torsional angle at 6.73^0 shows the uncoordinated pyridine ring slightly twisted with respect to the tetrazine ring. Similar results were also obtained for the bromide complex, where these angles are 0.05^0 and 5.78^0. On the other hand, the crystal data of **4c** show that both these angles, (-3.32^0 and 6.97^0, respectively) diverge more from planarity.

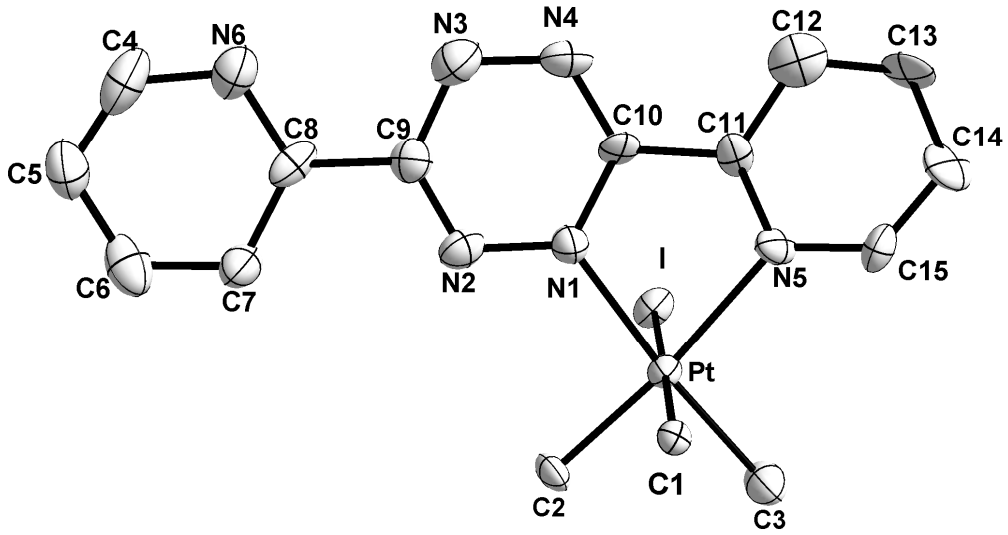

Fig. 2.4.3: *Molecular structure of* ***4c*** *in the crystal*

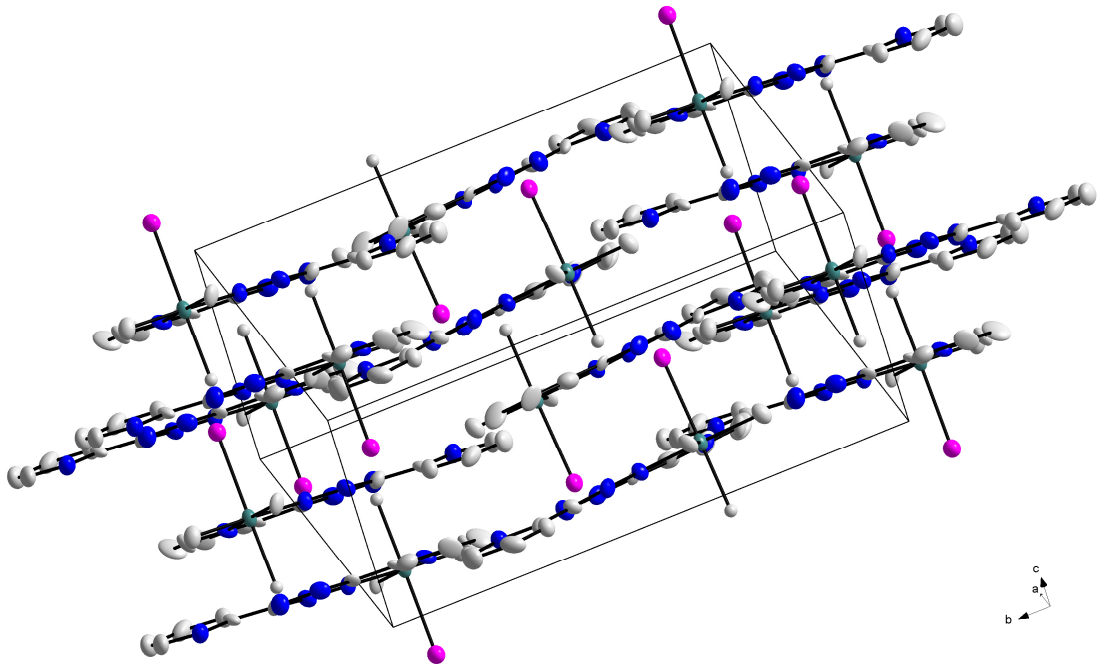

Fig. 2.4.4: *Arrangement of* ***4c*** *in the unit cell*

The Pt–C bond lengths vary according to the cis/trans influence [33,64] , i.e. the methyl group in trans position to the π-donating halide ligand exhibits a longer bond to the metal.[28] This effect is most pronounced for **4c**, where the Pt-C_{ax} bond distance is the longest (see table 2.4.1). Similar results given in (α-dimiine)$PtMe_4$ type complexes were mentioned to be a result of LLCT/SBLCT σ(Pt-C)→π* transitions.[64a,65-67] This effect is more efficient in bptz complexes than the previously reported bpym and abpy complexes of $[PtMe_3X]_4$. The Pt-C_{ax} bond lengths of Pt(bpym)Me_3Br, Pt(abpy)Me_3Br and Pt(abpy)Me_3I were found 2.053(18), 2.112(9) and 2.065(9) respectively.[41] Such transitions together with MLCT transitions are observed as weak bands in the visible area of the absorption spectra of the complexes (see part 2.5) and also described theoretically in part 2.6.

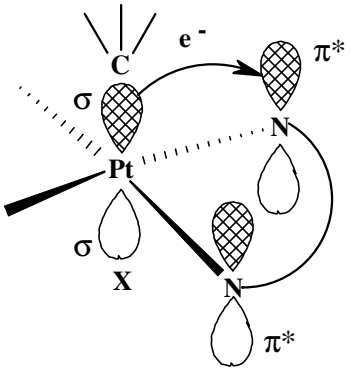

Fig. 2.4.5: *Possible SBLCT transition*[41]

Moreover, the Pt-$N_{pyridine}$ bond distances are somewhat longer than the Pt-$N_{tetrazine}$ bonds, reflecting that the tetrazine ring is a better π acceptor. Thus, a better back donation from $[Me_3Pt]^+$ to the coordinating N atom of the tetrazine ring results in shorter Pt-$N_{tetrazine}$ distances compared to Pt-$N_{methylpyridine}$. This was similarly shown earlier for a heterodinuclear complex of bptz, $[(C_5Me_5)ClRh(\mu\text{-bptz})Re(CO)_3Cl](PF_6)$.[68]

Pt$(CH_3)_3$I(bmptz) (5), and *anti*-[(μ-bmptz){*fac*-PtXMe_3}$_2$] (X:Cl (6a), Br (6b), I (6c))

Single crystals of the complexes *anti*-[(μ-bmptz){*fac*-Pt$ClMe_3$}$_2$], *anti*-[(μ-bmptz){*fac*-Pt$BrMe_3$}$_2$] and *anti*-[(μ-bmptz){*fac*-PtIMe_3}$_2$] were obtained by slow diffusion of hexane into the CH_2Cl_2 solutions of the complexes at -20^{0}C whereas the *fac*-Pt$(CH_3)_3$I(bmptz) was crystallized by slow evaporation of a benzene-CH_2Cl_2 solution mixture. Crystallographic data and parameters are given in Chapter 6. The molecular structures of the compounds are shown in Figs. 2.4.6-2.4.10. Selected bond lengths and angles of **6a-c** are listed in Table 2.4.2-2.4.4 and of **5** in Table 2.4.5.

Each of the dinuclear complexes **6a** and **6b** has 16, whereas **6c** and **5** have four molecules in their unit cells. **6a-b** crystallized in the orthorhombic *Fddd* space group, **6c** in triclinic $P\bar{1}$, and **5** in monoclinic $P2_1/c$. All of the complexes have a *fac*-arrangement of the methyl groups around the platinum centers.

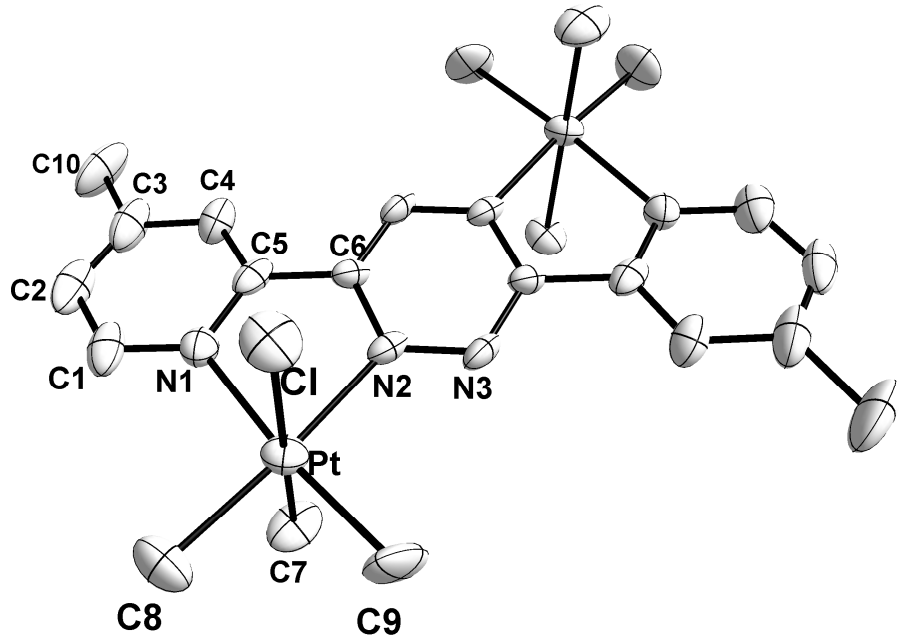

Fig. 2.4.6: *Molecular structure of* ***6a*** *in the crystal*

There are 4 structurally similar but crystallographically independent molecules in the unit cell of **6c**. Due to the low quality of the crystals of this compound, the hydrogen atoms around C7 atom could not be calculated. A benzene molecule co-crystallized with complex **5**.

Table 2.4.2: *Selected bond lengths (Å) and the angles (^{0}) of the complexes **6a** and **6b***

Distances	**6a**	**6b**
Pt-C8	2.048 (13)	2.073(16)
Pt-C7	2.057 (13)	2.084(19)
Pt-C9	2.091 (14)	2.041(17)
Pt-N2	2.118 (10)	2.137(11)
Pt-N1	2.177 (11)	2.195(14)
Pt-X[1)]	2.487 (3)	2.6064(17)
N1-C1	1.362 (16)	1.308(19)
N1-C5	1.381 (17)	1.388(19)
N2-N3	1.326 (13)	1.300(16)
N2-C6	1.359 (15)	1.357(18)
N3-C6	1.338 (15)	1.328(19)
C6-C5	1.463 (16)	1.475(19)
Angles		
C8—Pt—C7	88.0 (7)	85.5(8)
C8—Pt—C9	87.4 (7)	87.8(7)
C7—Pt—C9	87.4 (7)	91.0(8)
C8—Pt—N2	175.7 (6)	175.1(6)
C7—Pt—N2	94.2 (5)	94.6(6)
C9—Pt—N2	96.4 (5)	97.0(6)
C8—Pt—N1	99.9 (6)	97.5(6)
C7—Pt—N1	90.4 (5)	88.1(6)
C9—Pt—N1	172.3 (6)	174.5(6)
N2—Pt—N1	76.4 (4)	77.6(4)
C8—Pt—X	92.8 (5)	94.1(6)
C7—Pt—X	179.1 (5)	178.6(6)
C9—Pt—X	93.0 (5)	90.3(6)

[1)] *X : Cl for **6a**, Br for **6b***

The molecular structures of the complexes **6a-c** show little differences on going from chloride to iodide. Each of these dinuclear complexes possesses an inversion center. They have an anti arrangement of the halides with respect to the ligand plane. Such an anti configuration for the two halide ligands with respect to the central plane was also established structurally for the related {(μ-abpy)[$Re(CO)_3X]_2$} (X: Cl, Br, I) complexes.[42] The dihedral angles between the methylpyridine rings and the central tetrazine ring of **6a-c** range from 3.75° to 6.95^0, where **6c** has the most planar conformation and the **6a** deviates most from planarity. For the dirhenium complexes mentioned above a similar trend was also observed.[42] This angle for the free ligand (bmptz) was reported to be 10.5°.[52] Thus, a planarization between the methylpyridine rings and the tetrazine ring caused by metal fragment coordination occurs. A similar result can also be concluded for *fac*-$Pt(CH_3)_3I$(bmptz), where the coordinated methylpyridine ring and the tetrazine ring form a dihedral angle of 6.45^0, and the angle between the uncoordinated methylpyridine ring and the tetrazine ring is 12.92^0.

Table 2.4.3: *Selected bond lengths (*Å) of **6c**

Pt1-C8	2.049(14)	Pt2-C19	2.012(18)	Pt3-C28	2.048(15)	Pt4-C39	2.027(15)
$Pt1-C7_{(ax)}$	2.048(19)	$Pt2-C17_{(ax)}$	2.036(15)	$Pt3-C27_{(ax)}$	2.073(14)	$Pt4-C37_{(ax)}$	2.072(16)
Pt1-C9	2.041(18)	Pt2-C18	2.040(17)	Pt3-C29	2.052(14)	Pt4 C38	2.032(15)
Pt1-N2	2.161(12)	Pt2-N5	2.143(13)	Pt3-N8	2.135(11)	Pt4-N11	2.140(12)
Pt1-N1	2.168(14)	Pt2-N4	2.153(13)	Pt3-N7	2.172(12)	Pt4-N10	2.160(13)
Pt1-I1	2.7877(14)	Pt2-I2	2.7571(14)	Pt3-I3	2.7935(11)	Pt4-I4	2.7788(11)
N1-C1	1.351(19)	N4-C11	1.35(2)	N7-C21	1.329(19)	N10-C31	1.339(19)
N1-C5	1.334(18)	N4-C15	1.348(19)	N7-C25	1.385(19)	N10-C35	1.357(19)
N2-N3	1.315(17)	N5-N6	1.308(19)	N8-N9	1.315(16)	N11-N12	1.298(16)
N2-C6	1.324(19)	N5-C16	1.360(19)	N8-C26	1.356(17)	N11-C36	1.347(19)
N3-C6	1.349(18)	N6-C16	1.345(19)	N9-C26	1.346(18)	N12-C36	1.341(18)
C6-C5	1.48(2)	C15-C16	1.46(2)	C25-C26	1.45(2)	C35-C36	1.467(19)

The Pt-halogen bond lengths of the complexes **6a-c** vary according to the halide size. Unlike in **4a-c**, there is no significant difference between Pt-C_{ax} and Pt-C_{eq} bond lengths for all three dinuclear and the mononuclear **5** complexes. As a result of more planar structure of **6c,** the Pt-Pt distance in this molecule (6.95 Å) is slightly longer than that of **6a** and **6b**, which are 6.91 Å and 6.93 Å, respectively.

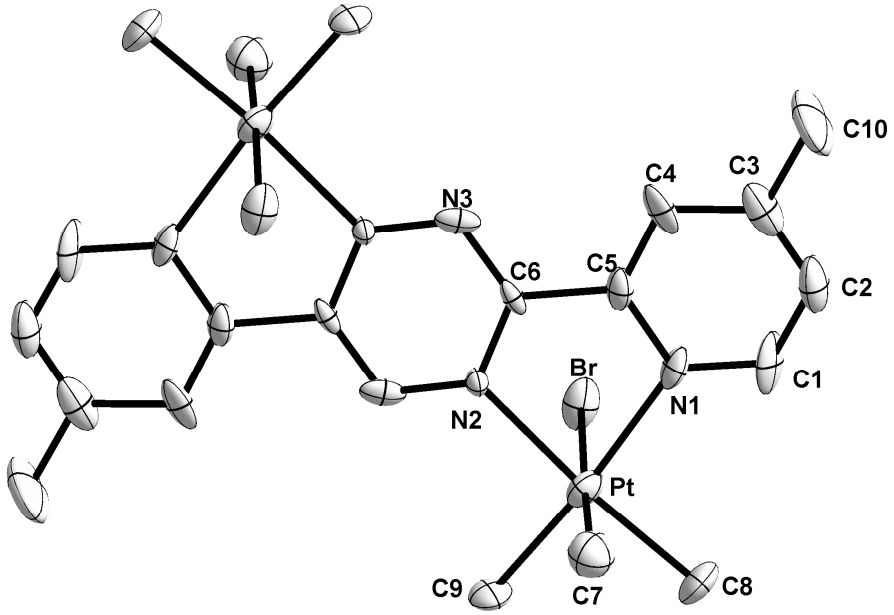

Fig. 2.4.7: *Molecular structure of* ***6b*** *in the crystal*

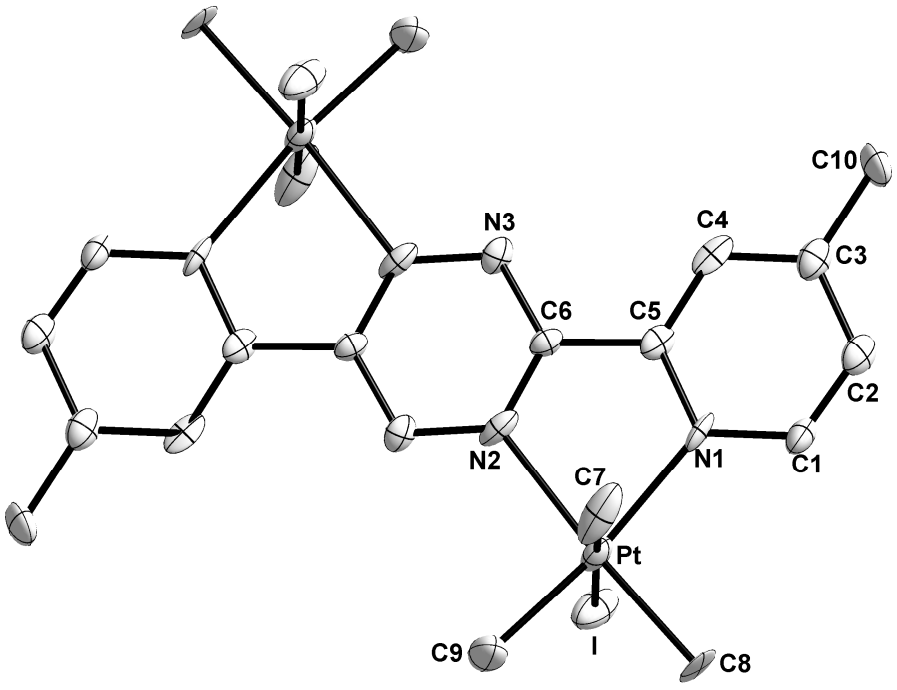

Fig. 2.4.8: *Molecular structure of* ***6c*** *in the crystal*

Table 2.4.4: *Selected angles (^{0})* of ***6c***

C9-Pt1-C7	85.5(9)	7C28-Pt3-C29	87.3(6)
C9-Pt1-C7	85.5(9)	C28-Pt3-C27	86.0(7)
C7-Pt1-C8	89.1(8)	C29-Pt3-C27	88.8(6)
C9-Pt1-N2	97.5(6)	C28-Pt3-N8	176.7(5)
C7-Pt1-N2	89.8(6)	C29-Pt3-N8	95.9(5)
C8-Pt1-N2	175.9(6)	C27-Pt3-N8	93.1(6)
C9-Pt1-N1	172.3(6)	C28-Pt3-N7	99.7(5)
C7-Pt1-N1	90.1(7)	C29-Pt3-N7	172.9(6)
C8-Pt1-N1	99.9(6)	C27-Pt3 N7	90.7(5)
N2-Pt1-N1	76.1(5)	N8-Pt3-N7	77.1(4)
C9-Pt1-I1	95.0(7)	C28-Pt3-I3	92.5(4)
C7-Pt1-I1	179.2(5)	C29-Pt3-I3	93.8(5)
C8-Pt1-I1	90.3(6)	C27-Pt3-I3	176.9(5)
C19-Pt2-C17	86.2(8)	C39-Pt4-C38	86.6(7)
C19-Pt2-C18	87.9(9)	C39-Pt4-C37	89.8(8)
C17-Pt2-C18	84.5(8)	C38-Pt4-C37	86.5(7)
C19-Pt2-N5	97.2(7)	C39-Pt4-N11	97.5(6)
C17-Pt2-N5	95.4(6)	C38-Pt4-N11	175.8(6)
C18-Pt2-N5	175.0(7)	C37-Pt4-N11	92.3(5)
C19-Pt2-N4	173.3(7)	C39-Pt4-N10	174.1(6)
C17-Pt2-N4	91.6(6)	C38-Pt4-N10	98.9(6)
C18-Pt2-N4	98.2(7)	C37-Pt4-N10	88.3(6)
N5-Pt2-N4	76.8(5)	N11-Pt4-N10	77.0(5)
C19-Pt2-I2	92.4(6)	C39-Pt4-I4	91.0(6)
C17-Pt2-I2	175.8(5)	C38-Pt4-I4	93.6(5)
C18-Pt2-I2	91.5(6)	C37-Pt4-I4	179.2(5)

Similar to the data of the complexes **4a-c**, the Pt-$N_{tetrazine}$ distances are shorter compared to Pt-$N_{methylpyridine}$ in **6a-c** and **5**, in **6a** it is the shortest at 2.118(10) Å, as a result of a stronger back donation from organoplatinum to the coordinating N atom of the tetrazine ring of the ligand.

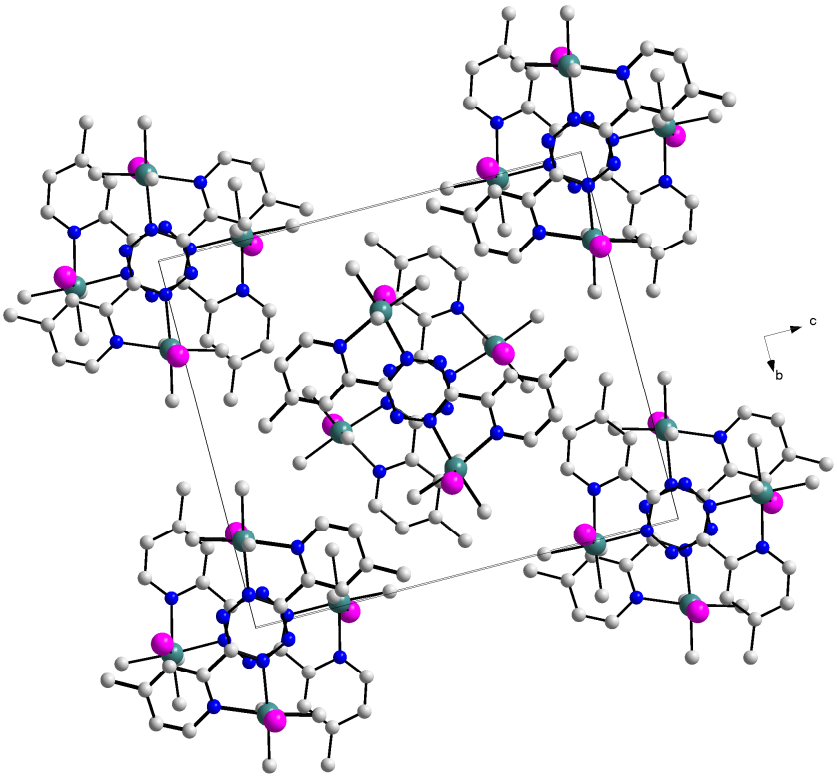

Fig. 2.4.9: *Arrangement of **6c** in the unit cell*

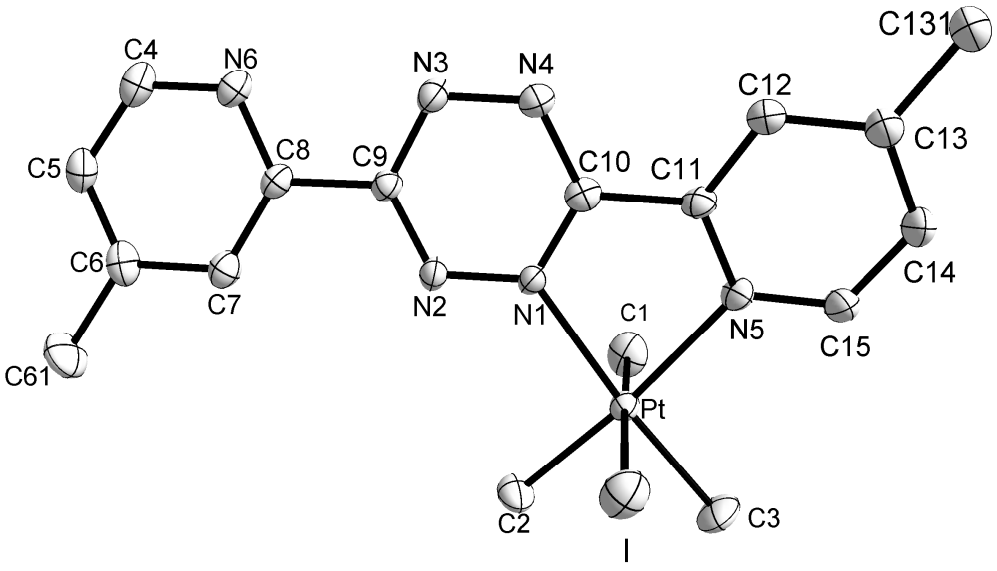

Fig. 2.4.10: *Molecular structure of **5** in the crystal*

Table 2.4.5: *Selected bond lengths (Å) and angles (^{0}) of complex* ***5***

Pt-C1	2.064(7)	C11-C10	1.476(8)
Pt-C2	2.041(6)	C9-C8	1.487(8)
Pt-C3	2.044(7)	N5-C15	1.331(8)
Pt-N1	2.148(5)	N5-C11	1.356(7)
Pt-N5	2.169(5)	N6-C8	1.340(8)
Pt-I	2.7912(6)	N6-C4	1.337(8)
N1-N2	1.334(6)	N1-C10	1.344(7)
N3-N4	1.333(7)	N2-C9	1.335(8)

N1-Pt-N5	76.44(18)	C3-Pt-I	92.2(2)
C2-Pt-C3	86.8(3)	C1-Pt-I	178.4(2)
C3-Pt-N1	175.1(3)	C10-N1-Pt	115.5(4)
C3-Pt-N5	98.8(3)	C11-N5-Pt	115.1(4)
C2-Pt-C1	87.8(3)	N2-N1-Pt	126.3(4)
C3-Pt-C1	87.7(3)	N1-C10-C11	117.0(5)
C2-Pt-N1	98.0(2)	N2-C9-C8	117.1(5)
C1-Pt-N1	91.3(3)	N5-C11-C10	115.4(5)
C1-Pt-N5	91.0(3)	N6-C8-C9	116.2(5)
C2-Pt-I	93.8(2)	N4-C10-C11	118.7(5)
C2-Pt-N5	174.3(2)	N3-C9-C8	117.7(5)
N1-Pt-I	88.66(14)	C7-C8-C9	120.0(5)

2.5 Electrochemistry

Cyclic Voltammetry

In order to study the redox behaviour of the complexes, cyclic voltammetry measurements were carried out. Table 2.5.1 summarizes the electrochemical data of the complexes.

fac-Pt(CH_3)$_3$Cl(bptz) (4a), *fac*-Pt(CH_3)$_3$Br(bptz) (4b) and *fac*-Pt(CH_3)$_3$I(bptz) (4c)

fac-Pt(CH_3)$_3$Cl(bptz) shows a reversible reduction wave at $E_{1/2}$= -0.74 V vs. $[FeCp_2]^{+/o}$ at room temperature in DMF / 0.1 M Bu_4NPF_6, which can be assigned to addition of one electron to the π^* orbital of the bptz ligand (Fig. 2.5.1). The easier reduction of **4a** than free bptz ligand is due to the capacity for σ-polarization exerted by platinum metal center. Similarly, reversible reduction was also observed for Pt(bptz)Cl_2.[41] The second reduction at -2.25 V was not reversible which can be attributed to the release of Cl^- halide. Previous studies of tetrazine complexes[45] showed generally very large differences of >1.0 V between the first and second reduction while the (irreversible) oxidation of the $PtMe_3X$ group must involve the halide or carbanionic ligands.[33]

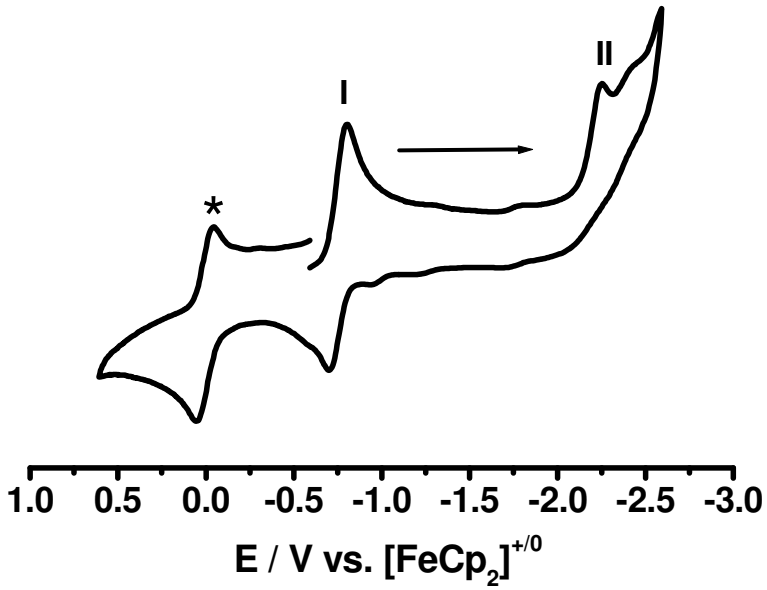

Fig. 2.5.1: *Cyclic voltammogram of **4a** in DMF / 0.1 M Bu_4NPF_6 at RT with a scan rate of 100 mV/sec*
**: ferrocene wave*

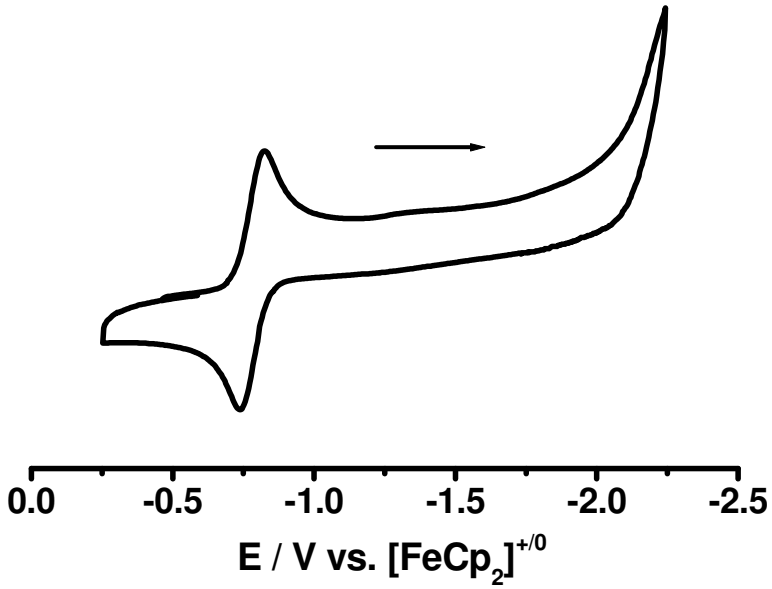

Fig. 2.5.2: *Cyclic voltammogram of* ***4b*** *in CH_2Cl_2 / 0.1 M Bu_4NPF_6 at –40 ^{0}C with a scan rate of 100 mV/sec*

fac-$Pt(CH_3)_3Br(bptz)$ (**4b**) exhibits irreversible reduction behaviour at room temperature. However, it is reversibly reduced at $E_{1/2}$ = -0.78 V vs. $[FeCp_2]^{+/o}$ at -40 ^{0}C in CH_2Cl_2 / 0.1 M Bu_4NPF_6 (Fig. 2.5.2). On the other hand, no reversibility was observed on reducing complex **4c** in the same solvent at both room temperature and -40 ^{0}C. These results suggest that among these three complexes, **4a** is the most stable complex upon one electron reduction. A comparable $E_{1/2}$ potential at -0.72 V vs. $[FeCp_2]^{+/o}$ for $Re(CO)_3Cl(bptz)$ complex was reported in the literature. [68]

Table 2.5.1: *Electrochemical Potentials[a] of ligands and the complexes from cyclic voltammetry[b]*

Compound	E_{pa}[c]	E_{pc}(I)[d]	E_{pc}(II)[e]	Solvent
4a	-	-0.74	-2.25	DMF
4b[f]	-	-0.78	-	CH_2Cl_2
6a	+1.40	-0.36	-1.86	CH_2Cl_2
6b	+1.02	-0.32	-1.80	CH_2Cl_2
6c	+0.73	-0.24	-1.71	CH_2Cl_2
Bptz[52]	-	-1.20	-2.81	DMF
Bmptz[52]	-	-1.23	-2.80	CH_3CN

[a] Potentials E in V vs. $FeCp_2^{0/+}$ (0.1 M Bu_4NPF_6 as electrolyte). [b] At 100 mV/s scan rate, at RT unless stated otherwise. [c] Anodic peak potential corresponding to an irreversible step. [d] Half-wave potential corresponding to a reversible step. [e] Cathodic peak potential corresponding to an irreversible step. [f] Measured at -40 ^{0}C.

$Pt(CH_3)_3I$(bmptz) (5), and *anti*-[(μ-bmptz){*fac*-$PtXMe_3$}$_2$] (X:Cl (6a), Br (6b), I (6c))

Whereas complex **5** decomposes on both reduction and oxidation in cyclic voltammetry, complexes **6a-c** display a similar electrochemical pattern as **4a** with the exception that the first electron reduction potentials are remarkably less negative at room temperature. Introducing a second electron acceptor metal fragment facilitates electron uptake.

The neutral *anti*-[(μ-bmptz){*fac*-$PtClMe_3$}$_2$] is reduced reversibly at $E_{1/2}$ = -0.36 V vs. $[FeCp_2]^{+/o}$ in CH_2Cl_2/0.1 M Bu_4NPF_6 to a persistent anion (Fig. 2.5.3) which can be assigned to the addition of one electron to the π* orbital of the bmptz ligand. Neither oxidation at +1.40 V anodic peak potential nor the second reduction at -1.86 V cathodic peak potential is reversible. Similarly, neutral anti-[(μ-bmptz){*fac*-$ReCl(CO)_3$}$_2$] was reported to have reversible reduction at $E_{1/2}$ = -0.26 V vs. $[FeCp_2]^{+/o}$.[52] In both cases it is remarkable that the first reduction step does not appreciably labilize the halides which would constitute excellent leaving groups.[33] Reductively caused metal-halide bond dissociation has been observed for several platinum metal complexes.[69]

Complex **6b** is reversibly reduced at a virtually same potential to **6a** ($E_{1/2}$ = -0.32 V vs. $[FeCp_2]^{+/o}$, Fig. 2.5.4) in CH_2Cl_2/0.1 M Bu_4NPF_6 forming a stable radical complex. The second reduction at E_{pc}: -1.80 V, which is assumed to involve the dissociation of the potential leaving group Br^- and the oxidation at Epa: +1.02 V were not reversible. The reduction potential compares with about –0.15 V vs. $[FeCp_2]^{+/o}$ for the similarly neutral *anti*-[(μ-bptz){*fac*-$ReBr(CO)_3$}$_2$].[30]

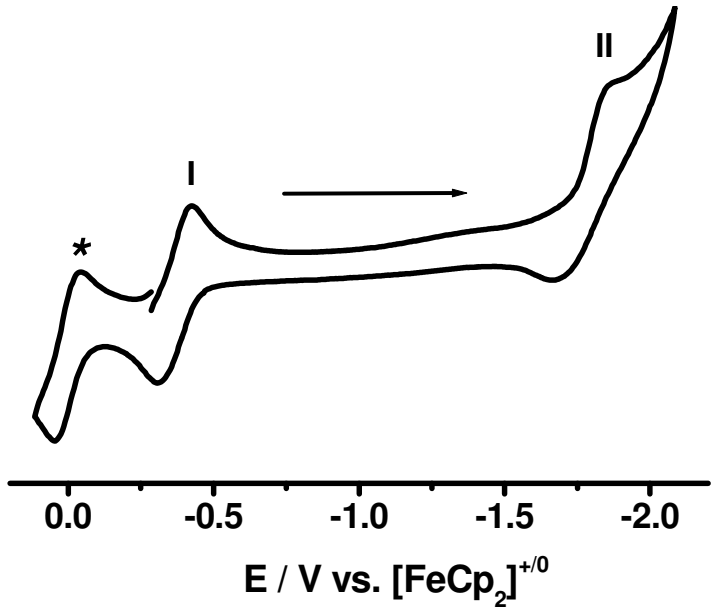

Fig. 2.5.3: *Cyclic voltammogram of* ***6a*** *in CH_2Cl_2 / 0.1 M Bu_4NPF_6 at RT with a scan rate of 100 mV/sec. *: ferrocene wave*

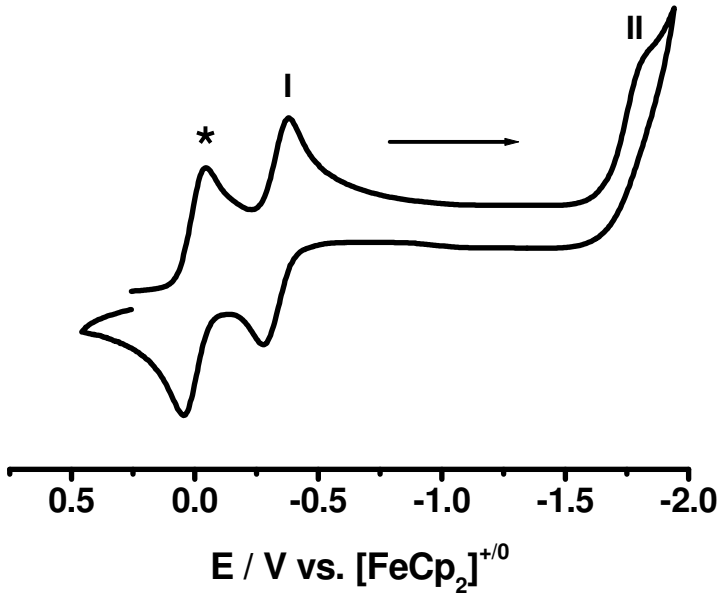

Fig. 2.5.4: *Cyclic voltammogram of* ***6b*** *in CH_2Cl_2 / 0.1 M Bu_4NPF_6 at RT with a scan rate of 100 mV/sec. *: ferrocene wave*

The neutral **6c** shows an even more facile reversible reduction at $E_{1/2}$ = -0.24 V vs. $[FeCp_2]^{+/o}$ in CH_2Cl_2/0.1 M Bu_4NPF_6. The second reduction with possible I^- dissociation at -1.71 V and the anodic wave at +0.73 V were not reversible. Fig. 2.5.5 illustrates the cyclic voltammogram of **6c**.

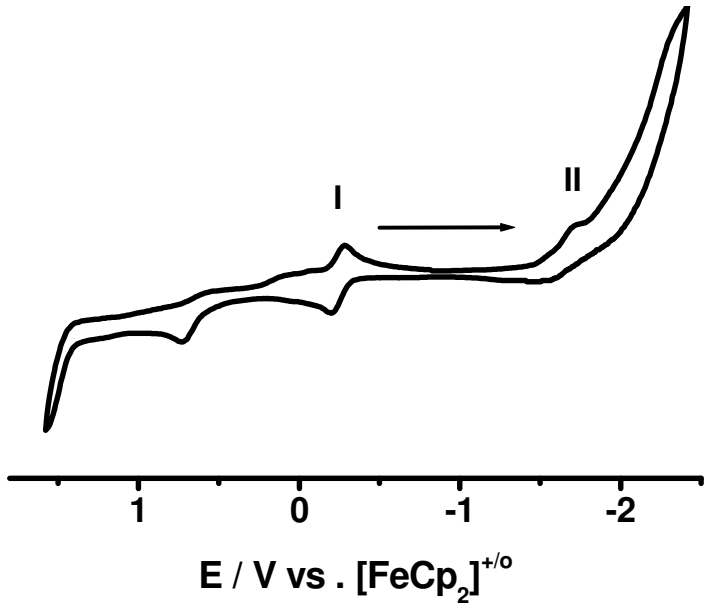

Fig. 2.5.5: *Cyclic voltammogram of* ***6c*** *in CH_2Cl_2 / 0.1 M Bu_4NPF_6 at RT with a scan rate of 100 mV/sec*

One interesting point worth discussing is the decrease of the second reduction potentials from **6a** to **6c**, indicating the progressive ease of metal-halide dissociation as the size of the halogen increases. This is indeed in agreement with the trend also observed for (a*bpy*)ReX(CO)$_3$ (X: Cl, Br, I) complexes.[42]

UV-Vis Spectroelectrochemistry

UV-Vis spectroelectrochemical investigations of the complexes **6a-c** were carried out in CH_2Cl_2 / 0.1 M Bu_4NPF_6 while **4a** was studied in DMF / 0.1 M Bu_4NPF_6 to overcome the solubility problem in an Optically Transparent Thin Layer Electrochemical (OTTLE)[70] cell. The measurements were performed to confirm the assumptions previously made on the reduction mechanism of these complexes. The results from the experiments are summarized in Table 2.5.2.

fac-Pt(CH$_3$)$_3$Cl(bptz), *fac*-Pt(CH$_3$)$_3$Br(bptz) and *fac*-Pt(CH$_3$)$_3$I(bptz)

Neutral *fac*-Pt$(CH_3)_3$Cl(bptz) exhibits an intense band in the UV-region with an absorption maximum at 300 nm ($\varepsilon = 16.7 \times 10^3$ M^{-1} cm^{-1}), and a broad band in the visible region at 500 nm ($\varepsilon = 1.4 \times 10^3$ M^{-1} cm^{-1}). The complex is not light sensitive.

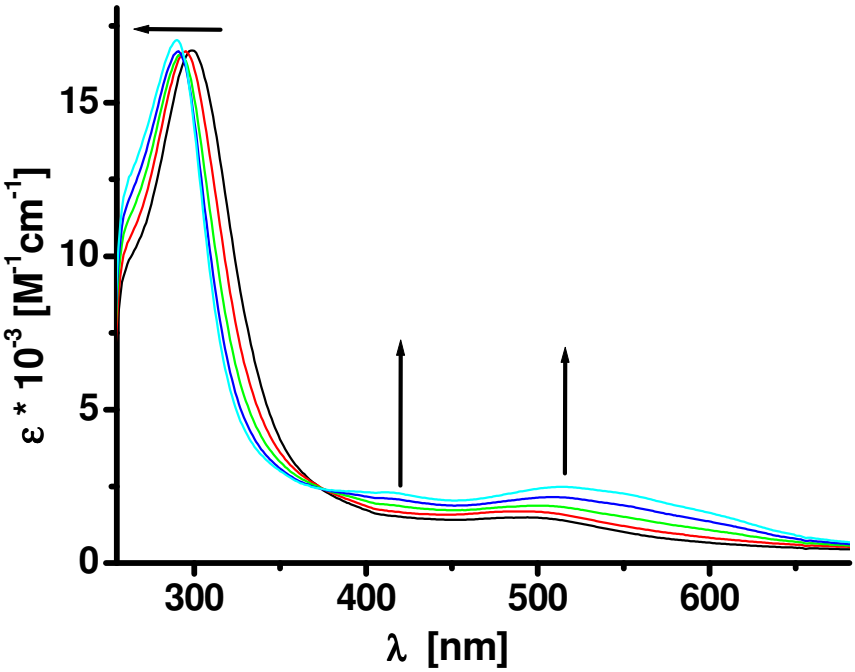

Fig. 2.5.6: *Uv-Vis Spectroelectrochemistry in DMF / 0.1 M Bu_4NPF_6 at RT of the transition* ***(4a)***$^{0\rightarrow(\bullet-)}$

The tetrazines have weak n-π* transitions around 550 nm (ε: 500 $M^{-1}cm^{-1}$) and intense π–π* transitions at about 300 nm.[45] For instance, free bmptz in dichloromethane has λ_{max} = 542 and 295 nm (ε = 430 and 22800 M^{-1} cm^{-1}), respectively.[33] In contrast to the non-reduced state, tetrazine radical anions exhibit no significant transitions in the UV-Vis or near infrared regions.

In addition to the intra-ligand transitions mentioned above, the intense singlet metal-to-ligand charge transfer (^{1}MLCT) bands in the UV region, possibly overlapping with the IL band and sigma-bond-to-ligand charge transfer (SBLCT) transitions and perhaps triplet features (^{3}MLCT) as further weak absorptions in the visible[33] should also be considered.

Table 2.5.2: *Absorption and UV-Vis spectroelectrochemical data of the complexes*

Compound	**λ_{max} [nm] (ε x 10^{-3} [M^{-1} cm^{-1}])**
4a	300 (16.7), 500 (1.4)
$4a^{\bullet-}$	289 (17.0), 413 (2.3), 513 (2.5)
4b[a)]	311 (23.2), 525 (0.46)
4c[a)]	312 (24.4), 498 (1.4)
5[a)]	314 (23.8), 497 (1.0)
6a	320 (22.9), 440 (3.0), 525 (2.5)
$6a^{\bullet-}$	268 (sh), 295 (19.3), 378 (sh), 493 (1.24), 530 (0.96)
6b	325 (27.0), 582 (1.64)
$6b^{\bullet-}$	270 (sh), 296 (24.2), 380 (sh), 495 (1.7), 532 (1.4)
6c	326 (28.2), 445 (5.3), 550 (2.55), 650 (2.1)
$6c^{\bullet-}$	268 (24.3), 295 (26.3), 379 (sh), 497 (1.72), 532 (1.4)

[a)] *Performed in CH_2Cl_2 solution at R.T.*

On one-electron reversible reduction of the complex **4a** (Fig. 2.5.6), the band at 300 nm makes a small shift to higher energy and appears at 289 nm ($\varepsilon = 17.0$ x 10^3 M^{-1} cm^{-1}) (IL and MLCT transitions) whereas the broad band in visible region is partially structured and appears at 413 ($\varepsilon = 2.3$ x 10^3 M^{-1} cm^{-1}) nm and at 513 nm ($\varepsilon = 2.5$ x 10^3 M^{-1} cm^{-1}). The latter two can be assigned to MLCT and SBLCT transitions. These assumptions are in good agreement with the theoretically found results for the model complex **4b** discussed in part 2.6.

Unlike **4a**, complexes **4b** and **4c** show no reversibility in the UV-Vis spectroelectrochemical investigation at room temperature.

Pt(CH$_3$)$_3$I(bmptz) (5), *anti*-[(μ-bmptz){*fac*-PtXMe$_3$}$_2$] (X:Cl (6a), Br (6b), I (6c))

Complexes **6a**, **6b** and **6c** in their neutral states show similar band patterns in the UV region with maxima at 320 ($\varepsilon = 22.9 \times 10^3$ M^{-1} cm^{-1}) 325 ($\varepsilon = 27.0 \times 10^3$ M^{-1} cm^{-1}) and 326 nm ($\varepsilon = 28.2 \times 10^3$ M^{-1} cm^{-1}), respectively, and absorption tails in the visible region until almost 650 nm.

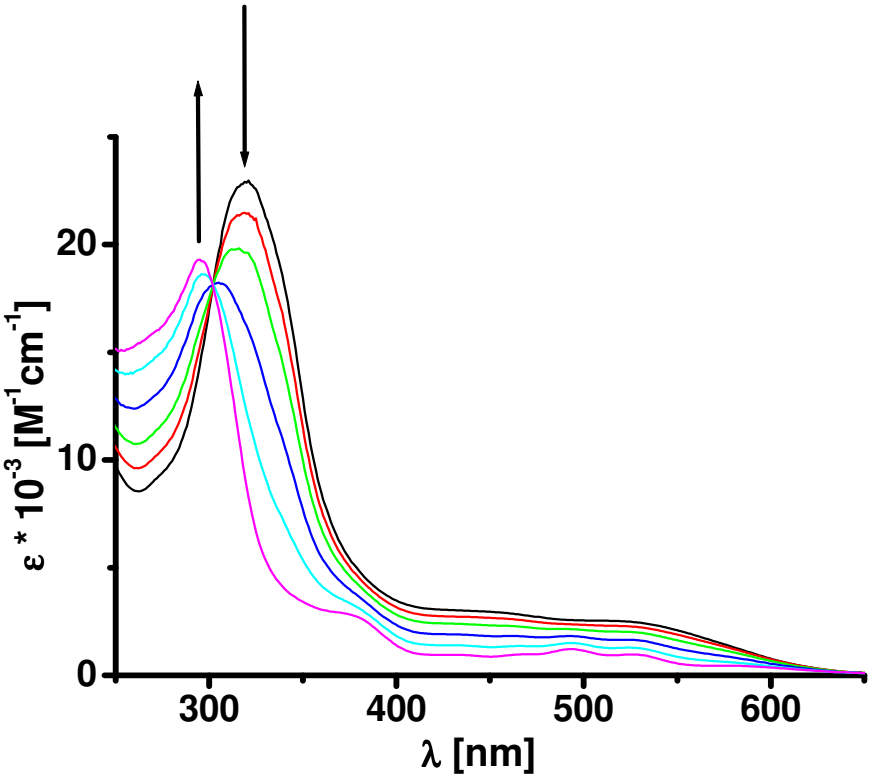

Fig. 2.5.7: *UV-Vis Spectroelectrochemistry in CH_2Cl_2 / 0.1 M Bu_4NPF_6 at RT of the transition* ***(6a)***$^{0\rightarrow(\bullet-)}$

On reversible reduction of the complexes as monitored by spectroelectrochemistry there is a high-energy shift and partial splitting of the UV bands (MLCT transitions overlapping with π–π* IL transitions). The isobestic points observed for all complexes on one-electron reduction processes indicate the homogeneity of the reaction systems studied.

The low-lying π* orbital of tetrazines is an excellent target for low-energy electronic transitions.[52] Thus, the coordination of tetrazine ligands with metals leads to long-wavelength MLCT transitions.

The bands in the visible region are diminished and partially structured for all complexes (see Table 2.5.2). As was mentioned previously, the one-electron reduced tetrazines do not show IL absorption in the visible or infrared region, therefore these bands, like in the case of **4a**, are assigned to MLCT and LLCT or more precisely SBLCT (σ(Pt-C)→π*(α-diimine)) transitions involving the singly occupied MO. This latter process is expected to weaken the σ bonds in the axial positions allowing selective activation of the metal-halide or metal-carbon bonds. [33] The X-ray data obtained for **6b** and **6c** support this idea since the C_{ax}-Pt bonds are somewhat longer than the C_{eq}-Pt bonds.

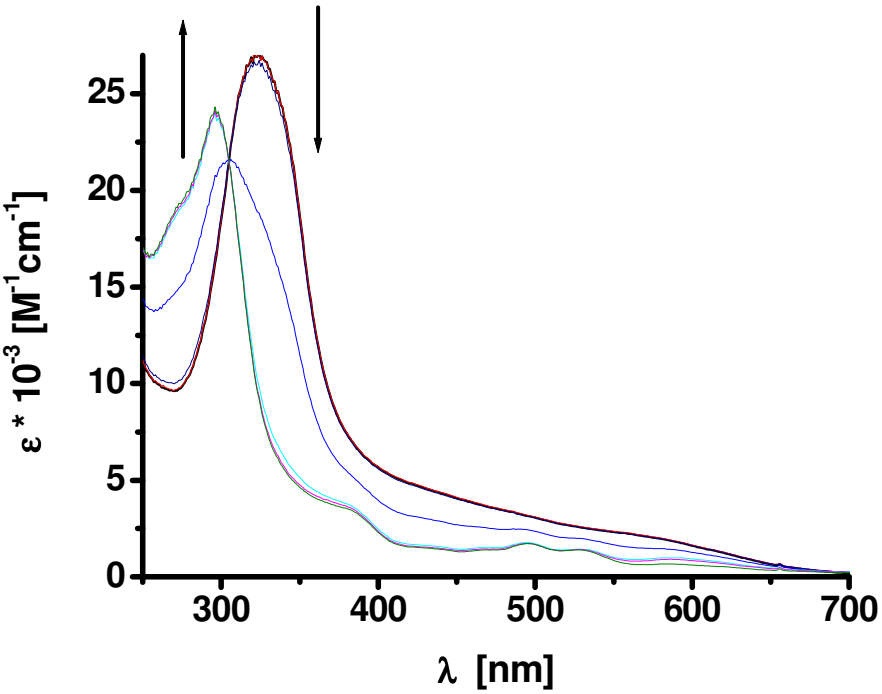

Fig. 2.5.8: *UV-Vis Spectroelectrochemistry in CH_2Cl_2 / 0.1 M Bu_4NPF_6 at RT of the transition* ***(6b)***$^{0\rightarrow(\bullet-)}$

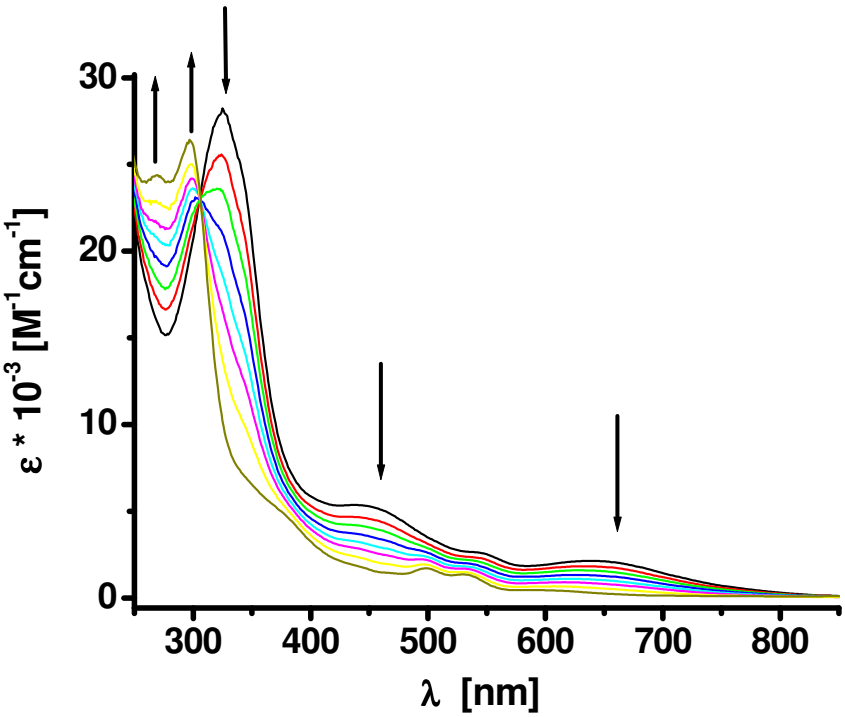

Fig. 2.5.9: *UV-Vis Spectroelectrochemistry in CH_2Cl_2 / 0.1 M Bu_4NPF_6 at RT of the transition* ***(6c)***$^{0\rightarrow(\bullet-)}$

EPR Spectroscopy

Theory

Electron Paramagnetic Resonance (EPR) is the ideal spectroscopic method for identification and characterization of radicals and metal-centered spin. The technique gives three sources of information.[71]

The isotropic *g* value: Deviations of *g* from the free electron value g_e can be attributed to the contribution of other excited states with non-zero angular momentum to the radical ground state. They arise from spin-orbit interactions which are proportional to the spin-orbit coupling constants of the involved atoms which increase with the atomic number as Z^5. The sign of the deviation is indicative of the frontier orbital situation according to Stone's approximation [72] :

$$g = g_e - \frac{2}{3}\sum_i \sum_n \sum_{kj} \frac{\langle \Psi_0 | \xi_k L_{ik} \delta_k | \Psi_n \rangle \langle \Psi_n | L_{ij} \delta_j | \Psi_0 \rangle}{E_n - E_0} = g_e + \Delta g_s$$

g_e = 2.0023

Ψ_0 : MO of the unpaired electron in the ground state

Ψ_n : all other MOs

ξ_k : spin-orbit coupling constant

$L_{ik/ij}$: angular momentum operator for AO at nucleus *k,j*

$L_{ik}\delta_k = 0$ except at atom k

E_0 : energy of a singly occupied molecular orbital (SOMO)

E_n: energies of empty or doubly occupied molecular orbitals (LUMO or HOMO)

Considering the denominator of the equation, only the neighboring levels have a significant contribution to Δg. This means that heavy atoms which are bound near the radical center have a large effect on the g value. However, two cases are possible:

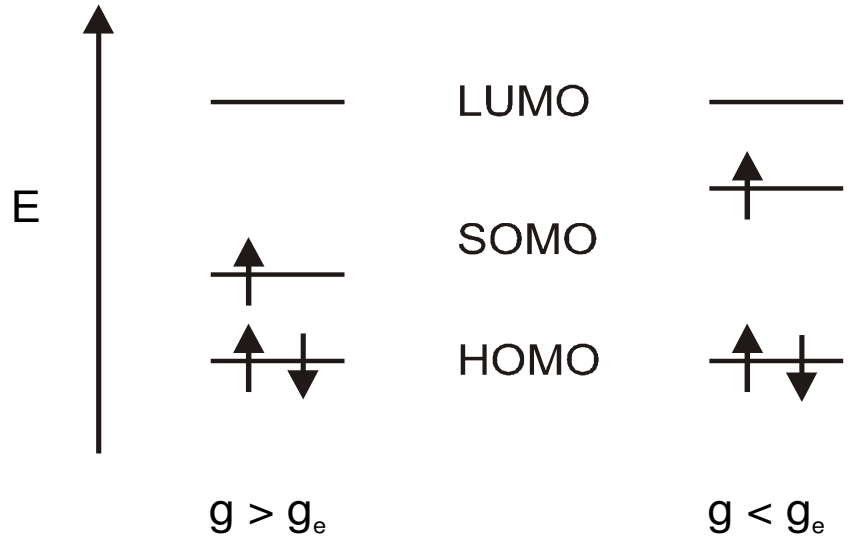

Fig. 2.5.10: *Energy level diagram.*

If $E_0 > E_n$, a deviation to higher values than g_e is to be expected. This means that the SOMO lies closer to the HOMO than to the LUMO.

If $E_0 < E_n$, the SOMO lies closer to LUMO than to the HOMO.

Even though anion radical complexes of transition metal fragments usually display rather small deviations of g_{iso} from g_e ($\Delta g_s \leq \pm 0.02$) because the spin is mainly delocalized over the light atoms of the ligand with small spin-orbit coupling constants, the characteristic changes on going from the ligand anion radical to the complexes can provide valuable information on the orbital ordering.

The *g* anisotropy ($\Delta g = g_1 - g_3$) from measurements of powders or glassy frozen solutions is largely a result of contributions from elements with high spin-orbit coupling constants. In the EPR spectra of transition metal complexes where the spin is predominantly on the metal centre, the g-anisotropy is usually quite large. However, in the case of transition metal complexes with anion radical ligands the *g* anisotropy is generally small, even in species which contain 5d metal centers like osmium or rhenium. Moreover, the broadness of the lines, sometimes in adjunction with insufficiently resolved metal hyperfine splitting, can preclude the determination of the expected *g* anisotropy for complexes with heavy transition metal elements at conventional EPR frequencies (X band). Thus, it is often necessary to go to high fields / high frequencies (≥ 95 GHz) to resolve it.

The hyperfine coupling between the unpaired electron and the various nuclei of the radical species is another most informative source of insight from EPR.[72c] Ideally, all nuclei with non-zero nuclear spins should couple to a certain extent with the unpaired electron and thus reveal the nature of the SOMO. Unfortunately, it is not always possible to obtain such information from conventional EPR experiments: the intrinsic line-width may be too large for the resolution of the hyperfine structure, the dominant metal hyperfine splitting can obscure the hyperfine splitting from the spin-bearing ligand atoms, and the low natural abundance and / or low nuclear magnetic moment of isotopes can lead to undetectable hyperfine coupling.

Results

The site of electron addition to a platinum complex can often be determined by EPR spectroscopy. While odd-electron platinum species like Pt^{III} are typically characterized by extremely shifted *g* factors[73] or even by EPR silence,[74] the tetrazines exhibit the distinct localization of an added electron on the four nitrogen atoms, leading to typically resolved spectra.[45,30] For symmetrically dinuclear complexes of bptz or bmptz radical anions two EPR hyperfine coupling constants to two pairs of ^{14}N nuclei ($I = 1$) are expected, additional coupling with the ^{195}Pt nuclei ($I = ½$, 33.8% natural abundance) is usually detectable[75] because of the large isotropic hyperfine constant a_o = 1227.84 mT.[76] The *g* factors of tetrazine radical anions and of their metal complexes are mostly near the free ligand radical value of about 2.004. [45]

Electrolytically generated *anti*-[(μ-bmptz){*fac*-PtBrMe$_3$}$_2$]$^{\bullet-}$ at room temperature in CH_2Cl_2/0.1 M Bu_4NPF_6 yielded a well resolved EPR spectrum (Fig. 2.5.11). The results obtained are in agreement with nearly complete spin localization at the tetrazine ring. The *g* factor at 2.0053, i.e. close to 2.004, suggests that the heavy Pt and Br atoms with their very large spin-orbit coupling constants do not appreciably contribute to the singly occupied molecular orbital. However, the hyperfine interaction does not only involve two pairs of ^{14}N nuclei with typical[30,45] coupling constants of 0.37 and 0.74 mT, it also requires the inclusion of ^{195}Pt coupling (2.35 mT, 2 Pt) and interaction with the ^{79,81}Br isotopes (0.55 mT, 2 Br) with their nuclear spin of *I*= 3/2.[76] The chelate situation and the binding to two of the spin bearing tetrazine nitrogen atoms seems to promote some hyperfine interaction via spin polarization.[33]

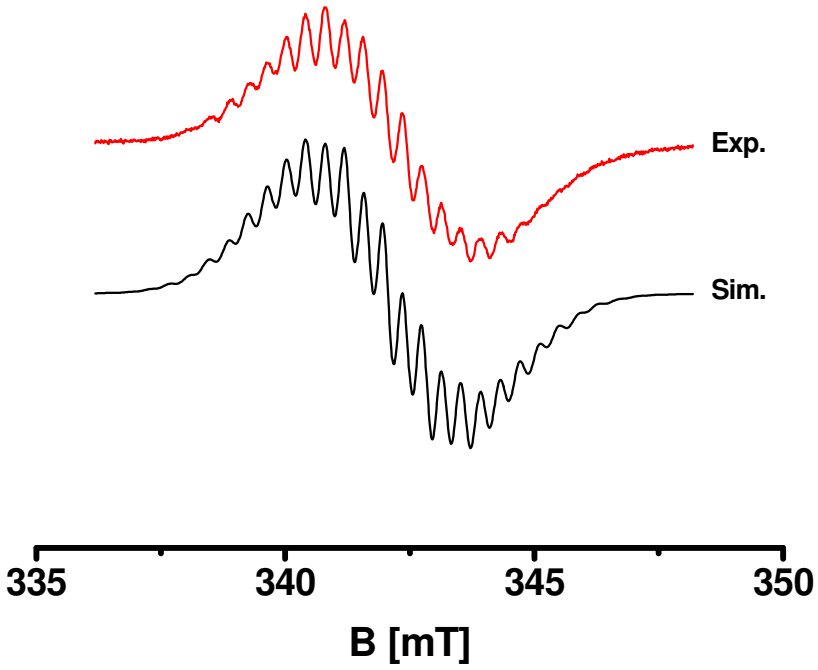

Fig. 2.5.11: *EPR spectrum of anti-[(μ-bmptz){fac-PtBrMe$_3$}$_2$]$^{\bullet-}$, generated by in situ electrolysis in CH_2Cl_2 / 0.1 M Bu_4NPF_6 (top) with computer simulation (bottom; 0.35 mT linewidth)*

2.6 TD-DFT Calculations

The electronic structures of the complexes [Pt(X)(bptz)(CH_3)$_3$] (X=Cl, Br) were calculated by density functional theory (DFT) methods using the Gaussian 03[77] and ADF2008.01[78] program packages. Low-lying singlet excited states were calculated by time-dependent DFT (TD-DFT) at the optimized ground-state geometry. Calculations were carried out by Dr. S. Záliš from J. Heyrovský Institute of Physical Chemistry, Prague and by Mr. O. Sarper at University of Stuttgart.

Gaussian calculations employed the hybrid Perdew, Burke and Ernzerhof [79] (PBE0) exchange and correlation functional. For H, C, N, Cl and Br atoms either 6-311G* polarized triple-ζ basis sets[80] for geometry optimization or cc-pvdz correlation consistent polarized valence double ζ basis sets[80] (TD-DFT) were used, together with quasirelativistic effective core pseudopotentials and corresponding optimized set of basis functions for Pt.[81] The solvent was described by the polarizable conductor calculation model (CPCM).[82]

Slater type orbital (STO) basis sets of quadruple-ζ quality with four polarization functions for the Pt atom, double-ζ with one polarization function for H and of triple-ζ with two polarization functions for the remaining atoms were employed within ADF. The calculations were done with the functional including Becke's gradient correction[82] to the local exchange expression in conjunction with Perdew's gradient correction[83] to the local correlation (ADF/BP). The scalar relativistic (SR) zero order regular approximation (ZORA) was used within ADF calculations.

The selected optimized DFT (ADF/BP) bond lengths and angles of *fac*-Pt(CH_3)$_3$Br(bptz) and *fac*-Pt(CH_3)$_3$Cl(bptz) (see Table 2.4.1) reasonably well describe experimental crystal structure of both complexes. ADF/BP underestimates Pt-C_{ax} distances, while larger underestimation is observed in the case of G03/PBE0 calculations.

Table 2.6.1 gives the composition of DFT calculated frontier molecular orbitals of *fac*-Pt(CH_3)$_3$Br(bptz) complex. The set of almost degenerate HOMO and HOMO-1 is mainly formed by the combination of p_π orbitals of Br ligand with the d(Pt) orbitals.

The contribution of π(bptz) orbitals to these orbitals is below 3%. HOMO-2 is a σ bonding Br-Pt-Me_{ax} orbital, lower lying occupied orbitals are formed by σ– or π(bptz) orbitals interacting with Pt orbitals. LUMO is composed from the first unoccupied π orbital of the free bptz ligand slightly perturbed by the 3% contribution of d_{XZ}(Pt) orbital. The next closely lying unoccupied molecular orbital originates from the second π orbital of bptz ligand. The analogous sequence of frontier MOs is obtained in the case of *fac*-Pt$(CH_3)_3$Cl(bptz) complex.

Table 2.6.1**:** *DFT (G03/PBE0/CPCM) calculated one-electron energies and percentage composition of frontier molecular orbitals of fac-Pt$(CH_3)_3$Br(bptz) expressed in terms of composing fragments.*

MO	E (eV)	Prevailing Character	Pt	bptz	Me_{ax}	Me_{eq}	Br
Unoccupied	-						
LUMO+1	-3.0	bptz (π_2^*)	-	99	-	-	1
LUMO	-3.46	bptz (π_1^*)	3	95	-	-	1
Occupied							
HOMO	-6.81	Br + Pt	16	1	1	1	80
HOMO-1	-6.83	Br + Pt	15	3	2	1	79
HOMO-2	-7.20	σ(Br-Pt-Me_{ax})	10	4	26	4	57
HOMO-3	-7.46	bptz (σ)	5	83	1	9	1
HOMO-4	-7.52	bptz (π)	3	95	-	1	1
HOMO-5	-7.75	bptz (σ)	47	22	4	27	-
HOMO-6	-7.90	Pt+ bptz (σ)	28	57	3	10	3
HOMO-7	-8.00	Pt+ bptz (π)	38	42	1	12	7
HOMO-8	-8.13	Pt+ bptz (π)	40	41	3	9	7
HOMO-9	-8.30	Pt+Me_{eq}+bptz(σ)	41	22	1	33	3

Table 2.6.2 compares TD-DFT calculated transitions with experimental ones for *fac*-Pt$(CH_3)_3$Br(bptz), molecular orbitals involved in excitations are depicted in Fig. 2.6.1. The non-intense absorption in the visible region at 525 nm is composed from several weak LLCT/MLCT transitions from the higher lying occupied orbitals into the LUMO. The intense absorption around 311 nm is well interpreted by TD-DFT calculations and can be described as a mixed MLCT and intraligand π – π* transition from low lying HOMO-8 and HOMO-9 into the LUMO.

Table 2.6.2: *Selected G03/PBE0/CPCM calculated lowest allowed TD-DFT singlet transitions of fac-Pt(CH_3)$_3$Br(bptz) with oscillator strength larger than 0.003*

		calculated		Experiment
State	**Main character (in %)**	**trans. energy[a]**	**osc. Str.**	**$\lambda_{max}/\varepsilon$ [b]**
a ^{1}A	38 (HOMO-1→LUMO); 45 (HOMO-3→LUMO)	2.32 (533)	0.003	525 / 0.46
a ^{1}A	49 (HOMO-1→LUMO); 40 (HOMO-3→LUMO)	2.52 (492)	0.006	
a ^{1}A	95 (HOMO-2→LUMO)	2.89 (428)	0.018	
b ^{1}A	82 (HOMO-4→LUMO)	3.29 (377)	0.019	
a ^{1}A	94 (HOMO-2→LUMO+1)	2.89 (428)	0.009	
c ^{1}A	51 (HOMO-8→LUMO); 22 (HOMO-9→LUMO)	3.73 (332)	0.076	
c ^{1}A	58 (HOMO-9→LUMO);20 (HOMO-4→LUMO+1)	3.79 (329)	0.137	311 / 23.2
d ^{1}A	42 (HOMO-8→LUMO);43 (HOMO-4→LUMO+1)	3.83 (324)	0.538	

[a] *Transition energies in eV (or wavelengths in nm)*
[b] *Absorption maxima in nm, molar extinction coefficients in 10^{-3} [M^{-1} cm^{-1}]*

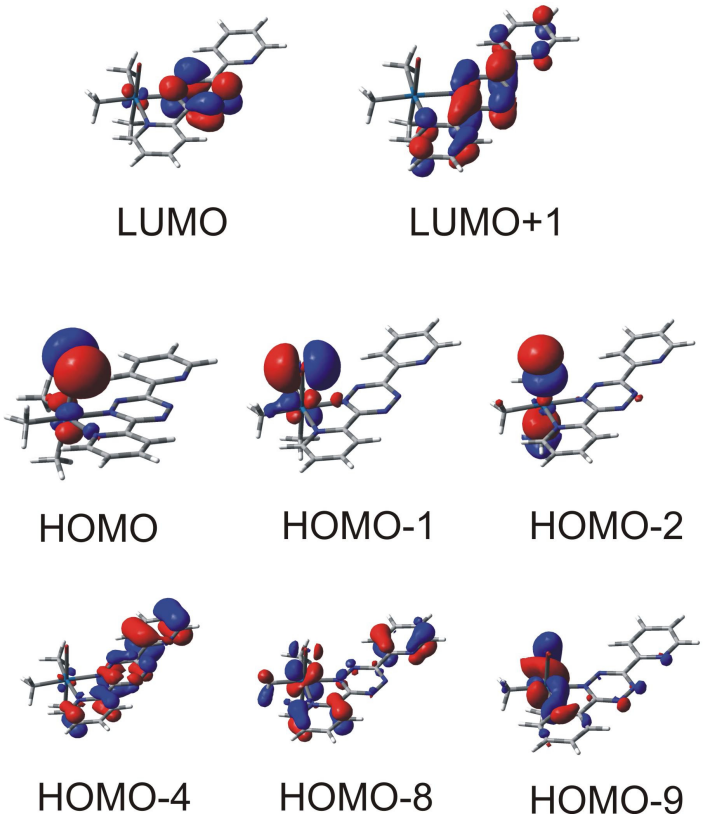

Fig. 2.6.1: *Frontier MOs involved in calculated excitations of fac-Pt(CH_3)$_3$Br(bptz)*

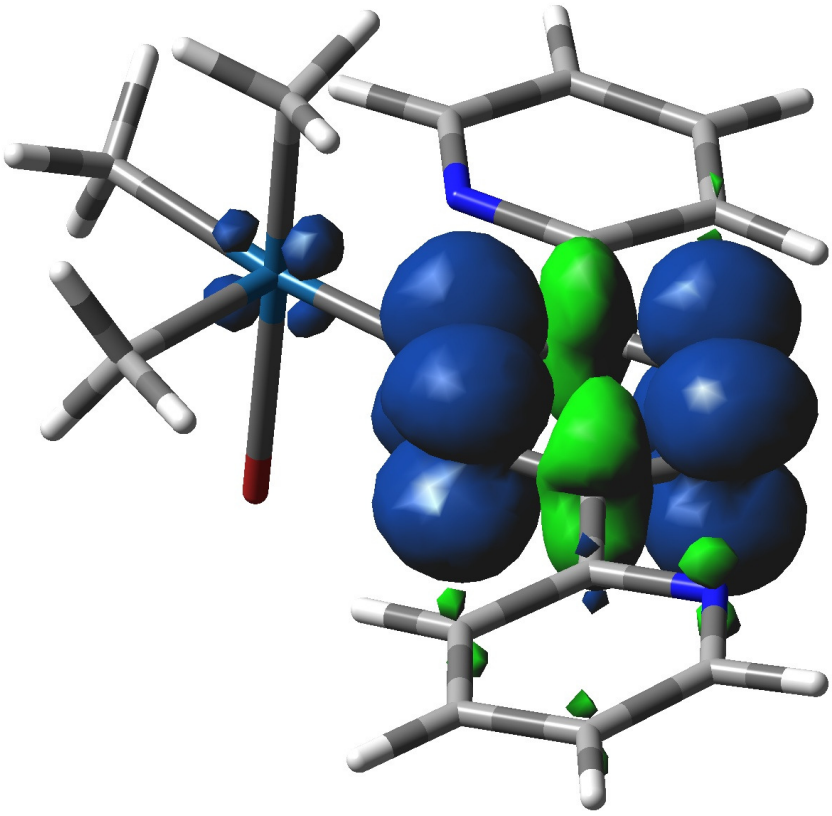

Fig. 2.6.2: *DFT calculated spin densities of fac-[PtBr(bptz)(CH$_3$)$_3$]$^{\bullet-}$*

Fig. 2.6.2 shows the calculated spin densities for *fac*-[PtBr(bptz)(CH$_3$)$_3$]$^{\bullet-}$. As a conclusion, the reduction of *fac*-Pt(CH$_3$)$_3$Br(bptz) and similar *fac*-Pt(CH$_3$)$_3$Cl(bptz) complexes should lead to the accepting of an electron predominantly by the bptz ligand orbital. However, there is also a small, non-zero Pt contribution to the spin density as can be seen from the figure.

2.7 Spectroscopic and Electrochemical studies on $Pt(abpy)(CH_3)_3Br$

Absorption Spectroscopy

The complex $Pt(abpy)Me_3Br$ shows an intense π–π^* absorption band in CH_2Cl_2 at 336 nm (ε : 11300 M^{-1} cm^{-1}) in the UV region, that is low energy shifted in comparison with the free ligand which exhibits the same band at 314 nm (ε : 14600 M^{-1} cm^{-1}) in CH_2Cl_2 (Fig. 2.7.1). In addition, there is a much less intense broad band appearing as a shoulder in the visible area, where the low intensity n-π^* absorption of the free ligand used to be around 450 nm. These results give a clue that the expected SBLCT is rather weak, indicating a large energy difference and poor overlap between σ(Pt-C) and π^* orbitals.

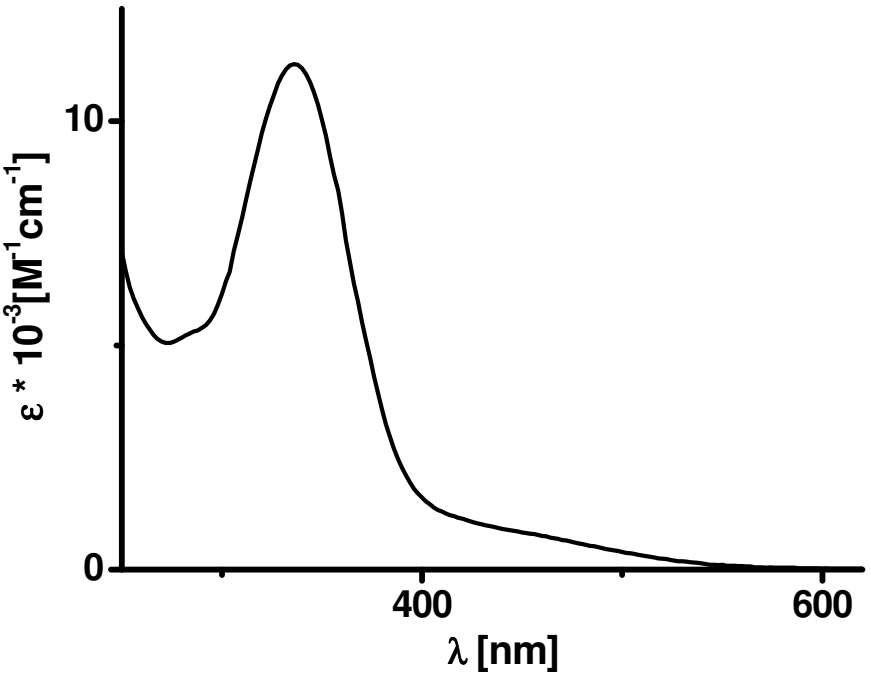

Fig. 2.7.1: *Absorption spectrum of $Pt(abpy)Me_3Br$ in CH_2Cl_2*

Cyclic Voltammetry

Pt(abpy)Me_3Br is reduced irreversibly at room temperature in CH_2Cl_2/0.1 M Bu_4NPF_6. However at 248 K the cyclic voltammetry experiment reveals an approximately Nernstian wave at -0.91 vs ferrocenium/ferrocene which is only about 0.5 V less negative than the reduction potential of the free ligand. Fig. 2.7.2 shows the cyclic voltammogram of the complex.

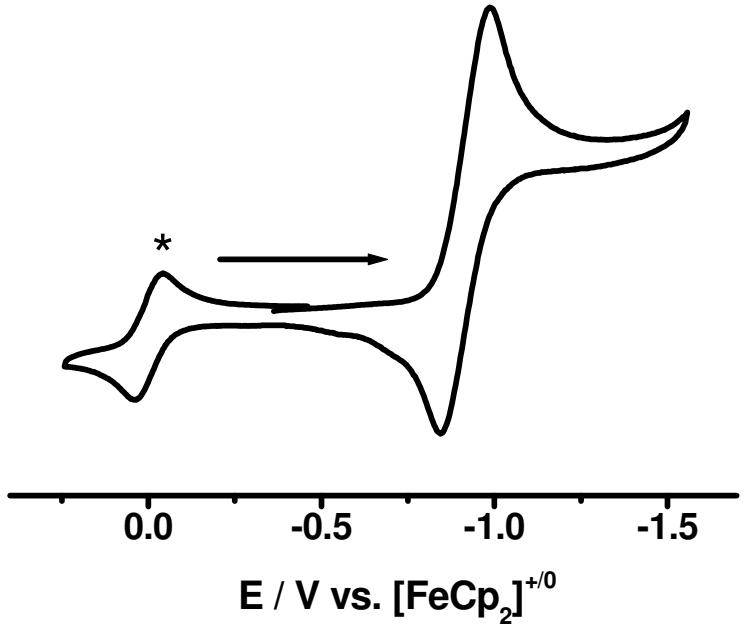

Fig. 2.7.2: *Cyclic voltammogram of Pt(abpy)Me_3Br in CH_2Cl_2 / 0.1 M Bu_4NPF_6 at 248 K with a scan rate of 100 mV/sec*

The I^- analog of the complex was reported to show a similar behavior, where it exhibited reversibility only at -0.86 V vs. $[FeCp_2]^{+/o}$ at -50 ^{0}C in CH_2Cl_2/0.1 M Bu_4NPF_6. On the other hand, the $Re(CO)_3X$(abpy) complexes (X: F, Cl, Br, I) can be reversibly one-electron reduced even at room temperature.[42]

EPR Spectroscopy

The reversibility of the $Pt(abpy)Me_3Br$ reduction, at least at lower temperatures allowed to obtain EPR information for the electrogenerated $[Pt(abpy)Me_3Br]^{\bullet -}$. In situ electrolysis at 250 K in CH_2Cl_2 / 0.1 M Bu_4NPF_6 resulted in a broad, unresolved EPR signal (ca. 12 mT wide) at g_{iso} = 1.995, i.e. close to the free electron value of g = 2.0023. The experiment, carried out in frozen solution at 110 K, yielded an asymmetric signal without resolution, indicating a slight g anisotropy between 2.01 > g > 1.97. This small effect in spite of the large spin orbit coupling constant of platinum(IV)[33,64a] is another clue for the notion of weak electronic interaction between the spin bearing π^* MO of abpy and Pt^{IV}.

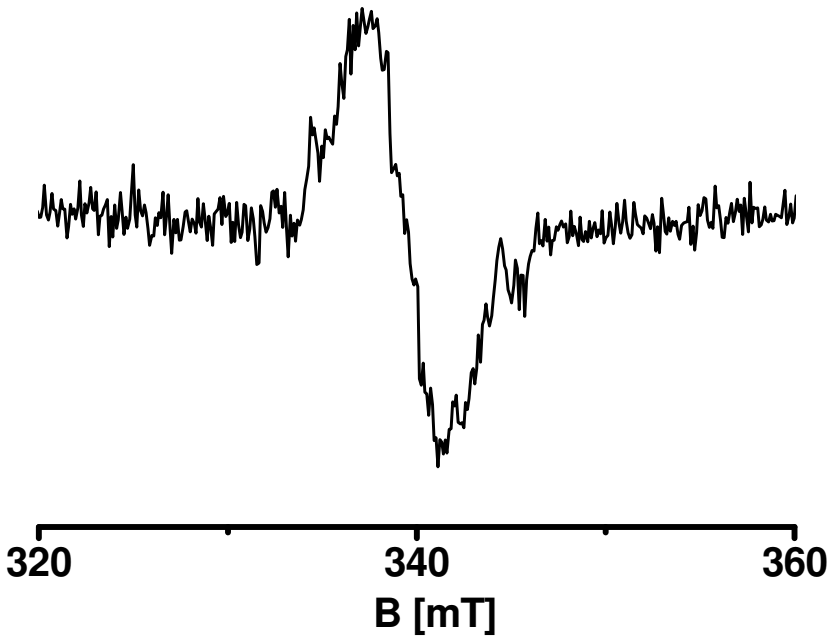

Fig. 2.7.3: *EPR spectrum of $[Pt(abpy)Me_3Br]^{\bullet -}$ generated by in situ electrolysis in CH_2Cl_2 / 0.1 M Bu_4NPF_6 at 250 K.*

As a summary, the evidence from spectroscopic and electrochemical studies of $Pt(abpy)Me_3Br$ leave only a marginal metal-to-ligand or sigma bond-to-ligand charge transfer, despite the strong π accepting capability of abpy.[56] The $d(Re)\rightarrow\pi^*(abpy)$ interaction in $Re(CO)_3X(abpy)$ complexes is more efficient than $\sigma(Pt\text{-}C)\rightarrow\pi^*(abpy)$ interaction in $Pt(abpy)Me_3X$ as also verified by the X-ray analyses.[28]

CHAPTER 3

Pt^{IV} Complexes of Imidazole Containing Ligands

3.1 Introduction

The frequent occurrence of two histidine binding sites for metal centers[84] at bioactive sites of proteins[85] has prompted the development of many imidazole-containing ligands. The properties of those ligands are not only limited to the modelling of metalloprotein active-site structures[86,87] but have also found application in systems for asymmetric catalysis and for the separation and detection of biomolecules[88]. Recently, the transition metal chemistry of those ligands is receiving attention as a result of their interesting redox properties and their potential catalytic properties.

Among those ligands, bis-(1-methyl-2-imidazolyl)ketone (bik)[89] **(1)** and the related, bis(1-methylimidazol-2-yl)glyoxal (big)[90-92] **(2)** and their reduced forms have previously been employed and their electrochemical properties were studied, also in connection with platinum(II) [93].

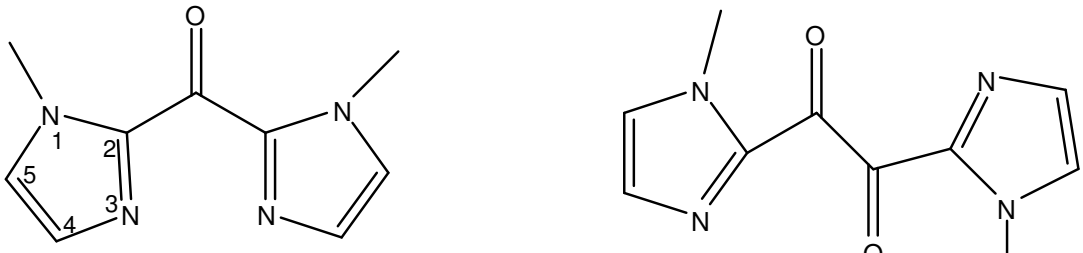

Fig. 3.1.1: *Molecular structure of bik and big*

The existence of an α–diketo moiety in big provides a low lying π* orbital in the coplanar formation which makes this ligand far more easily reducible than bik[93]. This moiety may also cause better π-back donation in case of metal coordination. A

recently reported DFT study on big and its Au^{III}, Pt^{II}, Cu^{II}, Re^{I}, and Zn^{II} complexes showed that it coordinates with metals potentially transferring charge to the ligand, and the low lying unoccupied π^* orbital can overlap with d orbitals of the metal according to the structure of the complex[94].

Another feature of big is that it is a potential tetradentate π acceptor ligand which provides various mono- and bis-chelating possibilities (Fig. 3.1.2). The possible coordination of a metal atom by either oxygen atoms or imidazole nitrogens can result in a mononuclear complex while coordination through one oxgen and nitrogen may occur in a dinuclear fashion containing either with five- or six-membered rings.

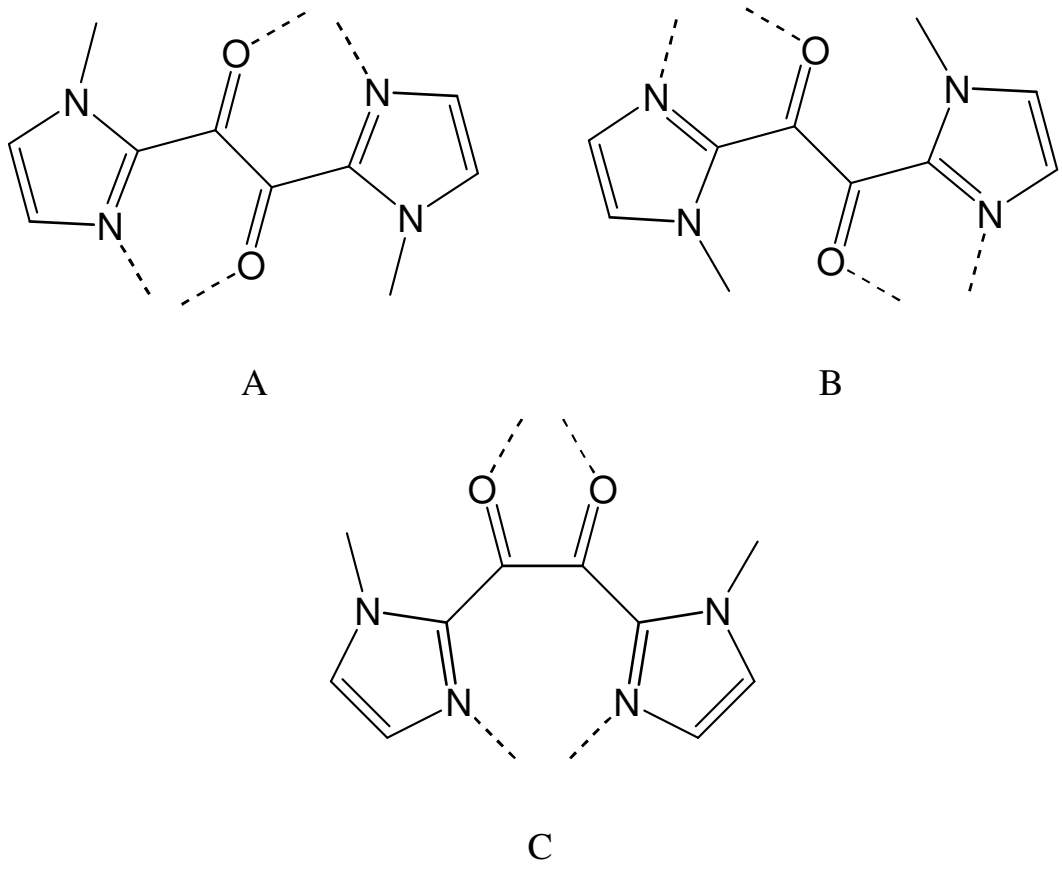

Fig. 3.1.2: *Alternative coordination possibilities for bis (chelate) complexes of big*

This chapter describes the syntheses, molecular structure and the spectroelectrochemical characterization of the first organoplatinum(IV) complexes of ligands big and bik, *fac*-$Pt(CH_3)_3I$(big) (**5**) and *fac*-$Pt(CH_3)_3I$(bik) (**6**). Moreover, two newly synthesized potential chelating ligands, 2,3-bis(1-methylimidazol-2-yl)quinoxaline (bmiq) **(3)** and 2,3-bis(1-methylimidazol-2-yl)-7,8-dimethylquinoxaline

(dibmiq) **(4)**, their reactivity towards tetrameric triiodomethylplatinum(IV), and DFT calculations of potential product complexes will also be mentioned.

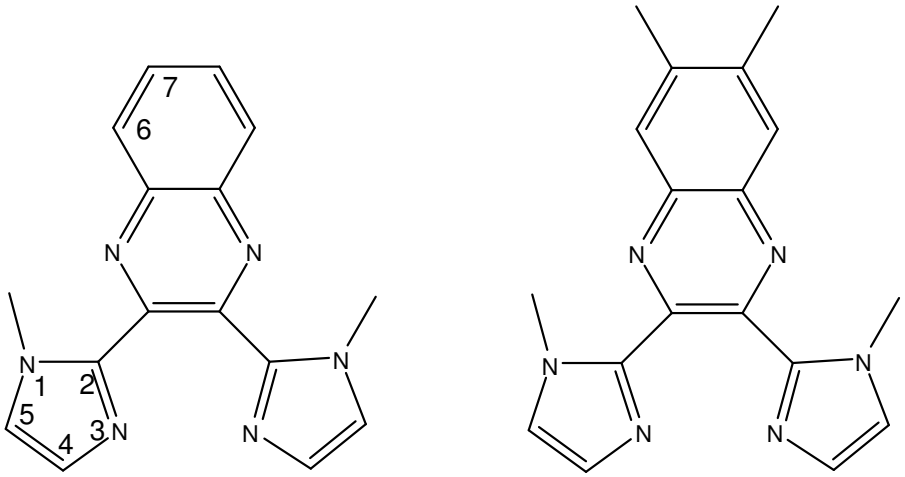

3
bmiq

4
dibmiq

Fig. 3.1.3: *Molecular structure of bmiq and dibmiq*

3.2 Syntheses

Big

The ligand **2** (big) was synthesized by reacting 1-methylimidazole with a slight excess amount of butyllithium at -70 ^{0}C overnight. The key point in the synthesis was to add the butyllithium very slowly, in small portions. Different from the known procedure[90-92], on the second day, oxalyl chloride was added. Purification of the product was done only by washing with ethanol. It was observed that application of any column chromatography decreases the yield, causing big to decompose. This modified precedure has increased the yield to around 10%. The reaction route is shown in Fig. 3.2.1.

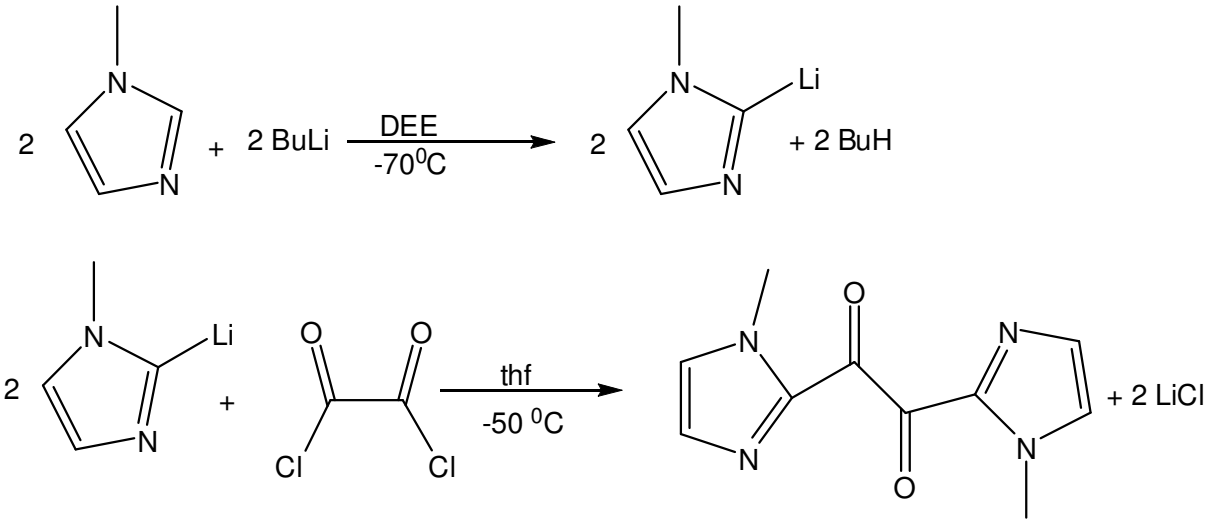

Fig. 3.2.1: *Synthesis of **2** (big)*

Pt(CH$_3$)$_3$I(big) and Pt(CH$_3$)$_3$I(bik)

Both complexes were synthesized by the reaction of equal moles of $[Pt(CH_3)_3I]_4$ and either **2** or **1** in acetonitrile. Due to the low solubility of big, complex **5** was synthesized at around 50^{0}C. The addition of excess amount of $[Pt(CH_3)_3I]_4$ did not yield any binuclear complex. Complexes were purified by washing several times with benzene.

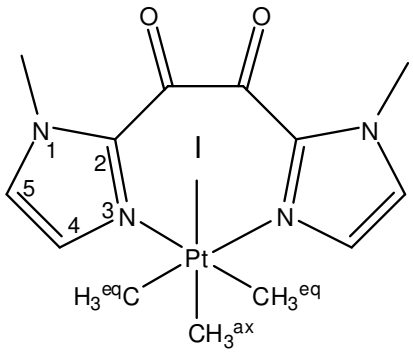

5

***fac*-Pt(CH$_3$)$_3$I(big)**

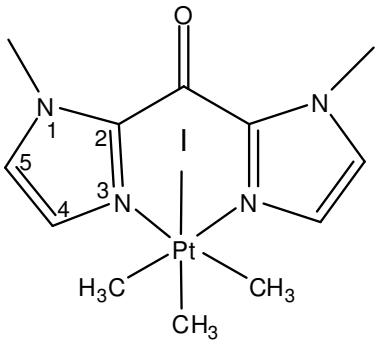

6

***fac*-Pt(CH$_3$)$_3$I(bik)**

Fig. 3.2.2: *Molecular structures of **5** and **6***

Bmiq and Dibmiq

Inspired by the literature [95], a derivative of **2**, the ligand bmiq was synthesized for the first time in our group by, Dr. Bulak, through a condensation reaction (or more specifically, nucleophilic addition-elimination reaction) of σ-phenylenediamine with big. Similarly, dibmiq was synthesized by reacting **2** with 4,5-dimethyl-σ-phenylenediamine. In both cases, for a good yield**,** an excess amount of amine is required. The purification of products could be achieved by column chromatography (1:1 ethyl acetate-ethanol).

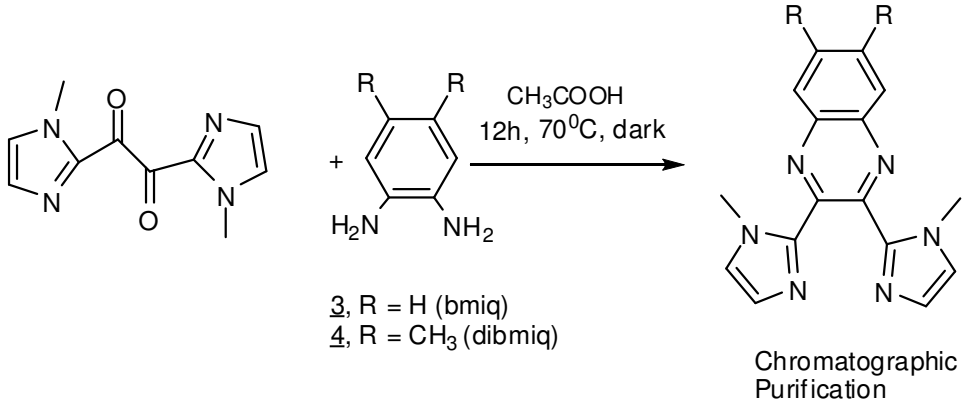

Fig. 3.2.3: *Synthesis of new quinoxaline ligands*

Pt(CH$_3$)$_3$I(bmiq)/ (Pt(CH$_3$)$_3$I)$_2$(bmiq) and Pt(CH$_3$)$_3$I(dibmiq)/ (Pt(CH$_3$)$_3$I)$_2$(dibmiq)

The reaction of $[Pt(CH_3)_3I]_4$ with **3** in 1:1 ratio in CH_2Cl_2 solution at room temperature resulted in the mixture of mononuclear seven-membered (**8a**) (63%) and dinuclear five-membered ring (**7a**) (37%) complexes. Doubling the amount of the Pt^{IV} precursor or varying the reaction temperature from 70 to -10^{0}C did not have any effect on the site of complexation. The existence and the composition of the mixture were verified by ^{1}H-NMR spectra. In order to find out any effect of an electron donating group on the site of the complexation, $[Pt(CH_3)_3I]_4$ was also reacted with the 4,5-dimethyl substituted ligand, **4,** in CH_2Cl_2 in 1:1 ratio at room temperature. This reaction led again to a mixture of **7b** (ca 35 %) and **8b** (ca 65%) as in the case of bmiq.

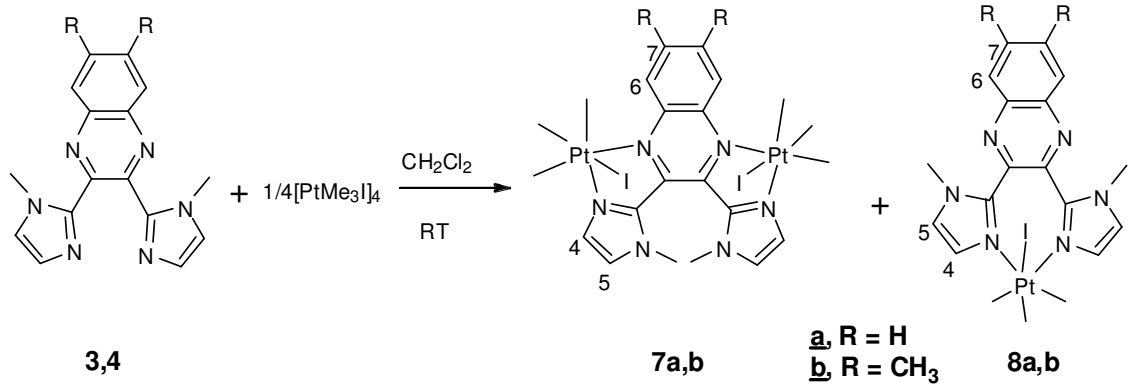

Fig. 3.2.4: *Reaction scheme*

In another attempt, **5** was prepared and reacted with σ–phenylenediamine in 1:1 molar ratio in acetic acid at 50^{0}C to obtain only the mononuclear complex, **8a**. Unexpectedly, the reaction gave exactly the same mixture as above with a slightly varied composition (**8a**: ca 68%, **7a**: ca 32%). A possible explanation can be the cleavage of Pt-N bonds in **5** and reconstruction of the complexes **7a** and **8a**. Attempts of an analytical separation by chromatography or recrystallization were not successful.

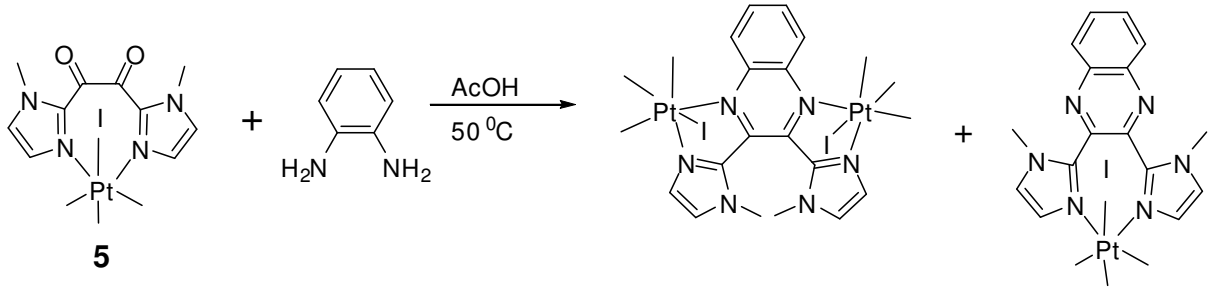

Fig. 3.2.5: *Reaction scheme between **5** and σ–phenylenediamine*

3.3 Characterization

^{1}H-NMR Spectroscopy

fac-Pt(CH$_3$)$_3$I(big) and fac-Pt(CH$_3$)$_3$I(bik)

The products were initially characterized by ^{1}H-NMR spectroscopy. The downfield shifts of the aromatic ring hydrogen peaks compared to free bik and big ligands, the appearance of satellites as a result of Pt-H$^{4,4'}$ coupling, and the changing position of the methyl peaks from the imidazole rings were taken as indication of formation of only **5** and **6**.

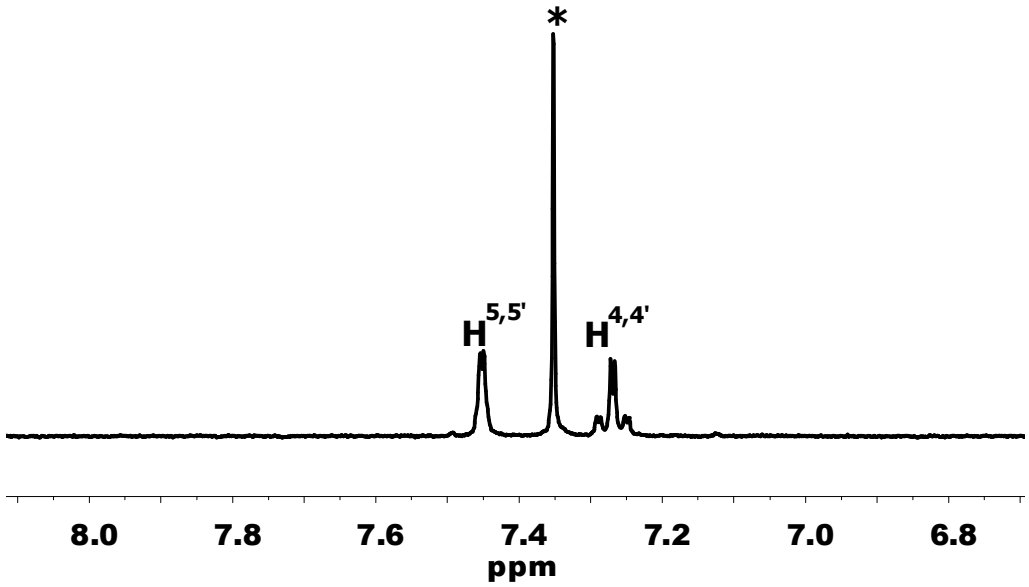

Fig. 3.3.1: *^{1}H-NMR spectrum (aromatic region) of **5** measured in acetone-d$_6$. * = free benzene solvent from recrystallization*

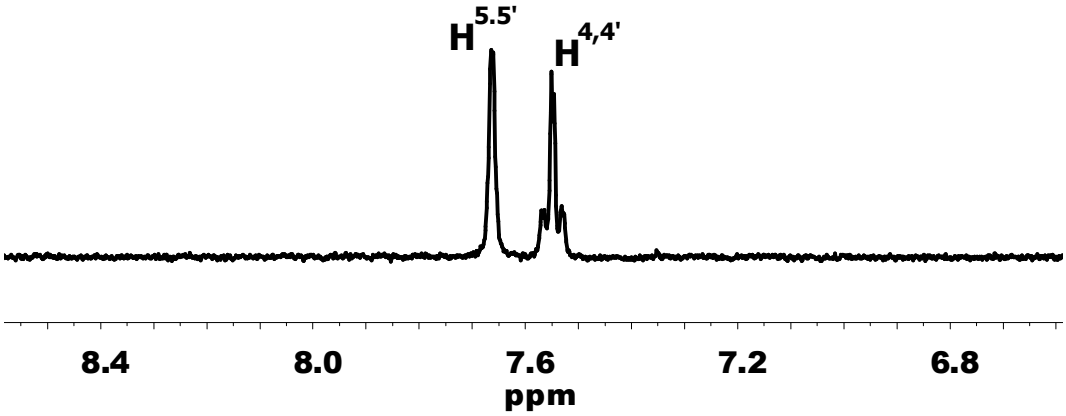

Fig. 3.3.2: *^{1}H-NMR spectrum (aromatic region) of **6** measured in acetone-d$_6$*

Another useful feature for characterization of **5** and **6** is the presence of [Pt-CH_3] shifts appearing in the aliphatic region. For both complexes, two different types of methyl peaks (axial and equatorial in 1:2 integration ratios) with ^{195}Pt satellites were observed. The chemical shifts and the *J* values of the complexes are shown below in Table 3.3.1.

Table 3.3.1: *^{1}H-NMR spectroscopic data of ligands and their Pt^{IV} complexes **5** and **6** in acetone-d_6*

	δ[ppm]					J[Hz]	
	CH_3^{ax}	**CH_3^{eq}**	**$H^{4,4'}$**	**$H^{5,5'}$**	**CH_3-im**	**Pt-CH_3^{ax}**	**Pt-CH_3^{eq}**
5	1.24	1.29	7.27	7.45	3.80	70.59	71.38
6	0.81	1.37	7.55	7.66	4.20	72.05	71.65
2	-	-	7.11	7.49	4.12	-	-
1	-	-	7.08	7.33	3.97	-	-

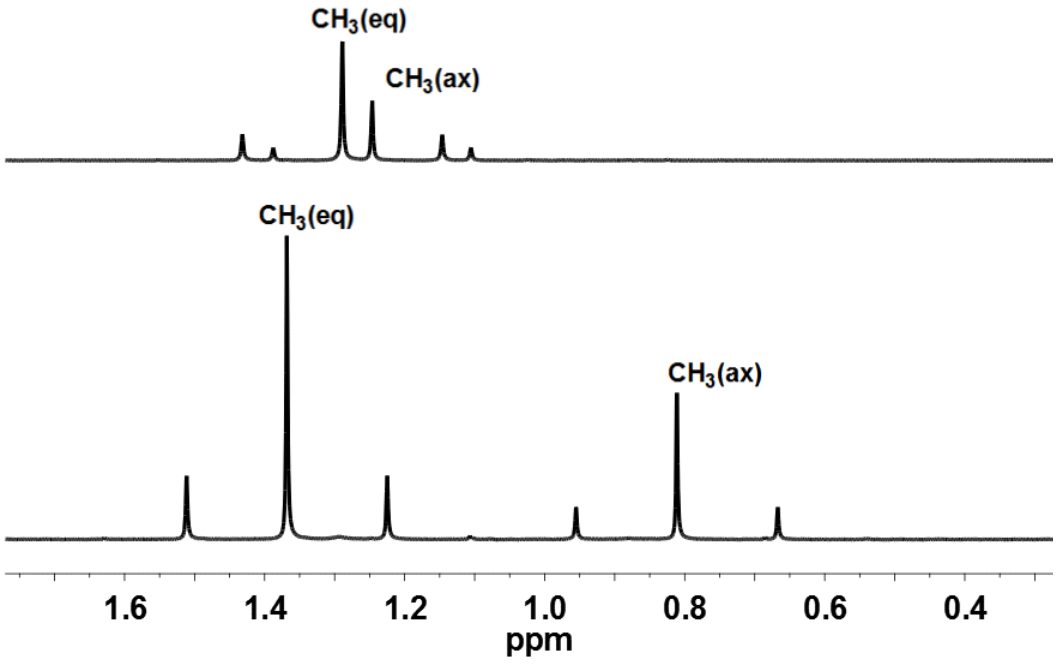

Fig. 3.3.3: *^{1}H-NMR spectra (aliphatic region) of **5** (top) **6** (bottom) measured in acetone-d_6*

Pt(CH$_3$)$_3$I(bmiq)/ (Pt(CH$_3$)$_3$I)$_2$(bmiq) and Pt(CH$_3$)$_3$I(dibmiq)/ (Pt(CH$_3$)$_3$I)$_2$(dibmiq)

The comparison of the ^{1}H-NMR spectra of free bmiq or dibmiq ligands and of the complexes **7a,b** and **8a,b** obtained after the reaction of the Pt^{IV} precursor with them indicated the formation of mixtures. Fig. 3.3.4 shows the overlapping ^{1}H-NMR spectra of **3** and the mixture of **7a** and **8a** formed during the reaction in 1:1 ratio at room temperature in acetone-d_6 solution.

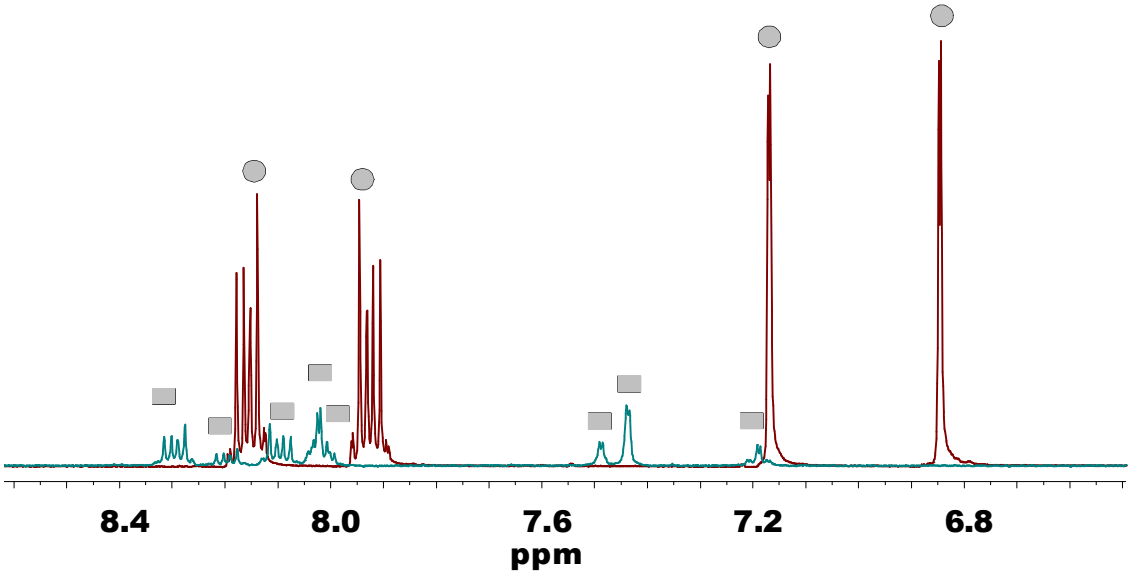

Fig. 3.3.4: *Superimposed ^{1}H-NMR spectra (aromatic region) of the product mixture and of the bmiq ligand. Both spectra were measured in acetone-d_6 ◯ : signals of free bmiq, ▭ : signals belonging to the mixture*

As is seen from the figure, there is no overlapping of the signals of **3** (bmiq) and the product mixture. This is clear evidence that there is no free ligand left in the product medium. Moreover, the total number of multiplets (as from the integration) in the aromatic region is eight. This can only happen if the final mixture consists of complexes **7a** and **8a**. In any other case, one would expect a higher number of multiplets caused by asymmetry.

***Table 3.3.2**: ^{1}H-NMR spectral data of quinoxaline ligands and their Pt^{IV} complexes (**7a,b** and **8a,b**) in acetone-d_6*

Compound	δ [ppm]							
	H^4	H^5	H^6	H^7	Ph-Me	N-CH_3	CH_3^{eq}	CH_3^{ax}
3	6.84	7.17	8.16	7.92	-	3.92	-	-
8a	8.03	7.43	8.30	8.09	-	3.92	1.23	0.35
7a	7.19	7.48	8.19	8.01	-	3.91	1.24	1.34
4	6.82	7.14	7.91	-	2.56	3.88	-	-
8b	8.00	7.34	8.03	-	2.62	3.90	1.21	0.33
7b	7.16	7.45	7.93	-	2.58	3.88	1.33	1.22

In aliphatic region there are four different proton peaks for the [Pt-CH_3] groups, which support the existence of two different complexes (two axial and two equatorial methyl groups, in 2:1 ratio). By using the integration method, it was also possible to assign the peaks for **7a** and **8a** separately. **8a** has only one axial CH_3 group. Each imidazole ring of **8a** has one Me which are identical to each other so the integration ratio of -CH_3^{ax} and N-CH_3 should be 3H:6H, 1:2. On the other hand, in bimetallic **7a**, there should be 2 CH_3 groups trans to the halide as well as two from the imidazole rings, which makes the same ratio 1:1. By combining the integration ratios of the proton signals in the aromatic region, assignments of the signals to the complexes were achieved. It was also possible to find out the ratio of **7a** and **8a** in the mixture. The integration showed that 63% of the mixture is **8a**, while 37% is **7a**.

A similar method was also applied for assignment of the products **7b** and **8b** resulting from a 1:1 reaction of $PtMe_3I$ with dibmiq at room temperature. For the mixture of **7b** and **8b**, a total of six different signals were observed as it was expected. Two different N-CH_3 and Ph-CH_3 signals as well as existence four different Pt-CH_3 peaks verified the mixture (Fig. 3.3.5). By using the integration, the complexes were identified and the percentages were found (ca 35% for **7b** and ca 65% for **8b**).

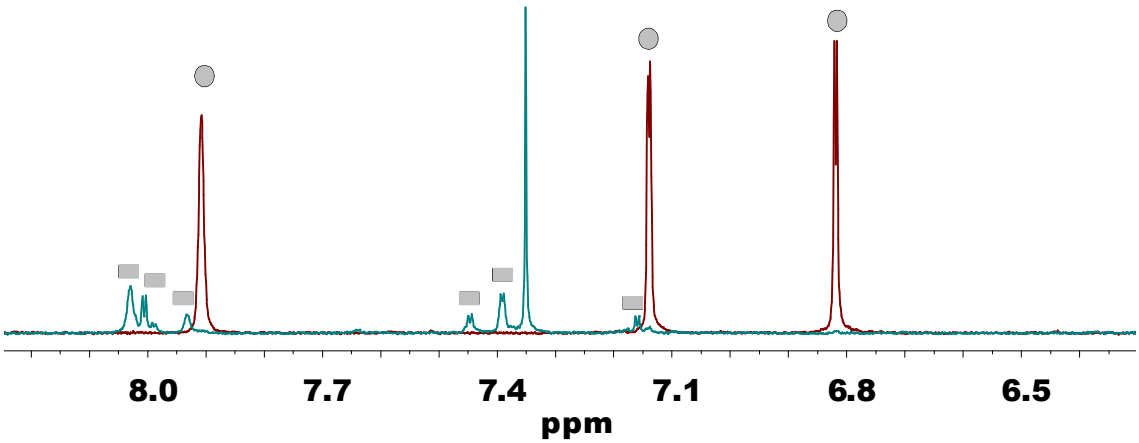

Fig. 3.3.5: *The superimposed ^{1}H-NMR spectra (aromatic region) of the product mixture and of the dibmiq ligand. Both spectra were measured in acetone-d_6 ◯ : signals of free bmiq, ▮ : signals belonging to the mixture*

Infrared Spectroscopy

fac-Pt(CH$_3$)$_3$I(big) and fac-Pt(CH$_3$)$_3$I(bik)

Another useful method to characterize the complexes **5** and **6** is to check the C=O stretching band frequencies. IR spectral analyses of both Pt(CH$_3$)$_3$I(big) and Pt(CH$_3$)$_3$I(bik) in the solid state show a sharp band of $\nu_{C=O}$ (1668 cm^{-1} and 1658 cm^{-1}, respectively) shifted to the higher wavenumber in comparison to the free ligand values of 1660 cm^{-1} and 1633 cm^{-1} for big and 1638 cm^{-1} and 1616 cm^{-1} for bik. Positively charged metal atom takes electron density from the C=O bonds where the free ligand has an anti-bonding character; the bond order of the CO group increases, so it shifts towards higher energy.

Table 3.3.3: *CO stretching data of ligands and Pt^{IV} complexes*

Compound	C=O band (cm^{-1})
1	1638 , 1616
2	1660 , 1633
5	1668
6	1658

All measurement were made in solid state

UV-Vis Spectroscopy

fac-Pt(CH_3)$_3$I(big) and fac-Pt(CH_3)$_3$I(bik)

The UV-Vis spectrum of **5** in acetonitrile exhibits an intense band at 297 nm (ε : 16670 $M^{-1}cm^{-1}$), similar as the free ligand[92] (Fig. 3.3.6). The band at 297 nm may be assigned as a π–π^* transition. A similar transition for Pt(big)Cl_2 was reported to be at 318 nm in CH_2Cl_2, which was assumed to overlap with a MLCT band[93]. There is also a low intensity absorption at around 360 nm (ε: 880 $M^{-1}cm^{-1}$). This absorption can be tentatively attributed to the σ(Pt-C)$\rightarrow \pi^*$ transition. Such transitions are likely because of a possible interaction between the electron rich σ molecular orbital of an alkyl-metal compound and the low lying π^* acceptor orbital of a ligand[35].

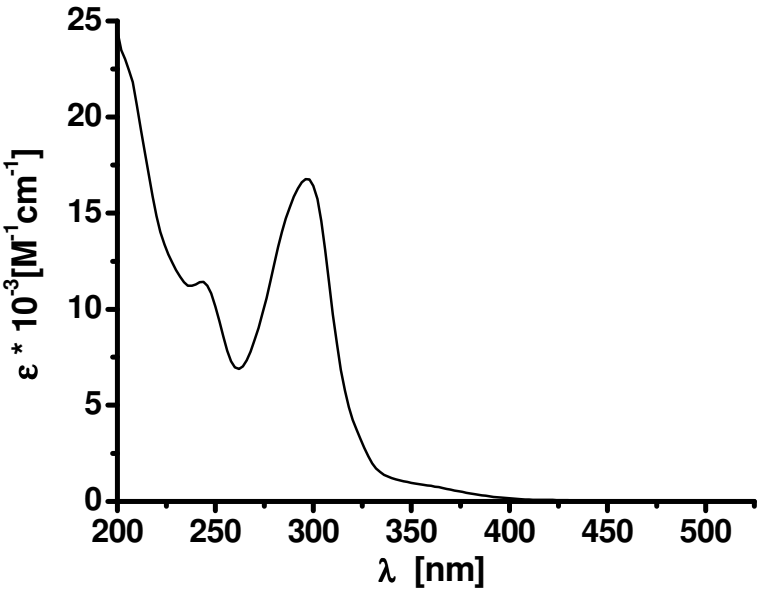

Fig. 3.3.6: *UV-Vis spectrum of fac-Pt(CH_3)$_3$I(big) in acetonitrile*

Pt(CH_3)$_3$I(bik) shows two intense absorptions at 245 nm (ε: 12660 $M^{-1}cm^{-1}$) and at 330 nm (14720 $M^{-1}cm^{-1}$) and one more band at 290 (ε: 9093 $M^{-1}cm^{-1}$), which can be assigned as IL transitions. Both **5** and **6** are not light sensitive.

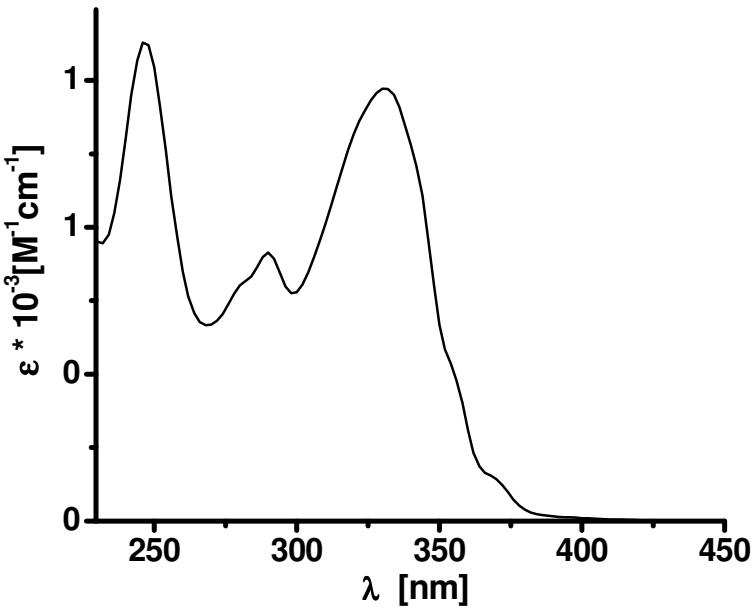

Fig. 3.3.7: *UV-Vis spectrum of fac-Pt(CH$_3$)$_3$I(bik) in CH$_3$CN*

Table 3.3.4: *UV-Vis absorption data and colour of **1** and **2** and of their Pt^{IV} complexes*

Compound	λ_{max} (ε) [c)]	Colour
2[a)]	227(5300), 297(27000)	light yellow
5[b)]	242(sh), 297(16672), 360(877)	orange
1[b)]	230(2416), 278(sh), 290(sh), 322(12815), 365(sh)	off-white
6[b)]	246(16340), 279(sh), 290(9093), 331(14724), 355(sh), 370(sh)	colorless

[a)] *Measured in CH$_3$CN*[96]
[b)] *Measured in CH$_3$CN*
[c)] *Absorption maximum in nm, molar extinction coefficient ε in M^{-1} cm^{-1}*

3.4 Structural Investigation of *fac*-Pt(CH$_3$)$_3$I(big) and *fac*-Pt(CH$_3$)$_3$I(bik)

fac-Pt(CH$_3$)$_3$I(big) (5)

Orange needles suitable for X-ray diffraction were obtained by slow diffusion of n-hexane into the CH_2Cl_2 solution of **5** at -20 ^{0}C. The complex crystallized in the triclinic space group $P\bar{1}$. The unit cell contains 8 structurally similar but 4 crystallographically different molecules of *fac*-Pt(CH$_3$)$_3$I(big). Some important bond lengths are given in Table 3.4.1, angles in Table 3.4.2, including values for calculated molecules **5** and **5**$^{\bullet-}$. The crystal structure of *fac*-Pt(CH$_3$)$_3$I(big) is shown in Fig. 3.4.1. Details of the crystallographic parameters are given in Chapter 6.4.8.

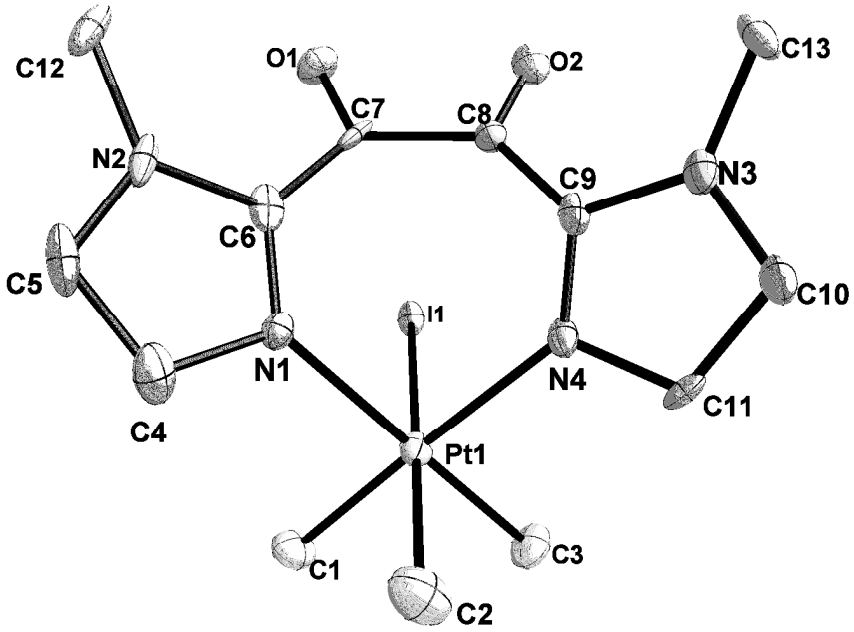

Fig. 3.4.1: *Molecular structure of **5** in the crystal (one out of four crystallographically independent molecules)*

The structure of the **5** confirms the N,N´-coordination of the metal center. A seven-membered chelate ring with a boat confirmation results, as was previously found for *fac*-Re(CO)$_3$Cl(big)[96]. Pt^{IV} has an octahedral structure configuration as expected. The α-diketo group became co-planar through metal coordination.

Table 3.4.1: *Selected distances for* ***5*** and $\mathbf{5}^{\bullet-}$. Bond lengths are given in Å

bond	5	5 [a)]	($5^{\bullet-}$) [a)]
Pt1 - C1	2.069(10)	2.063	2.068
Pt1 - C2	2.071(12)	2.078	2.086
Pt1 - C3	2.064(10)	2.063	2.068
Pt2 - C14	2.058(9)		
Pt2 - C15	2.078(10)		
Pt2 - C16	2.054(9)		
Pt3 - C27	2.056(9)		
Pt3 - C28	2.068(11)		
Pt3 - C29	2.055(8)		
Pt4 - C40	2.056(9)		
Pt4 - C41	2.068(10)		
Pt4 - C42	2.058(9)		
Pt1 - N1	2.169(7)	2.240	2.219
Pt1 - N4	2.152(7)	2.240	2.219
Pt2 - N5	2.136(7)		
Pt2 - N8	2.161(8)		
Pt3 - N9	2.149(7)		
Pt3 - N12	2.160(8)		
Pt4 - N13	2.140(7)		
Pt4 - N16	2.160(7)		
Pt1 - I1	2.779(1)	2.882	2.897
Pt2 - I2	2.7830(8)		
Pt3 - I3	2.7799(8)		
Pt4 - I4	2.7853(8)		
C7 - O1	1.210(11)	1.219	1.260
C8 - O2	1.207(11)	1.219	1.260
C20 -O3	1.224(11)		
C21 - O4	1.199(12)		
C33 - O5	1.208(11)		
C34 - O6	1.206(12)		
C46 - O7	1.219(11)		
C47 - O8	1.220(13)		
C7 - C8	1.564(13)	1.567	1.461
C20 - C21	1.601(13)		
C33 - C34	1.581(13)		
C46 - C47	1.566(13)		
N1 - C6	1.338(13)	1.336	1.342
N4 - C9	1.326(12)	1.336	1.342
C19 - N5	1.320(11)		
C22 - N8	1.315(13)		
C32 - N9	1.339(11)		
C35 - N12	1.321(12)		
C45 - N13	1.330(12)		
C48 - N16	1.321(13)		

[a)] *From DFT calculations*

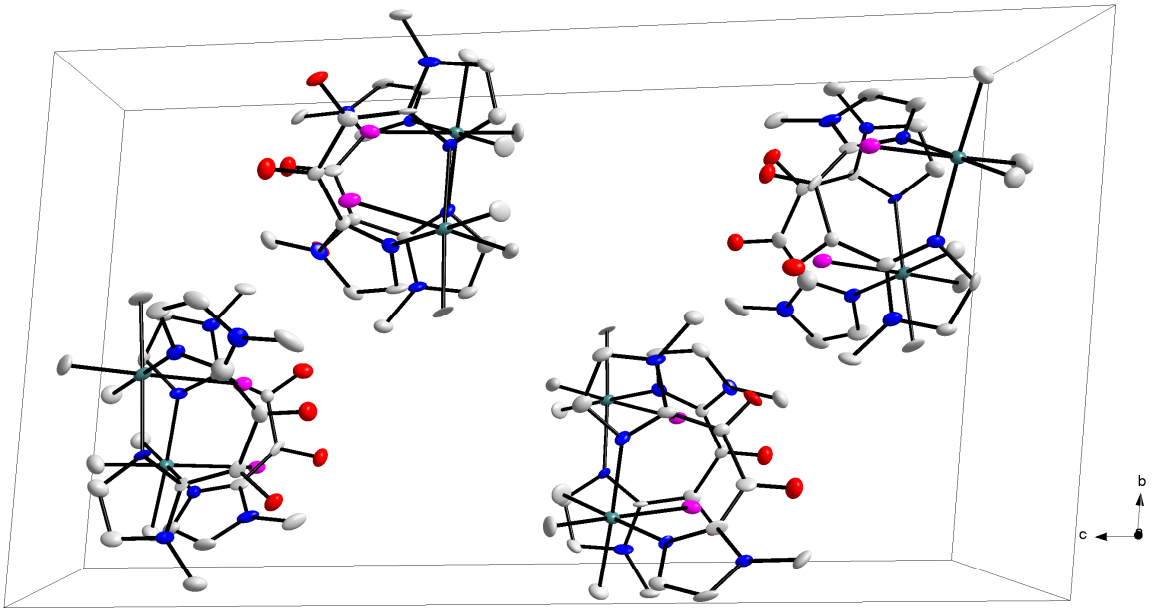

Fig. 3.4.2: *Arrangement of* ***5*** *in the unit cell*

The Pt-$C_{(ax)}$ bond, trans to the Pt–halide bond, is somewhat longer than the Pt-C(eq) bonds, like in the case of previously reported halogenotrimethylplatinum(IV) complexes[28,33,41]. The Pt-N bond lengths ranging from 2.136(7) Å to 2.169(7) Å are significantly longer than the corresponding bond length in $PtCl_2$(big) at 2.003(6) Å and 2009(6) Å[93]. The explanation can be the lower π back donation of the Pt^{IV}methylhalo moiety compared to the [$Pt^{II}Cl_2$] to "big".

The average N-Pt-N angle for the Pt^2, Pt^3 and Pt^4 centered molecules was found at 87.6^0 whereas it is 87.0^0 for the Pt^1 containing molecule. This angle was found at $91.2(3)^0$ for $Re(CO)_3Cl$(big) in the literature.[96] DFT results of **5** suggested even a smaller angle (85.30^0). The angle between the two imidazole planes was found at approximately 58.5^0. The α–diketo moiety do not completely planarize although there is a significant change from the perpendicular arrangement. The O-(C)-(C´)-O´ torsional angles for the *fac*-$Pt(CH_3)_3I$(big) molecules in the unit cell varies from 0.45^0 to 1.87^0, where it was calculated to be 0.34^0 theoretically.

Table 3.4.2: *Selected angles (^{0}) of four crystallographically independent molecules of* ***5***

angle	5[1)]	5 [a)]	(5¯) [a)]	angle	5[2)]
C1 - Pt1 - C3	86.9(4)	85.69	86.16	C16 - Pt2 - C14	87.8(4)
C1 - Pt1 - C2	87.6(4)	89.68	90.30	C16 - Pt2 - C15	89.2(4)
C2 - Pt1 - C3	89.8(5)	89.05	90.15	C14 - Pt2 - C15	90.3(5)
C1 - Pt1 - N1	93.7(4)	94.35	93.59	C16 - Pt2 - N8	92.8(4)
C1 - Pt1 - N4	177.2(4)			C16 - Pt2 - N5	178.6(4)
C2 - Pt1 - N1	89.5(4)	89.83	87.46	C15 - Pt2 - N8	88.9(4)
C2 - Pt1 - N4	89.7(4)	89.89	87.43	C15 - Pt2 - N5	89.5(4)
C3 - Pt1 - N1	179.0(4)			C14 - Pt2 - N8	179.0(4)
C3 - Pt1 - N4	92.3(4)	94.63	93.74	C14 - Pt2 - N5	91.7(4)
N1 - Pt1- N4	87.01(3)	85.30	86.40	N5 - Pt2 - N8	87.7(3)
angle		**5[3)]**		**angle**	**5[4)]**
C29 - Pt3 - C27		86.9(4)		C40 - Pt4 - C42	87.9(4)
C27 - Pt3 - C28		90.3(5)		C40 - Pt4 - C41	90.1(4)
C29 - Pt3 - C28		87.8(4)		C42 - Pt4 - C41	88.0(4)
C27 - Pt3 - N9		91.5(3)		C40 - Pt4 - N13	91.2(4)
C27 - Pt3 - N12		178.8(4)		C40 - Pt4 - N16	178.0(4)
C28 - Pt3 - N9		89.9(3)		C41 - Pt4 - N13	89.9(4)
C28 - Pt3 - N12		88.8(4)		C41 - Pt4 - N16	88.3(4)
C29 - Pt3 - N9		177.2(4)		C42 - Pt4 - N13	177.7(4)
C29 - Pt3 - N12		93.9(3)		C42 - Pt4 - N16	93.2(3)
N9 - Pt3 - N12		87.7(3)		N13 - Pt4 - N16	87.6(3)

[a)] *From DFT calculations.* [1)] *Molecule 1.* [2)] *Molecule 2.* [3)] *Molecule 3.* [4)] *Molecule 4.*

***fac*-Pt(CH$_3$)$_3$I(bik) (6)**

Yellow needle-like crystals of **6** were obtained in CH_2Cl_2 solution by layering with n-hexane at -20 ^{0}C. The space group was found to be monoclinic ($P2_1/m$). Some selected bond lengths and angles are given in Table 3.4.3 and Table 3.4.4, respectively. Crystallographic parameters are given in Chapter 6.4.9.

There are 4 structurally similar but 2 crystallographically independent molecules in the unit cell. The mirror plane joining the CO bond to the Pt and bisecting the C1-Pt-C1´ angle makes both sides of the complex symmetrical, and the bond lengths identical.

The X-ray structure analysis of **6** revealed the formation of boat-shaped six-membered chelate rings. Fig. 3.4.3 shows the molecular structure of the complexes.

Unexpectedly, the distance between the Pt-C_{ax} bond was not found longer than the Pt-C_{eq} bond distances. The average of Pt-N bond lengths was found to be 2,15 Å, which is longer than the previously reported Zn-N bond distances in $[Zn(bik)_2]^{2+}$.[97] For $[AuCl_2(bik)]Cl$, the Au-N bond lengths were given as 2.04(7) and 2.03(7) Å.[84]

No significant change was observed for the CO double bond distance by complexation with Pt^{IV} in comparison to the free ligand bik which was reported as 1.223(2) in the literature.[84] It is also comparable with the values found in $[Zn(bik)_2]^{2+}$ (1.215(17) and 1.224(15))[97] , and in $[AuCl_2(bik)]Cl$ complex (1.21(1)).[84]

Table 3.4.3: *Selected distances (Å) for* ***6*** *and* ***6•−***

Bond	exp.	6 [a)]	(**6•−**) [a)]
Pt1 - C1	2.054(5)	2.062	2.071
Pt1 - C1'	2.054(5)	2.063	2.071
Pt1 - C2	2.050(7)	2.081	2.074
Pt2 - C8	2.061(5)		
Pt2 - C8'	2.061(5)		
Pt2 - C9	2.051(8)		
Pt1 - N1	2.151(4)	2.246	2.186
Pt1 - N1'	2.151(4)	2.235	2.186
Pt2 - N3	2.156(4)		
Pt2 - N3'	2.156(4)		
Pt1 - I1	2.8092(5)	2.902	2.970
Pt2 - I2	2.8261(5)		
N1 - C5	1.337(6)	1.339	1.352
N1' - C5'	1.337(6)	1.338	1.352
N3 - C12	1.339(6)		
N3' - C12'	1.339(6)		
N1 - C3	1.363(6)	1.358	1.370
N1' - C3'	1.363(6)	1.359	1.370
N3 - C10	1.353(6)		
N3' - C10'	1.353(6)		
O1 - C6	1.231(8)	1.235	1.289
O2 - C13	1.220(8)		
C5 - C6	1.470(5)	1.471	1.456
C5' - C6	1.470(5)	1.472	1.456
C12 - C13	1.481(6)		
C12' -C13'	1.481(6)		

[a)] *From DFT calculations*

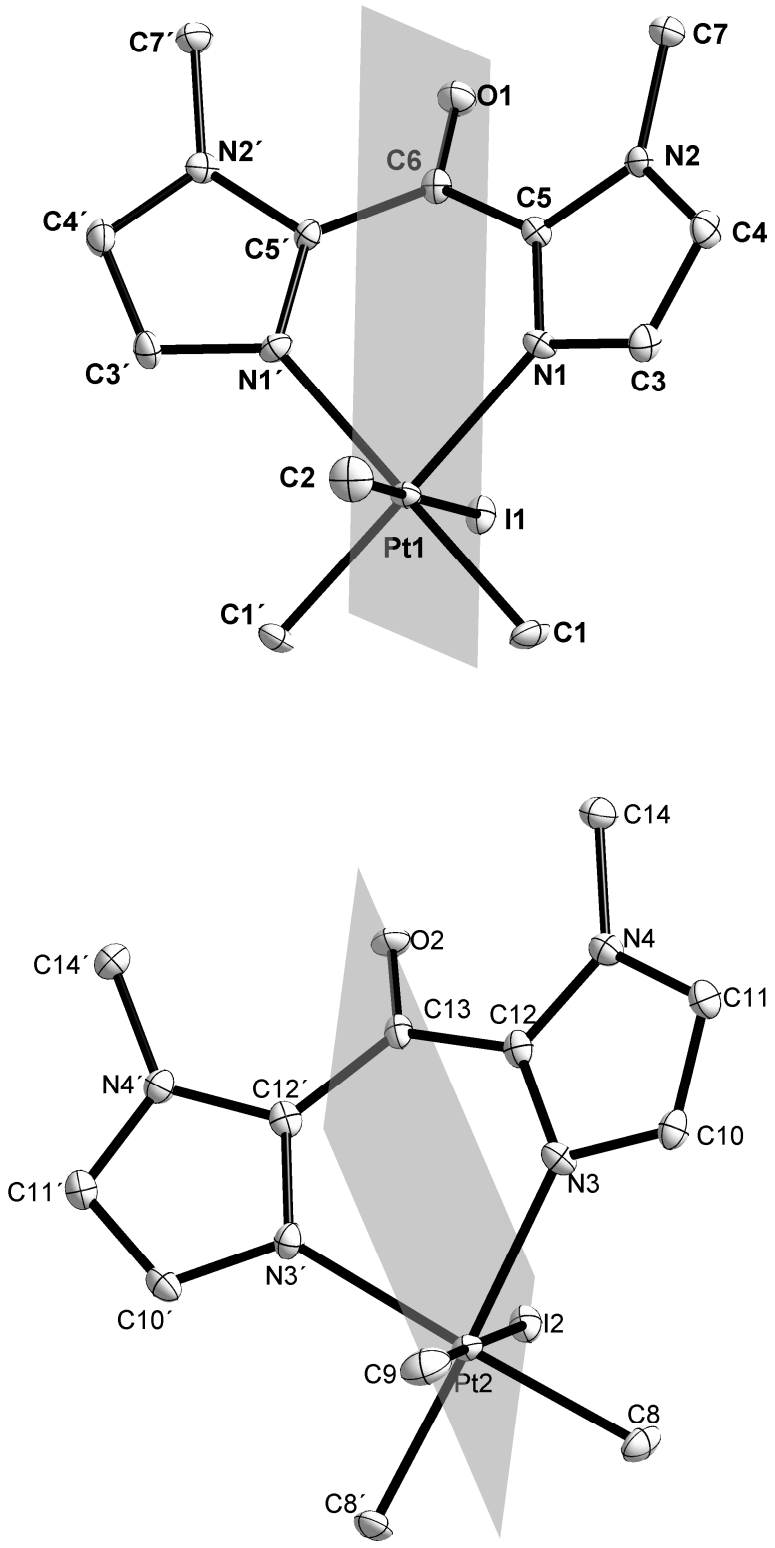

Fig. 3.4.3: *Molecular structure of two crystallograhically independent fac-Pt(CH_3)$_3$I(bik) molecules in the crystal with mirror planes*

Two imidazole planes on molecule 1, N1-C5-N2-C4-C3 and N1'-C5'-N2'-C4'-C3' as well as N3-C12-N4-C11-C10 and N3'-C12'-N4'-C11'-C10' of molecule 2, are not coplanar in between each other, having dihedral angles of ca. 34.5^0 and 23.3^0, respectively.

The Pt1-N1-C5-C6 torsional angle is ca. 5.19^0 whereas this value is around 6.9^0 for Pt2-N3-C12-C13. The average N-Pt-N bond angle of the two crystallographically different Pt complexes was found to be 85.5^0.

Table 3.4.4: *Selected angles (^{0}) for* ***6*** *and* ***6$^{\bullet-}$***

angle	exp	6 [a)]	(***6$^{\bullet-}$***) [a)]
C1-Pt1-C1'	85.6(3)	86.63	89.64
C2-Pt1-N1	90.4(2)	93.69	91.31
C1'-Pt1-N1'	94.67(18)	94.40	92.84
C1-Pt1-N1	94.67(18)	95.28	93.03
N1-Pt1-N1'	85.0(2)	83.73	84.41
C1-Pt1-I1	92.06(15)	93.88	91.70
N1-Pt1-I1	89.23(11)	86.50	91.31
C5'-C6-C5	117.9(6)	120.97	119.12
C5'-C6-O1	120.8(3)	119.42	120.37
C9-Pt2-C8	86.2(2)		
C8-Pt2-C8'	90.1(3)		
C9-Pt2-N3	93.3(2)		
C8-Pt2-N3	91.90(18)		
C8-Pt2-N3'	177.87(17)		

[a)] *From DFT calculations*

3.5 DFT Calculations

Density functional (DFT) calculations were carried out using the program package GAUSSIAN[77]. The B3LYP/LAN2DZ hybrid functional was used to optimize the geometry of the complexes. Calculations involving the ligand bmiq were done by Prof. Varnali at Bogazici University Istanbul. The *fac*-$Pt(CH_3)_3I$(big) and *fac*-$Pt(CH_3)_3I$(bik) systems were calculated by Mr. O. Sarper at the University of Stuttgart.

***fac*-$Pt(CH_3)_3I$(big) and *fac*-$Pt(CH_3)_3I$(bik)**

Both the X-ray description in solid state and theoretical calculations of the ligand big showed that the molecule adopts a structure in which two halves of the molecule are non-conjugated and perpendicular to each other.[98] The π acceptor carbonyl groups have favoured π interactions with the neighbouring π donor imidazole rings and thus stay in the same plane. However, since these carbonyl groups have unfavourable π interactions with each other, the two halves stay in perpendicular arrangement where the interaction is at a minimum.[98]

When an electron is added to the molecule big, the α-diketo group of the formed anion radical is reported to get planarized so that the carbonyls become conjugated and the (O)-C-C'-(O') bond has double bond character, as also reported previously.[98]

The facile reduction of metal complexes of big in comparison (see Part 3.6) with the free ligand big shows the stabilization of π* orbitals.

The DFT results for *fac*-$Pt(CH_3)_3I$(big) show similarities with those for the free ligand. The LUMO of the complex is mainly distributed over the α-diketo moiety with bonding character over the C-C bond and antibonding character over the C=O's. The calculated bond distances are mostly in agreement with the experimentally found values except for Pt-N and Pt-I bond lengths which are longer than the experimentally observed ones (see Table 3.4.1).

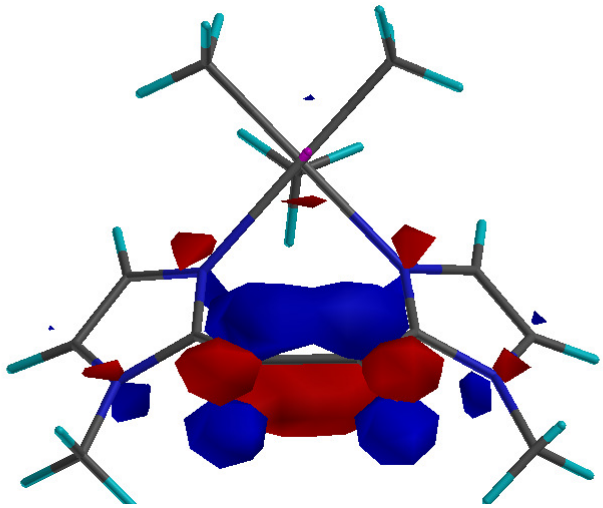

Fig. 3.5.1: *LUMO of optimized* ***5***

The one-electron reduced form of *fac*-Pt(CH_3)$_3$I(big), $\mathbf{5}^{\bullet-}$ was also studied by a DFT calculation and the SOMO of the complex is shown in Fig. 3.5.2.

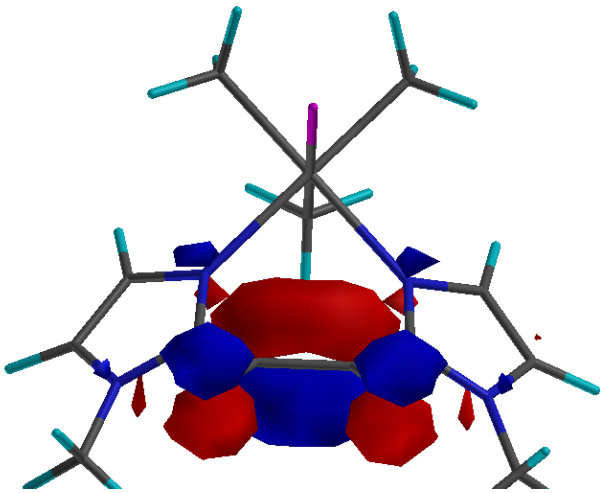

Fig. 3.5.2: *SOMO of* $\mathbf{5}^{\bullet-}$

As is seen in the figure, the SOMO of $\mathbf{5}^{\bullet-}$ is mainly composed from the α-diketo moiety of the ligand with bonding character over the C-C bond and antibonding character over the carbonyls, like in the neutral complex. This shows that when an electron is added to the complex, it is delocalized over this part of the molecule causing the C-C bond length to decrease and the C-O distance to increase.

Theoretically it was found that the value of 1.567 Å for the C7-C8 bond length decrease to 1.461 Å whereas the CO bond lengths increase from 1.219 Å to 1.260 Å. Additionally, the Pt-N bond lengths also decrease to 2.219 Å, indicating a stronger π-interaction. These theoretical results are also in harmony with the EPR spectrum (g_{iso}: 2.0061, close to free electron value) and the IR spectroelectrochemistry of the complex discussed in Part 3.6.

DFT calculations which were also carried out for **6** showed that LUMO of the molecule is mostly localized on the ketone part of the complex with an anti-bonding character of the CO group.

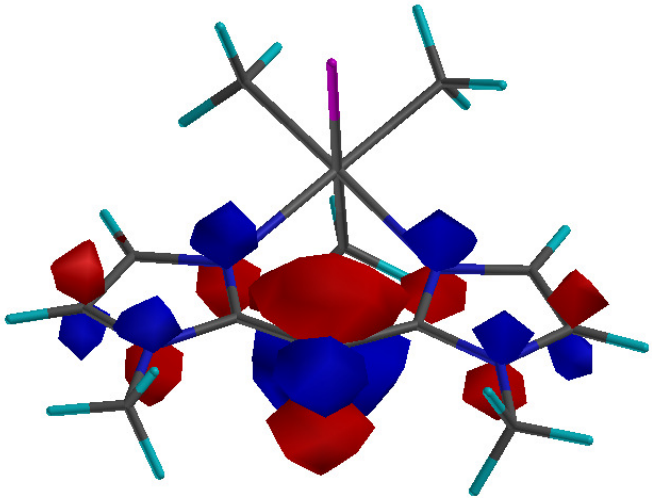

Fig. 3.5.3: *LUMO of optimized* ***6***

Calculated and experimentally found bond distances and angles for **6** are in good agreement with the exception that the Pt-N and Pt-I bond lengths were estimated to be longer, like in **5** (see Table 3.4.3 and 3.4.4).

On reduction to $\mathbf{6}^{\bullet-}$, the major bond length change calculated is the lengthening of CO double bond as befits a ketyl type radical, where SOMO was found to be distributed mainly as shown in Fig. 3.5.4, although there are also contributions from imidazole rings.

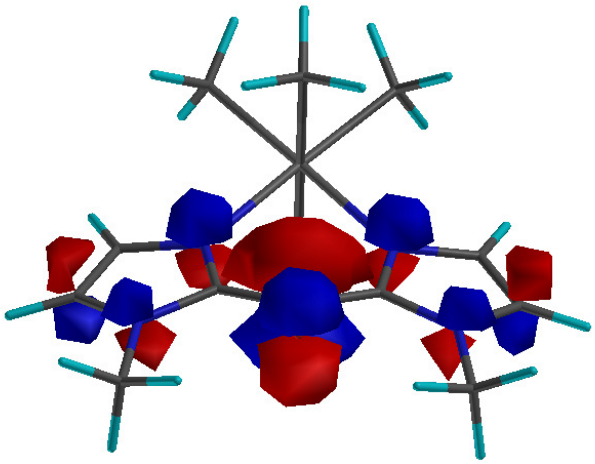

Fig. 3.5.4: *SOMO of optimized* ***6***$^{\bullet-}$

From these results, the occurrence of a possible ligand-based reduction can be considered when one electron is added to the molecule. The Pt^{IV} center showed no effect on the SOMO. On the contrary, in a previously reported $AuCl_2$(bik)Cl complex there was almost no contribution from the organic ligand to the singly occupied MO upon one-electron reduction of the molecule, since the SOMO is mainly between Au-Cl bonds.[84]

Pt(CH$_3$)$_3$I(bmiq) / (Pt(CH$_3$)$_3$I)$_2$(bmiq)

In order to find out an explanation for the formation of **7a** and **8a** together even though different ratios of precursors were used, DFT calculations of possible complexes of bmiq with [$PtMe_3I$] were performed, and were compared with those for the free bmiq ligand.

The result of the calculations showed that the difference between the formation energies of five-membered mononuclear and seven-membered mononuclear [PtMeI] chelate complexes of bmiq is 12 kcal/mole, in favour of the seven-membered mononuclear complex.

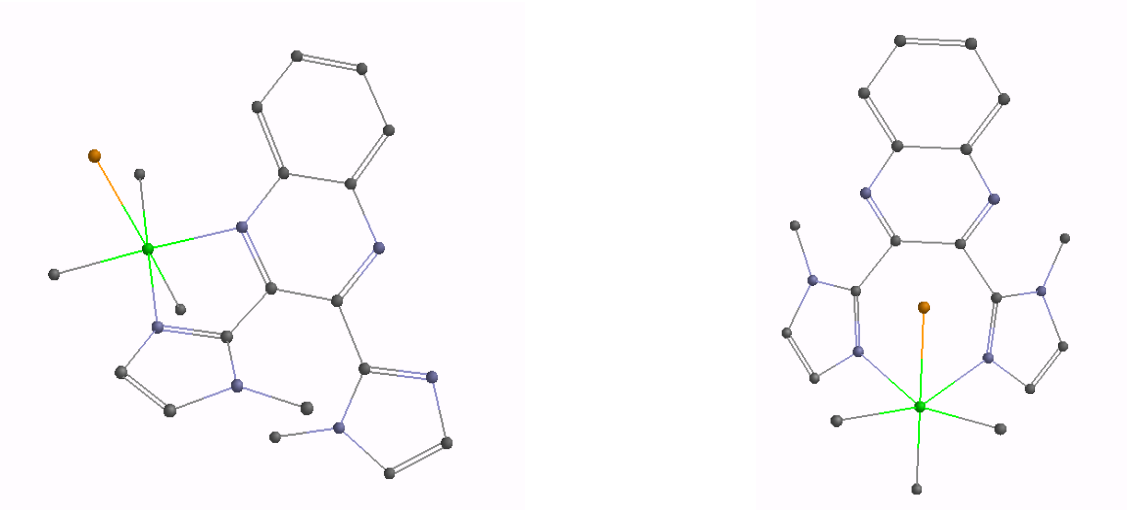

Fig. 3.5.5: *Postulated structures of mononuclear five-membered- (left) and mononuclear seven-membered (right) chelate ring* $Pt(CH_3)_3I(bmiq)$ complexes

The energy of the HOMO of a possible mononuclear five-membered ring complex (-0.18631 eV) is found to be higher than that of the free bmiq ligand (-0.21286 eV) whereas the LUMO of the same complex is lower than that of bmiq (-0.11598 eV for complex and -0.08330 eV for free bmiq). This energy difference can be an explanation of the facile formation of bimetallic five-membered ring compound after formation of any monomeric five-membered ring molecule. The higher energy of the HOMO reveals a higher reactivity of the five-membered ring mononuclear complex than the free ligand. On the other hand, the lower energy of the LUMO of the monomeric five-membered ring molecule than free bmiq is an indication of easy back bonding in the complexation, in other words, it sets off the formation of a bimetallic **8a** complex.

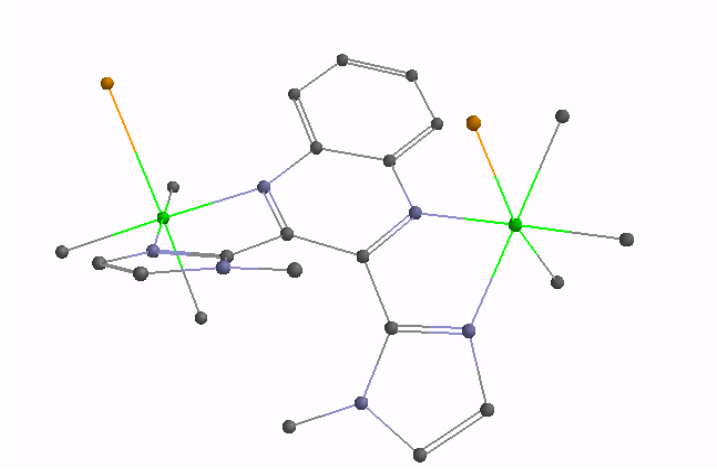

Fig. 3.5.6: *Postulated structure of* $(Pt(CH_3)_3I)_2(bmiq)$ ***(8a)*** *complex*

As a conclusion it can be postulated that monomeric seven- and five-membered ring complexes are formed simultaneously. Because of the higher reactivity of the monomeric five-membered ring molecule than the free ligand, it preferably reacts with the Pt^{IV} center forming the corresponding binuclear **8a** complex. As a result both **7a** and **8a** exist in the product mixture with a higher abundance of **8a**, as it was found experimentally.

3.6 Electrochemistry

Cyclic Voltammetry

fac-$Pt(CH_3)_3I(big)$ (5)

This complex shows an irreversible reduction wave at -1.0 V at room temperature in CH_3CN / 0.1 M Bu_4NPF_6 which turns into a reversible one at -30° C at -1.02 V with respect to $Fc^{0/+}$. Further reduction at -1.85 V and the oxidation at 0.65 V were not found to be reversible. The second irreversible reduction process may involve the dissociation of I^-. In relation to the free ligand (-1.66 V), the facile reduction of the complex illustrates the polarization of the ligand π system through metal coordination[93,99] and structural change. The same effect was also observed for *fac*-$Re(CO)_3Cl(big)$[96] complex, where the reduction potential was -0.95 V in CH_2Cl_2 / 0.1 M Bu_4NPF_6. Fig. 3.6.1 shows the cyclic voltammogram of the complex **5**.

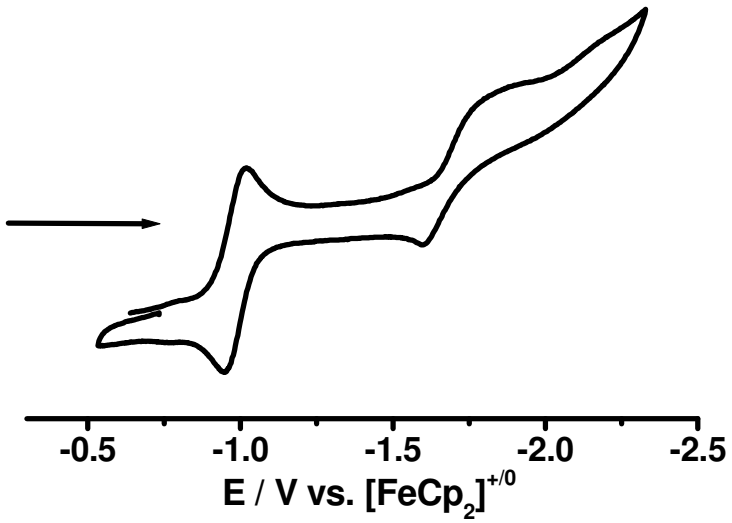

Fig. 3.6.1: *Cyclic voltammogram of* ***5*** *in CH_3CN / 0.1 M Bu_4NPF_6 at – 30 ^{0}C with a scan rate of 100 mV/sec*

$Pt(CH_3)_3I(bik)$ (6)

Complex **6** shows a reversible reduction wave only at -80 ^{0}C at -1.72 V in CH_2Cl_2 / 0.1 M Bu_4NPF_6.

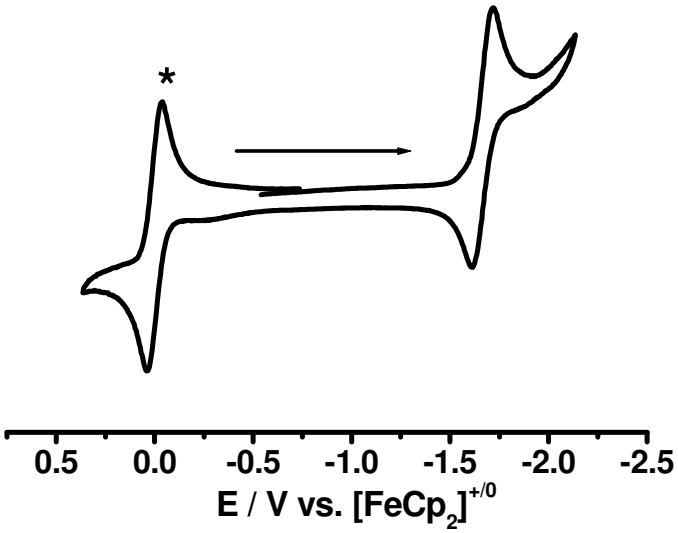

Fig. 3.6.2: *Cyclic voltammogram of **6** in CH_2Cl_2 / 0.1 M Bu_4NPF_6 at – 80 ^{0}C with a scan rate of 50 mV/sec. *: ferrocene wave*

The reduction at -1.72 V occurs on the C=O group causing a ketyl-type radical. The same polarization effect that was mentioned above was also observed here, the complex showed a less negative reduction potential than the free ligand (-2.25 V).[100]

The reversible character of the reduction of the bik complex **6** only at much lower temperature than that of the big complex of Pt^{IV} can be attributed to the lower π accepting capability of bik. The occurrence of a second carbonyl group makes big and its Pt^{IV} complex easily reducible than bik and the Pt^{IV}-bik complex.

Table 3.6.1: *Electrochemical data of big and bik ligands and of their complexes* [a)]

Compound	E_{pa}	E_{pc1}	E_{pc2}
fac-Pt(CH_3)$_3$I(big) [b)]	0.65 (irr)	-0.98 [f)]	-1.85 (irr)
big [c)]	-	-1.66 (116 mV)	-
fac-Pt(CH_3)$_3$I(bik) [d)]	0.66 (irr)	-1.66 [f)]	-
bik [e)]	-	-2.25 (80 mV)	-

[a)] *vs.ferrocene.* [b)] *In CH_3CN / 0.1 M Bu_4NPF_6 at – 30 ^{0}C with a scan rate of 100 mV/sec.* [c)] *In CH_3CN / 0.1 M Bu_4NPF_6 with a scan rate of 100 mV/sec*[100]. [d)] *CH_2Cl_2 / 0.1 M Bu_4NPF_6 at – 80 ^{0}C with a scan rate of 50 mV/sec.* [e)] *In DMF*[100]. [f)] *Reversible, $E_{1/2}$ is given*

IR Spectroelectrochemistry

fac-Pt(CH_3)$_3$I(big)

The metal carbonyl stretching bands of the ligands big and bik in the infrared region were monitored during the electron transfer processes through spectroelectrochemistry using an OTTLE cell[70].

IR spectroelectrochemistry of **5** was done in n-butyronitrile solution at -60 ^{0}C. The carbonyl band of the ligand at around 1673 cm^{-1} shifts to lower wavenumbers on reduction of *fac*-Pt(CH_3)$_3$I(big) (Fig. 3.6.4) and a new band appears at 1533 cm^{-1}. This lowering of the energy of the CO band indicates that the added electron is accumulated on the α-diketone moiety where the ligand has its LUMO[98a] (see also Part 3.5) resulting in the formation of α-semidione compound.

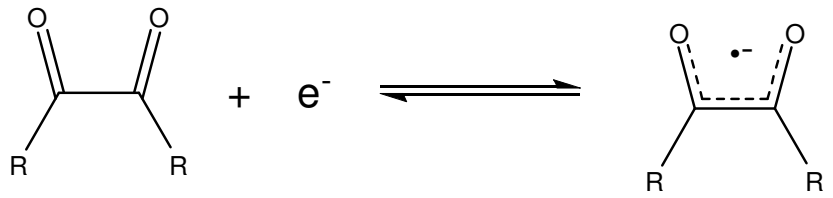

Fig. 3.6.3: *Formation of α-semidione ligand by one electron reduction of* ***5***

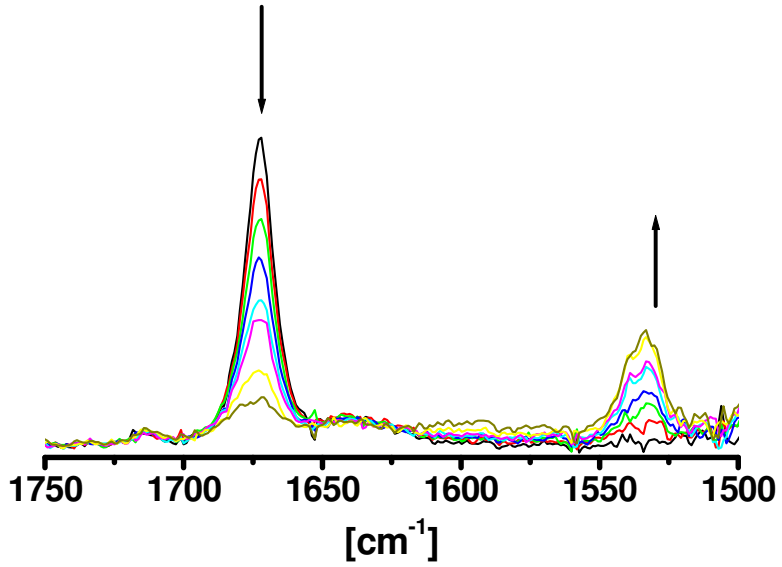

Fig. 3.6.4: *Spectroelectrochemical reduction of **5** at -60 ^{0}C in n-butyronitrile / 0.1 M Bu_4NPF_6*

Table 3.6.2: *IR Spectroelectrochemical data of **5** and big*

Compund	ν(C=O) band (cm^{-1})
[a] ***fac*-Pt$(CH_3)_3$I(big)**	1673
[a] ***fac*-Pt$(CH_3)_3$I(big)$^{\bullet-}$**	1533
[b] **big**	1675
[b] **big$^{\bullet-}$**	1404

[a] *Measured in n-butyronitrile / 0.1 M Bu_4NPF_6 at -60 ^{0}C*
[b] *Measured in CH_2Cl_2 / 0.1 M Bu_4NPF_6 at RT*[96]

***fac*-Pt$(CH_3)_3$I(bik)**

Although it was previously shown in Part 3.5 and in Table 3.4.2 that the CO bond distance is getting longer while there is a shortening of C5-C6 and C5´-C6 bond lengths on reduction showing that the added electron is delocalized between C5-C6-O-C5´-C6 bonds, which can also be an indication of the formation of a ketyl type radical, in the IR spectroelectrochemistry of *fac*-Pt$(CH_3)_3$I(bik) that was measured in CH_2Cl_2 at -60 ^{0}C, the CO band occurring at around 1655 cm^{-1} diminished but did not occur again at a lower wavenumber; the experiment showed no reversibility.

EPR Spectroelectrochemistry

fac-Pt(CH$_3$)$_3$I(big)

The reversible reduction of **5** at least at lower temperatures allowed us to obtain EPR information for electronically generated *fac*-Pt(CH$_3$)$_3$I(big)$^{\bullet-}$.

In situ electrolysis at 253 K in CH$_3$CN/0.1 M Bu$_4$NPF$_6$ yielded an unresolved EPR signal (ca 0.8 mT) at g_{iso}=2.0061, i.e. close to the free electron value of g = 2.0023. This supports the idea of a ligand based reduction. The poor resolution of the spectrum did not allow to obtain any information on the hyperfine interaction of the involving atoms, especially the ^{195}Pt (I = ½, 33.8% abundance) center. However, the negligible metal contribution is evident from marginal g shift relative to big$^{\bullet-}$ that was reported having g_{iso}= 2.0054.[92,96] Small metal coupling and g value shift were also reported for the Re(CO)$_3$Cl(big) complex, and the reason for binding of ReCO)$_3$Cl not at the spin-bearing oxygen atoms but at the imine nitrogen centres with their only marginal spin population.[96]

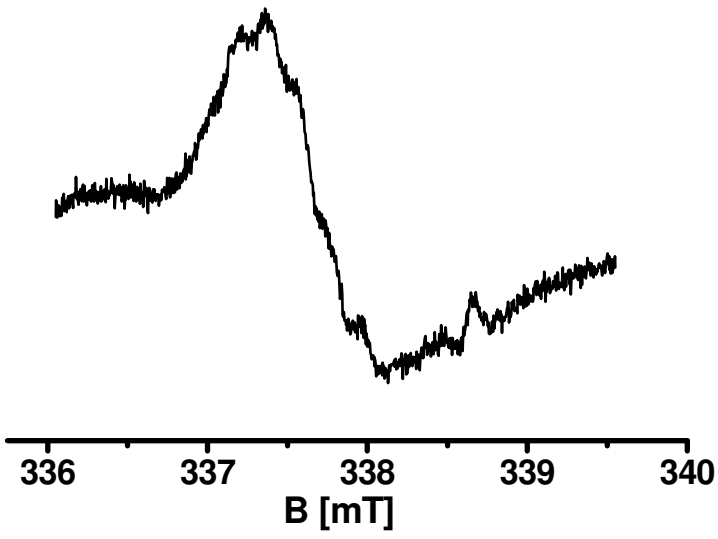

Fig. 3.6.5: *EPR spectrum of* ***5***$^{\bullet-}$ in *CH$_3$CN/0.1 M Bu$_4$NPF$_6$ at 253 K*

CHAPTER 4

A Tetranuclear Pt^{IV} Complex: Molecular Rectangle

4.1 Introduction

Self assembly is the most efficient means for the synthesis of a variety of discrete supramolecular species.[101-103] Molecular rectangles synthesized via self assembly with suitable bridging ligands and transition metals at the corners are stated as representative classes for such supramolecular complexes.[104]

In addition to the fascinating shapes, the capability of detecting substrates [105], the interaction with light (antenna function)[106], and the intramolecular magnetic exchange coupling[107] are other attractive aspects of these systems.

The last but not the least interesting property of these structures is the hosting capability of them for small molecules as a result of their cavities. The vast majority of currently known hosts are reasonably flexible organic molecules such as calixarenes[108], crown ethers[109] and related species that preferentially bind cationic guests.[110] There has been an intense interest in this “host-guest” chemistry including more rigid inorganic, organometallic and anionic selective hosts in last two decades. These molecules are potentially useful in sieving and separation applications as a result of their cavities that tend to align to form channels in the solid state.[104a,111] In addition, by changing the geometry (variation of the bridging ligands) the size of the molecules to be stored can be varied.

To date, a number of molecular rectangles or squares have been synthesized by usage of self assembly methodology. However, only few of them were electrochemically investigated.[43,104a,106a,112]

In this chapter, a new Pt^{IV} rectangle, $[\{Pt(CH_3)_3\}_4(\mu\text{–}bp)_2(\mu\text{–}bpym)_2](OTf)_4$, **(1)** that was synthesized via self assembly by using bp (4,4´-bipyridine) and bpym (2,2´-bipyrimidine) bridging ligands will be reported.

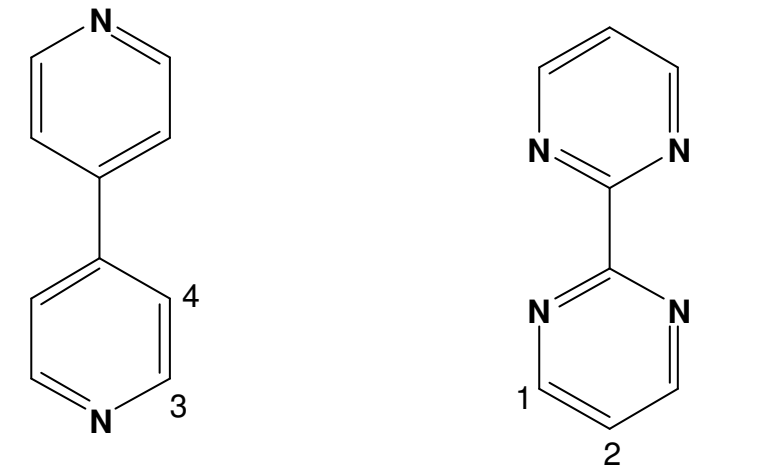

Fig. 4.1.1: *Molecular structure of bp and bpym*

Synthetic methods, characterization, electrochemical and spectroelectrochemical properties of the molecule will be discussed and the results will be compared with previously studied rhenium(I)[43] and platinum(II)[112] molecular rectangles.

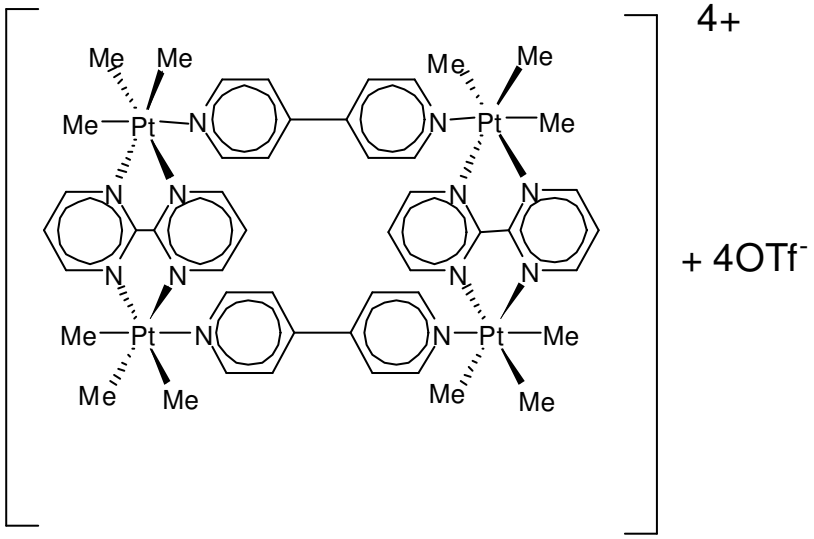

1

Fig. 4.1.2: *Molecular structure of [{Pt(CH$_3$)$_3$}$_4$(μ–bp)$_2$(μ–bpym)$_2$](OTf)$_4$*

4.2 Syntheses

The neutral dinuclear precursor for the rectangle, *syn*-[PtI(Me)$_3$]$_2$(μ–bpym) **(2)**, was synthesized in two different ways. In both methods, a mixture of *cis* and *trans* (*syn* and *anti*) isomers were obtained as also reported previously.[113]

In the first route, two equivalents of [PtIMe$_3$] were reacted with bpym:

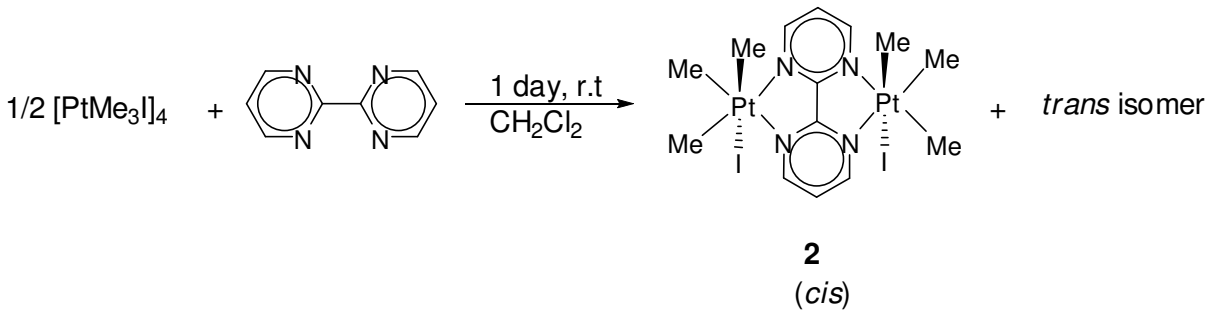

Fig. 4.2.1: *Reaction between [PtMe$_3$I]$_4$ and bpym*

In the second method, Pt$_2$(Me)$_4$(μ–S(Me)$_2$)$_2$ and bpym were reacted in an appropriate ratio in CH_2Cl_2 to give a dark suspension of dinuclear Pt$_2$Me$_4$(μ–bpym), which was further treated with MeI forming orange *cis* and *trans* isomers by an oxidative addition reaction:

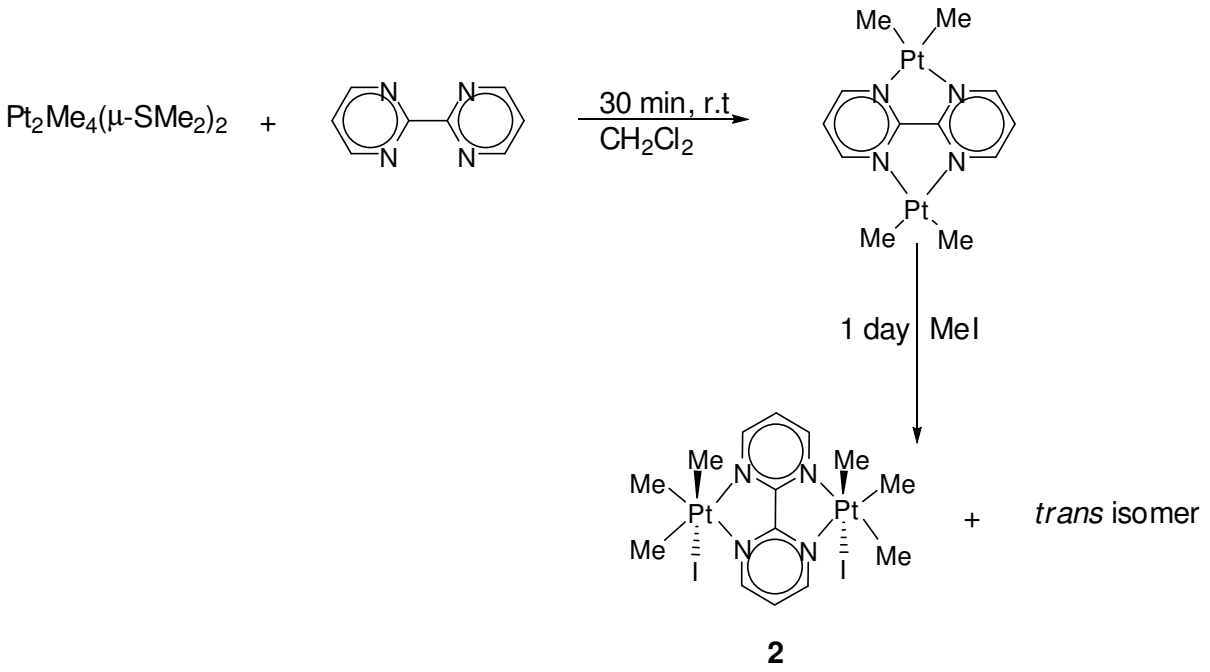

Fig. 4.2.2: *Reaction scheme for the synthesis of **2***

The *cis* isomer is needed for the required rectangle to be formed. It was possible to remove the *trans* isomer by washing the product mixture several times with CH_2Cl_2. The existence of only **2** was verified by ^{1}H-NMR.

In the next step, I^- was removed by reacting **2** with slightly more than two equivalents of AgOTf (OTf : triflate) in dried and oxygen free acetone. The AgI formed during the reaction was filtered through celite on a glass frit and the solvent was removed in vacuum. The crude product was dissolved in CH_2Cl_2, filtered by same method, and to the filtered solution one equivalent of bp was added:

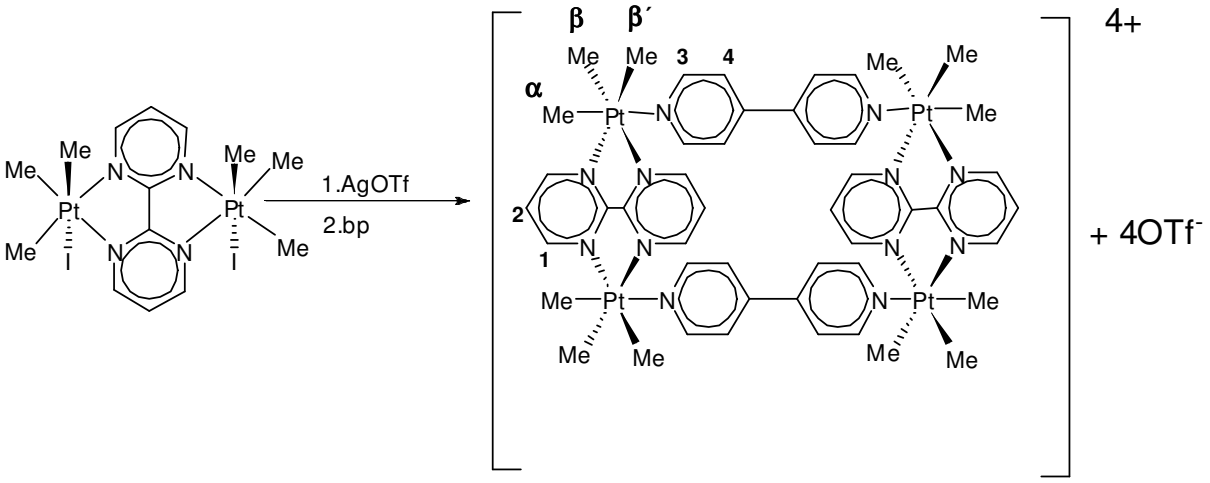

Fig. 4.2.3: *Reaction scheme for the synthesis of* ***1***

As is suggested for many of the molecular squares[114], a colorless precipitate eventually occurred when the formation of rectangle was completed. Thus, the intermediate species remained in solution, presumably as solvento complexes, until all their metal centers and all ligand nitrogen atoms are coordinated.[115]

4.3 Characterization

Several attempts of obtaining single crystals of the complex in acetone and acetonitrile failed due to the low solubility of **1**; whereas in dimethylformamide and dimethylsulfoxide, it decomposed. Eventhough this rectangular molecule is quite stable in the solid state its instability in solution hinders crystallization by slow evaporation. Still, the product was identified by ^{1}H-NMR, ^{195}Pt-NMR, elemental analysis and mass spectroscopy. Fig. 4.3.1 shows the aromatic region of the ^{1}H-NMR spectrum. In fact, ^{1}H-NMR gives fairly enough clues for the existence of the desired complex.

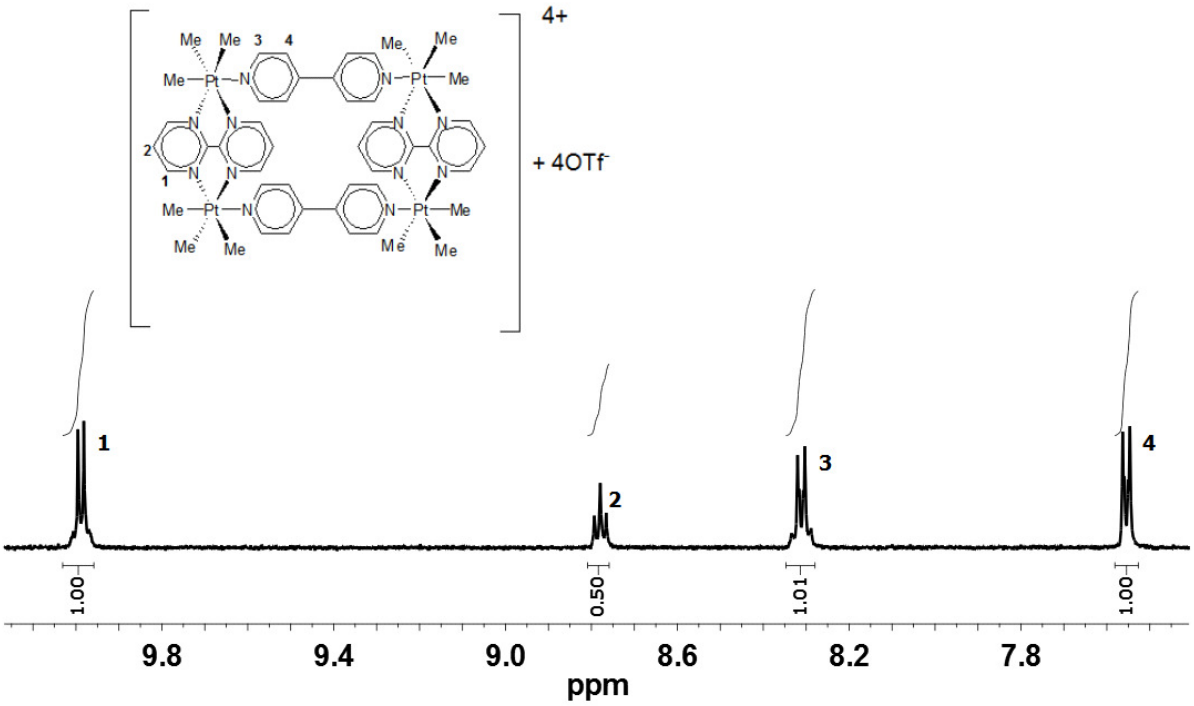

Fig. 4.3.1: *^{1}H-NMR (aromatic region) of **1** measured in acetone-d_6*

In the aromatic region of the spectrum, there are four signals from bridging bp and bpym ligands as expected. Free bp ligand has characteristic dd peaks at 8.72 and 7.75 ppm in acetone-d_6. Shifts of these peaks to higher field of the spectrum and the satellites occurring as a result of ^{195}Pt-H^{3} couplings are clear proofs for the binding of N-atoms of bp to the vacant positions of the Pt^{IV} centers. The other two signals, one doublet and one triplet, belong to the 1st and 2nd protons on bpym, H^{1} and H^{2} respectively. The integration of all four signals of protons numbered here as 1, 2, 3

and 4 are in 2:1:2:2 ratio respectively, as expected and as is strong evidence for the formation of the rectangle.

Table 4.3.1: *^{1}H-NMR data of ligands and related complexes in acetone-d_6 (aromatic signals. ^{195}Pt-H couplings of **1** are also given)*

	δ [ppm]				J[Hz]	
Compound	**H^1**	**H^2**	**H^3**	**H^4**	**Pt-H^1**	**Pt-H^3**
1	9.99	8.78	8.31	7.55	14.06	18.49
2	9.71	8.50	-	-		
$[(PtMe_3)_2(bpym)](OTf^-)_2$	9.78	8.67	-	-		
bpym	9.71	8.50	-	-		
bp	-	-	8.72	7.75		

In the aliphatic region, there exist two different types of methyl peaks that also have Pt satellites. They are in 1:2 integration ratio (24 H's from Me's trans to bpym and 12 H's from Me's trans to bp) which also fit well for the rectangle. There are no more signals of any precursor in both the aromatic and aliphatic regions.

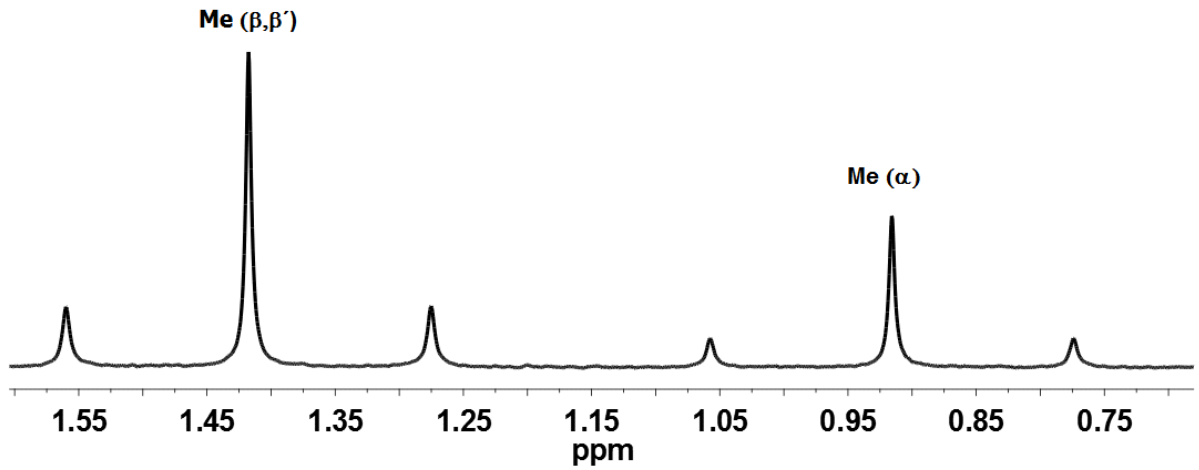

Fig. 4.3.2: *^{1}H-NMR (aliphatic region) of **1** measured in acetone-d_6*

Table 4.3.2: *^{1}H-NMR data of complexes **1** and **2** in acetone-d_6 (aliphatic signals and Pt-CH_3 couplings)*

δ [ppm]			J[Hz]	
Compound	**$CH_3^{(\alpha)}$**	**$CH_3^{(\beta,\beta')}$**	**Pt-$CH_3^{(\alpha)}$**	**Pt-$CH_3^{(\beta,\beta')}$**
1	0.92	1.41	70.61	71.17
2	0.84	1.65	70.81	74.70

^{195}Pt-NMR is another method used for the characterization of complex **1**. Fig. 4.4.3 shows the spectrum obtained from two-dimensional [^{1}H, ^{195}Pt] heteronuclear multiple quantum coherence (HMQC) experiment performed for the solution of **1** in acetone-d_6.

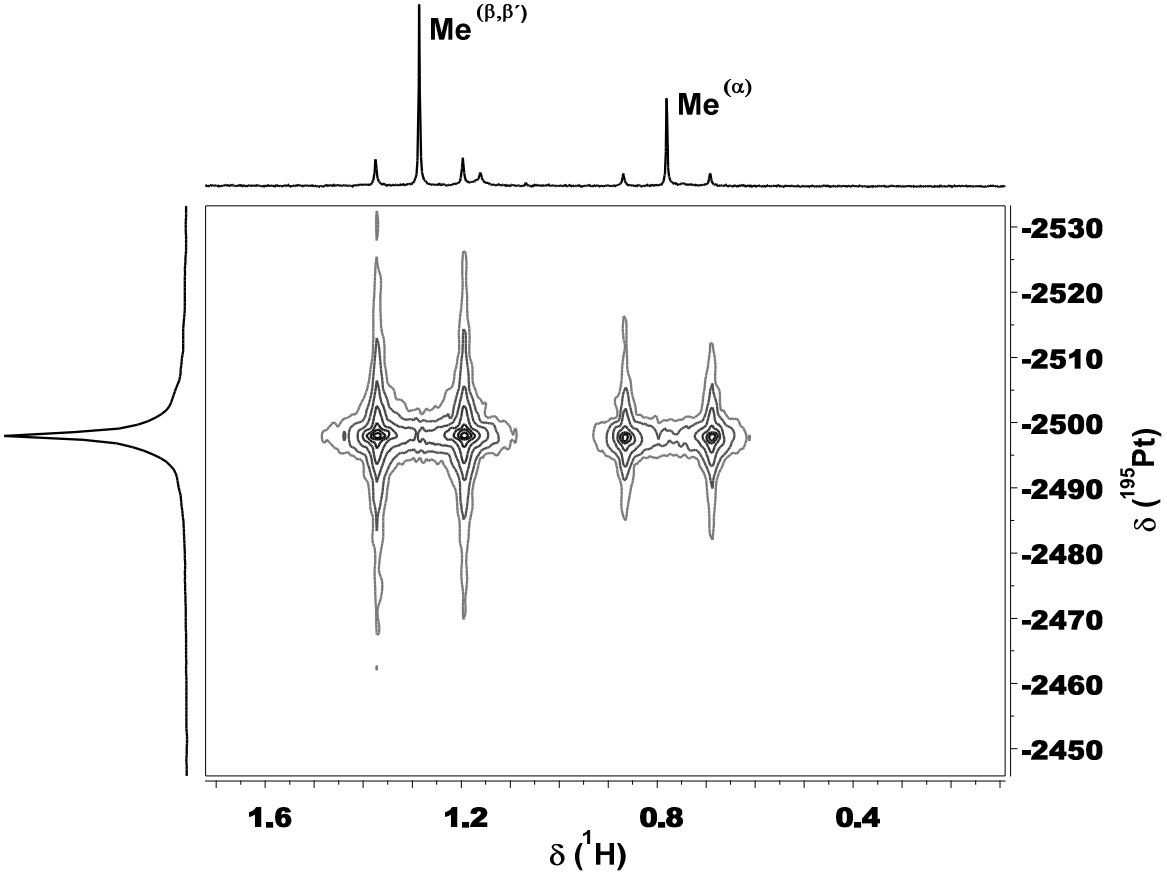

Fig. 4.3.3: *Expansion of the [^{1}H, ^{195}Pt] –HMQC spectrum of **1** in acetone-d_6 referenced to external 1.2 M Na_2PtCl_6 in D_2O [Ξ =21.496784 MHz, ^{195}Pt]*

The spectrum displays ^{195}Pt satellites clearly visible for the Pt-$CH_3^{(\beta,\beta')}$ and Pt-$CH_3^{(\alpha)}$ [^{2}J(Pt,H)≈ 70 Hz)] couplings of complex **1**. The ^{195}Pt singlet at δ = -2498 is in expected resonance range of Pt^{IV}-complexes and around 400 ppm down-field shifted than complex **2** (-2836 ppm and -2842 ppm for major and minor isomers, referenced

to *external K_2PtCl_6 [Ξ =21.496784 MHz, ^{195}Pt]*).[116] Existence of only one singlet peak of ^{195}Pt supports also the idea of formation of exclusively only complex **1**.

Another proof of **1** is obtained from mass spectroscopy. The ESI-MS spectrum of the complex showed peaks centered at *m/z* = 2036.3 for $\{[\{Pt(CH_3)_3\}_4(\mu\text{-bp})_2(\mu\text{-bpym})_2](OTf)_3)^+$. In addition, the isotopic distribution pattern is consistent with the calculated composition of the species (Fig.4.3.4). Thus, the mass measurement is in excellent agreement with the predicted mass and furnishes another evidence for **1**.

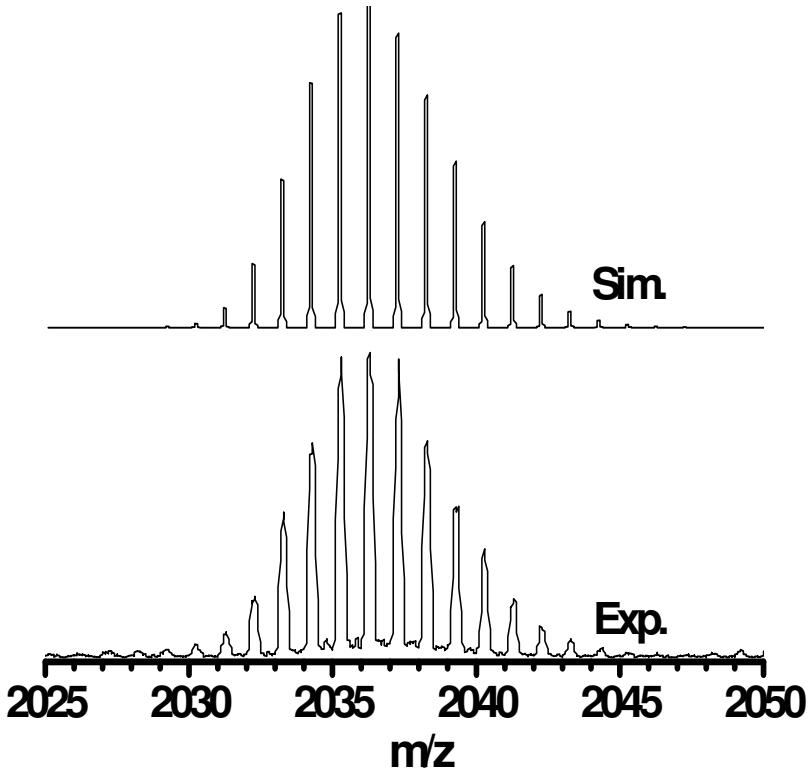

Fig. 4.3.4: *ESI-MS spectrum of **1** (M- $^{-}$OTf) with experimental result (top) and simulation (bottom)*

4.4 Electrochemistry

Cyclic / Differential Pulse Voltammetry

Because of the presence of four reversibly reducible bridging ligands in the complex and the possible "electron reservoir" capability of the molecule, electrochemical studies were performed for the product **1**.

Cyclic voltammetry (CV) of **1** in CH_3CN / 0.1 M Bu_4NPF_6, at room temperature, shows several sets of reversible reduction waves. Waves I and II correspond to two electron reduction process whereas III and IV are single electron processes. Further reduction at -2.34 V vs. $[FeCp_2]^{+/o}$ is not fully reversible, and no oxidation process is observed until +2.00 V. Fig. 4.4.1 shows the CV of complex **1**. Table 4.4.1 summarizes the data obtained from CV and differential pulse voltammetry (DPV) experiments.

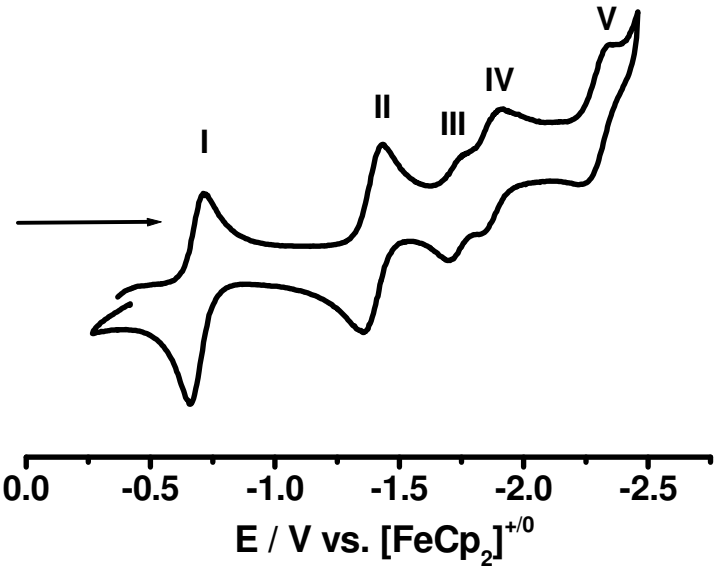

Fig. 4.4.1: *Cyclic voltammogram of **1** in CH_3CN / 0.1 M Bu_4NPF_6 at RT with a scan rate of 100 mV/sec*

The previously synthesized and electrochemically investigated tetra-rhenium rectangle $[Re_4(CO)_{12}(\mu\text{-bp})_2(\mu\text{-bpym})_2](OTf)_4$, (**3**) (bp = 4,4´-bipyridine und bpym = 2,2´-bipyrimidine) was discussed in the literature to have a similar cyclic voltammetry pattern in DMF / 0.1 M Bu_4NPF_6, exhibiting four sets of two electron reduction waves, two of which at the most negative potentials showed a clear splitting into two one-electron processes. The first two reductions were reported to be two electron uptakes

of bpym, while the third fourth, fifth and finally sixth reductions were attributed to reductions of the bp ligands in each step although the last electron uptake could not be spectroelectrochemically investigated owing to decomposition of the complex. [43] The first two electron reductions are likely to be reversible reductions of bpym. Previous work revealed more facile reduction of bpym than bp.[44,117,118] In comparison to bp, bpym contains two more electronegative nitrogen atoms instead of two CH groups. In addition, the metal coordination to four N centers of bpym is likely to shift the reduction potential to less negative values via stabilization of the π* MO.[44]

In order to confirm the ratio of the added electrons in each step, DPV was employed to the complex and the first four reductions are shown in Fig. 4.4.2.

Table 4.4.1: *Electrochemical potentials of **1** and $[Re_4(CO)_{12}(\mu\text{-bp})_2(\mu\text{-bpym})_2](OTf)_4$[43], (**3**)*

Differential Pulse Voltammetry[a]						
Complex	**E_{pc}(I)**	**E_{pc}(II)**	**E_{pc}(III)**	**E_{pc}(IV)**		
1	-0.70	-1.39	-1.73	-1.85		
Cyclic Voltammetry[b]						
Complex	**E_{red}(I)**	**E_{red}(II)**	**E_{red}(III)**	**E_{red}(IV)**	**E_{red}(V)**	**E_{red}(VI)**
1	-0.68(50)[c]	-1.40(73)[c]	-1.72(41)	-1.86(58)	-2.34(irr)[d]	-
3[e]	-0.48[c]	-1.13[c]	-1.59	-1.70	-2.27	-2.37

[a] *Potentials in V vs. $FeCp_2^{0/+}$ measured in CH_3CN/ 0.1 M Bu_4NPF_6 at 10mV/s scan rate at RT.* [b] *Half wave potentials in V vs. $FeCp_2^{0/+}$ measured in CH_3CN/ 0.1 M Bu_4NPF_6 at 100mV/s scan rate at RT, numbers given in parentheses correspond to peak potential differences ($\Delta E = E_{pc}-E_{pa}$).* [c] *Two electron waves.* [d] *Cathodic peak potential corresponding to an irreversible step.* [e] *$[Re_4(CO)_{12}(\mu\text{-bp})_2(\mu\text{-bpym})_2](OTf)_4$[43]*

The ratio of the areas under the first and second waves is 1:1, which means that the number of electrons added in the first two reductions should be same. The asymmetric pattern of the last two waves can be an indication of their not totally reversible character, leading to the decomposition of the complex. Due to the almost overlapping nature of these latter two waves, the area under these final two waves

could not be calculated easily; however the total area under these two last waves is equal to the area under each of the former wave. Thus, it can be assumed that the first two waves occur as a result of two two-electron reductions of the bpym sites whereas the third and fourth involve single electron uptake by presumably two different bp ligands, since a Baranski analysis [119] applied for the first wave of the previously studied similar $[Re_4(CO)_{12}(\mu\text{-bp})_2(\mu\text{-bpym})_2](OTf)_4$ showed a clear two-electron reduction behaviour.[43] The splitting of the third two-electron reduction wave into two close but separate waves is probably stimulated by the increased negative charge on the complex (Coulombic repulsion)[120]; such cases were also reported before.[43,112]

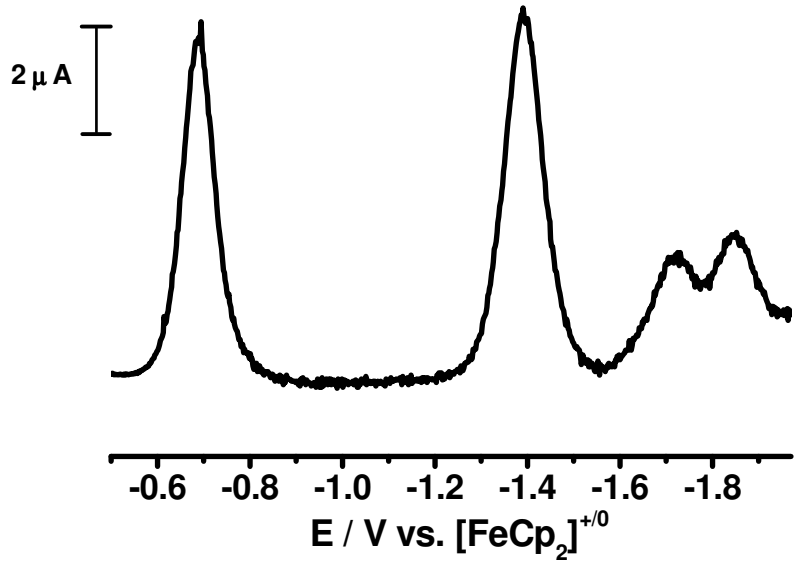

Fig. 4.4.2: *DP voltammogram of **1** in CH_3CN / 0.1 M Bu_4NPF_6 at RT with a scan rate of 10 mV/sec*

UV-Vis Spectroelectrochemistry:

OTTLE spectroelectrochemistry of **1** in the UV-Vis region at room temperature was performed to find out the details about electron addition.

The complex **1** shows intense IL bands in the UV region, possibly overlapping with MLCT transitions (Fig. 4.4.3). In addition, there is a shoulder at 340 nm; a band at around 380 nm was reported before for a Re^I containing rectangular $[Re_2(OCH_2CH_2OH)_2(CO)_6(bp)]_2$ molecule.[123b] It is present in all such rectangles and has been previously assigned by Tapolsky et. al.[121-123a] as a $\pi-\pi^*$ transition. A much less intense band in the visible region at 650 nm (ε = 600 M^{-1} cm^{-1}) was also

observed. This band can be assigned to σ(Pt-C)→π^*(bpym) transition. Such a transition of the complex (bpym)[$PtMe_4$]$_2$ was reported before.[124]

The $bp^{\bullet-}$[125] and $bpym^{\bullet-}$ chromophors[126] differ sufficiently, especially in the long wavelength features, because of the different sites of electron uptake. While $bp^{\bullet-}$ exhibits a fairly intense structured band around 600 nm[125], familiar from colouring of the reduced "methylviologen", the radical anion $bpym^{\bullet-}$ and the dianion $bpym^{2-}$ display much weaker, forbidden, and usually vibrationally structured $\pi \rightarrow \pi^*$ ($\pi_7 \rightarrow \pi_8$) transitions with maxima beyond 750 nm in the near-infrared region.[126]

By a reversible addition of two electrons to the complex **1**, three bands at 370, 445, 480 nm and two shoulders at 360 and 430 nm emerge. In addition, a broad weak band system between 600 and 1200 nm, which changes barely after addition of two more electrons, is also observed (Fig. 4.4.3). This latter behaviour can be related to the simultaneous reduction of both bpym ligands of the rectangle. These spectroelectrochemical observations are almost identical with those of the complex [$Re_4(CO)_{12}$(μ-bp)$_2$(μ-bpym)$_2$](OTf)$_4$, reported in an earlier work.[43] The second reduction step ($\mathbf{1}^{2+} \rightarrow \mathbf{1}^{0}$) also causes the bands at 370, 445 and 480 nm to diminish; the decrease in intensity of these bands can be attributed to the $bpym^{\bullet-}$ to $bpym^{2-}$ reduction (Fig. 4.4.4). Such a trend for Pt(bpym)Cl_2[41] and for [$Mo(CO)_4$]$_2$(bpym)[126] was reported before. A very small amount of adsorption of the neutral complex during the second reduction process was also detected.

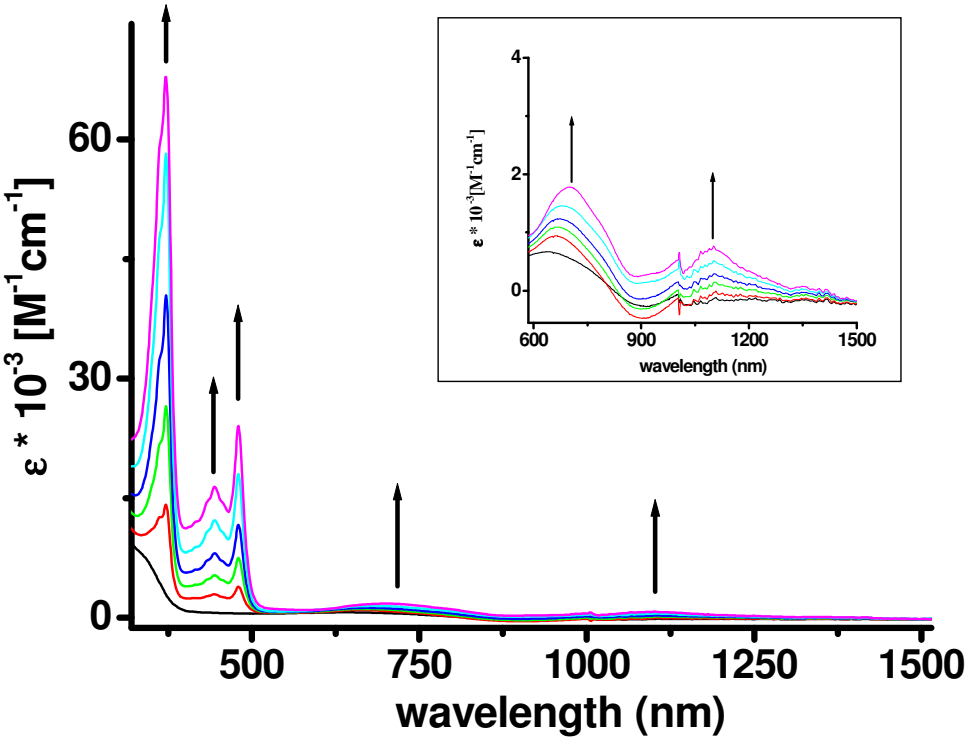

Fig. 4.4.3: *Spectroelectrochemical reduction of* $[\mathbf{1}]^{4+}$ *to* $[\mathbf{1}]^{2+}$ *in* CH_3CN */ 0.1 M* Bu_4NPF_6

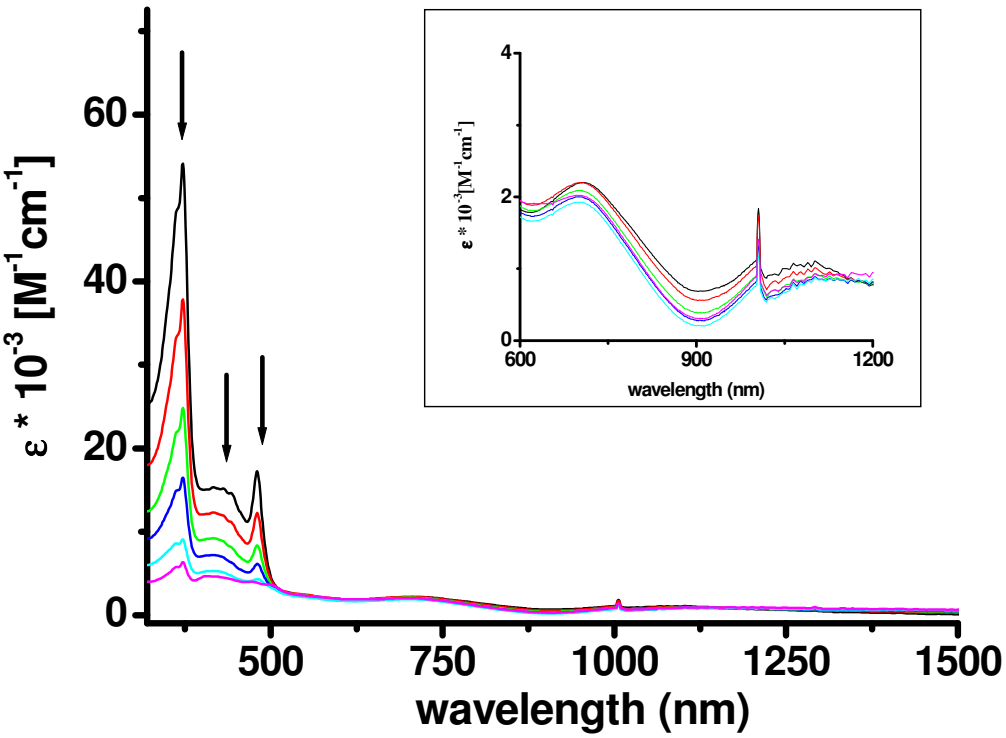

Fig 4.4.4: *Spectroelectrochemical reduction of* $[\mathbf{1}]^{2+}$ *to* $[\mathbf{1}]^{0}$ *in* CH_3CN */ 0.1 M* Bu_4NPF_6

The stepwise addition of the fifth and sixth electrons are observed as a combined two electron reduction step in the OTTLE spectroelectrochemistry involving adsorption/desorption of the neutral intermediate, and labilizes the negatively charged complex. An intense structured band system emerges in the visible region with the maximum at 570 nm and other features at 625, 765, 870 and at 1000 nm which are in fact rather similar to $bp^{\bullet -}$ in MTHF (585, 650, 845, 970 nm).[125] From this similar pattern, it is reasonable to assume that the 5th and 6th electrons would be accommodated on the bp ligands (Fig. 4.4.5).

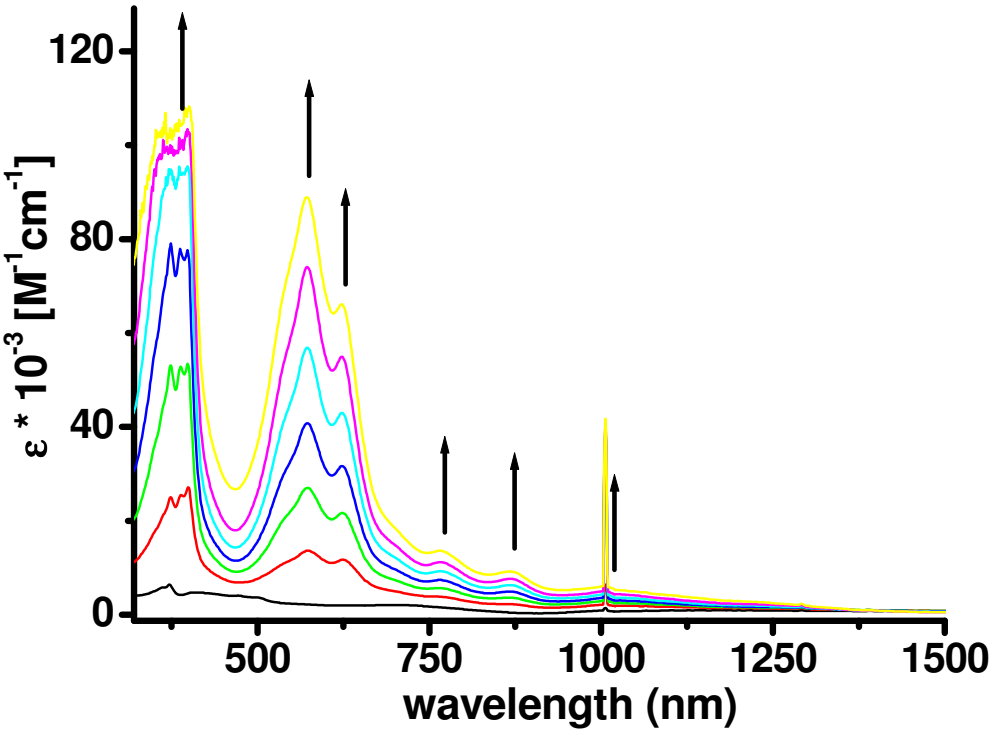

Fig. 4.4.5: *Electrochemical stepwise double one-electron addition to [**1**]^0 in CH_3CN / 0.1 M Bu_4NPF_6*

Table 4.4.2: *Data for* $\mathbf{1}^{n}$ *from and UV-Vis Spectroelectrochemistry*[a)]

UV-Vis Spectroelectrochemistry	
n	λ_{max} **(ε)**
4+	243(57300), 268(63600), 290(sh), 340(sh), 650(600)
2+	242(59600), 268(67200), 288(sh), 360(sh), 370(67700), 430(sh), 445(16500), 480(24200), 700(1800), 1100(730)
0	240(24200), 270(sh), 360(sh), 370(6400), 500(sh), 710(2000)
$\mathbf{1}^{\bullet-}$ / $\mathbf{2}^{-}$	240(74800), 267(89000), 395(106000), 540(sh), 570(88900), 625(66700), 765(13600), 870(9200), 1000(5800)

a) *In CH_3CN/0.1 M Bu_4NPF_6 (OTTLE cell) at RT, absorption maxima in nm, (molar extinction coefficients in M^{-1} cm^{-1}).*

EPR Spectroscopy

The EPR spectrum of the electrochemically generated $\mathbf{1}^{2+}$ at RT in CH_3CN/0.1 M Bu_4NPF_6 exhibits an unresolved signal (peak-to-peak linewidth = 1.28 mT) at g_{iso}= 1.990 which is rather close to the free $bpym^{\bullet-}$ value of g_{iso}= 2.0030[127] and not very different from values of corresponding dinuclear Pt^{II} and Pt^{IV} complexes.[28,41,124,128] Due to insufficient resolution it was not possible to analyze the hyperfine structure. Fig. 4.4.6 illustrates the EPR spectrum measured at room temperature.

In the glassy frozen state at 110 K, the two-electron reduced form of **1** yields an asymmetric signal, with g components at g_X = 2.0106, g_y = 2000 and g_z =1.959; similar to those found in the previously studied (bpym)$[PtMe_4]_2$[124], $PtMe_3Br(abpy)^{\bullet-}$[28] and $[Pt_4(PEt_3)_8(\mu\text{-anth})_2(\mu\text{-bp})_2]^{2+}$ [112] radicals. The broadening of the g_z component may be related due to the hyperfine coupling from ^{195}Pt. The comparatively small g anisotropy ($\Delta g = g_1 - g_3$) of 0.0516 confirms the predominant localization of the spin on the bridging ligands $bpym^{\bullet-}$ which do not seem to interact strongly across the rectangle.

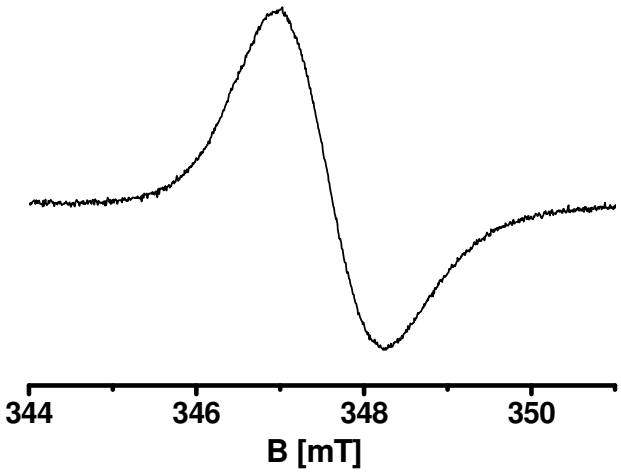

Fig. 4.4.6**:** *X-band EPR spectrum of* $\mathbf{1}^{2+}$ *obtained by in situ electrolysis at RT in* CH_3CN */ 0.1 M* Bu_4NPF_6

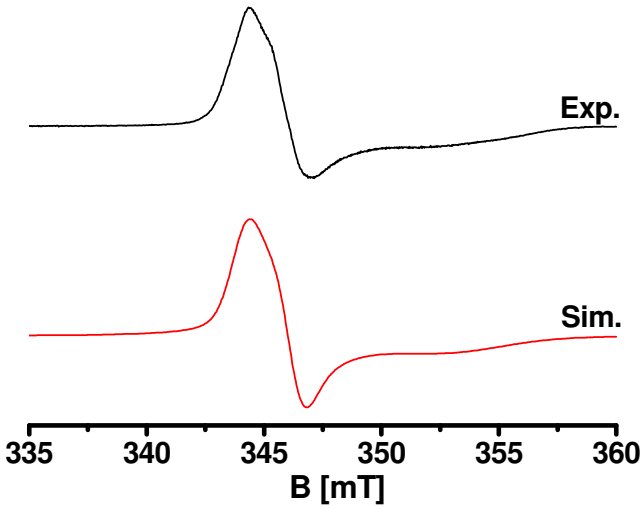

Fig. 4.4.7**:** *X-band EPR spectrum of* $\mathbf{1}^{2+}$ *obtained by in situ electrolysis at 110 K in* CH_3CN */ 0.1 M* Bu_4NPF_6 *(top) with computer simulation (bottom),* g_x*=2.0106,* g_y*= 2.000,* g_z*=1.959; linewidth (in G) X=12, Y=15.3, Z=45*

From the spectroelectrochemical data obtained, a sequence of electron processes can be suggested as shown in Fig. 4.4.8.

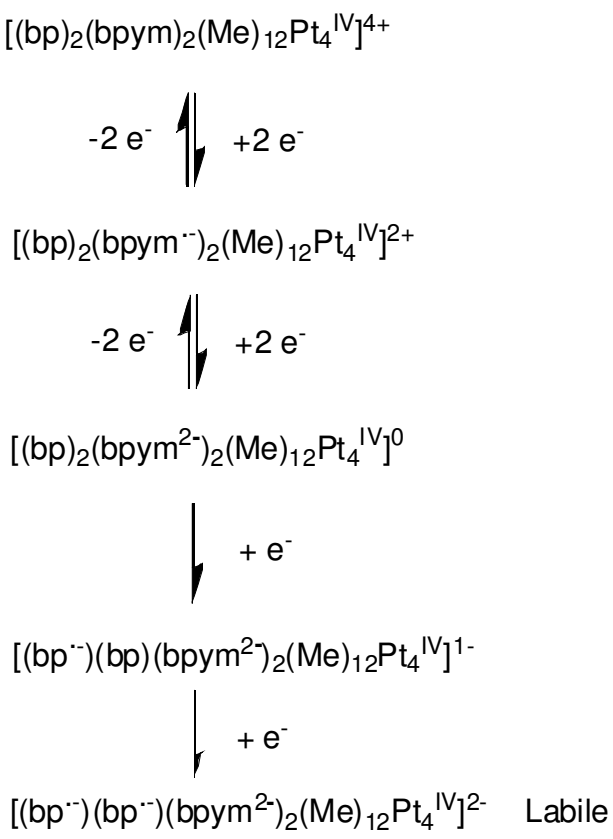

Fig. 4.4.8: *Electron transfer sequence purposed for the electronic reduction steps of* ***1***

A similar rectangular system with PF_6^- as the counter ion instead of OTf^- was also synthesized and spectroelectrochemically investigated in DMF/ 0.1 M Bu_4NPF_6. However, the same decomposition problem even with a greater extent just after second step was encountered again (4^{th} electron addition).

As a conclusion, complex **1** can serve as an electron reservoir for only up to four electrons upon which the rectangle starts to slowly disintegrate. Changing the solvent to DMF or the counter ion to PF_6^- does not make the system more stable against the addition of more than four electrons. In contrast, the previously synthesized $[Re_4(CO)_{12}(\mu\text{-bp})_2(\mu\text{-bpym})_2](OTf)_4$ could add up to seven electrons reversibly using the same OTTLE cell in DMF/ 0.1 M Bu_4NPF_6.[43] One possible explanation for this difference can be the effect of carbonyl groups that $Re_4(CO)_{12}(\mu\text{-bp})_2(\mu\text{-bpym})_2](OTf)_4$ owns. Carbonyls are good π-acceptor ligands. As the charge density increases by each of the reduction processes, it can be distributed successfully over the carbonyl co-ligands due to their acceptor ability. The infrared spectroelectrochemistry investigation of the Re rectangular system confirms this idea. Each of the reduction

steps causes a low energy shift of the carbonyl stretching frequencies,[43] so the C=O bond weakens as a result of an efficient π-interaction. On the other hand, complex **1** does not have this extra charge “balancing” possibility because of the presence of only σ-donor methyl groups. Thus the stability of **1** against reduction is less in comparison with rhenium system, probably as a result of increasing electrostatic repulsion in the molecule already after the addition of fourth electron.

CHAPTER 5

Pt^{IV} Complexes of TCNX Type Ligands

5.1 Introduction

Unsaturated polycyano compounds such as TCNE (tetracyanoethene), TCNQ, (7,7,8,8-tetracyano-*p*-quinodimethane) and TCNB (1,2,4,5-tetracyanobenzene) are termed generally as TCNX ligands, and are established as very special and versatile ligands in coordination chemistry.[129]

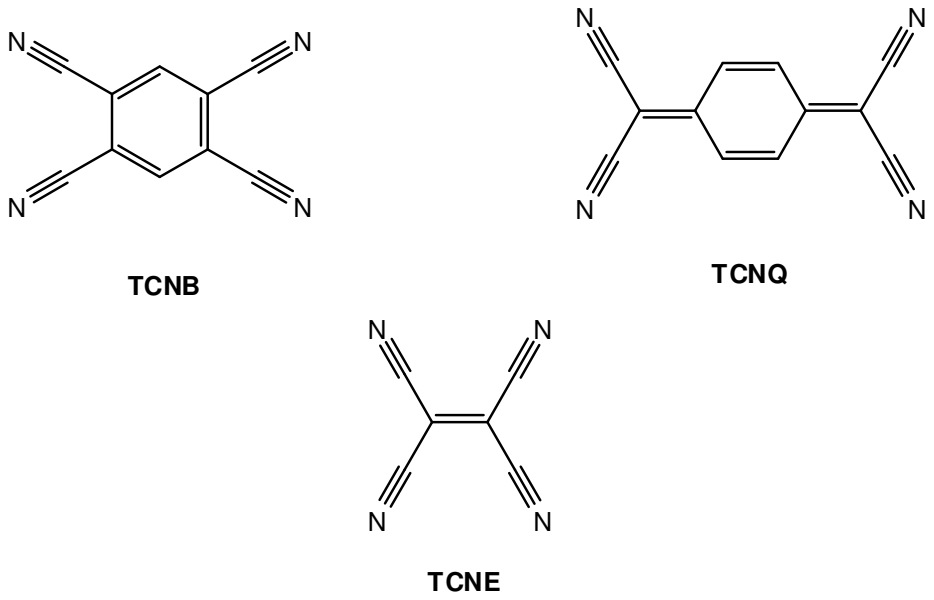

Fig. 5.1.1: *TCNX ligands*

These ligands can interact with metal fragments to form ion pairs[130-134], charge transfer complexes[135-138], π–complexes by coordination to C=C or react in σ-fashion via the nitrogen atom of the nitrile group, which can involve up to four metal centers per bridging TCNX ligand [129,139] (Fig. 5.1.2).

TCNE and TCNQ, in particular are among the least innocent[140] of ligands in coordination chemistry due to their very low lying π* orbitals. Thus, they can

coordinate not only as neutral molecules, but often as radical anions $TCNX^{\bullet-}$ or even $TCNX^{2-}$.

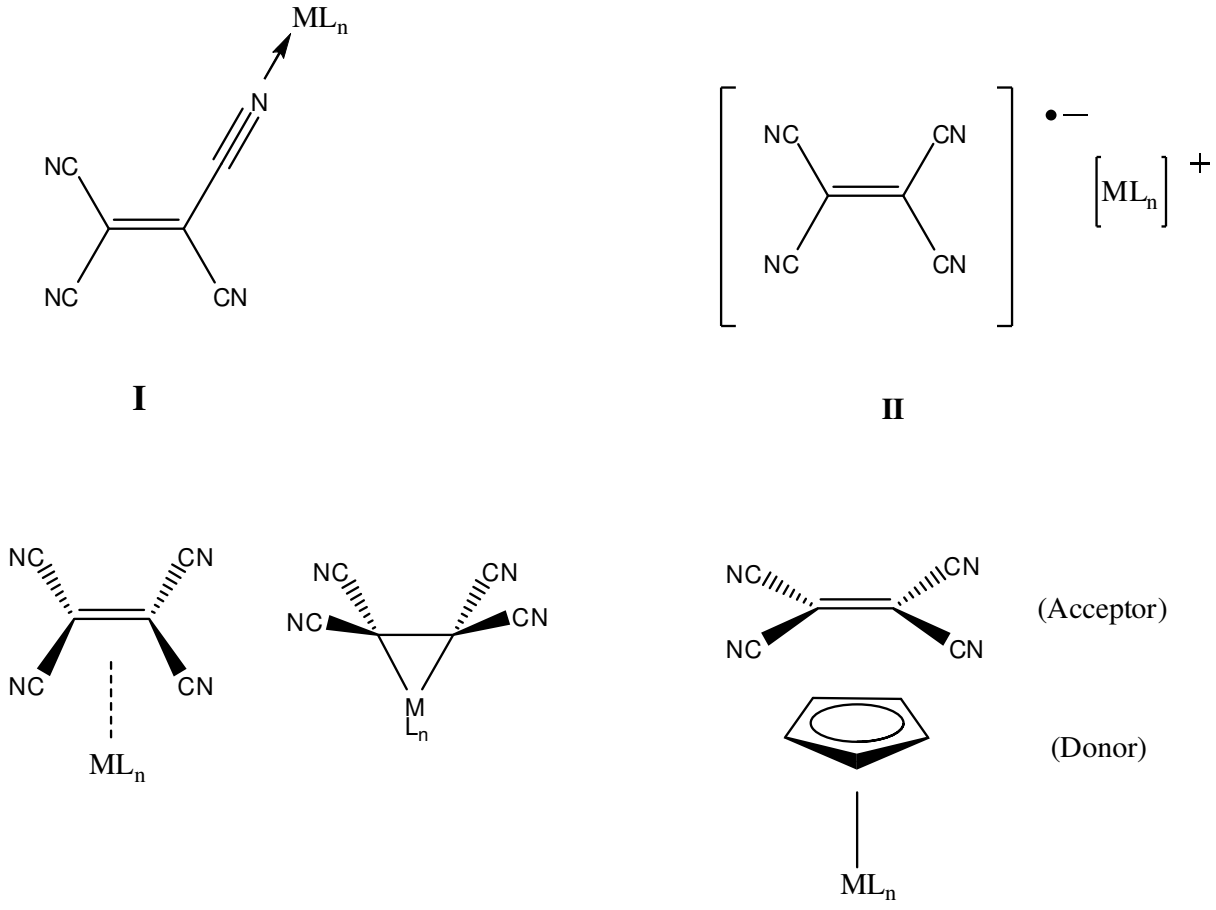

Fig. 5.1.2: *Different interaction possibilities of a TNCE ligand with a metal fragment: σ-coordination via nitrogen atom (**I**); ion pairs (**II**); π–complex formation (**III**); complexation by charge transfer (**IV**)*

The complexes of TCNX ligands often show unusual physical properties like anisotropic electrical conductivity, near infrared absorption, non-linear optical behaviour or ferromagnetism.[141] As a result of these unique properties, they have found applications in organic conductor research[142], in concepts for molecular computing[143] and in molecular magnetism.[144,145] Indeed, one of the most remarkable materials containing a TCNX ligand reported by Miller et. al. in 1991, is the molecular magnet with approximate composition $V[TCNE]_x.ys$ (x = 2, y = 0.5, s = solvent) which has a Curie temperature (Tc) of about 400 K.[144d] Despite the lacking X-ray structural evidence, detailed studies of this material have strongly suggested a

molecule where one-electron reduced TCNE bridges four vanadium(II) centers.[144d] The knowledge of molecular and electronic structure of this type of complexes may be helpful to design new molecular magnets with special magnetic properties.[60] In addition, the ability of bridging up to four metal centers as mentioned above makes them promising ligands for the design of network materials based on polymer coordination compounds.[146]

Mononuclear and oligonuclear complexes[129] of TCNX ligands are well documented. However, discrete tetranuclear complexes reported are very few. [139-141] Obviously, it is very challenging to synthesize and isolate TCNX complexes with four metals centers.

This chapter is concerned with the reactions of TCNX ligands with $[Pt(CH_3)_3(bpy)](OTf)$. The synthetic routes are described and the results of the reactions are discussed In the light of the data obtained from elemental analyses, ^{1}H-NMR, IR and UV-Vis spectroscopies and cyclic voltammetry.

5.2 Synthesis

Fig. 5.2.1 illustrates the route followed for the synthesis of $[\{Pt(CH_3)_3(bpy)\}_4TCNQ](OTf)_4$, (**3**).

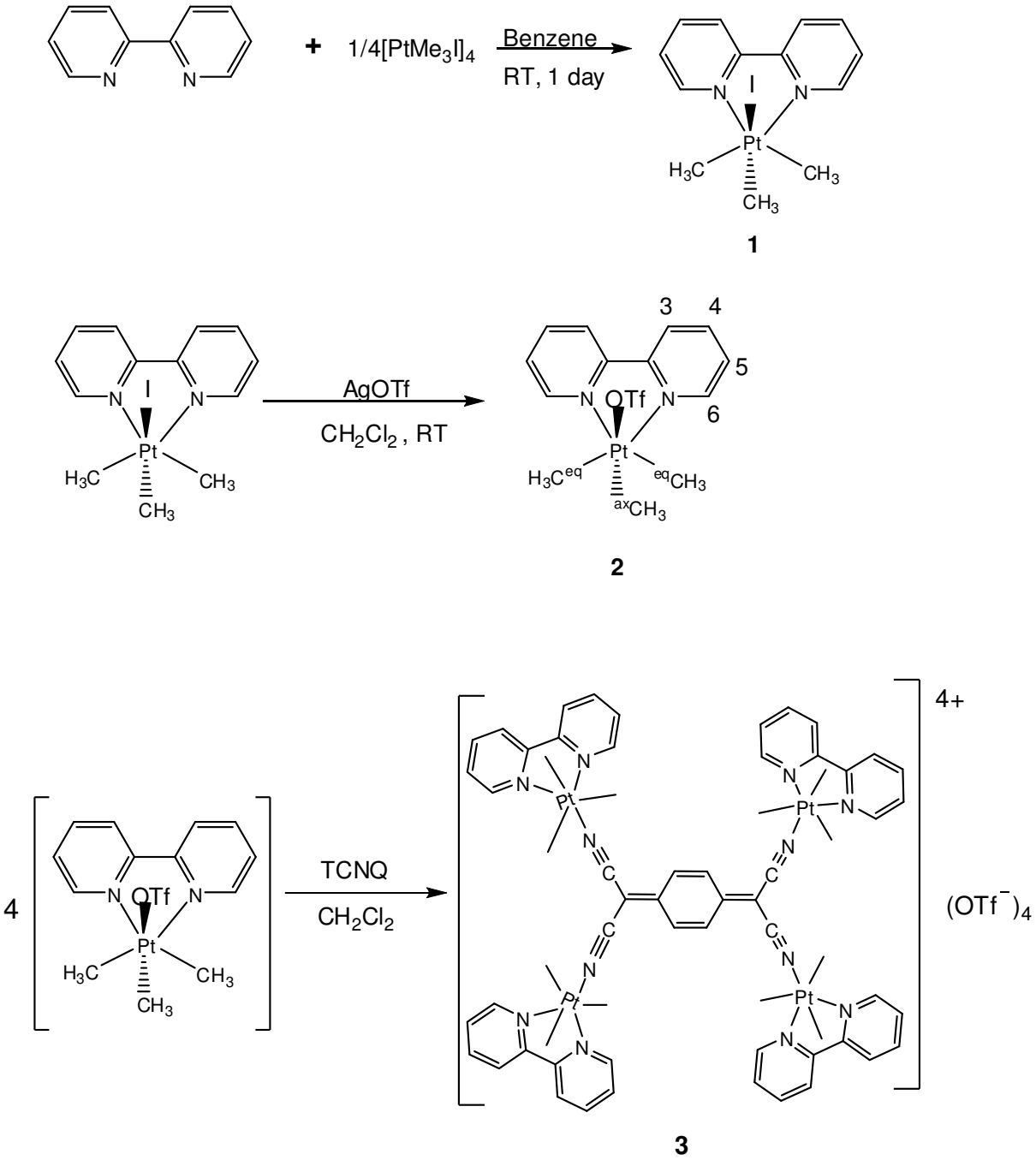

Fig. 5.2.1: *Synthesis of* $[\{Pt(CH_3)_3(bpy)\}_4TCNQ](OTf)_4$

$PtMe_3I(bpy)$ was synthesized by reacting 2,2'-bipyridine and ¼$[PtMe_3I]_4$ at room temperature for one day. The removal of I^- was achieved by addition of AgOTf to a CH_2Cl_2 solution of the complex in dark. The resulting AgI was filtered over celite, and to the filtrate ¼ equivalents of TCNQ was added, upon which a sudden color change from colorless to greenish-yellow was observed. The reaction mixture was stirred at room temperature for 24 hours and precipitated from a CH_2Cl_2 / hexane mixture.

In a second attempt, the CH_2Cl_2 solution of $[Pt(CH_3)_3(bpy)](OTf)$ and TCNQ was heated at 65 ^{0}C under argon in the dark for one day. At the end of the reaction a dark green product was obtained, which was further washed with small portions of CH_2Cl_2 and precipitated again from CH_2Cl_2 / hexane mixture. However, the experimentally found CHN analyses result of the product and the calculated values did not match with each other, the error percentage was very high. In addition, the ^{1}H-NMR spectrum of the complex did not exhibit any signals indicating the existence of paramagnetic species. Thus, this method did not yield to the desired complex formation.

Whereas TCNB did not react at all with $[Pt(CH_3)_3(bpy)](OTf)$, the reaction with TCNE gave a mixture of products as verified by ^{1}H-NMR and elemental analysis, which could not be separated and characterized due to the low stability of the complexes.

5.3 Characterization of $[\{Pt(CH_3)_3(bpy)\}_4TCNQ](OTf)_4$

Complex **3** was characterized by elemental analysis, ^{1}H-NMR, infrared and UV-Vis spectroscopic methods. Several attempts made for obtaining single crystals were unsuccessful due to the rapid decomposition of the complex in solution.

The results of the elemental analysis of the product match with the theoretically calculated values data. Table 5.3.1 summarizes the elemental analysis data.

Table 5.3.1: *CHN analysis of* ***3***

	Calculated for $C_{68}H_{72}N_{12}F_{12}O_{12}Pt_4S_4$ (2386.01 g / mol)	**Found**
C	34.22	34.22
H	3.04	3.09
N	7.04	7.43

On formation of tetranuclear **3**, the ^{1}H-NMR shifts of the proton signals in both the aromatic and aliphatic regions are very small relative to complex **2**. Similar results were also reported previously for the structurally characterized $\{(\mu_4\text{-TCNQ})[Re(CO)_3(bpy)]_4\}(PF_6)_4$ complex.[140] This small change can be an evidence for only very marginal charge transfer between the metal-complex fragments and TCNQ. While no coalescence of the methyl proton signals was observed, especially the axial methyl resonances of both complexes **2** and **3** are somewhat broader in comparison with the corresponding signal in the complex **1** at room temperature. (Figs. 5.3.1, 5.3.2 and 5.3.3). This can be because of a rapid exchange equilibrium involving trigonal-bipyramidal or square-pyramidal structures after removal of I^-. To overcome this problem, the ^{1}H-NMR spectroscopy experiment of complex **3** was repeated at -50 ^{0}C, where signals were sharper.

In the aromatic region of the ^{1}H-NMR spectrum of **3** measured at -50 ^{0}C, four signals belonging to the bpy ligands and a singlet from TCNQ are seen. The bpy protons and the H-(TCNQ) signals are in approximately 2:1 integration ratio, in agreement with the expectation for the complex. The existence of two types of singlets in 2:1 ratio for

two equatorial and one axial methyl groups points to the formation of only one type of complex. The ^{195}Pt satellites as a result of Pt-CH_3 coupling are also present within the typical coupling constant range. Tables 5.3.2 and 5.3.3 summarize the ^{1}H-NMR data of the complexes.

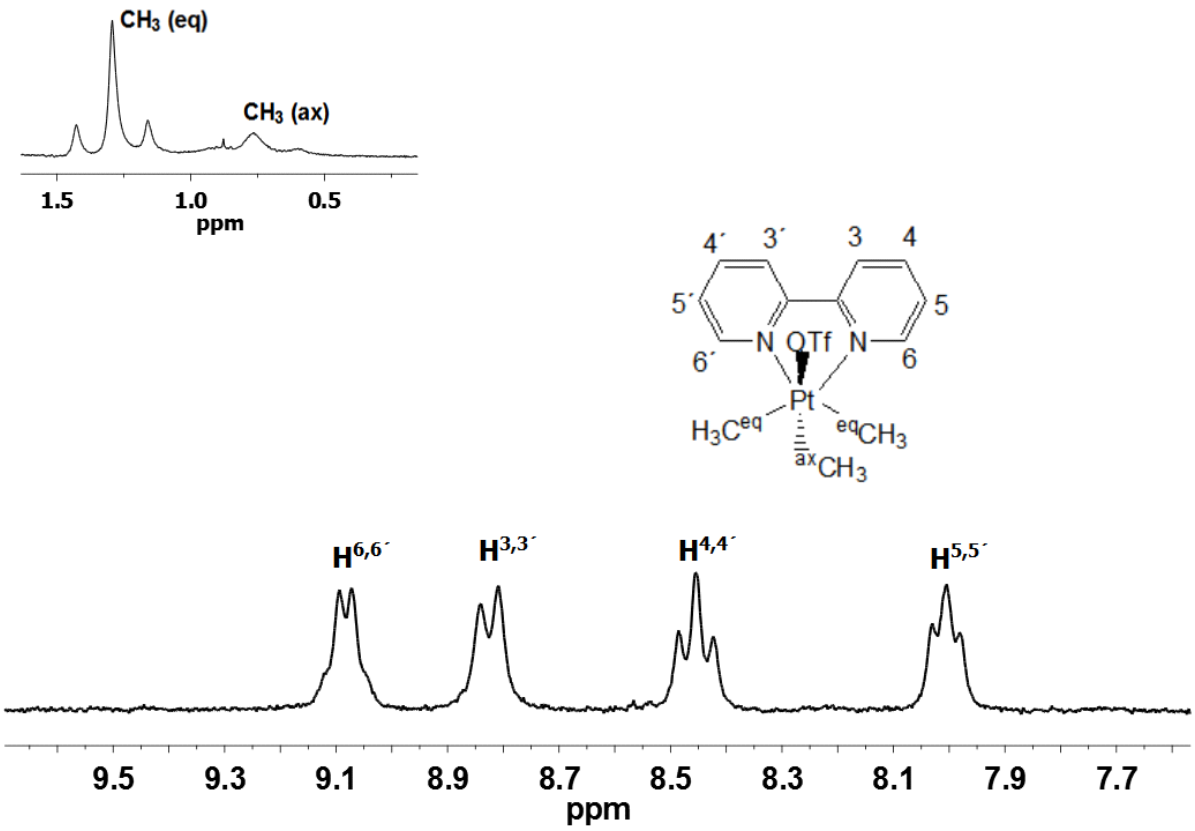

Fig. 5.3.1: *^{1}H-NMR spectrum of **2** measured in acetone-d_6*

Table 5.3.2: *^{1}H-NMR spectroscopic data (aromatic region) of the complexes in acetone-d_6*

	δ [ppm]				
Complexes	**$H^{6,6´}$**	**$H^{5,5´}$**	**$H^{4,4´}$**	**$H^{3,3´}$**	**H-TCNQ**
1	9.029	7.849	8.297	8.688	-
2	9.084	8.007	8.453	8.825	-
3	9.077	7.996	8.443	8.814	7.696
3[a)]	9.092	8.043	8.501	8.916	7.725

[a)] *Measured at -50 ^{0}C*

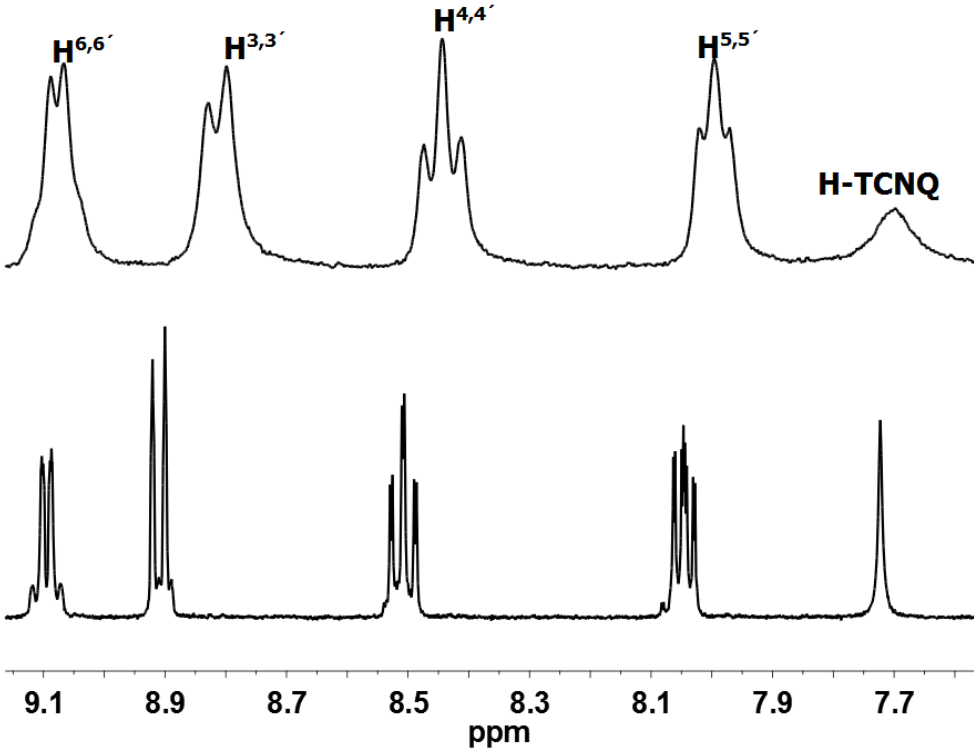

Fig. 5.3.2: *^{1}H-NMR spectra (aromatic region) of **3** measured in acetone-d_6 at RT (top) and at -50 ^{0}C (bottom)*

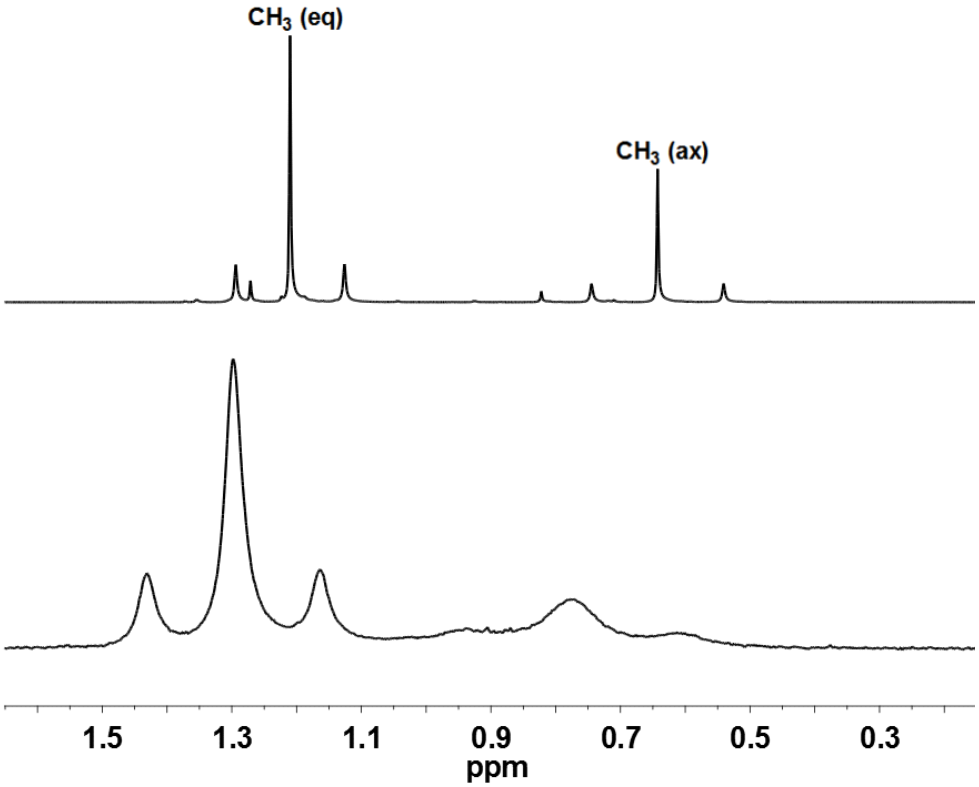

Fig. 5.3.3: *^{1}H-NMR spectra (aliphatic region) of **3** measured in acetone-d_6 at -50 ^{0}C (top) and at RT (bottom)*

Table 5.3.3: *^{1}H-NMR spectroscopic data (aliphatic region) of the complexes in acetone-d_6*

	δ [ppm]		J [Hz]	
	$^{eq}CH_3$	$^{ax}CH_3$	Pt-$^{eq}CH_3$	Pt-$^{ax}CH_3$
1	1.468	0.587	70.86	72.40
2[a)]	1.294	0.767	66.73	
3[a)]	1.298	0.776	66.96	
3[b)]	1.210	0.643	67.18	81.60

[a)] *$^2J_{Pt\text{-}Me(ax)}$ could not be calculated due to the broadening.* [b)] *Measured at -50 ^{0}C*

Infrared Spectroscopy

Infrared spectroscopy is a very efficient method to characterize the complexes of TCNX ligands. Especially the CN stretching frequencies are very informative. Occupation of the π* MOs of the TCNX ligands through either external reduction or intramolecular metal-to-ligand electron transfer lowers the ν_{CN}[147] while a high energy shift would be indicative of very little or no back donation.[141] The structure of the compound can also be predicted from the number and the pattern of the bands i.e. tetranuclear species (D_{2h} symmetry) exhibit a low intense broad band[141] or two bands while mononuclear (C_s symmetry) and trinuclear species show four such bands.[141]

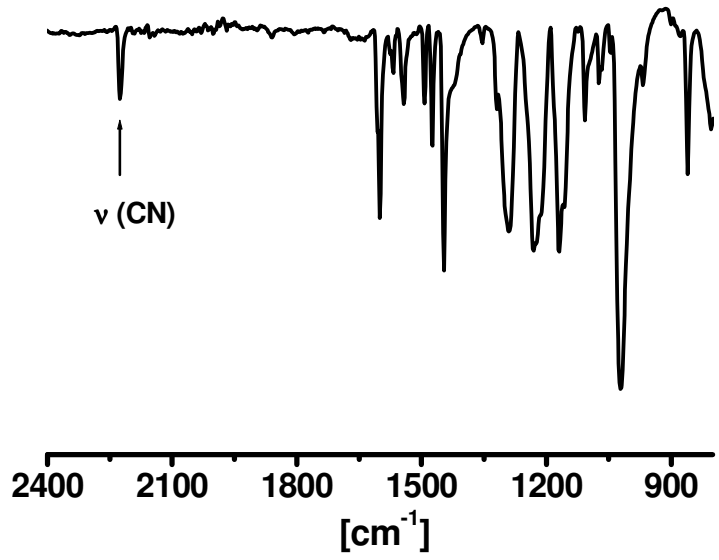

Fig. 5.3.4: *Infrared spectrum of **3** measured in the solid state*

The solid state IR spectrum of complex **3** gives (Fig. 5.3.4) one broad band for ν(C≡N) at 2226 cm^{-1} which is very close but a little high energy shifted relative to free TCNQ (2223 cm^{-1}). In addition, the C=C stretching frequency of the complex **3**, observed at 1543 cm^{-1}, is very similar to that of the free ligand at 1541 cm^{-1}. These results are indications for absent π-back donation from Pt^{IV} to the TCNQ ligand. The tetrarhenium complex $\{(\mu_4\text{-TCNQ})[Re(CO)_4Cl]_4$ has ν_{CN} = 2245 and 2140 cm^{-1} and was reported to contain neutral TCNQ as bridging ligand,[148] whereas $\{(\mu_4\text{-TCNQ})[Re(CO)_3(bpy)]_4\}(PF_6)_4$ shows a weak and broad CN band (D_{2h} symmetry) at 2235 cm^{-1} in CH_2Cl_2 which is slightly higher than that of the free ligand in solution (2227 cm^{-1}).[140]

UV-Vis Spectroscopy

MLCT or LMCT bands of the TCNQ complexes in their absorption spectra are usually observed at long wavelengths; $\{(\mu_4\text{-TCNQ})[Re(CO)_3(bpy)]_4\}(PF_6)_4$ has λ_{max} at 680 nm which is assigned as to an MLCT transition.[140] There are other TCNQ complexes having λ_{max} values at even lower energy, around 1000 nm in the NIR region.[140]

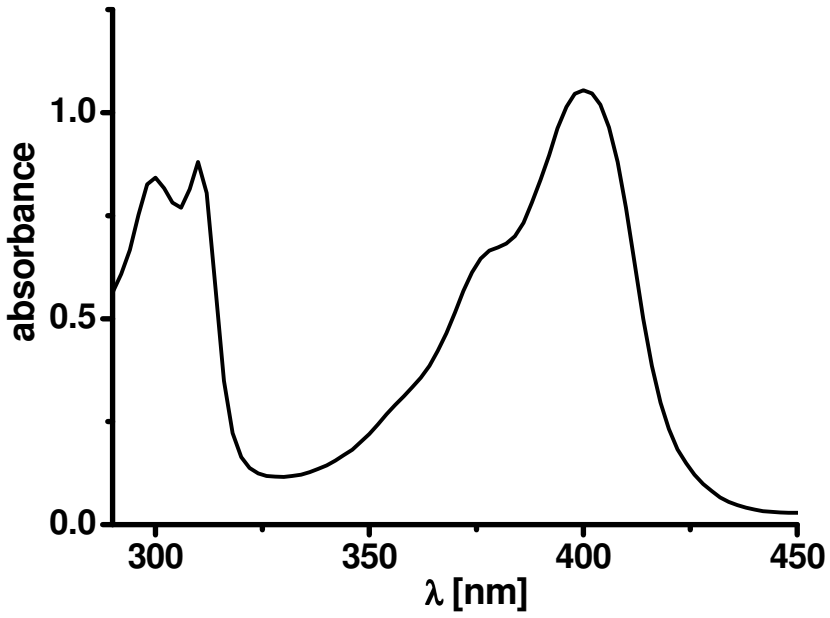

Fig. 5.3.5: *Absorption spectrum of **3** measured in CH_2Cl_2*

The absorption spectrum of complex **3**, measured in CH_2Cl_2, does not reveal such a low energy band; the band system is similar to that of the free ligand except for maxima at 290 and 310 nm which can be attributed to the IL transitions of $[PtMe_3bpy]^+$. Fig. 5.3.5 illustrates the absorption spectrum of complex **3**.

The band at 398 nm and the shoulder at 376 nm are very close to IL bands of the free ligand at 400 nm and 370(sh). The absence of any MLCT bands supports the idea of almost no d(M)→π*(L) transition in the complex.

5.4 Electrochemistry

Cyclic Voltammetry

The redox properties of complex **3** were investigated by cyclic voltammetry. Fig. 5.4.1 shows the cyclic voltammogram of the compound. Table 5.4.1 summarizes the data obtained.

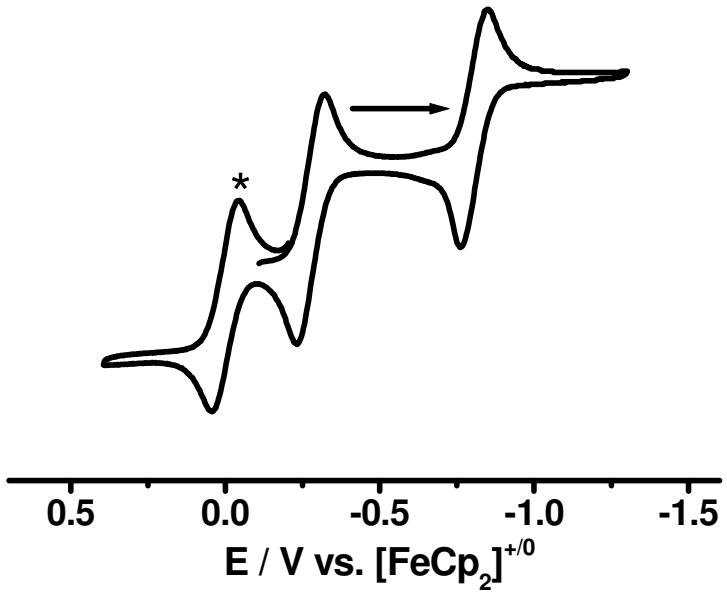

Fig. 5.4.1: *Cyclic voltammogram of **3** in CH_2Cl_2 / 0.1 M Bu_4NPF_6 at – 60 ^{0}C with a scan rate of 100 mV/sec. * : ferrocene wave*

Table 5.4.1: *Cyclic voltammetry data[a)] of TCNQ and the complexes*

Compound	E_{red}(I)	$\Delta E(I)^{c)}$	E_{red}(II)	$\Delta E(II)^{c)}$	Solvent
3[d)]	-0.27[b)]	90	-0.80[b)]	90	CH_2Cl_2
TCNQ[d)]	-0.38[e)]	200	-0.98[e)]	190	CH_2Cl_2
{(μ_4-TCNQ)[Re(CO)$_3$(bpy)]$_4$}(PF_6)$_4$[140]	+0.45[b)]		+0.09[b)]		CH_2Cl_2

[a)] *Potentials E in V vs. $FeCp_2^{0/+}$ (0.1 M Bu_4NPF_6 as electrolyte), at 100mV/sec scan rate.* [b)] *Half-wave potential corresponding to a reversible step.* [c)] *Peak potential differences $\Delta E=E_{pc}-E_{pa}$.* [d)] *Measured at -60 ^{0}C.* [e)] *Cathodic peak potentials of a quasi-reversible step*

Complex **3** exhibits no reversible wave in both oxidation and reduction areas unless the experiment is carried out at -60 ^{0}C, where two reversible reductions at E_{pc}(I) = -0.32 V and E_{pc}(II)= -0.84 V are observed which are relatively close but still less

negative than the free TCNQ ligand values of E_{pc}(I) = -0.38 V and E_{pc}(II) = -0.98 V. Thus, the presence of the positively charged platinum(IV) center does not effect the reduction potential so much, this can be attributed to the very poor charge transfer occurring between Pt^{IV} and the TCNQ ligand.

To conclude, the reaction between TCNQ and [$Pt(CH_3)_3$(bpy)](OTf) leads to the formation of complex **3** according to the CHN analyses and ^{1}H-NMR, which were obtained after several times of washing. However, almost no significant change observed in IR and absorption spectra as well as in the cyclic voltammetry experiment can be the result of nearly zero π interaction between Pt^{IV} and the TCNQ. Thus, the very weak σ-dative bond between the Pt^{IV} and the TCNQ may cause complex **3** to easily decompose. This work can be extended by variation of the experimental conditions and the precursors; the reaction time, temperature variation, solvent selection or changing the counter ion to e.g. PF_6^- may lead to a more stable complex formation which can be handled and spectroscopically investigated more easily.

CHAPTER 6

Experimental Section

6.1 Instrumentation

NMR Spectroscopy:

^{1}H-NMR spectra at frequencies 250 MHz and 400 MHz were performed on a Bruker AV-250 and AV-400 spectrometer by Ms. Török. Tetramethylsilane (TMS) was used as the external standard. [^{1}H, ^{195}Pt] HMQC experiment was performed by Prof. D. Gudat and referenced to 1.2 M Na_2PtCl_6 in D_2O [Ξ =21.496784, ^{195}Pt].

EPR Spectroscopy:

X-band EPR spectra at around 9.5 GHz were obtained from Bruker system ESP 300 equipped with a Hewlett-Packard Frequency counter 5350B, a Bruker ER035M gaussmeter for g values determination as a Bruker system EMX and a continuous flow cryostat ESR 900 of Oxford instruments for measurements at liquid helium temperature (4 K). For measurements between 110-300 K, same instrumental configuration was used with liquid nitrogen cryostat. The measurements were carried out by Dr. Brigitte Schwederski and Dr. Biprajit Sarkar at Institüt für Anorganische Chemie, Universität Stuttgart.

A two-electrode capillary served to generate intermediates for X band EPR studies.[149] Bruker WINEPR / Simfonia programs were used for the simulations of the spectra.

UV-Vis-NIR Spectroscopy:

UV-Vis-NIR absorption spectra were recorded on J&M TIDAS (200-2350 nm) and on Shimadzu UV-160 (200-1100 nm) spectrophotometers. Measurements were carried out in solution using quartz cuvettes.

UV-Vis-NIR and IR spectroelectrochemistry:

UV-Vis-NIR and IR spectroelectrochemistry measurements were done by Jan Fiedler and Dr. Anders Gabrielsson, under argon atmosphere using an Optically Transparent Thin Layer Electrochemical (OTTLE) cell which consists of two CaF_2 window plates.[70] Between the cell working (platinum mesh), auxiliary (platinum mesh) and reference electrodes (silver wire as pseudo reference) are melt-sealed.

Cyclic Voltammetry:

Cyclic voltammetry was carried out using a three-electrode configuration (glassy carbon or platinum working electrode, Pt counter electrode, Ag wire pseudo-reference) and a PAR 273 potentiostat and function generator. The ferrocene/ferrocenium (Fc/Fc^+) couple served as internal reference. All the experiments were carried out under argon atmosphere, and pre-purified solvents.

IR Spectroscopy:

IR spectra were measured using Nicolet 6700 FT-IR spectrometer equipped with high performance diamond ATR unit called Smart Orbit.

Elemental analysis:

C, H and N analyses were performed on Perkin Elmer Analyzer 240 by Mrs. B. Förtsch.

6.2 Starting Materials and Working conditions:

Solvents were dried by refluxing under argon over:
-Calcium hydride (dichloromethane, acetonitrile, and hexane)
-Sodium (toluene, diethyl ether)
-Sodium-potassium (tetrahyrofuran)
-Calcium chloride (acetone)
They were also degassed by freeze-pump-thaw method.
P.A. quality nitromethane and benzene were used as received from chemical store.

$[PtMeCl]_4$, $[PtMeI]_4$, $[\{Pt(CH_3)_3\}_4(\mu\text{–}bp)_2(\mu\text{–}bpym)_2](OTf)_4$, $[Pt(CH_3)_3(bpy)](OTf)$, $[\{Pt(CH_3)_3(bpy)\}_4TCNQ](OTf)_4$ and the ligands big and bik were synthesized under inert conditions using Schlenk techniques. The rest of the complexes and ligands were prepared in air.

6.3 Syntheses:

Following compounds were commercially available:

- K_2PtCl_6, K_2PtI_6, 2,2'-bipyrimidine, 1-methylimidazole, butyllithium, oxalylchloride, AgOTf, $AgPF_6$, phenylenediamine, 4,5-dimethyl-o-phenylenediamine, 7,7,8,8-Tetracyanoquinodimethane from Aldrich,
- Methyllithium, 4,4-bipyridine, from Acros,
- K_2PtCl_4, 2-cyano-4-methylpyridine from Alfa Aesar,
- $NH_2NH_2.H_2O$ from Fluka,
- NaBr, 2,2- bipyridine from Merck.

The ligands bmptz[54], bik[89] and the metal precursor $Pt_2Me_4(\mu\text{-}SMe_2)_2$[150] were synthesized according to the literature. $[Pt(CH_3)_3X]_4$ (X:Cl, I)[62] by a modification of the route reported.

6.3.1 Syntheses in Chapter 2:

6.3.1.1 Synthesis of $[Pt(CH_3)_3Br]_4$

This compound was synthesized by a halogen exchange reaction. An amount of 0.1 g (0.09 mmol) of $[Pt(CH_3)_3Cl]_4$ was dissolved in 20 ml of CH_2Cl_2. In a separate flask, 0.38 g (3.6 mmol) NaBr were dissolved in 20 ml methanol and these two solutions were mixed and stirred for 3 days. The colourless residue after removing the solvents was treated with 20 ml of CH_2Cl_2 and stirred. The mixture was filtered and 20 ml of CH_2Cl_2 was again added to the solid. After stirring and filtering, the filtrates were combined and the solvent removed. The colourless residue was washed with methanol.
Yield is 90 mg (77%).
^{1}H–NMR ($CDCl_3$) δ / ppm: 1.51 (s, 9H, CH_3, J_{Pt-H}: 79.20 Hz).

6.3.1.2 Synthesis of *fac*-$Pt(CH_3)_3Cl(bptz)$

0.100 g of $[Pt(CH_3)_3Cl]_4$ (0.09 mmol) and 0.086 g of bptz (0.364 mmol) were dissolved in 35 ml of dried benzene and stirred for 2 days at room temperature to yield an orange precipitate. The mixture was filtered and the solid washed twice with 10 ml portions of benzene and dried under vacuum. The product was precipitated from dichloromethane and hexane.
Yield is 130 mg (70 %) of the dichloromethane solvate.

Elemental analysis: $C_{16}H_{19}N_6Cl_3Pt$ (596.81 g/mol)

Calculated:	C: 32.20 %, H: 3.21 %, N: 14.08%
Experimental:	C: 32.20 %, H: 3.37 %, N: 14.09%

^{1}H–NMR (CD_3NO_2) δ / ppm: 9.18 (ddd, 1H, H^3 , $^3J_{H3-H4}$: 7.94 Hz, $^4J_{H3-H5}$: 1.35 Hz, $^5J_{H3-H6}$: 0.78 Hz), 9.05 (dm, 1H, H^6) 8.97 (ddd, 1H, $H^{6'}$, $^3J_{H6'-H5'}$: 4.73 Hz, $^4J_{H6'-H4'}$: 1.75 Hz, $^5J_{H6'-H3'}$: 0.91 Hz), 8.82 (dt, 1H, $H^{3'}$, $^3J_{H3'-H4'}$: 7.93 Hz, $^4J_{H3'-H5'}$: 1.14 Hz), 8.49 (td, 1H, H^4, $^3J_{H4-H5}$: 7.83 Hz), 8.19 (td, 1H, $H^{4'}$,$^3J_{H4'-H5'}$: 7.85 Hz), 8.11 (ddd, 1H, H^5),

7.76 (ddd, 1H, $H^{5'}$), 1.51 (s, 3H, C$\mathbf{H}_3{}^3$, $^2J_{Pt\text{-}H}$: 72.04 Hz), 1.42 (s, 3H, C$\mathbf{H}_3{}^2$, $^2J_{Pt\text{-}H}$: 72.25 Hz), 0.58 (s, 3H, C$\mathbf{H}_3{}^1$, $^2J_{Pt\text{-}H}$: 75.10 Hz).

6.3.1.3 Synthesis of *fac*-Pt$(CH_3)_3$Br(bptz)

Amounts of 0.100 g of $[Pt(CH_3)_3Br]_4$ (0.078 mmol) and 0.074 g of bptz (0.313 mmol) were dissolved in 20 ml of dried benzene and stirred for a day at room temperature. The colour of the solution changed from red-pink to orange. The solvent was removed and the residue was washed twice with 10 ml portions of benzene and dried under vacuum.
Yield is 141 mg (81 %).

Elemental analysis: $C_{15}H_{17}N_6BrPt$ (556.33 g/mol)
Calculated: C: 32.38 %, H: 3.08 %, N: 15.11 %
Experimental: C: 31.97 %, H: 3.04 %, N: 14.69 %

^{1}H–NMR (CD_3NO_2) δ / ppm: 9.18 (dm, 1H, H^3 , $^3J_{H3\text{-}H4}$: 7.94 Hz), 9.08 (dm, 1H, H^6, $^3J_{H6\text{-}H5}$: 5.71 Hz), 8.97 (dm, 1H, $H^{6'}$, $^3J_{H6'\text{-}H5'}$: 5.05 Hz), 8.82 (dt, 1H, $H^{3'}$, $^3J_{H3'\text{-}H4'}$: 7.93 Hz, $^4J_{H3'\text{-}H5'}$: 1.10 Hz), 8.48 (td, 1H, H^4, $^3J_{H4\text{-}H5}$: 7.85 Hz), 8.19 (td, 1H, $H^{4'}$, $^3J_{H4'\text{-}H5'}$: 7.80 Hz), 8.11 (m, 1H, H^5), 7.76 (m, 1H, $H^{5'}$), 1.59 (s, 3H, C$\mathbf{H}_3{}^3$, $^2J_{Pt\text{-}H}$: 72.36 Hz), 1.51 (s, 3H, C$\mathbf{H}_3{}^2$, $^2J_{Pt\text{-}H}$: 72.71 Hz), 0.68 (s, 3H, C$\mathbf{H}_3{}^1$, $^2J_{Pt\text{-}H}$: 74.92 Hz).

6.3.1.4 Synthesis of *fac*-Pt$(CH_3)_3$I(bptz)

0.100 g of $[Pt(CH_3)_3I]_4$ (0.068 mmol) and 0.064 g of bptz (0.270 mmol) were dissolved in 20 ml of benzene and stirred for a day at room temperature. The colour of the solution changed from red-pink to orange. The solvent was removed and the residue was washed twice with 10 ml portions of benzene and dried under vacuum. The product was precipitated from dichloromethane and hexane.
Yield is 121 mg (74 %).

Elemental analysis: $C_{15}H_{17}N_6IPt$ (603.33 g/mol)

Calculated: C: 29.86 %, H: 2.84 %, N: 13.93 %

Experimental: C: 28.45 %, H: 2.84 %, N: 12.08 %

^{1}H–NMR ($CDCl_3$) δ / ppm: 9.12 (m, 2H, $H^{3,6}$, two signals are overlapping), 9.04 (m, 1H, $H^{6'}$), 8.78 (dm, 1H, $H^{3'}$), 8.30 (m, 1H, H^4), 8.07 (m, 1H, $H^{4'}$), 7.93 (m, 1H, H^5), 7.66 (m, 1H, $H^{5'}$), 1.91 (s, 3H, C**H**$_3{}^3$, $^2J_{Pt-H}$: 73.01 Hz), 1.80 (s, 3H, C**H**$_3{}^2$, $^2J_{Pt-H}$: 73.10 Hz), 0.80 (s, 3H, C**H**$_3{}^1$, $^2J_{Pt-H}$: 72.19 Hz).

6.3.1.5 Synthesis of *anti*-[(μ-bmptz){*fac*-PtCl(CH$_3$)}$_2$]

Amounts of 0.104 g of $[Pt(CH_3)_3Cl]_4$ (0.095 mmol) and 0.050 g of bmptz (0.189 mmol) were dissolved in 20 ml of dried benzene and stirred for a day at room temperature. The solution changed its colour from purple to dark orange during this time. After removal of the solvent, the solid was washed twice with 10 ml portions of benzene. Removal of the solvent and precipitation from dichloromethane and hexane yielded 96 mg (62 %) product of the dichloromethane solvate.

Elemental analysis: $C_{21}H_{32}N_6Cl_4Pt_2$ (900.51 g/mol)

Calculated: C: 28.01 %, H: 3.58 %, N: 9.33 %

Experimental: C: 28.20 %, H: 3.61 %, N: 9.36 %

^{1}H–NMR ($CDCl_3$) δ / ppm: 8.89 (d, 2H, $H^{6,6'}$, $^3J_{H6-H5}$: 5.48 Hz, $^3J_{H6-Pt}$: 17.61 Hz), 8.83 (m, 2H, $H^{3,3'}$), 7.81 (dm, 2H, $H^{5,5'}$, $^3J_{H5-H6}$: 5.39 Hz), 2.73 (s, 6H, C**H**$_3$ on pyridyl), 1.71 (s, 6H, C**H**$_3{}^3$, $^2J_{Pt-H}$: 71.85 Hz), 1.70 (s, 6H, C**H**$_3{}^2$, $^2J_{Pt-H}$: 72.38 Hz) 0.71 (s, 6H, C**H**$_3{}^1$ trans. to halogen, $^2J_{Pt-H}$: 74.49 Hz).

6.3.1.6 Synthesis of *anti*-[(μ-bmptz){*fac*-PtBrMe$_3$}$_2$]

Amounts of 0.150 g of $[Pt(CH_3)_3Br]_4$ (0.117 mmol) and 0.062 g of bmptz (0.234 mmol) were dissolved in 35 ml of benzene and stirred 2 days at room temperature to yield a brown precipitate. The mixture was filtered and the solid washed twice with 10 ml portions of benzene and dried under vacuum. Recrystallization from dichloromethane and hexane yielded 120 mg (57 %) of the dichloromethane solvate.

Elemental analysis: $C_{21}H_{32}Br_2Cl_2N_6Pt_2$ (989.38)

Calculated: C: 25.50 %, H: 3.26 %, N: 08.49 %

Experimental: C: 25.65 %, H: 3.33 %, N: 08.45 %

^{1}H–NMR ($CDCl_3$) δ / ppm: 8.90 (d, 2H, $H^{6,6'}$, $^3J_{H6-H5}$: 5.64 Hz, $^3J_{H6-Pt}$: 17.82 Hz), 8.84 (m, 2H, $H^{3,3'}$), 7.81 (dm, 2H, $H^{5,5'}$, $^3J_{H5-H6}$: 5.43 Hz), 2.74 (s, 6H, C**H**$_3$ on pyridyl), 1.79 (s, 6H, C**H**$_3{}^3$, $^2J_{Pt-H}$: 72.11 Hz), 1.78 (s, 6H, C**H**$_3{}^2$, $^2J_{Pt-H}$: 72.78 Hz), 0.80 (s, 6H, C**H**$_3{}^1$, $^2J_{Pt-H}$: 74.06 Hz).

6.3.1.7 Synthesis of *anti*-[(μ-bmptz){*fac*-PtI(CH$_3$)}$_2$]

A mixture of 0.166 g of $[Pt(CH_3)_3I]_4$ (0.113 mmol) and 0.060 g of bmptz (0.227 mmol) was suspended in 30 ml of dried benzene and stirred for a day at room temperature. The solution changed its colour from purple to dark green at the end of this time. The solvent was removed and the solid residue was washed twice with 10 ml portions of benzene and dried under vacuum. The product was recrystallized from dichloromethane and hexane.
Yield is 150 mg (66 %) of the dichloromethane solvate.

Elemental analysis: $C_{21}H_{32}N_6Cl_2I_2Pt_2$ (1083.39 g/mol)

Calculated: C: 23.28 %, H: 2.97 %, N: 07.75 %

Experimental: C: 23.59 %, H: 2.91 %, N: 07.62 %

^{1}H–NMR ($CDCl_3$) δ / ppm: 8.95 (d, 2H, $H^{6,6'}$, $^3J_{H6-H5}$: 6.00 Hz, $^3J_{H6-Pt}$: 17.75 Hz), 8.85 (m, 2H, $H^{3,3'}$), 7.80 (dm, 2H, $H^{5,5'}$), 2.75 (s, 6H, C**H**$_3$ on pyridyl), 1.90 (s, 6H, C**H**$_3{}^3$, $^2J_{Pt-H}$: 72.75 Hz), 1.89 (s, 6H, C**H**$_3{}^2$, $^2J_{Pt-H}$: 73.60 Hz), 0.91 (s, 6H, C**H**$_3{}^1$ trans. to halogen, $^2J_{Pt-H}$: 71.87 Hz).

ESI-Mass Spectroscopy: 1030.52 (m/z calculated for [M+CH_3OH]); 1029.01 (m/z observed as parental peak).

6.3.1.8 Synthesis of *fac*-$Pt(CH_3)_3I(bmptz)$

Amounts of 0.058 g of $[Pt(CH_3)_3I]_4$ (0.039 mmol) and 0.042 g of bmptz (0.159 mmol) were dissolved in 10 ml of CH_2Cl_2 and stirred for an hour at 10°C. The solvent was removed and the residue was washed twice with 10 ml portions of benzene to get rid of any existing binuclear complex and free ligand. It is then dried under vacuum. The product was recrystallized from dichloromethane and benzene.
Yield is 50 mg (50 %)

Elemental analysis: $C_{17}H_{21}N_6PtI$ (631.37 g/mol)

Calculated: C: 32.33 %, H: 3.35 %, N: 13.31 %

Experimental: C: 32.27 %, H: 3.33 %, N: 12.88 %

^1H–NMR ($CDCl_3$) δ / ppm: 8.92 (d, 1H, H^6, $^3J_{H6-H5}$: 4.71 Hz, $^3J_{H6-Pt}$: 17.97 Hz), 8.91 (s, 1H, H^3), 8.88 (d, 1H, $H^{6'}$, $^3J_{H6'-H5'}$: 4.88 Hz), 8.57 (m, 1H, $H^{3'}$), 7.71 (dm, 1H, H^5), 7.47 (dm, 1H, $H^{5'}$), 2.71 (s, 3H, C**H**$_3$ on pyridyl), 2.58 (s, 3H, C**H**$_3$ on pyridyl), 1.88 (s, 3H, C**H**$_3^3$, $^2J_{Pt-H}$: 72.78 Hz), 1.77 (s, 3H, C**H**$_3^2$, $^2J_{Pt-H}$: 73.22 Hz), 0.78 (s, 3H, C**H**$_3^1$ trans to halogen, $^2J_{Pt-H}$: 72.39 Hz).

6.3.2 Syntheses in Chapter 3:

6.3.2.1 Synthesis of big

The synthesis of big was accomplished by an adapted literature procedure.[90,100] 14.4 ml (180 mmol) of 1-metyhlimidazole was dissolved in diethyl ether and cooled down to -70 ^{0}C with the help of liquid nitrogen-acetone bath. To this solution, 80 ml of 2.5 M butyllithium (200 mmol) was added in 10 ml of portions in every 10 minutes and the mixture was stirred overnight. The solution became turbid and the colour changed from light yellow to dark orange. The mixture was brought back to room temperature and dissolved in thf. An amount of oxalyl chloride (7.7 ml; 90 mmol) was then added at -50 ^{0}C, and the mixture was left for stirring overnight at this temperature. The following day, a braun emulsion was obtained. 30 ml of ethanol was added to get rid of excess amount of butyllithium. Solvent was removed and the residue was washed several times with ethanol to get rid of any side products and

starting compounds and filtrated. The final light yellow product was one more time purified by decantation with ethanol.
Yield is 6.28 g (32 %).

Elemental analysis: $C_{10}H_{10}N_4O_2$ (218.08 g / mol)
Calculated: C: 55.04 %, H: 4.62 %, N: 25.68 %
Experimental: C: 54.59 %, H: 4.61 %, N: 25.67 %

^{1}H –NMR (dmso-d_6) δ / ppm: 7.67 (s, 2H, H^5), 7.17 (s, 2H, H^4), 4.050 (s, 6H, N-C**H**$_3$).
^{1}H –NMR (acetone-d_6) δ / ppm: 7.49 (s, 2H, H^5), 7.11 (s, 2H, H^4), 4.12 (s, 6H, N-C**H**$_3$).

IR (solid): 1660.05, 1633 cm^{-1} ($\nu_{C=O}$).

6.3.2.2 Synthesis of *fac*-$Pt(CH_3)_3I$(big)

0.100 g of $[Pt(CH_3)_3I]_4$ (0.068 mmol) and 0.059 g (0.270 mmol) of big were suspended in acetonitrile and stirred for 1 day at 50 ^{0}C. The solution became clear and changed its colour from light yellow to orange. It was then dried under vacuum, washed several times with benzene and recrystallized from dichloromethane and hexane.
Yield is 116 mg (73 %).

Elemental analysis: $(C_{13}H_{19}IN_4O_2Pt).0.5(C_6H_6)$ (624.37 g / mol)
Calculated: C: 30.78 %, H: 3.55 %, N: 08.97 %
Experimental: C: 30.78 %, H: 3.59 %, N: 08.78 %

^{1}H –NMR (acetone-d_6) δ / ppm: 7.45 (d, 2H, $H^{5,5'}$, $^3J_{H5-H4}$: 1.24 Hz), 7.27 (d, 2H, $H^{4,4'}$, $^3J_{H4-H5}$:1.38 Hz , J_{H4-Pt}: 9.93 Hz), 3.80 (s, 6H, N-C**H**$_3$), 1.29 (s, 6H, C**H**$_3^{eq}$, $^2J_{Pt-H}$: 71.38 Hz), 1.24 (s, 3H, C**H**$_3^{ax}$, $^2J_{Pt-H}$: 70.59 Hz).

ESI-Mass Spectroscopy: 458.41 (m/z calculated for M- $^-$I); 458.12 (m/z observed).
IR (solid): 1668 cm^{-1} ($\nu_{C=O}$).

UV / Vis (CH_3CN): λ_{max} / nm (ε / $M^{-1}cm^{-1}$) = 242(sh), 297 (16672), 360(877).

6.3.2.3 Synthesis of *fac*-$Pt(CH_3)_3I(bik)$

0.081 g of $[Pt(CH_3)_3I]_4$ (0.055 mmol) and 0.0416 g of bik (0.219 mmol) were dissolved in acetonitrile and stirred for 12 hours at room temperature. The yellow colour of the reaction mixture became more intense. The solvent was removed, and the solid was purified by column chromatography with 10:1 etyhlacetate-hexane mixture.
Yield is 100 mg (82 %).

Elemental analysis: $C_{12}H_{19}IN_4OPt$ (557.30 g / mol)

Calculated:	C: 25.86 %, H: 3.44 %, N: 10.05 %
Experimental:	C: 25.84 %, H: 3.49 %, N: 09.88 %

^1H –NMR (acetone-d_6) δ / ppm: 7.66 (d, 2H, $H^{5,5'}$, $^3J_{H5-H4}$: 1.06 Hz), 7.55 (d, 2H, $H^{4,4'}$, $^3J_{H4-H5}$:1.250 Hz , J_{H4-Pt}: 9.29 Hz), 4.20 (s, 6H, N-C**H**$_3$), 1.37 (s, 6H, C**H**$_3^{eq}$, $^2J_{Pt-H}$: 71.66 Hz), 0.81 (s, 3H, C**H**$_3^{ax}$, $^2J_{Pt-H}$: 72.06 Hz).

ESI-Mass Spectroscopy: 430.40 (m/z calculated for M- $^-$I); 429.09 (m/z observed).
IR (solid): 1658 cm^{-1} ($\nu_{C=O}$).
UV / Vis (CH_3CN): λ_{max} / nm (ε / $M^{-1}cm^{-1}$)= 246(16340), 279(sh), 290(9093), 331(14724), 355(sh), 370(sh).

6.3.2.4 Synthesis of Bmiq

A solution of 0.406 g of big (1.86 mmol) and 0,5 g of phenylenediamine (4.6 mmol) in glacial acetic acid was heated overnight at 70 ^{0}C. Colour of the solution became dark orange. Solvent was removed using rotary evaporator and the solid was purified by column chromatography first with ethyl acetate to get rid of the impurities and then a solution mixture of 1:1 ethyl acetate – ethanol to obtain 300 mg (56%) of the product.

^{1}H –NMR (acetone-d_6) δ / ppm: 8.16 (m, 2H, phenyl-**H^6**), 7.92 (m, 2H, phenyl-**H^7**), 7.17 (d, 2H, im-**H^5**, $^3J_{H5-H4}$: 1.05 Hz) 6.84 (d, 2H, im-**H^4** $^3J_{H4-H5}$: 1.10 Hz), 3.92 (s, 6H, N-C**H**$_3$).

6.3.2.5 Synthesis of Dibmiq

Similar to synthesis of bmiq, 0.20 g of big (0.917 mmol) and 0.31 g of 4,5'-dimethylphenylenediamine (2.276 mmol) were dissolved in glacial acetic acid and stirred at 70 ^{0}C for 12 hours. Solvent was removed and the residue was purified by chromatography on a silica column with the eluent 1:1 ethyl acetate-ethanol mixture, which gave 157 mg (54%) of pure product.

^{1}H –NMR (acetone-d_6) δ / ppm: 7.91 (s, 2H, phenyl-**H^6**), 7.14 (d, 2H, im-**H^5**, J_{H5-H4}: 1.15 Hz), 6.82 (d, 2H, im-**H^4** J_{H4-H5}: 1.09 Hz), 3.88 (s, 6H, N-C**H**$_3$), 2.56 (s, 6H, Phenyl-C**H**$_3$).

6.3.2.6 Synthesis of $Pt(CH_3)_3I(bmiq)$ / $(Pt(CH_3)_3I)_2(bmiq)$

The reaction of $[PtMe_3I]_4$ and bmiq in 1:1 molar ratio resulted in the mixture of $Pt(CH_3)_3I(bmiq)$ / $(Pt(CH_3)_3I)_2(bmiq)$.

0.1 g of $[PtMe_3I]_4$ (0.068 mmol) was dissolved in 25 ml of CH_2Cl_2 and into this solution, 0.079 g (0.272 mmol) of bmiq was added. The reaction mixture was stirred for one day. The volume of the solution was reduced approximately to half and kept at -20 ^{0}C for two hours. The greenish yellow precipitate was filtrated and washed three times with 10 ml portions of benzene. It was then precipitated from CH_2Cl_2 and hexane.

^{1}H –NMR (acetone-d_6) δ / ppm:

$Pt(CH_3)_3I(bmiq)$: 8.30 (m, 2H, $H^{6,6'}$), 8.09 (m, 2H, $H^{7,7'}$), 8.03 (m, 2H, $H^{4,4'}$), 7.43 (d, 2H, $H^{5,5'}$, $^3J_{H5-H4}$: 1.39 Hz), 3.92 (s, 6H, N-C**H**$_3$), 1.23 (s, 6H, C**H**$_3$-Pt trans to N, $^2J_{Pt-H}$: 71.29 Hz), 0.35 (s, 3H, C**H**$_3$-Pt trans to iodine, $^2J_{Pt-H}$: 73.84 Hz).

$(Pt(CH_3)_3I)_2$(bmiq): 8.19 (m, 2H, $H^{6,6'}$), 8.01 (m, 2H, $H^{7,7'}$), 7.48 (d, 2H, $H^{5,5'}$, $^3J_{H5-H4}$: 1.48 Hz), 7.19 (d, 2H, $H^{4,4'}$, $^3J_{H4-H5}$: 1.50 Hz, $^3J_{H4-Pt}$: 9.34 Hz), 3.91 (s, 6H, N-C**H**$_3$), 1.34 (s, 12H, C**H**$_3$-Pt trans to N, $^2J_{Pt-H}$: 71.43 Hz), 1.24 (s, 6H, C**H**$_3$-Pt trans to iodine, $^2J_{Pt-H}$: 70.11 Hz).

6.3.2.7 Synthesis of $Pt(CH_3)_3I$(dibmiq) / $(Pt(CH_3)_3I)_2$(dibmiq)

The reaction of $[PtMe_3I]_4$ and dibmiq in 1:1 molar ratio resulted in the mixture of $Pt(CH_3)_3I$(dibmiq) / $(Pt(CH_3)_3I)_2$(dibmiq).

A mixture of 0.1 g $[PtMe_3I]_4$ (0.068 mmol) and 0.086 g (0.272 mmol) of dibmiq in CH_2Cl_2 was stirred for 24 hours at room temperature. The volume of the solvent was reduced and kept at -20 ^{0}C for 3 hours. The greenish yellow precipitate was separated and washed several times with benzene. The residue was then precipitated from dichloromethane-hexane mixture.

^1H –NMR (acetone-d_6) δ / ppm:

$Pt(CH_3)_3I$(dibmiq): 8.03 (s, 2H, $H^{6,6'}$), 8.00 (d, 2H, $H^{4,4'}$, $^3J_{H4-H5}$: 1.41 Hz), 7.34 (d, 2H, $H^{5,5'}$, $^3J_{H5-H4}$: 1.31 Hz), 3.90 (s, 6H, N-C**H**$_3$), 2.62 (s, 6H, Ph-C**H**$_3$), 1.21(s, 6H, C**H**$_3$-Pt trans to N, $^2J_{Pt-H}$: 71.01 Hz), 0.33 (s, 3H, C**H**$_3$-Pt trans to iodine, $^2J_{Pt-H}$: 73.80 Hz).

$(Pt(CH_3)_3I)_2$(bmiq): 7.93 (s, 2H, $H^{6,6'}$), 7.45 (d, 2H, $H^{5,5'}$, $^3J_{H5-H4}$: 1.51 Hz), 7.16 (d, 2H, $H^{4,4'}$, $^3J_{H5-H4}$: 1.54 Hz), 3.88 (s, 6H, N-C**H**$_3$), 2.58 (s, 6H, Ph-C**H**$_3$), 1.33 (s, 12H, C**H**$_3$-Pt trans to N, $^2J_{Pt-H}$: 71.52 Hz), 1.22 (s, 6H, C**H**$_3$-Pt trans to iodine, $^2J_{Pt-H}$: 70.80 Hz).

6.3.3 Syntheses in Chapter 4:

6.3.3.1 Synthesis of syn-[{$PtI(CH_3)$}$_2$(μ-bpym)]

This complex was synthesized in two different ways:

Method 1:

This method was adapted from literature [113]. 0.2 g of $Pt_2Me_4(\mu\text{-}SMe_2)_2$ (0.348 mmol) and 0.027 g of 2,2'-bipyrimidine (0.170 mmol) were dissolved in CH_2Cl_2 and stirred

for 30 minutes at room temperature. The colour of the solution became dark red, giving a black insoluble precipitate, $[Pt_2(CH_3)_4(\mu\text{-bpym})]$. This complex was washed several times with CH_2Cl_2 and suspended in acetone-CH_2Cl_2 mixture. An excess amount of MeI (4 ml) was then added to the suspension, and an immediate colour change to pale yellow was observed. It was stirred for 24 hours at room temperature. At the end of this time, a colour change to dark orange was observed. Solvent was removed by rotary evaporator and the residue was washed several times with CH_2Cl_2. The product was recrystallized from dichloromethane and hexane.
Yield is 99 mg (65%).
Method 2:
A solution of 0.138 g $[Pt(CH_3)_3I]_4$ (0.094 mmol) in benzene was added to a solution of 0.030 g 2,2'-bipyrimidine (0.190 mmol) in benzene and stirred for 24 hours to yield an orange precipitate. The mixture was filtered and the solid was washed several times with 10 ml portions of CH_2Cl_2 to get rid of any anti isomer of the complex.
Yield is 143 mg (85%).

Elemental analysis: $C_{14}H_{24}N_4I_2Pt_2$ (892.33 g / mol)
Calculated: C: 18.84 %, H: 2.71 %, N: 06.28 %
Experimental: C: 18.97 %, H: 2.64 %, N: 06.19 %

^1H –NMR (acetone-d_6) δ / ppm: 9.70 (d, 4H, $H^{4,4'}$, $^3J_{H4\text{-}H5}$: 5.34 Hz, $^3J_{Pt\text{-}H4}$: 15.4), 8.50 (t, 2H, $H^{5,5'}$, $^3J_{H5\text{-}H4}$: 5,58 Hz), 1.65 (s, 6H, C**H**$_3$ trans to N, $^2J_{Pt\text{-}H}$: 74.701 Hz), 0.84 (s, 3H, C**H**$_3$ trans to I, $^2J_{Pt\text{-}H}$: 70.818 Hz).

6.3.3.2 Synthesis of $[\{Pt(CH_3)_3\}_4(\mu\text{–}bp)_2(\mu\text{–}bpym)_2](OTf)_4$

To a solution of 0.12 g $[\{PtI(CH_3)\}_2(\mu\text{-bpym})]$ (0.134 mmol) in water and oxygen free CH_2Cl_2, 0.087 g. AgOTf (0.34 mmol) was added rapidly and stirred for 2 hours at room temperature. The solution became colourless yielding AgI precipitate. Solution was filtrated by celite on a glass frit and the solvent was removed by rotary evaporator. Product was one more time dissolved in CH_2Cl_2, filtrated with same methode and in to the filtrate, 0.021 g of 4,4'-bipyridine (0.13 mmol) were added. An

immediate precipitation with white colour was observed. It was left for stirring overnight. Mixture was filtrated and the solid was washed 4 times 15 ml portions of CH_2Cl_2. Final product was dried under vacuum.
Yield is 123 mg (80%).

Elemental analysis: $C_{52}H_{64}N_{12}F_{12}O_{12}Pt_4S_4$ (2185.77 g / mol)
Calculated: C: 28.57 %, H: 2.95 %, N: 07.69 %
Experimental: C: 27.75 %, H: 3.04 %, N: 07.07 %

^{1}H –NMR (acetone-d_6) δ / ppm: 9.99 (d, , 8H, H^1, $^3J_{H1-H2}$: 5.49 Hz, $^3J_{Pt-H1}$: 14.06), 8.78 (t, 4H, H^2, $^3J_{H2-H1}$: 5.53 Hz), 8.31(d, 8H, H^3, $^3J_{H3-H4}$: 5.33 Hz, $^3J_{H3-Pt}$: 18.49 Hz), 7.55 (d, 8H, H^4, $^3J_{H4-H3}$:5.26 Hz), 1.41(s, 24H C**H**$_3$ trans to N's of bpym, $^2J_{Pt-H}$: 71.18 Hz), 0.89 (s, 12H, C**H**$_3$ trans to N's of bp, $^2J_{Pt-H}$: 70.61 Hz).
^{195}Pt-NMR(acetone-d_6): -2498 ppm.

ESI-Mass Spectroscopy: (m/z calculated for M- $^-$OTf); 2036.3 (m/z observed for $[\{Pt(CH_3)_3\}_4(\mu\text{–bp})_2(\mu\text{–bpym})_2]^+(OTf)_3$).

UV / Vis (CH_3CN): λ_{max} / nm (ε / $M^{-1}cm^{-1}$) = 243(57300), 268(63600), 290(sh), 340(sh), 650(600).

6.3.4 Syntheses in Chapter 5:

6.3.4.1 Synthesis of $[Pt(CH_3)_3(bpy)](OTf)$

0.2 g of $[Pt(CH_3)_3I(bpy)]$ (0.382 mmol) was dissolved in dry acetone and into this solution, a slight excess amount of AgOTf (0.11 g) was added rapidly. The schlenk glass was covered with aluminium foil for light protection. After an hour, the color solution lost faded away giving AgI precipitate. Solution was filtrated by celite on a glass frit and the solvent was removed under vacuum.
Yield is 60 mg (30%)
^{1}H –NMR (acetone-d) δ / ppm: 9.08 (d, br, 2H, $H^{6,6'}$, $^3J_{H6-H5}$: 5.44 Hz), 8.82 (d,br, 2H, $H^{3,3'}$, $^3J_{H3-H4}$: 7.97 Hz), 8.45(t, br, 2H, $H^{4,4'}$, $^3J_{H4-H3,5}$: 7.55 Hz,), 8.00 (t, br, 2H, $H^{5,5'}$,

$^{3}J_{H5\text{-}H4,6}$: 6.74 Hz), 1.29(s, 6H, C**H**$_3$ trans to N, $^{2}J_{Pt\text{-}H}$: 66.73 Hz), 0.76 (s, br, 3H, C**H**$_3$ trans to OTf).

6.3.4.2 Synthesis of [{Pt(CH$_3$)$_3$(bpy)}$_4$ TCNQ](OTf)$_4$

0.055 g of [Pt(CH$_3$)$_3$(bpy)](OTf) (0.1 mmol) and 0,005 g of TCNQ (0.024 mmol) was dissolved in 20 ml of acetone in a dark schlenk and stirred for 18 hours. The colour of the solution changed immediately from colourless to greenish-yellow. The solvent was removed under reduced pressure and the solid was washed 3 times with 10 ml portions of dried CH_2Cl_2. Product was dried under vacuum precipitated from acetone-hexane mixture.

Yield is 22 mg (37%).

Elemental analysis: $C_{68}H_{72}N_{12}F_{12}O_{12}Pt_4S_4$ (2386.01 g / mol)

Calculated: C: 34.22 %, H: 3.04 %, N: 07.04 %

Experimental: C: 34.22 %, H: 3.09 %, N: 07.33 %

^{1}H –NMR (acetone-d$_6$) δ / ppm: 9.07 (d, br, 8H, H^6, $^{3}J_{H6\text{-}H5}$: 5.43 Hz), 8.81 (d, br, 8H, H^3, $^{3}J_{H3\text{-}H4}$: 7.51 Hz), 8.44 (t, br, 8H, H^4, $^{3}J_{H4\text{-}H3,5}$: 7.39 Hz), 7.99 (t, br, 8H, H^5, $^{3}J_{H5\text{-}H4,6}$: 6.39 Hz), 7.70(s, 4H, **H**-TCNQ), 1.29 (s, 6H, C**H**$_3$ trans to N, $^{2}J_{Pt\text{-}H}$: 66.97 Hz), 0.77 (s, br, 3H, C**H**$_3$ trans to OTf).

^{1}H –NMR (acetone-d$_6$), -50^{0}C, δ / ppm: 9.09 (dd, 8H, H^6, $^{3}J_{H6\text{-}H5}$: 5.53 Hz, $^{4}J_{H6\text{-}H4}$: 0.89 Hz, $^{3}J_{Pt\text{-}H6}$: 18.22 Hz), 8.91 (d, 8H, H^3, $^{3}J_{H3\text{-}H4}$: 8.142 Hz), 8.50(td, 8H, H^4, $^{3}J_{H4\text{-}H3,5}$: 7.71 Hz, $^{4}J_{H4\text{-}H6}$: 1.53 Hz), 8.04 (ddd, 8H, H^5, $^{3}J_{H5\text{-}H3}$: 1.137 Hz), 7.72(s, **H**-TCNQ), 1.21 (s, 6H, C**H**$_3$ trans to N, $^{2}J_{Pt\text{-}H}$: 67.18 Hz), 0.64 (s, 3H, C**H**$_3$ trans to OTf, $^{2}J_{Pt\text{-}H}$: 81.60 Hz).

IR (solid): 2226 cm^{-1} (ν_{CN}).

UV / Vis (CH$_3$CN): λ_{max} / nm = 290, 310, 376(sh), 398.

6.4 Crystallography

Crystallographic data collection and Structure solving were carried out by Dr. F. Lissner, Priv. Doz. Dr. M. Niemeyer, Dr. I. Hartenbach and Mr. D. Bubrin from University of Stuttgart and by Prof. Cheng-Yong Su from Sun Yat-Sen University, China.

Data collection carried out in University of Stuttgart was performed on four circle diffractometer NONIUS Kappa-CCD or Siemens P4 with a Mo-K_α radiation of 0.71073 Å (graphite-monocromatized) at 293 K or 173 K. The crystals were sealed in capillaries for the measurements.

The structure were solved via direct methods using the programme SHELXS-97.[151] Refinement was carried out by the full matrix least squares method employing the programme SHELXL-97.[152] All non-hydrogen atoms are refined anisotropically, hydrogen atoms were introduced in proper positions with coupled isotropic factors using the riding model. Absorption corrections were performed numerically using the programme HABITUS.[153] The programme DIAMOND 3.2b[154] was used for structure drawing.

Crystallographic parameters:

$GOF = \{\Sigma w(|F_o|^2 - |F_c|^2)^2 / (n - m)\}^{1/2}$ where n = number of data and m = number of variables

$R = (\Sigma||F_o| - |F_c||) / \Sigma|F_o|$

$wR = \{\Sigma[w(|F_o|^2 - |F_c|^2)^2] / \Sigma[w(F_o^4)]\}^{1/2}$

6.4.1 *fac*-$Pt(CH_3)_3Cl(bptz)$

Red plates for X-ray diffraction were obtained by slow evaporation of a solution of *fac*-$Pt(CH_3)_3Cl(bptz)$ in nitromethane.

Empirical formula	$C_{15}\,H_{17}\,Cl_1\,N_6\,Pt_1$
Formula wt.	511.88 g mol^{-1}
Crystal size	0.25 x 0.20 x 0.15 mm
Temperature	173 K
Wavelength	0.71073 Å
Crystal system	monoclinic
Space group	$P2_1/c$
Unit cell dimension	a = 13.835(3) Å α = 90°
	b = 16.266(3) Å β = 93.725(16)°
	c = 7.1161(14) Å γ = 90°
Cell volume	1598.0(6) $Å^3$
Calculated density	2.128 g cm^{-3}
Absorption coefficient	8.956 mm^{-1}
θ range for data collection	1.93 to 27.5°
Index ranges	$-17 \le h \le 17$
	$-21 \le k \le 16$
	$-8 \le l \le 9$
Formula units per cell, Z	4
Reflection collected	3947
Independent reflections	3654 [R(int) = 0.0298]
GOF / F^2	1.119
Data / restraints / parameter	3654 / 0 / 210
R indices (for all data)	R1 = 0.0590, wR2 = 0.0890
R indices (for I > 2σ(I))	R1 = 0.0382, wR2 = 0.0816
Largest residual densities	1.598, - 0.947e $Å^{-3}$

6.4.2 *fac*-$Pt(CH_3)_3Br(bptz)$

Red crystals of *fac*-$Pt(CH_3)_3Br(bptz)$ for X-ray diffraction were obtained by slow evaporation of its nitromethane solution.

Empirical formula	$C_{15}\ H_{17}\ Br_1\ N_6\ Pt_1$
Formula wt.	556.35 g mol^{-1}
Crystal size	0.10 x 0.06 x 0.05 mm
Temperature	293 K
Wavelength	1.54178 Å
Crystal system	monoclinic
Space group	$P2_1/c$
Unit cell dimension	a = 13.9288(2) Å α = 90°
	b = 16.4769(3) Å β = 92.442(2)°
	c = 7.20610(10) Å γ = 90°
Cell volume	1652.32(4) $Å^3$
Calculated density	2.236 g cm^{-3}
Absorption coefficient	18.785 mm^{-1}
θ range for data collection	4.16 to 64.06°
Index ranges	-16≤ *h* ≤16
	-19≤ *k* ≤18
	-8≤ *l* ≤7
Formula units per cell, Z	4
Reflection collected	7359
Independent reflections	2670 [R(int) = 0.0205]
GOF / F^2	1.034
Data / restraints / parameter	2670 / 12 / 208
R indices (for all data)	R1 = 0.0279, wR2 = 0.0492
R indices (for I > 2σ(I))	R1 = 0.0212, wR2 = 0.0482
Largest residual densities	0.693, -0.631 e.$Å^{-3}$

6.4.3 *fac*-$Pt(CH_3)_3I(bptz)$

Brown plates for X-ray diffraction were grown by slow diffusion of hexane into nitromethane solution of *fac*-$Pt(CH_3)_3I(bptz)$.

Empirical formula	$C_{15}\ H_{17}\ I_1\ N_6\ Pt_1$
Formula wt.	603.33 g mol^{-1}
Temperature	293 K
Wavelength	0.71073 Å
Crystal system	monoclinic
Space group	$P2_1/c$
Unit cell dimension	a = 13.951(2) Å α = 90°
	b = 16.828(3) Å β = 91.529(11)°
	c = 7.3572(11) Å γ = 90°
Cell volume	1726.6(5) $Å^3$
Calculated density	2.321 g cm^{-3}
Absorption coefficient	9.922 mm^{-1}
θ range for data collection	2.42 to 27.48°
Index ranges	$-18 \le h \le 18$
	$-21 \le k \le 21$
	$-5 \le l \le 9$
Formula units per cell, Z	4
Reflection collected	3971
Independent reflections	3691 [R(int) = 0.0642]
GOF / F^2	1.000
Data / restraints / parameter	3691 / 0 / 206
R indices (for all data)	R1 = 0.1400, wR2 = 0.1768
R indices (for I > 2σ(I))	R1 = 0.0672, wR2 = 0.1447
Largest residual densities	3.064, -1.682 e.$Å^{-3}$

6.4.4 *anti*-[(μ-bmptz){*fac*-PtCl(CH$_3$)}$_2$]

Orange crystals for X-ray diffraction were grown by slow diffusion of hexane into CH_2Cl_2 solution of *anti*-[(μ-bmptz){*fac*-PtCl(CH$_3$)}$_2$]

Empirical formula	$C_{20}\ H_{30}\ Cl_2\ N_6\ Pt_2$
Formula wt.	815.58 g mol^{-1}
Temperature	293 K
Wavelength	0.71073 Å
Crystal system	orthorhombic
Space group	*Fddd*
Unit cell dimension	a = 15.537(3) Å α = 90°
	b = 17.167(3) Å β = 90°
	c = 41.705(8) Å γ = 90°
Cell volume	11124(4) Å^3
Calculated density	1.948 g cm^{-3}
Absorption coefficient	10.259 mm^{-1}
θ range for data collection	1.95 to 27.00°
Index ranges	$0 \le h \le 19$
	$0 \le k \le 21$
	$0 \le l \le 53$
Formula units per cell, Z	16
Reflection collected	3044
Independent reflections	3044 [R(int) = 0.0000]
GOF / F^2	1.167
Data / restraints / parameter	3044 / 0 / 140
R indices (for all data)	R1 = 0.0889, wR2 = 0.1276
R indices (for I > 2σ(I))	R1 = 0.0532, wR2 = 0.1161
Largest residual densities	1.575, -1.247e.Å^{-3}

6.4.5 *anti*-[(μ-bmptz){*fac*-PtBr(CH_3)$_2$}$_2$]

Orange-red crystals for X-ray diffraction were grown by slow diffusion of hexane into CH_2Cl_2 solution of *anti*-[(μ-bmptz){*fac*-PtBr(CH_3)$_2$}$_2$]

Empirical formula	$(C_{20}\ H_{30}\ Br_2\ N_6\ Pt_2).H_2O_1$
Formula wt.	922.48 g mol^{-1}
Crystal size	0.20 x 0.20 x 0.04 mm
Temperature	173 K
Wavelength	0.71073 Å
Crystal system	orthorhombic
Space group	*Fddd*
Unit cell dimension	a = 15.719(2) Å α = 90°
	b = 17.365(2) Å β = 90°
	c = 41.478(7) Å γ = 90°
Cell volume	11322(3) $Å^3$
Calculated density	2.162 g cm^{-3}
Absorption coefficient	12.719 mm^{-1}
θ range for data collection	1.82 to 27.50°
Index ranges	$-15 \le h \le 20$
	$-15 \le k \le 22$
	$-43 \le l \le 53$
Formula units per cell, Z	16
Reflection collected	3837
Independent reflections	3253 [R(int) = 0.0586]
GOF / F^2	0.883
Data / restraints / parameter	3253 / 2 / 139
R indices (for all data)	R1 = 0.1203, wR2 = 0.1743
R indices (for I > 2σ(I))	R1 = 0.0748, wR2 = 0.1649
Largest residual densities	3.951, -4.748 e.$Å^{-3}$

6.4.6 *anti*-[(μ-bmptz){*fac*-PtI(CH_3)$_3$}$_2$]

Dark green crystals for X-ray diffraction were grown by slow diffusion of hexane into CH_2Cl_2 solution of *anti*-[(μ-bmptz){*fac*-PtI(CH_3)$_3$}$_2$].

Empirical formula	$(C_{20}\ H_{30}\ I_2\ N_6\ Pt_2).1/2(H_2O_1)$
Formula wt.	1007.47 g mol^{-1}
Temperature	293 K
Wavelength	0.71073 Å
Crystal system	triclinic
Space group	$P\bar{1}$
Unit cell dimension	a = 11.4707(4) Å α = 88.674(2)°
	b = 15.8673(5) Å β = 87.534(2)°
	c = 17.1664(5) Å γ = 69.048(2)°
Cell volume	2915.05(16) $Å^3$
Calculated density	2.312 g cm^{-3}
Absorption coefficient	11.727 mm^{-1}
θ range for data collection	2.94 to 27.11°
Index ranges	$-14 \le h \le 14$
	$-20 \le k \le 20$
	$-21 \le l \le 21$
Formula units per cell, Z	4
Reflection collected	22206
Independent reflections	12581 [R(int) = 0.0708]
GOF / F^2	1.047
Data / restraints / parameter	12581 / 0 / 544
R indices (for all data)	R1 = 0.1107, wR2 = 0.1425
R indices (for I > 2σ(I))	R1 = 0.0630, wR2 = 0.1230
Largest residual densities	5.798, -3.489 e.$Å^{-3}$

6.4.7 *fac*-$Pt(CH_3)_3I(bmptz)$

Red plates of *fac*-$Pt(CH_3)_3I$(bmptz) for X-ray diffraction were gathered by slow evaporation of a benzene-dichloromethane solution mixture.

Empirical formula	$(C_{17}\ H_{21}\ I_1\ N_6\ Pt_1).C_6H_6$	
Formula wt.	709.49 g mol^{-1}	
Crystal size	0.28 x 0.25 x 0.06 mm	
Temperature	173 K	
Wavelength	0.71073 Å	
Crystal system	monoclinic	
Space group	$P2_1/c$	
Unit cell dimension	a = 17.3979(19) Å	α = 90.00°
	b = 7.4253(9) Å	β = 105.560(8)°
	c = 19.635(2) Å	γ = 90.00°
Cell volume	2443.6(5) $Å^3$	
Calculated density	1.918 g cm^{-3}	
Absorption coefficient	7.022 mm^{-1}	
θ range for data collection	2.15 to 28.01°	
Index ranges	$0 \le h \le 22$	
	$0 \le k \le 9$	
	$-25 \le l \le 24$	
Formula units per cell, Z	4	
Reflection collected	6083	
Independent reflections	5898 [R(int) = 0.0273]	
GOF / F^2	0.902	
Data / restraints / parameter	5898 / 0 / 290	
R indices (for all data)	R1 = 0.0524, wR2 = 0.0915	
R indices (for I > 2σ(I))	R1 = 0.0383, wR2 = 0.0892	
Largest residual densities	1.951, -1.887e.$Å^{-3}$	

6.4.8 *fac*-$Pt(CH_3)_3I$(big)

Orange needles suitable for X-ray diffraction were obtained by slow diffusion of n-hexane into the CH_2Cl_2 solution of *fac*-$Pt(CH_3)_3I$(big) at -20 ^{0}C.

Empirical formula	$(C_{13}\ H_{19}\ I_1\ N_4\ O_2Pt_1).C_1H_2Cl_2$	
Formula wt.	670.24 g mol^{-1}	
Temperature	293 K	
Wavelength	0.71073 Å	
Crystal system	triclinic	
Space group	$P\bar{1}$	
Unit cell dimension	a = 12.0639(5) Å	α = 95.883^0(2)
	b = 13.5687(6) Å	β = 100.509^0(3)
	c = 25.1345(12) Å	γ = 90.064^0(3)
Cell volume	4023.2(3) $Å^3$	
Calculated density	2.213 g cm^{-3}	
Absorption coefficient	8.790 mm^{-1}	
θ range for data collection	0.83 to 27.88^0	
Index ranges	$-15 \le h \le 15$	
	$-17 \le k \le 17$	
	$-33 \le l \le 33$	
Formula units per cell, Z	8	
Reflection collected	28711	
Independent reflections	17662 [R(int) = 0.0452]	
GOF / F^2	1.128	
Data / restraints / parameter	17662 / 0 / 877	
R indices (for all data)	R1 = 0.0797, wR2 = 0.1035	
R indices (for I > 2σ(I))	R1 = 0.0514, wR2 = 0.0941	
Largest residual densities	2.945, -1.962 e $Å^3$	

6.4.9 *fac*-$Pt(CH_3)_3I$(bik)

Yellow needle like crystals suitable for X-ray diffraction were obtained by slow diffusion of n-hexane into the CH_2Cl_2 solution of *fac*-$Pt(CH_3)_3I$(bik) at -20 ^{0}C.

Empirical formula	$(C_{12}\ H_{19}\ I_1\ N_4\ O_1 Pt_1).C_1H_2Cl_2$
Formula wt.	642.23 g mol^{-1}
Temperature	293 K
Wavelength	0.71073 Å
Crystal system	monoclinic
Space group	$P2_1/m$
Unit cell dimension	a = 8.6447(3)Å α = 90^0
	b = 13.4486(4) Å β = 100.808^0(2)
	c = 14.7626(4) Å γ = 90^0
Cell volume	1685.84(9) $Å^3$
Calculated density	2.391 g cm^{-3}
Absorption coefficient	10.317 mm^{-1}
θ range for data collection	2.84 to 28.16^0
Index ranges	$-11 \le h \le 11$
	$-17 \le k \le 15$
	$-19 \le l \le 19$
Formula units per cell, Z	4
Reflection collected	19733
Independent reflections	4265 [R(int) = 0.0785]
GOF / F^2	1.128
Data / restraints / parameter	4265 / 0 / 218
R indices (for all data)	R1 = 0.0348, wR2 = 0.0751
R indices (for I > 2σ(I))	R1 = 0.0323, wR2 = 0.0740
Largest residual densities	1.457, -2.211 e $Å^3$

CHAPTER 7

Summary

In this thesis, a series of mononuclear and dinuclear trimethylplatinum(IV)halide (halide: Cl, Br, I) complexes of several π-accepting α-diimine ligands is presented. The electrochemical and spectroscopic behaviour of these complexes is influenced by the properties of the ligands. Fig. 7.1 shows the α-diimine ligands used in this work.

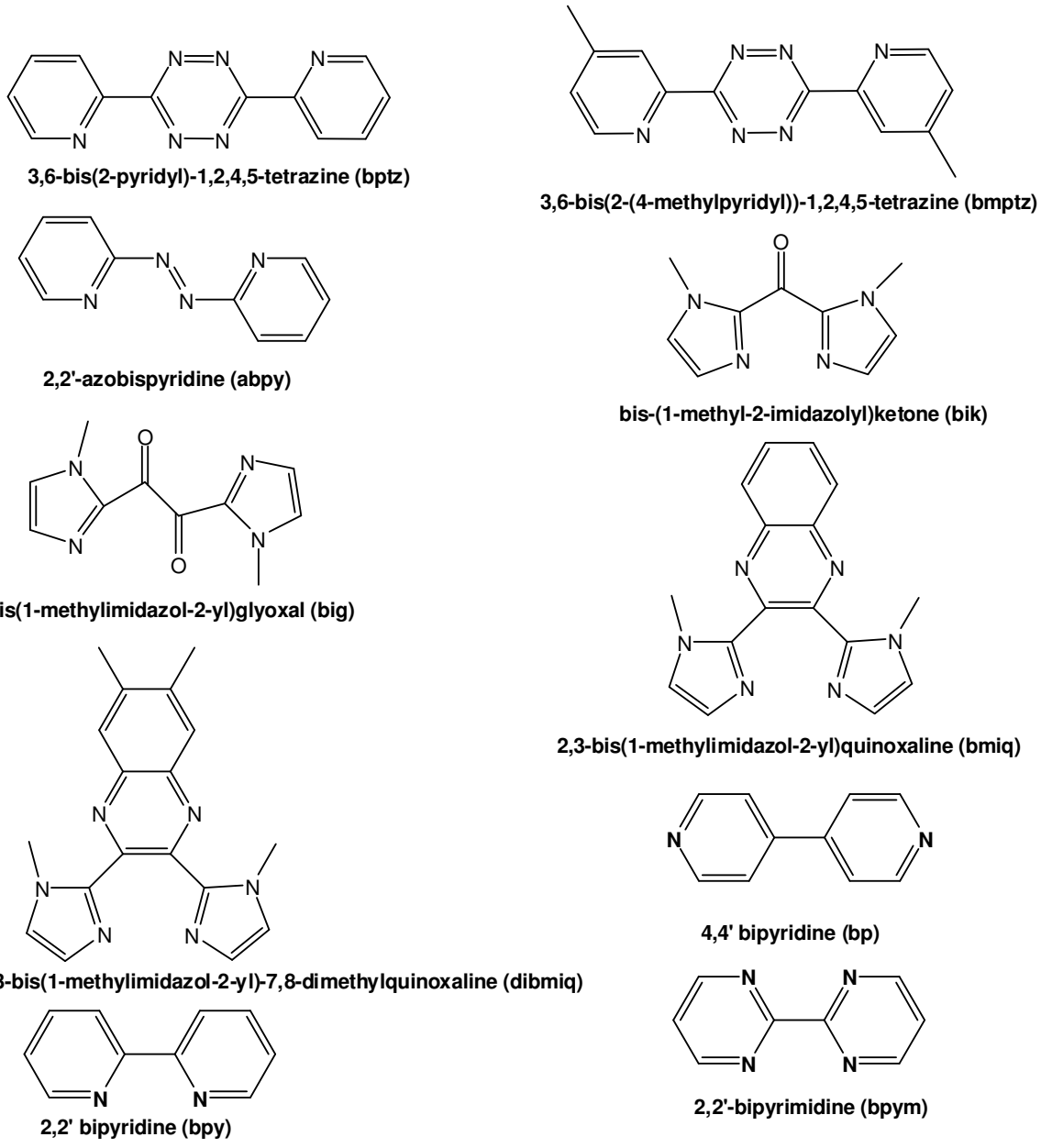

Fig. 7.1: *The α-diimine ligands used in this work*

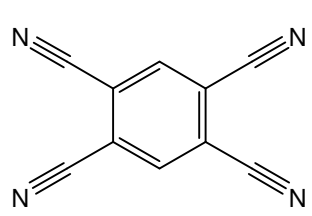

1,2,4,5-tetracyanobenzene (TCNB)

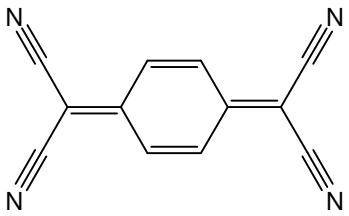

7,7,8,8-tetracyano-p-quinodimethane (TCNQ)

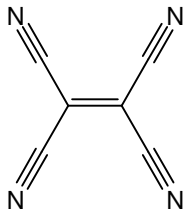

tetracyanoethene (TCNE)

Fig. 7.2: *TCNX ligands*

In chapter 2, the syntheses, structural and electrochemical properties of new mononuclear and dinuclear complexes formed from strongly π accepting tetrazine containing bptz and bmptz ligands and $[PtMe_3X]_4$ (X: Cl, Br, I) are discussed. In addition, spectroscopic and electrochemical properties of previously reported $Pt(abpy)Me_3Br$[41] are presented and compared with those of $Re(CO)_3X(abpy)$ (X: Cl, Br, I)[42] complexes.

Seven complexes could be characterized by X-ray crystal structure analysis, and the data of *fac*-$Pt(CH_3)_3Cl(bptz)$ and *fac*-$Pt(CH_3)_3Br(bptz)$ were rationalized by DFT calculations. The complexes reveal an octahedral configuration around the platinum(IV) center and a *fac* arrangement of the methyl groups. The dinuclear bmptz complexes [(μ-bmptz){*fac*-$PtXMe_3$}$_2$] (X:Cl, Br, I) crystallize in the *anti* form. Fig. 7.3 illustrates the crystal structure of *anti*-[(μ-bmptz){*fac*-$PtBrMe_3$}$_2$].

The Pt-$CH_{3(ax)}$ bond lengths in the mononuclear bptz complexes are remarkably longer than the Pt-$CH_{3(eq)}$ bond distances due to the different *trans* influence. A possible SBLCT transition is also expected to elongate the axial methyl-platinum bond. However, this effect is less pronounced for *fac*-$Pt(CH_3)_3I(bmptz)$ and for the dinuclear bmptz complexes. The coordination of the metal fragments causes a planarization of the bridging ligand.

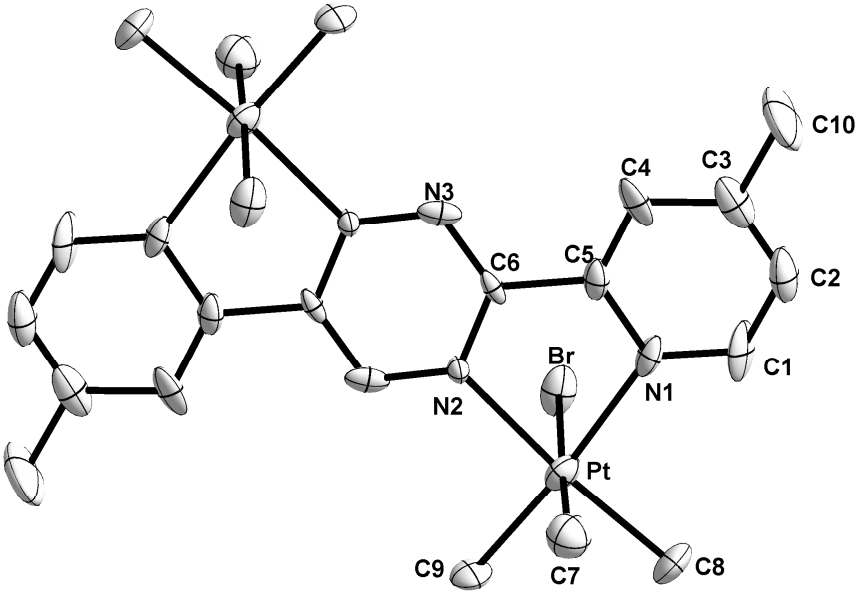

Fig. 7.3: *Molecular structure of anti-[(μ-bmptz){fac-PtBrMe$_3$}$_2$] in the crystal*

.

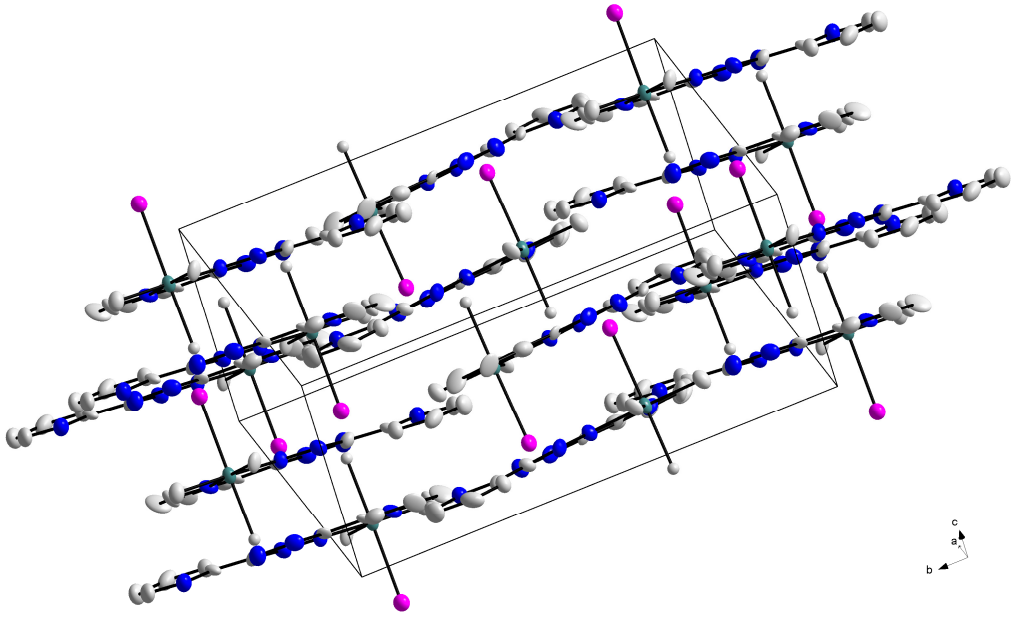

Fig. 7.4: *Arrangement of fac-Pt(CH$_3$)$_3$I(bptz) in the unit cell*

Only *fac*-Pt(CH$_3$)$_3$Cl(bptz) and dinuclear *anti*-[(μ-bmptz){*fac*-PtXMe$_3$}$_2$] (X: Cl, Br, I) complexes exhibit a reversible reduction wave at room temperature in the cyclic voltammetry. Moreover, changing the halide from Cl^- to I^- in dinuclear bmptz complexes of [PtMe$_3$X] causes both reversible first and irreversible second reductions to occur at less negative potentials.

UV-Vis Spectroelectrochemistry of the *fac*-Pt(CH_3)$_3$Cl(bptz) and all three dinuclear *anti*-[(μ-bmptz){*fac*-PtXMe_3}$_2$] compounds shows isobestic points for the one electron reduction processes, indicating the homogeneity of the systems studied. The bands in the visible region are partially structured and are assigned as MLCT and SBLCT transitions.

The electrochemically generated radical anion *anti*-[(μ-bmptz){*fac*-PtBrMe_3}$_2$]$^{\bullet-}$ was analyzed by EPR spectroscopy (Fig. 7.5). The g factor at 2.0053 which is close to the free electron value indicates nearly complete spin localization on the tetrazine ring. The TD-DFT calculations performed for *fac*-Pt(CH_3)$_3$Br(bptz) are also in agreement with the acceptance of an electron predominantly by the tetrazine ring.

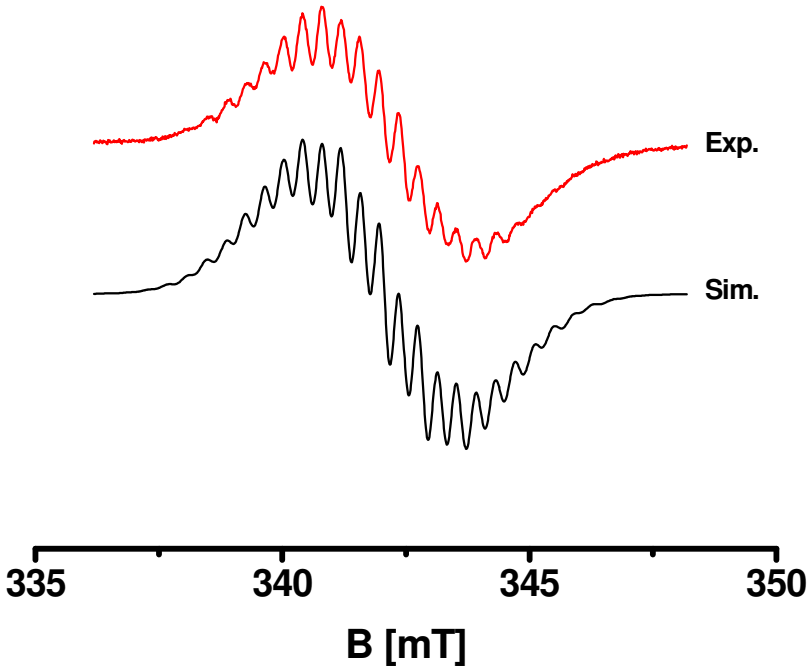

Fig. 7.5: *EPR spectrum of anti-[(μ-bmptz){fac-PtBrMe_3}$_2$]$^{\bullet-}$, generated by in situ electrolysis in CH_2Cl_2/0.1 M Bu_4NPF_6 (top) with computer simulation (bottom; 0.35 mT linewidth)*

The weak charge transfer band observed in the visible region of the absorption spectrum, the small shift of the reduction potential in comparison to the free ligand (Fig. 7.6) and the small g anisotropy in the EPR spectrum of Pt(abpy)$Me_3Br^{\bullet-}$ shows that there exists only a marginal π interaction between the platinum(IV) fragment and the strong π acceptor abpy in this complex. The short N=N bond distance of the complex at around 1.26 Å [28] also supports this statement.

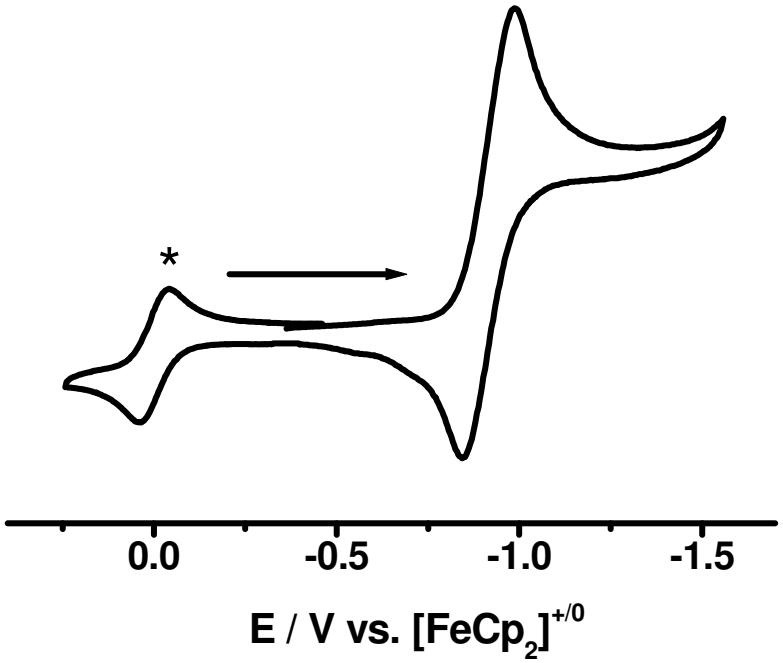

Fig. 7.6: *Cyclic voltammogram of Pt(abpy)Me_3Br in CH_2Cl_2/0.1 M Bu_4NPF_6 at 248 K (v = 100 mV/s) (* = ferrocene wave)*

Chapter 3 deals with the structural, spectroscopic and electrochemical investigation of the first organoplatinum(IV) complexes of the ligands big and bik, *fac*-$Pt(CH_3)_3I$(big) and *fac*-$Pt(CH_3)_3I$(bik). The reaction products of $[PtMe_3I]_4$ with two newly synthesized ligands 2,3-bis(1-methylimidazol-2-yl)quinoxaline (bmiq) and 2,3-bis(1-methylimidazol-2-yl)-7,8-dimethylquinoxaline (dibmiq) are also discussed.

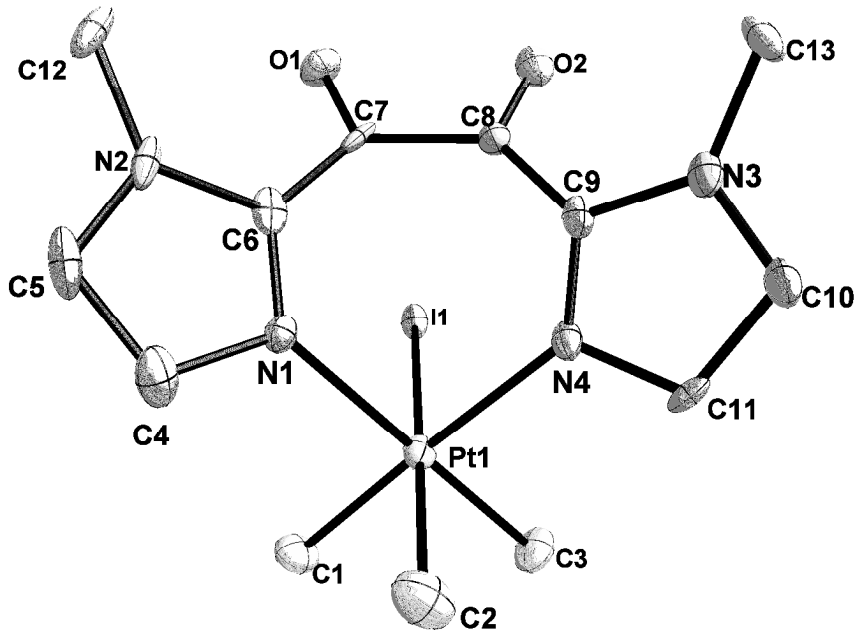

Fig. 7.7: *Molecular structure of fac-Pt(CH$_3$)$_3$I(big) in the crystal*

The spectroscopic analyses of *fac*-Pt(CH$_3$)$_3$I(big) and *fac*-Pt(CH$_3$)$_3$I(bik) showed the existence of only mononuclear complexes while ^{1}H-NMR spectroscopy verified the formation of both mononuclear and dinuclear compounds as a product mixture in the reaction of bmiq or dibmiq with [PtMe$_3$I]$_4$.

The data obtained from an X-ray diffraction analysis of *fac*-Pt(CH$_3$)$_3$I(big) (Fig. 7.7) and *fac*-Pt(CH$_3$)$_3$I(bik) are supported by DFT calculations. In both complexes Pt^{IV} has an octahedral enviroment as expected.

Both complexes can be reduced reversibly only at low temperatures, *fac*-Pt(CH$_3$)$_3$I(big) at -30 ^{0}C and *fac*-Pt(CH$_3$)$_3$I(bik) at -80 ^{0}C. The reversible character of the first reduction waves of the complexes at least at low temperatures prompted an attempt to study low temperature spectroelectrochemistry of the complexes. Only *fac*-Pt(CH$_3$)$_3$I(big) shows reversibility in the IR-spectroelectrochemistry; a shift of the CO stretching frequency to lower wavenumbers (1673 cm^{-1} → 1533 cm^{-1}) indicates that the added electron is located on the α-diketo moiety resulting in the formation of an α–semidione compound (Fig. 7.8). This result is well supported by calculations, which showed that the SOMO of *fac*-Pt(CH$_3$)$_3$I(big)$^{\bullet-}$ is mainly composed of the α-diketo moiety of the ligand with bonding character of the C-C bond and antibonding

character of the C=O bonds. The g factor of 2.0061 found in the EPR spectrum of electrogenerated *fac*-$Pt(CH_3)_3I(big)^{\bullet-}$ is also a strong evidence for a ligand based reduction.

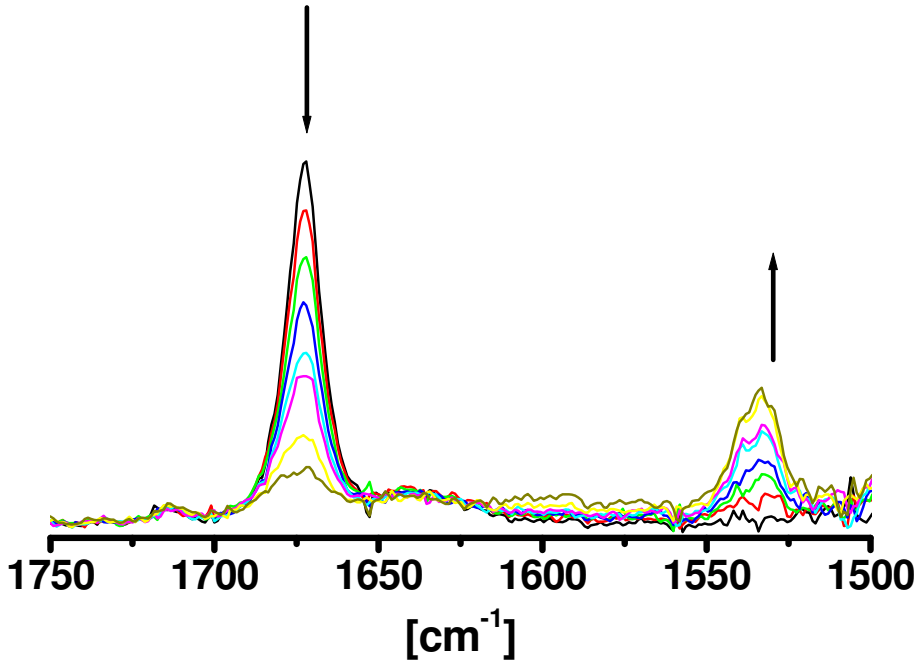

Fig. 7.8: *Spectroelectrochemical reduction of fac-$Pt(CH_3)_3I(big)$ at -60 ^{0}C in n-butyronitrile / 0.1 M Bu_4NPF_6*

In chapter 4, the first organo-Pt^{IV} containing rectangular molecule, $[\{Pt(CH_3)_3\}_4(\mu\text{–}bp)_2(\mu\text{–}bpym)_2](OTf)_4$ (bp = 4,4´-bipyridine, bpym = 2,2´-bipyrimidine, OTf = CF_3SO_3), its characterization, electrochemical and spectroelectrochemical properties are discussed. Molecular rectangles are accepted as a representative class for supramolecular complexes and take attention due to their potential electron reservoir capacities.

Analytical measurements (^{1}H- and ^{195}Pt-NMR, CHN analysis, mass spectroscopy) confirm the formation of the desired rectangular complex. Cyclic voltammetry and UV-Vis spectroelectrochemistry measurements support the idea of simultaneous localization of first two electrons on the bpym ligands, the next two electrons also on the bpym ligands whereas the following reduction steps occur in one electron fashion on the bp ligands. However, the complex starts slowly to disintegrate after the addition of the fifth and sixth electrons which are observed as a combined two electron reduction step in the OTTLE spectroelectrochemistry, involving

adsorption/desorption of the neutral intermediate. The related $[Re_4(CO)_{12}(\mu\text{-bp})_2(\mu\text{-bpym})_2](OTf)_4$, reported before[43] serves as a more efficient electron reservoir since it can be reversibly reduced with up to seven electrons. A possible explanation of this difference could be the existence of π-acceptor CO ligands in the Re rectangle.

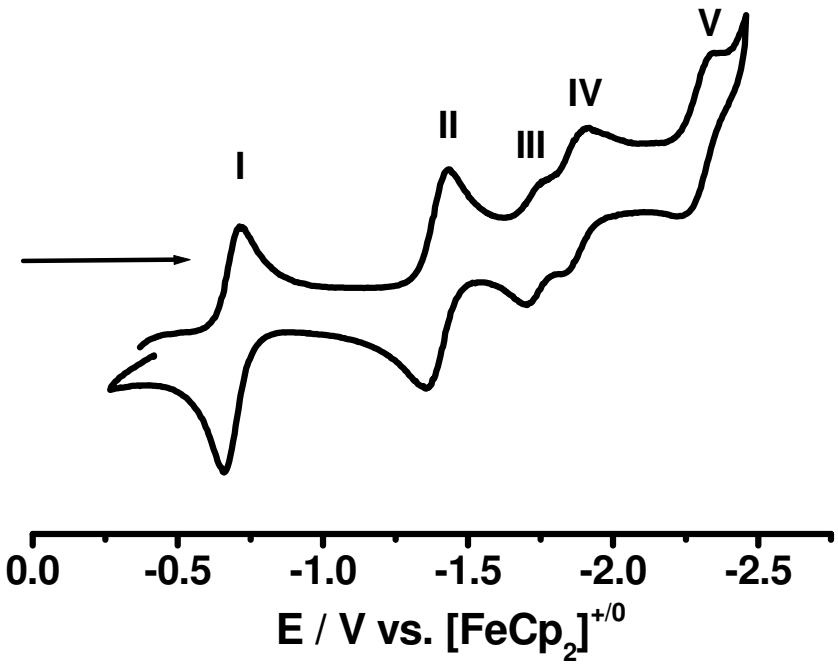

Fig. 7.9: *Cyclic voltammogram of $[\{Pt(CH_3)_3\}_4(\mu\text{–bp})_2(\mu\text{–bpym})_2](OTf)_4$ in CH_3CN / 0.1 M Bu_4NPF_6 at RT with a scan rate of 100 mV/sec*

The bpym ligand-based reduction of $[\{Pt(CH_3)_3\}_4(\mu\text{–bp})_2(\mu\text{–bpym})_2](OTf)_4$ by initial two electron addition is also supported by EPR spectroscopy. An unresolved signal at g_{iso}= 1.990, i.e. close to the free $bpym^{\bullet-}$ value of g_{iso}= 2.0030, was observed in the EPR spectrum of the electrochemically generated $Pt(CH_3)_3\}_4(\mu\text{–bp})_2(\mu\text{–bpym})_2]^{2+}$ at room temperature. In the glassy frozen state, it exhibits a relatively small g anisotropy ($\Delta g = g_1\text{-}g_3$) of 0.0516, indicating that the spin is mainly on bridging ligands, ($bpym^{\bullet-}$) which do not seem to show strong spin-spin interaction across the rectangle (Fig. 7.10).

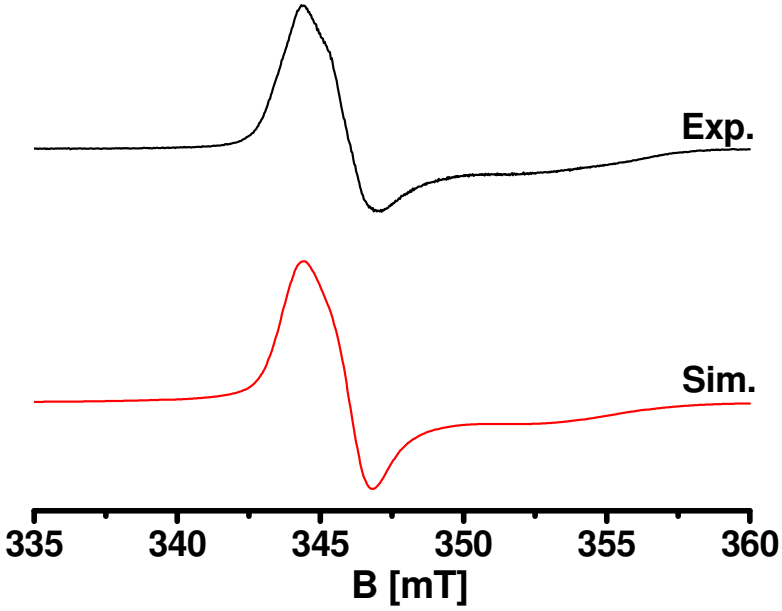

Fig. 7.10**:** *X-band EPR spectrum of of $Pt(CH_3)_3\}_4(\mu\text{–}bp)_2(\mu\text{–}bpym)_2]^{2+}$ obtained by in situ electrolysis at 110 K in CH_3CN / 0.1 M Bu_4NPF_6 (top) with computer simulation (bottom), g_x=2.0106, g_y= 2.000, g_z=1.959; linewidth (in G) X=12, Y=15.3, Z=45*

In chapter 5, the result of the reaction between $[Pt(CH_3)_3(bpy)](OTf)$ and the TCNX ligands (TCNX: TCNB, 1,2,4,5-tetracyanobenzene; TCNE, tetracyanoethene; and TCNQ, 7,7,8,8-tetracyano-*p*-quinodimethane) are presented and supported by analytical analyses and cyclic voltammetry techniques.

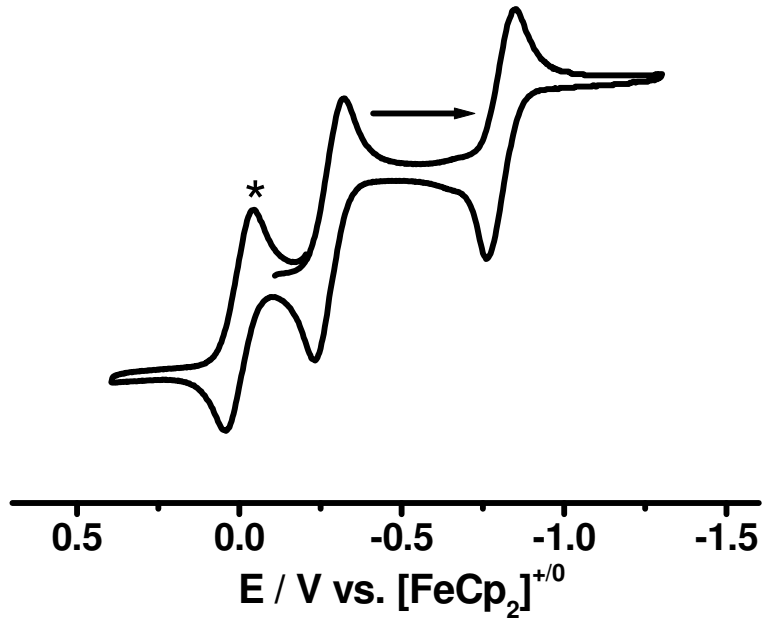

Fig. 7.11: *Cyclic voltammogram of $[\{Pt(CH_3)_3(bpy)\}_4TCNQ](OTf)_4$ in CH_2Cl_2 / 0.1 M Bu_4NPF_6 at -60 ^{0}C with a scan rate of 100 mV/sec (* = ferrocene wave)*

No complexation was observed from the reaction of $[Pt(CH_3)_3(bpy)](OTf)$ with TCNB, whereas the reaction with TCNE resulted in a mixture of products which could not be separated. The reaction between TCNQ and $[Pt(CH_3)_3(bpy)](OTf)$ is believed to lead to the formation of $[\{Pt(CH_3)_3(bpy)\}_4TCNQ](OTf)_4$, relying on the data obtained from elemental analysis and ^{1}H-NMR spectroscopy. However, the fairly small shifts of the proton signals in the ^{1}H-NMR-spectrum with respect to the starting $[Pt(CH_3)_3(bpy)](OTf)$ compound, the similar CN stretching frequency (at 2226 cm^{-1}) to that of free TCNQ (2223 cm^{-1}), the absence of an MLCT band in the visible-NIR spectrum and the slight shift of the reduction potential to less negative values in the cyclic voltammetry (Fig. 7.11) suggest that almost no π-interaction occurs between the TCNQ ligand and the Pt^{IV} metal centers.

CHAPTER 8

Zusammenfassung

In dieser Arbeit wird eine Reihe von ein- und zweikernigen Trimethylplatin(IV)halogen Komplexen mit einigen π-Akzeptor-α-Diimin-Liganden vorgestellt. Das elektrochemische sowie spektroskopische Verhalten dieser Komplexe wird von den Eigenschaften der Liganden beeinflusst. Abb. 8.1 zeigt die in dieser Arbeit verwendeten Liganden.

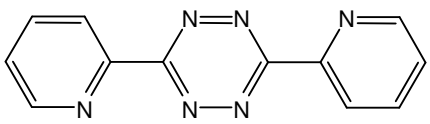

3,6-bis(2-pyridyl)-1,2,4,5-tetrazin (bptz)

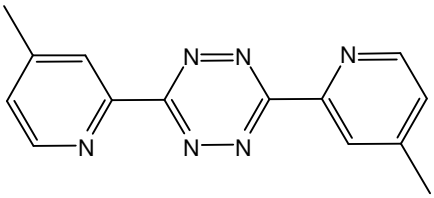

3,6-bis(2-(4-methylpyridyl))-1,2,4,5-tetrazin (bmptz)

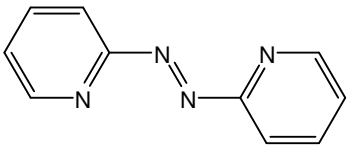

2,2'-azobispyridin (abpy)

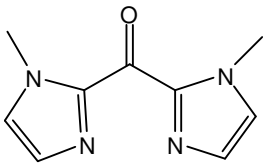

bis-(1-methylimidazol-2-yl)keton (bik)

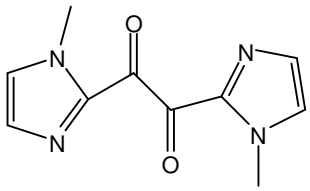

bis(1-methylimidazol-2-yl)glyoxal (big)

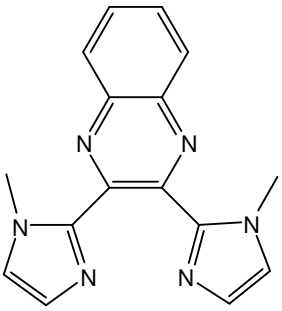

2,3-bis(1-methylimidazol-2-yl)chinoxalin (bmiq)

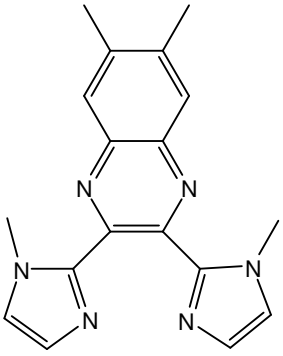

2,3-bis(1-methylimidazol-2-yl)-7,8-dimethylchinoxalin (dibmiq)

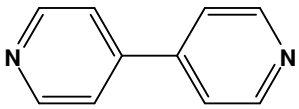

4,4' bipyridin (bp)

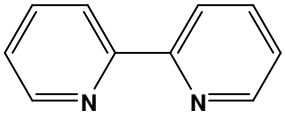

2,2'- bipyridin (bpy)

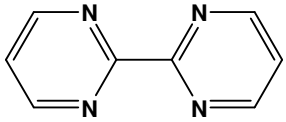

2,2'-bipyrimidin (bpym)

Abb. 8.1: *In dieser Arbeit verwendete Liganden*

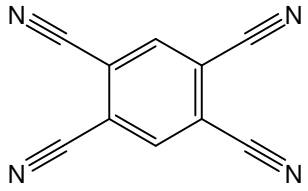

1,2,4,5-tetracyanobenzol (TCNB)

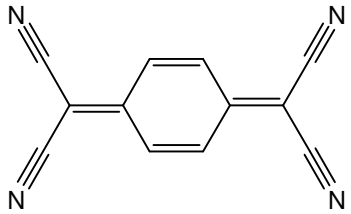

7,7,8,8-tetracyano-p-chinodimethan (TCNQ)

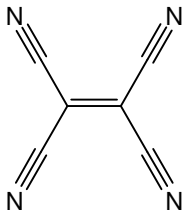

tetracyanoethen (TCNE)

Abb. 8.2: *TCNX Liganden*

Im zweiten Kapitel werden die Synthesen sowie strukturelle Eigenschaften und das elektrochemische Verhalten von neuen Komplexen aus Tetrazin-π-Akzeptor-Liganden wie bptz und bmptz und $[PtMe_3X]_4$ (X: Cl, Br, I) besprochen. Zusätzlich wird das spektroskopische und elektrochemische Verhalten von bereits bekanntem $Pt(abpy)Me_3Br$[41] mit dem von $Re(CO)_3X(abpy)$[42] (X: Cl, Br, I) verglichen.

Sieben Komplexe konnten röntgenkristallographisch aufgeklärt werden, die Daten von *fac*-$Pt(CH_3)_3Cl(bptz)$ und *fac*-$Pt(CH_3)_3Br(bptz)$ wurden mit DFT berechnet und diskutiert. Diese Komplexe zeigen eine oktaedrische Konfiguration am Platin(IV) Zentrum sowie eine *fac* Anordnung der Methyl Gruppen. Die zweikernigen Komplexe kristallisieren in der *anti*-Form, wie in Abb. 8.3 gezeigt.

Die Pt-$CH_{3(ax)}$ Bindungen in den einkernigen bptz Komplexen sind bedeutend länger als die Pt-$CH_{3(eq)}$ Bindungen, was auf den unterschiedlichen *trans*-Einfluss zurückzuführen ist. Außerdem wird erwartet, dass ein möglicher SBLCT-Übergang die axialen Methyl-Platin-Bindungen verlängert. Dieser Effekt ist allerdings für *fac*-$Pt(CH_3)_3I(bmptz)$ sowie die zweikernigen bmptz-Komplexe weniger ausgeprägt. Die Koordination der Metallkomplexfragmente bewirkt eine Planarisierung der Brückenliganden.

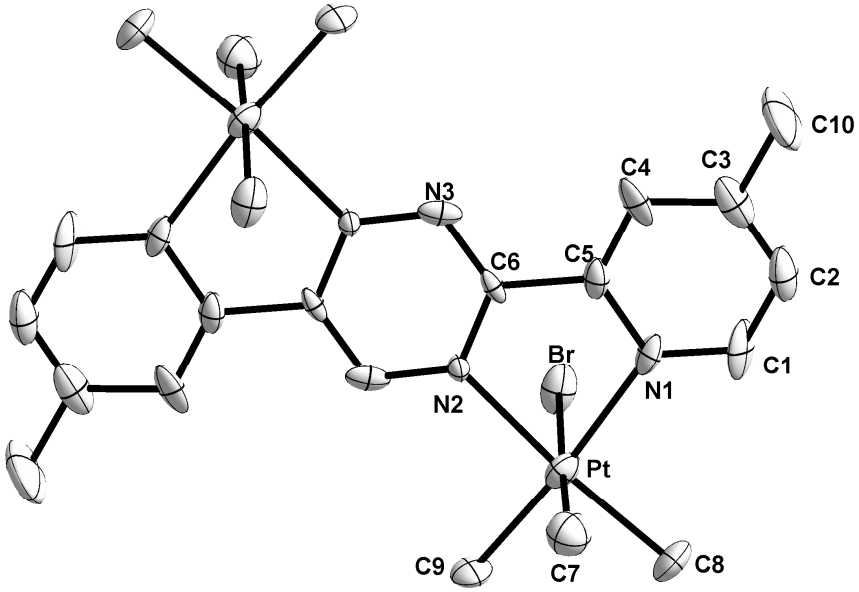

Abb. 8.3: *Molekülstruktur von anti-[(μ-bmptz){fac-PtBrMe$_3$}$_2$]*

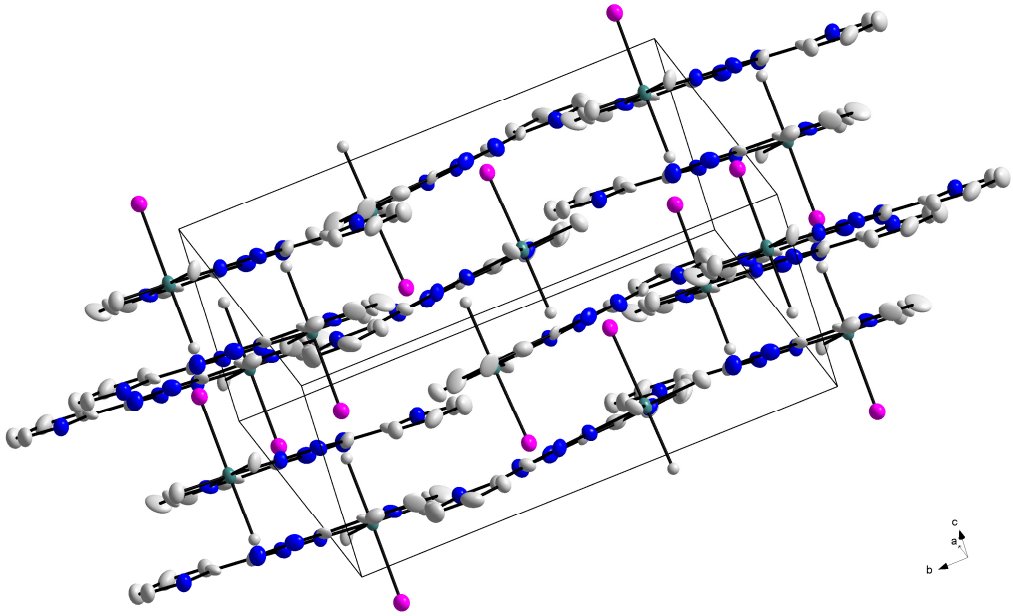

Abb. 8.4: *Anordnung von fac-*Pt(CH$_3$)$_3$I(bptz) *Molekülen im Kristall*

Nur einkerniges *fac*-Pt(CH$_3$)$_3$Cl(bptz) und zweikernige Komplexe *anti*-[(μ-bmptz){*fac*-PtXMe$_3$}$_2$] (X: Cl, Br, I) weisen bei Raumtemperatur eine reversible Reduktion im Cyclovoltammogramm auf. Zudem bewirkt ein Austausch der Halogene vom Cl$^-$ gegen I$^-$ im zweikernigen bmptz-Komplex von [PtMe$_3$X] eine Verschiebung der ersten reversiblen wie auch der zweiten irreversiblen Reduktion zu weniger negativen Potentialen.

UV-Vis Spektroelektrochemie von *fac*-Pt$(CH_3)_3$Cl(bptz) und allen drei zweikernigen *anti*-[(μ-bmptz){*fac*-PtXMe_3}$_2$] Verbindungen zeigen für den Einelektronenreduktionsprozess isosbestische Punkte, was auf die Homogenität der untersuchten Reaktionen hinweist. Die Banden im sichtbaren Bereich sind teilweise strukturiert und können MLCT- und SBLCT-Übergängen zugeordnet werden.

Das elektrochemisch generierte Radikal-Anion *anti*-[(μ-bmptz){*fac*-PtBrMe_3}$_2$]$^{\bullet-}$ wurde mit ESR-Spektroskopie untersucht (Abb. 8.5). Der g Faktor von 2.0053, nahe dem eines freien Elektrons, ist ein Indiz für eine fast vollständige Lokalisierung des Spins auf dem Tetrazin-Ring. Die TD-DFT Berechnungen für *fac*-Pt$(CH_3)_3$Br(bptz) bestärken die Akzeptanz des Elektrons vorwiegend durch den Tetrazin-Ring.

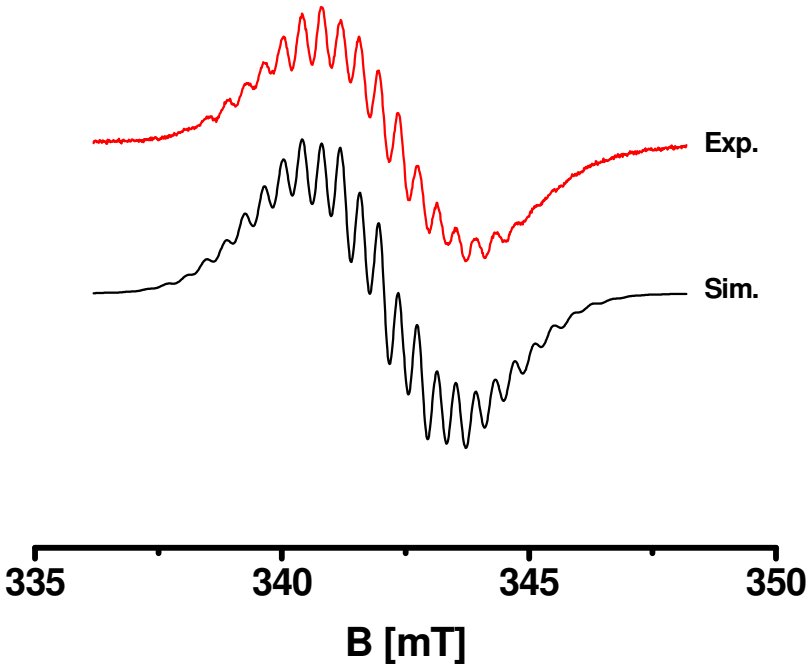

Abb. 8.5: *EPR-Spektrum, erhalten durch in situ-Elektrolyse des anti-[(μ-bmptz){fac-PtBrMe_3}$_2$]$^{\bullet-}$ in CH_2Cl_2/0.1 M Bu_4NPF_6 bei RT (oben) mit Computersimulation (unten; 0.35 mT Linienbreite)*

Die schwache Charge-Transfer Bande im sichtbaren Bereich des Absorptions-Spektrums, die kleine Verschiebung des Reduktionspotentials im Vergleich zum freien Liganden (Abb. 8.6) und die geringe g-Anisotropie im ESR Spektrum von Pt(abpy)$Me_3Br^{\bullet-}$ weisen darauf hin, dass nur geringfügige π-Wechselwirkungen zwischen dem Platin(IV) Fragment und dem starken π Akzeptor abpy in diesem

Komplex vorhanden sind. Die kurze N=N Bindung dieses Komplexes von 1.26 Å[28] bekräftigt diese Aussage.

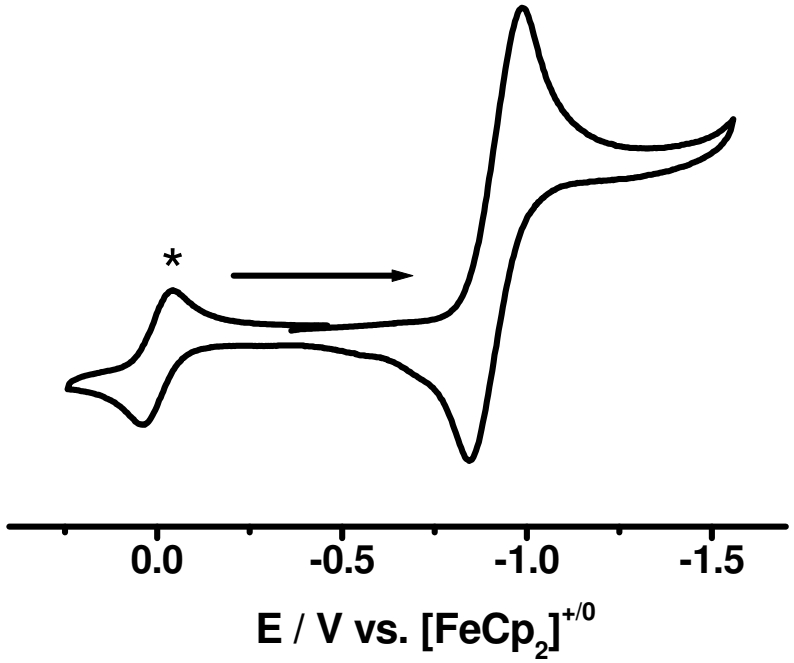

Abb. 8.6: *Cyclovoltammogramm von Pt(abpy)Me_3Br in CH_2Cl_2 / 0.1 M Bu_4NPF_6 bei 248 K (v = 100 mV/s, * = Ferrocen-Welle)*

Kapitel 3 handelt von den strukturellen, spektroskopischen und elektrochemischen Untersuchungen der ersten Organoplatin(IV) Komplexe mit den Liganden big und bik, *fac*-$Pt(CH_3)_3I$(big) und *fac*-$Pt(CH_3)_3I$(bik). Außerdem werden die Reaktionsprodukte von $[PtMe_3I]_4$ mit zwei neu synthetisierten Liganden 2,3-Bis(1-methylimidazol-2-yl)chinoxalin (bmiq) und 2,3-Bis(1-methylimidazol-2-yl)-7,8-dimethylchinoxalin (dibmiq) besprochen.

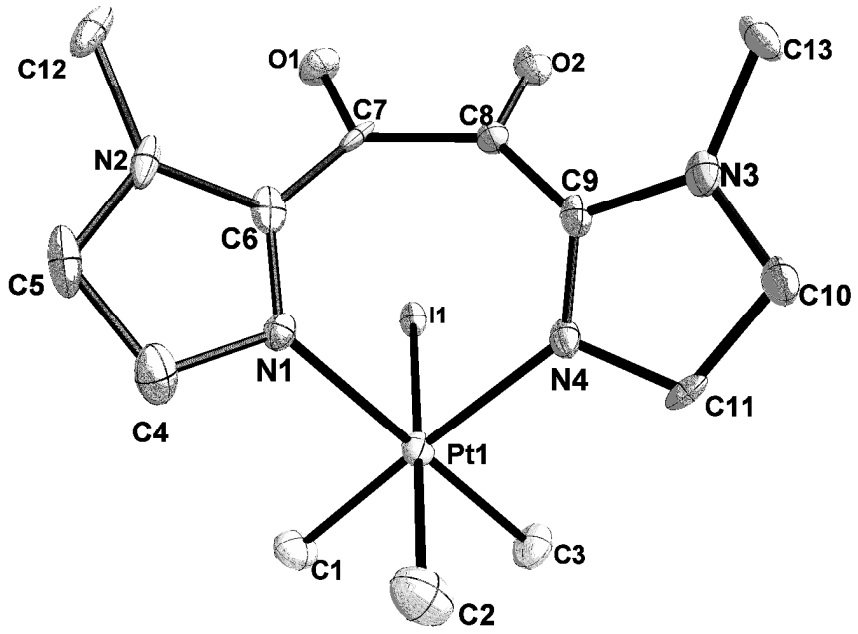

Abb. 8.7: *Molekülstruktur von fac-Pt(CH$_3$)$_3$I(big) (eines von vier kristallographisch unabhängigen Molekülen)*

Die spektroskopischen Untersuchungen von *fac*-Pt(CH$_3$)$_3$I(big) und *fac*-Pt(CH$_3$)$_3$I(bik) zeigen ausschließlich die Existenz einkerniger Komplexe, die ^{1}H-NMR Spektroskopie hingegen verifiziert die Bildung einkerniger wie auch zweikerniger Verbindungen im Produktgemisch der Reaktion zwischen bmiq oder dibmiq mit [PtMe$_3$I]$_4$.

Die Daten der röntgenkristallographischen Untersuchungen wurden durch DFT Berechnungen bestätigt. In beiden Komplexen hat das Pt^{IV} wie erwartet eine oktaedrische Umgebung.

Beide Komplexe können nur bei tiefen Temperaturen reversibel reduziert werden, *fac*-Pt(CH$_3$)$_3$I(big) bei -30°C und *fac*-Pt(CH$_3$)$_3$I(bik) bei -80°C. Der reversible Charakter der ersten Reduktionswelle bei tiefen Temperaturen hat den Versuch angeregt, eine spektroelektrochemische Untersuchung bei tiefen Temperaturen durchzuführen. Nur *fac*-Pt(CH$_3$)$_3$I(big) zeigt Reversibilität in der IR-Spektroelektrochemie. Die Verschiebung der CO Streckschwingung zu kleineren Wellenzahlen (1673 cm^{-1} → 1533 cm^{-1}) weist auf eine Lokalisierung des hinzugefügten Elektrons auf dem α-Diketo-Teil des Liganden hin, woraus sich die Bildung einer α-Semidion-Verbindung ergibt (Abb.8.8). Dieses Ergebnis wird von

Rechnungen belegt, welche zeigen, dass das SOMO von *fac*-$Pt(CH_3)_3I(big)^{\bullet-}$ vor allem aus dem α-Diketo Teil des Liganden mit C-C-Bindungscharakter sowie C=O-Antibindungscharakter besteht. Der g-Faktor von 2.0061 aus dem ESR-Spektrum der elektrochemisch generierten *fac*-$Pt(CH_3)_3I(big)^{\bullet-}$ Ions ist auch ein starker Beleg für eine ligandenzentrierte Reduktion.

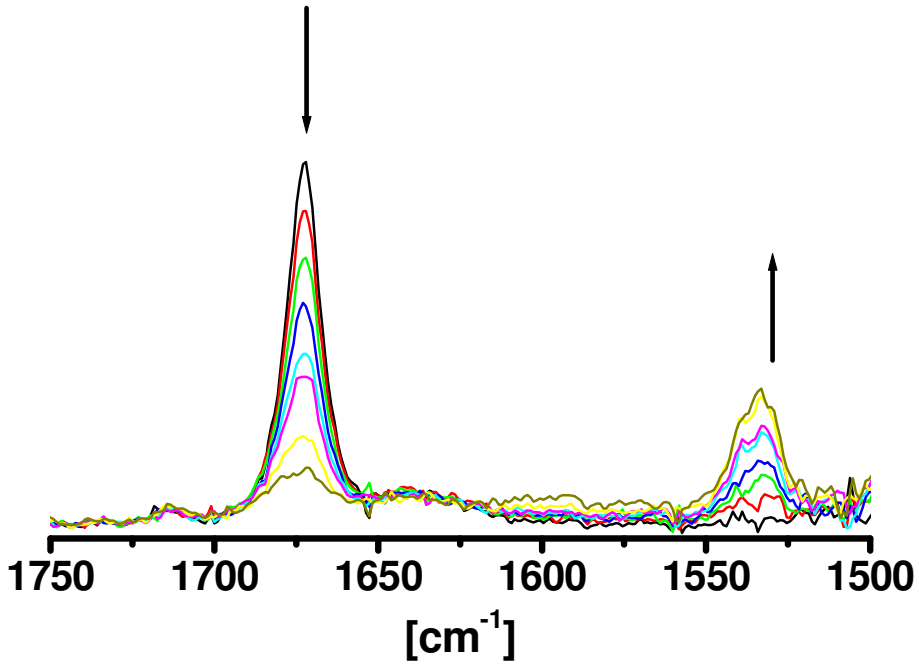

Abb. 8.8: *IR-Spektroelectrochemische Reduktion von fac*-$Pt(CH_3)_3I(big)$ *bei -60 ^{0}C in n-Butyronitril / 0.1 M Bu_4NPF_6*

Im Kapitel 4 werden die Charakterisierung sowie die elektrochemischen und spektroelektrochemischen Eigenschaften der ersten Rechteck-Organoplatin(IV) Verbindung, $[\{Pt(CH_3)_3\}_4(\mu\text{–bp})_2(\mu\text{–bpym})_2](OTf)_4$ (bp = 4,4´-Bipyridin, bpym = 2,2´-Bipyrimidin, OTf = CF_3SO_3) diskutiert. Molekulare Rechteckverbindungen gelten als charakteristische supramolekulare Verbindungen und werden wegen ihrer potentiellen Elektronenspeicher-Kapazitäten als interessant angesehen.

^{1}H- and ^{195}Pt-NMR, die CHN-Analyse und massenspektroskopische Untersuchungen bestätigen die Bildung des gewünschten Rechteck-Komplexes. Cyclovoltammetrische und UV-Vis-spektroelektrochemische Messungen bekräftigen die Vorstellung einer simultanen Lokalisierung der ersten beiden Elektronen der Reduktion, wie auch der nächsten beiden Elektronen, auf dem bpym-Liganden, hingegen sind die folgenden Einelektronenreduktionen auf dem bp-Liganden lokalisiert. Indes zersetzt sich der Komplex nach dem fünften und sechsten Elektron

langsam, wie in einer kombinierten 2 Elektronenreduktion in der OTTLE-Spektroelektrochemie, Adsorption/Desorption der neutralen Zwischenprodukte beinhaltend, beobachtet wurde. Das vorher vorgestellte $[Re_4(CO)_{12}(\mu\text{-bpy})_2(\mu\text{-bpym})_2]$[43] fungiert als ein effizienteres Elektronenreservoir, da es mit bis zu sieben Elektronen reversibel reduziert werden kann. Eine mögliche Erklärung für diesen Unterschied könnte die Existenz von CO-π-Akzeptoren in der rechtecksförmigen Re-Verbindung liefern.

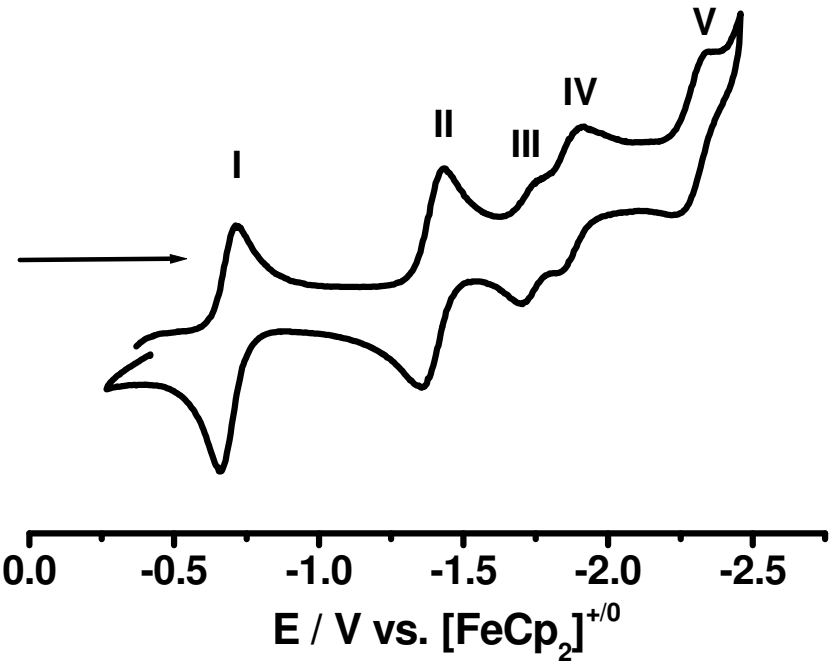

Abb. 8.9: *Cyclovoltammogramm des $[\{Pt(CH_3)_3\}_4(\mu\text{–}bp)_2(\mu\text{–}bpym)_2](OTf)_4$ in CH_3CN / 0.1 M Bu_4NPF_6 bei RT mit einer Vorschubgeschwindigkeit von 100 mV/sec*

Die bpym-Ligand-zentrierte Reduktion mit anfänglich zwei Elektronen von $[\{Pt(CH_3)_3\}_4(\mu\text{–}bp)_2(\mu\text{–}bpym)_2](OTf)_4$ wird auch vom ESR-Experiment bekräftigt. Bei Raumtemperatur wurde in einer ESR-Messung des elektrochemisch generierten $Pt(CH_3)_3\}_4(\mu\text{–}bp)_2(\mu\text{–}bpym)_2]^{2+}$ ein schlecht aufgelöstes Signal bei g_{iso}= 1.990, also im Bereich des freien $bpym^{\bullet-}$ -Radikals mit g_{iso}= 2.0030, beobachtet. Im gefrorenen Zustand weist diese Verbindung eine relativ kleine g-Anisotropie ($\Delta g = g_1\text{-}g_3$) von 0.0516 auf, was darauf hinweist, dass der Spin sich hauptsächlich auf dem Brückenligand befindet ($bpym^{\bullet-}$) und dem Anschein nach keine starken Spin-Spin Wechselwirkungen über das Rechteck hinweg zeigt (Abb.8.10).

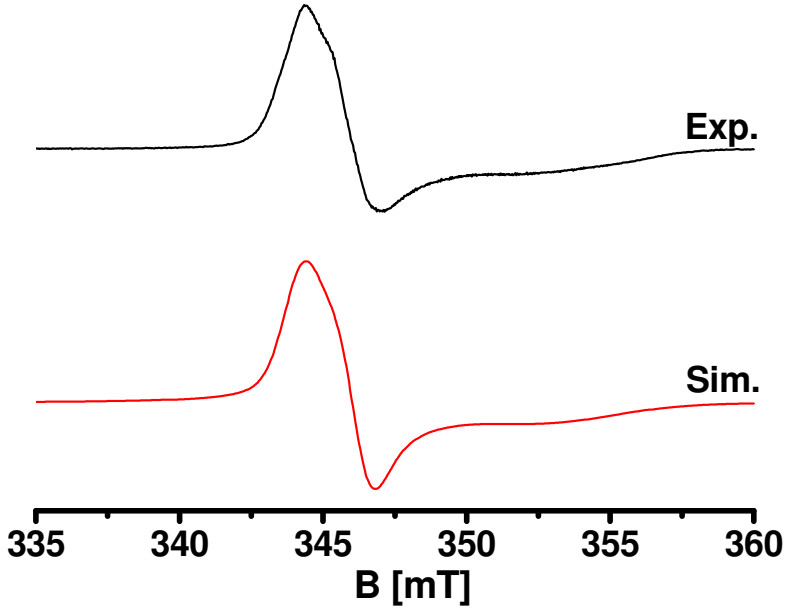

Abb.8.10: *X-Band-ESR-Spektrum erhalten durch in situ Reduktion des $Pt(CH_3)_3\}_4(\mu\text{–}bp)_2(\mu\text{–}bpym)_2]^{2+}$ in CH_3CN/0.1 M Bu_4NPF_6 bei 110 K (oben) mit Computersimulation (unten), g_x=2.0106, g_y= 2.000, g_z=1.959; Linienbreite (in G) X=12, Y=15.3, Z=45*

Im Kapitel 5 werden die Ergebnisse der Reaktion von $[Pt(CH_3)_3(bpy)](OTf)$ mit TCNX-Liganden (TCNX: TCNB, 1,2,4,5-Tetracyanobenzol; TCNE, Tetracyanoethen und TCNQ, 7,7,8,8-Tetracyano-*p*-chinodimethan) vorgestellt und mit verschiednen Analysemethoden sowie auch mit Cyclvoltammetrie bekräftigt.

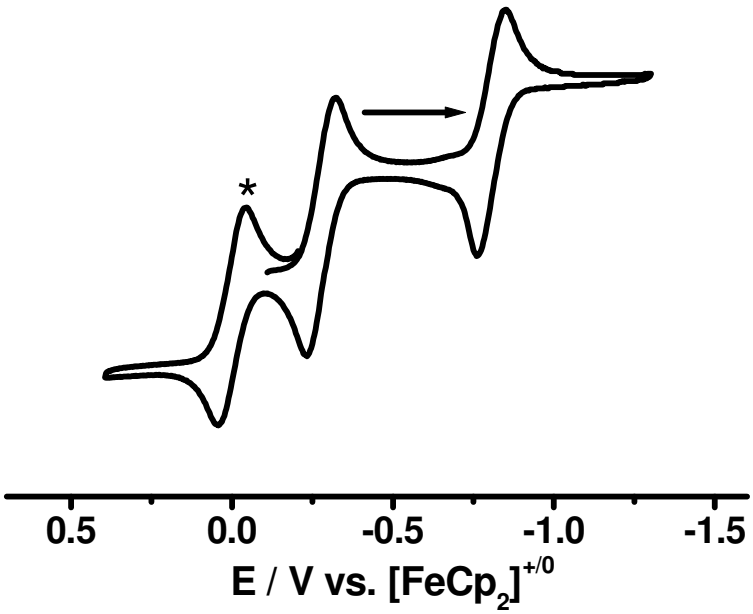

Abb.8.11: *Cyclovoltammogramm des $[\{Pt(CH_3)_3(bpy)\}_4TCNQ](OTf)_4$ in CH_2Cl_2 / 0.1 M Bu_4NPF_6 bei -60 ^{0}C mit einer Vorschubgeschwindigkeit von 100 mV/sec (* = Ferrocen-Welle)*

In der Reaktion von [Pt(CH_3)$_3$(bpy)](OTf) und TCNB wurde keine Komplexierung beobachtet, in der Reaktion mit TCNE hingegen wurde ein nicht trennbares Gemisch erhalten. Auf die Ergebnisse der ^{1}H-NMR Spektroskopie und der Elementaranalyse gestützt wird vermutet, dass aus Reaktion von [Pt(CH_3)$_3$(bpy)](OTf) und TCNQ ein [{Pt(CH_3)$_3$(bp)}$_4$TCNQ](OTf)$_4$-Komplex entsteht. Die ziemlich kleinen Verschiebungen der Protonen-Signale im ^{1}H-NMR-Spektrum im Vergleich zum Edukt [Pt(CH_3)$_3$(bpy)](OTf), die gleiche CN-Streckschwingung bei 2226 cm^{-1} im Vergleich zum freien TCNQ-Ligand (2223 cm^{-1}), die fehlende MLCT-Bande im NIR Spektrum, wie auch die geringe Verschiebung des Reduktionspotentials zu weniger negativen Werten in der Cyclovoltammetrie (Abb. 8.11) suggerieren, dass fast keine π-Wechselwirkungen zwischen dem TCNQ-Liganden und dem Pt^{IV}-Zentrum auftreten.

Appendix

Bibliography

[1] Swaddle, T.W.; *Applied Inorganic Chemistry*, University of Calgary Press, Calgary, **1992**.

[2] Zeise,W.C. Mag.Pharm. **1830**, *35*, 105.

[3] Werner, A. *Zeitschr.Anorg.Chem.*, **1893**, *3*, 267-330.

[4] Lagowski, J.J., Ed. *Chemistry Foundations and Applications*, **3**, Thomson Gale, **2004**, 267–268.

[5] Hartley, F.R. *The Chemistry of Platinum and Palladium*, Applied Science Publishers LTD London, **1973**, 5.

[6] Lide, D. R. *CRC Handbook of Chemistry and Physics*. **4**. New York, CRC Press, 2007-2008, 26.

[7] Kauffman, G.B. *Inorganic Syntheses*, **1967**, *9*, 182–185.

[8] Jain,V.K.; Rao, G.S.; Jain, L. *The organic Chemistry of Platinum(IV)*, *Adv. In Organometallic Chem.* **1987**, *27*, 113.

[9] Peilert, M.; Weissbach, S.; Freisinger, E.; Korsunsky, V.I.; Lippert, B. *Inorg. Chim. Acta***, 1997,** *265*, 187-195.

[10] McDonald, D.;Hunt, L.B. *A History of Platinum and its Allied Metals*, Johnson Matthey, **1982**.

[11] George, M. W. *Mineral Yearbook 2006: Platinum-Group Metals*. United States Geological Survey, **2007**.

[12] Buchanan, D.L. *Platinum-Group Element Exploration*, Elsevier, **1988.**

[13] Hartley, F.R. *The Chemistry of the Platinum Group Metals, Recent Developments*, Elsevier, **1991**.

[14] Rosenberg, B.; Van Camp, L.; Krigas, T. *Nature*, **1965**, *205*, 698.

[15] Rosenberg, B.; Van Camp, L.; Trosko, J. E.; Mansour, V. H. *Nature*, **1969**, *222*, 385.

[16] Garrido-Suarez,C.; Braichotte, D.; Van den Bergh, H. *Appl. Phys. A*, **1988**, *46,4,* 285-290.

[17] Viguie, J.C.; Spitz, J. *J. Electrochem. Soc*. **1975**, *122, 4*, 585-589.

[18] Periana, R. A.; Taube, D. J.; Gamble, S.; Taube, H.; Satoh, T.; Fujii,H. *Science,* **1998**, *280*, 560.

[19] (a) Goldberg, K.I.; Goldman, A.S. *Activation and Functionalization of C-H Bonds; Am. Chem. Soc*. Washington, DC, **2004**. (b) Lersch, M.; Tilset, M. *Chem. Rev*. **2005**, *105*, 2471. (c) Labinger, J.A.; Bercaw, J.E. *Nature (London)* 2002, *417*, 507.

[20] (a) Puddephatt, R.J. *Angew. Chem. Int. Ed*. **2002**, *41*, 261. (b) Roy, S.; Puddephatt, R.J.; Scott, J.D. *J. Chem. Soc., Dalton Trans*. **1989**, 2121. (c) Brown, M.P.; Puddephatt, R.J.; Upton, C.E.E. *J Chem. Soc. Dalton Trans*. **1974**, 2457.

[21] Zhao, S.-B.; Wang, R.-Y. ; Wang, S. *Organometallics*, **2009**, *28*, 2572-2582.

[22] (a) Fekl, U.; Kaminsky, W.; Goldberg, K.I. *J. Am. Chem. Soc*. **2003**, *125*, 15286. (b) Fekl, U.; Goldberg, K.I. *J. Am. Chem. Soc*. **2002**, *124*, 6804.

[23] (a) Luedtke, A.T.; Goldberg, K.I. *Inorg. Chem*. **2007**, *46*, 8496. (b) Kloek, S.M.; Goldberg, K.I.; *J. Am. Chem. Soc*. **2007**, *129*, 3460. (c) Fekl, U.; Kaminsky, W.; Goldberg, K.I. *J. Am. Chem. Soc*. **2001**, *123*, 6423.

[24] Reinartz, S.; White, P.S.; Brookhart, M.; Templeton, J.L. *J. Am. Chem. Soc*. **2001**, *123*, 6425.

[25] Pendyala, L.; Cowens, J.W.; Madajewkz, S.; Creanen, P.J. in: Hacker, M.P.; Douple, E.P.; Krako, I.H. (Eds.), *Platinum Coordination Complexes in Cancer Chemotherapy: Clinical Pharmacokinetics of cis-dichloro-trans-dihydroxy-bis(isopropylamine)platinum(IV)*, Nijho. (Martinus), Boston, **1984**, p. 114.

[26] Judson, I.; Mckeage, M.; Hanwell, J.; Berry, C.; Mistry, P.; Raymand, F.; Poon, G.; Murrer, B.; Harrap, K. in: *Platinum and Other Metal Coordination Complexes in Cancer Chemotherapy: The Clinical Development of the Oral Platinum Anticancer Agent JM216*, H.M. Press, New York, **1996**, p. 83.

[27] Shamsuddin, S.; Santillan, C.C.; Stark, J.L.; Whitmire, K.H.; Siddik, Z.H.; Khokhar, A.R. *Jour. Inorg. Biochem*. **1998**, *71*, 29-35.

[28] Dogan, A.; Kavakli, C.; Sieger, M.; Niemeyer, M.; Sarkar, B.; Kaim, W. *Z. Anorg. Chem*. **2008**, *634*, 2527-2531.

[29] (a) Kaim, W.; Olbrich-Deussner, B.;Gross, R.; Ernst, S.; Kohlmann, S.; Bessenbacher, C. *in Importance of Paramagnetic Organometallic Species in Activation, Selectivity and Catalysis*, Ed. M. Chanon, Kluwer Academic Publishers (Dordrecht), **1989**, p 283. (b) Kaim, W.; *Top. Curr. Chem*. **1994**, *169*, 231.

[30] (a) Kaim, W.; Kohlmann, S. *Inorg. Chem*. **1990**, *29*, 2909. (b) Sarkar, B.; Kaim, W.; Schleid, T.; Hartenbach, I.; Fiedler, J. *Z. Anorg. Allg. Chemie*, **2003**, *629*, 1353. (c) Hartmann, H.; Scheiring, T.; Fiedler, J.; Kaim, W. *J. Organomet. Chem*. **2000,** *604*, 267.

[31] (a) Schanze, K.S.; MacQueen, D.B.; Perkins, T.A.; Cabana, L.A.; *Coord. Chem. Rev.* **1993**, *122*, 63. (b) Wei L.; Babich, J.W.; Ouellette, W.; Zubieta, *J. Inorg. Chem.* **2006**, *45*, 3057.

[32] Kaim, W.; Klein, A.; Hasenzahl, S.; Stoll, H.; Zalis, S.; Fiedler, *J. Organometallics*, **1998**, *17*, 237.

[33] Kavakli, C.; Gabrielsson, A.; Sieger, M.; Schwederski, B.; Niemeyer, M.; Kaim, W.; *J. Organometallic Chem*. **2007**, *692*, 3151-3155.

[34] (a) Hasenzahl, S.; Kaim, W.; Stahl, T.; *Inorg. Chim Acta* **1994**, *225*, 23.

[35] Kaim, W.; *Acc. Chem. Res*. **1985**, *18*, 160. (b) Kaim, W.; *in Electron and Proton Transfer in Chemistry and Biology*, Müller, A.; Diemann, E.; Junge, W.; Ratajycak (Eds), H. Elsevier, Amsterdam, **1992**, p 45.

[36] Procelewska, J.; Zahl, A.; Liehr, G.; vanEldik, R.; Smythe, N.A.; Williams, B.S., Goldberg, K.I. *Inorg. Chem*. **2005**, *44*, 7732.

[37] Pope, W. J.; Peachy, S. J. *J. Chem. Soc.,* **1909**, *95*, 571

[38] Jain, V. K.; Rao, G. S.; Jain, L. *Adv. Organomet. Chem*., **1987**, *27*, 137.

[39] Donnay, G.; Coleman, L. B.; Krieghoff, N. G.; Cowan, D. O. *Acta Cystallogr.,* **1968**, *B24*, 157.

[40] Baldwin, J. C.; Kaska, W. C. *Inorg. Chem.* **1975**, *14 (8)*, 2020.

[41] Dogan, A. *Ph.D. Thesis*, Universität Stuttgart, **2004.**

[42] Frantz, S*. Ph.D. Thesis*, Universität Stuttgart, **2003.**

[43] Hartmann, H.; Berger, S.; Winter, R.; Fiedler, J.; Kaim, W. *Inorg. Chem*. **2000**, *39*, 4977, 4980.

[44] Kaim, W.; Kohlmann, S. *Inorg. Chem*. **1987**, *26*, 68-77.

[45] Kaim, W. Coord. *Chem. Rev*. **2002**, *230*, 127

[46] El-Qisairi, A. K. *Jour. of Coord*. *Chem.* **2007**, *60*, 1069-1076

[47] Sarkar, B.; Schurr, T.; Hartenbach, I.; Schleid, T.; Fiedler, J.; Kaim, W. *J. Organometallic Chem*. **2008**, *693*, 1703-1706

[48] Katritzky, A.R. *Handbook of Heterocyclic Chemistry*, Pergamon Press, New York, **1986**

[49] (a) Gleiter, R.; Schehlmann, V.; Spanget-Larsen, J.; Fischer, H.; Neugebauer, F.A. *J. Org. Chem*. *1988*, *53*, 5756. (b) Audebert, P.; Miomandre, F.; Clavier, G.; Verniéres, M.-C.; Badré, S.; Meallet-Renault, R. *Chem. Eur. J*. **2005**, *11*, 5667. (c)Janowska, I.; Miomandre, F. ; Clavier, G. ; Audebert, P. ; Zakrzewski, J.; thi, K.H.; Ledoux-rak, I. *J. Phys. Chem. A*, **2006,** *110,* 12971.

[50] (a) Kohlmann, S.; Ernst, S.; Kaim, W. *Angew. Chem. Int. Ed.* **1985**, *97*, 698 (b) Kohlmann, S.; Ernst, S.; Kaim, W. *Angew. Chem. Int. Ed. Engl*. **1985**, *24*, 684

[51] Kaim, W.; Ernst, S.; Kohlmann, S.; Welkerling, P*. Chem. Phys. Lett.* **1985,** *118,* 431.

[52] Sarkar, B. *Ph.D. Thesis*, Universität Stuttgart, **2005.**

[53] A. Hantzsch and M. Lehmann, *Ber. Dtsch. Chem. Ges*., **1900**, *33*, 3668.

[54] F. H. Case, *J. Heterocycl. Chem.* **1968**, *5*, 431

[55] *(a)* Kaim W.; Kohlmann, S. *Inorg. Chem.*, 1986, **25**, 3442.; *(b)* Schwach, M.; Hausen, H.-D.; Kaim, W. *Inorg. Chem.*, 1999, **38**, 2242.; *(c)* Glöckle, M.; Hübler, K.; Kümmerer, H.-J.; Denninger ,G. Kaim, W. *Inorg. Chem.*, 2001, **40,** 2263.

[56] Kaim, W. Coord. *Chem. Rev*. **2001**, *219-221*, 463

[57] Kirpal, A.; Reiter, L. *Ber. Dtsch. Chem. Ges*. **1927**, *60*, 664

[58] Baldwin, D.A.; Lever, A.B.P.; Parish, R.V. *Inorg. Chem*. **1969**, *8*, 107.

[59] Haim, A. *Prog. Inorg. Chem*. **1983**, *30*, 273.

[60] Kahn, O. *Molecular Magnetism*, New York, VCH, **1993**

[61] Kaim, W.; Klein, A.; Glöckle, M. Acc. Chem. Res. **2000**, *33*, 755.

[62] Von Dahlen. K.H.; Lorberth, J. *J. of Organometallic Chem*. **1974**, *65*, 267-273

[63] Clegg, D.E.; Hall, J.R. *Inorg. Syn*. **1967**, 10, 71

[64] (a) Hasenzahl, S.; Hausen H.-D.; Kaim, W. *Chem.Eur. J.* 1995, *1*, 95. (b) Bayler, A.; Canty, A. J.; Skelton, B. W.; White, A. H. *J. Organomet. Chem.* **2000**, *595*, 296. (c) Baar, C.R.; Carbray, P.; Jennings, M.C.; Puddephatt, R.J. *Organometallics*, **2000**, *19*, 2482

[65] Van Slageren, J.; Stufkens, D. J.; Zalis, S.; Klein, A. *J. Chem. Soc., Dalton Trans.,* **2002**, 218.

[66] Hux, J. E.;. Puddephatt, R J. *J. Organomet. Chem.,* **1992**, *437*, 251.

[67] Van Slageren, J.; Klein, A.; Zalis, S.; Stufkens D. J. *Coord. Chem. Rev.,* **2001**, *219-221*, 937

[68] Scheiring, T.; Fiedler J.; Kaim, W. *Organometallics*, 2001, **20**, 1437

[69] Dogan, A.; Sarkar, B.; Klein, A.; Lissner, F.; Schleid, T.; Fiedler, J.; Zalis, S.; Jain, V.K.; Kaim, W. *Inorg. Chem*. **2004**, *43*, 5973.

[70] Krejcik, M.; Danek, M.; Hartl, F. *J. Electroanal. Chem.* **1991**, *317*, 179.

[71] Heilmann, M.; Baumann, F.; Kaim, W.; Fiedler, J. *J. Chem. Soc., Faraday Trans.* **1996**, *92*, 4227

[72] (a) Stone, A. J. *Mol. Physc.*, **1964**, *7*, 311. (b) Fischer, H. in *Free Radicals, Vol. II;* Kochi, Ed., J. K. Wiley, New York, **1973**, p. 452. (c) Kaim, W. In *Electron Transfer in* Chemistry; Balzani, Ed., V. Wiley-VCH: Weinheim, **2001.**

[73] Geoffroy, M.; Bernardinelli, G.; Castan, P.; Chermette, H.; Deguenon, D.; Nour, S.; Weber, J.; Wermeille, M*. Inorg. Chem*. **1992**, *31*, 5056.

[74] Klein, A.; Hausen, H.-D.; Kaim, W. J. Organomet. Chem. 1992, 440, 207. (b) Klein, A.; Kaim, W. *Organometallics*, **1995,** *14,* 1176

[75] Kaim, W.; Dogan, A.; Wanner, M.; Klein, A.; Tiritiris, I.; Schleid, T.; Stufkens, D.J.; Snoeck, T.L.; Mcinnes, E.J.L.; Fiedler, J.; Zalis, S. *Inorg. Chem*. **2002,** *41*, 4139

[76] Weil, J.A.; Bolton, J.R.; Wertz, J.E. *Electron Paramagnetic Resonance*, Wiley, New York, **1994**

[77] Gaussian 03, Revision C.02, Frisch, M. J.; Trucks, G.; Schlegel, H. B.; Scuseria, G. E.; Robb, M. A.; Cheeseman, J. R.; Montgomery, J. A., Jr.; Vreven, T.; Kudin, K. N.; Burant, J. C.; Millam, J. M.; Iyengar, S. S.; Tomasi, J.; Barone, V.; Mennucci, B.; Cossi, M.; Scalmani, G.; Rega, N.; Petersson, G. A.; Nakatsuji, H.; Hada, M.; Ehara, M.; Toyota, K.; Fukuda, R.; Hasegawa, J.; Ishida, M.; Nakajima, T.; Honda, Y.; Kitao, O.; Nakai, H.; Klene, M.; Li, X.; Knox, J. E.; Hratchian, H. P.; Cross, J. B.; Bakken, V.; Adamo, C.; Jaramillo, J.; Gomperts, R.; Stratmann, R. E.; Yazyev, O.; Austin, A. J.; Cammi, R.; Pomelli, C.; Ochterski, J. W.; Ayala, P. Y.; Morokuma, K.; Voth, G. A.; Salvador, P.; Dannenberg, J. J.; Zakrzewski, V. G.; Dapprich, S.; Daniels, A. D.; Strain, M. C.; Farkas, O.; Malick, D. K.; Rabuck, A. D.; Raghavachari, K.; Foresman, J. B.; Ortiz, J. V.; Cui, Q.; Baboul, A. G.; Clifford, S.; Cioslowski, J.; Stefanov, B. B.; Liu, G.; Liashenko, A.; Piskorz, P.; Komaromi, I.; Martin, R. L.; Fox, D. J.; Keith, T.; Al-Laham, M. A.; Peng, C. Y.; Nanayakkara, A.; Challacombe, M.; Gill, P. M. W.;

Johnson, B.; Chen, W.; Wong, M. W.; Gonzalez, C.; Pople, J. A.,Gaussian, Inc., Wallingford CT, **2004**.

[78] (a) te Velde, G.; Bickelhaupt, F. M.; van Gisbergen, S. J. A.; Fonseca Guerra, C.; Baerends, E. J.; Snijders, J. G.; Ziegler, T.; *J. Comput. Chem.* **2001**, *22*, 931. (b) ADF2008.01, SCM, Theoretical Chemistry, Vrije Universiteit, Amsterdam, The Netherlands, http://www.scm.com.

[79] Perdew, J. P.; Burke, K.; Ernzerhof, M. *Phys. Rev. Lett.* **1996**, *77*, 3865

[80] Krishnan R., Binkley, J. S., Seeger, R., Pople, J. A. *J. Chem. Phys.* **1980**, 72, 650.

[81] Andrae, D.; Häussermann, U.; Dolg, M.; Stoll, H.; Preuss, H. *Theor. Chim. Acta* **1990**, *77*, 123.

[82] Becke, A. D. *Phys. Rev. A* **1988**, *38*, 3098.

[83] Perdew, J. P. *Phys. Rev. B* **1986**, *33*, 8822.

[84] Bulak, E.; Sarper, O.; Dogan, A.; Lissner, F.; Schleid T.; Kaim, W. *Polyhedron*, **2006**, *25*, 2577.

[85] (a) Bertini, I.; Sigel, H., Eds. *Handbook on Metalloproteins,* Marcel Dekker, New York, **2001**; (b) Messerschmidt, A. *Handbook of Metalloproteins*, Wiley, New York, **2004**; (c) Kaim, W.; Schwederski, B. *Bioinorganic Chemistry,* Wiley, Chichester, U.K., **1994.**

[86] (a) So´va´go´, I.; Va´rnagy, K.; Osz, K., *Comments Inorg. Chem.*, **2002**, 23, 149; (b) S. Abuskhuna, M.; McCann, J.; Briody, M.; Devereux, V.; McKee, *Polyhedron* , **2004**, 23 1731; (c) Ruether, T.; Cavell, K.J.; Braussaud, N.C.; Skelton, B.W.; White, A.H., *J. Chem. Soc., Dalton Trans.*, **2002**, 4684; (d) Bhalla, R.; Helliwell, M. R.L.; Beddoes, D.; Collison, C.D.; Garner, *Inorg. Chim. Acta,* **1998**, 273, 225.

[87] (a) Gorun, S.M.; Papaefthymiou, G.C.; Frankel, R.B.; Lippard, S.J.; *J.Am. Chem. Soc*., **1987**, *109*, 4244; (b) Gorun, S.M.; Lippard, S.J.; *Inorg. Chem.,* **1988**, *27*, 149; (c) See also Tolman, W.B.; Bino, A.; Lippard, S.J., *J. Am. Chem. Soc*., **1989,** *111,* 8522; (d) Bloemink, M.J.; Engelking, H.; Karentzopoulos, S.; Krebs, B.; Reedijk, J., *Inorg. Chem*., **1996,** *35,* 619.

[88] Kumar, A.; Galaev, I.Yu.; Mattiasson, B., *Bioseperation*, **1998,** *7*, 185.

[89] (a) Byers, P. K.; Canty, A. J.; Engelhardt, L. M.; Patrick, J. M.; White, A. H., *J. Chem. Soc., Dalton Trans*. **1985**, 981. (b) Chen, X.-M.; Xu, Z.-T.; Mak, T. C. W., *Polyhedron* **1995**, *35*, 1295. (c) Grehl, M.; Krebs, B., *Inorg. Chem.* **1994**, *33*, 3877. (d) Reusmann,G.; Grehl, M.; Reckordt, W.; Krebs, B., *Z. Anorg. Allg. Chem.* **1994**, *620*, 199.

[90] Fournari, P.; de Cointet, P.; Laviron, E., *Bull. Soc. Chim. Fr.*, **1968**, *6*, 2438

[91] Albrecht, M.; Kaim, W., *Z. Anorg. Allg. Chem.*, **2000**, *626*, 1341

[92] Knödler, A.; Wanner, M.; Fiedler, J.; Kaim, W., *J. Chem. Soc., Dalton Trans*., **2002**, 3079

[93] Bulak, E.; Leboschka, M.; Schwederski, B.; Sarper, O.; Varnali, T.; Fiedler, J.; Lissner, F.; Schleid, T.; Kaim, W., *Inorg. Chem.*, **2007**,*46*, 5562-5566

[94] Sarper, O.; Bulak, E.; Kaim, W.; Varnali, T., *Molecular Physics*, **2006**, *104*, 833-838

[95] Anzenbacher, P.; Try, A. C.; Miyaj, H.; Jursikova, K.; Lynch, V.M.; Marquez, M.; Sessler, J.L. *J. Am. Chem. Soc*. **2000**, *122*, 10268-10272.

[96] Knödler, A., *Ph.D. Thesis*, Universität Stuttgart, **2002**

[97] Chen, Xiao-Ming; Xu, Zhi-Tao; Mak, T.C.W., *Polydehron,* **1995**, *14*, 319-322

[98] (a) Sarper, O., *Master Thesis*, Bogazici University, Istanbul, **2005** (b) Sarper, O.; Bulak, E.; Kaim, W.; Varnali, T., *Theo Chem*, **2006**, *733*, 35-42

[99] Scheiring, T., *Ph.D. Thesis*, Universität Stuttgart, **2000**

[100] Albrecht, M., *Ph.D. Thesis*, Universität Stuttgart, **2000**

[101] (a) Philip, D.; Stoddart, J. F. *Angew. Chem., Int. Ed. Engl.* **1996**, *35*, 1154-1196. (b) Tour, J. M. *Chem. Re*V*.* **1996**, *96*,537-553. (c) Lehn, J.-M. *Supramolecular Chemistry: Concepts and PerspectiVes*; VCH Publishers: Weinheim, **1995**. (d) Amabilino, D. B.; Stoddart, J. F. *Chem. Re*V*.* **1995**, *95*, 2725-2828. (e) Lawrence, D. S.; Jiang, T.; Levett, M. *Chem. Re*V*.* **1995**, *95*, 2229-2260. (f) Philip, D.; Stoddart, J. F. *Angew. Chem., Int. Ed. Engl.* **1995**, *35*, 1154-1196. (g) Whitesides, G. M.; Simanek, E. E.; Mathias, J. P.; Seto, C. T.; Chin, D. N.; Mammen, M.; Gordon, D. M. *Acc. Chem. Res.* **1995**, *28*, 37-44. (h) Cram, D. J.; Cram, J. M. *Container Molecules and Their Guests*; The Royal Society of Chemistry: Cambridge, England, **1994**. (i) Ball, P. *Designing the Molecular World*; Princeton University Press: Princeton, NJ, **1994**.

[102] (a) *Monographs in Supramolecular Chemistry 1-5*; Stoddart, J. F., Ed.; Royal Society of Chemistry: Cambridge, **1989**; **1991**; and **1994-1995**. (b) *Supramolecular Chemistry*; Balzzani, V., DeCola, L., Eds.; Kluwer Academic Publishers: The Netherlands, **1992**. (c) *Inclusion Phenomena and Molecular Recognition*; Atwood, J. L., Ed.; Plenum: New York, **1990**. (d) *Molecular Inclusion and Molecular Recognition-Clathrates II (Topics in Current Chemistry*, *Vol. 149*); Weber, E., Ed.; Springer-Verlag: New York, **1987**. (e) *Host-Guest Complex Chemistry/Macrocycles*; Vogtle, F., Weber, E., Eds.; Springer-Verlag: Berlin, **1985**.

[103] Drexler, K. E. Nanosystems: Molecular Machinery, Manufacturing, and Computation; Wiley; New York, 1992.

[104] (a) Stang, P.J.; Olenyuk, B. *Acc. Chem. Res.*, **1997**, *30*, 502. (b)Leininger, S.; Olenyuk, B.; Stang, P.J. *Chem. Rev.* **2000**, *100*, 853.

[105] (a) Whiteford, J. A.; Lu, C. V.; Stang, P.,J. J. *Am. Chem. Soc*., **1997**, *119*. 2524. (b) Whiteford, J. A.; Stang, P. J.; Huang, S. D. *Inorg. chem*., **1998**, *37*, 5595. (c) Beer, P. D.; Gale, P. A. *Angew. Chem*., **2001**, *115*, 503; *Angew. Chem., Int. Ed*., **2001**, *40*, 486. (d) Johnson, D. W.; Raymond, K. N. *Supramol. Chem*. **2001**, *13*, 639.

[106] (a) Slone, R.V.; Benkstein, K.D.; Bélanger, S.; Hupp, J.T.; Guzei, I. A.; Rheingold, A.L. *Coord. Chem. Rev*. **1998**, *171*, 221. (b) Sun, S.-S.; Lees, A. *J. Inorg. Chem*. **1999**, *38*, 4181.

[107] Campo-Fernandez, C.S.; Clérac, R.; Dunbar, K.R. *Angew. Chem*. **1999**, *111*, 3686; *Angew. Chem., Int. Ed*. **1999,** *38*, 3477.

[108] Vicens, J.; Bohmer, V., Eds. *Calixarenes: A Versatile Class of Macrocyclic Compounds*; Kluwer Academic Press: The Netherlands, **1990.** Gutsche, C. D. *Calixarenes*; The Royal Society of Chemistry: London, **1989**

[109] Pedersen, C. J.; Frensdorff, K. K. *Angew. Chem., Int. Ed. Engl.* **1972**, *11*, 16. Pedersen, C. J. *J. Am. Chem. Soc.* **1967**, *89*, 7017. Patai, S., Rappoport, Z., Eds. *Crown Ethers and Analogues*; Wiley: New York, 1989. Hiraoka, M., Ed. *Crown Compounds*; Elsevier: Amsterdam, 1982.

[110] Stang, P.J.; Cao, D.H.; Shinichi, S.; Arif, A. M. *J. Am.Chem. Soc*. **1995**, *117*, 6273.

[111] Slone R. V.; Hupp, j.T.; Stern, C.L.; Albrecht-schmitt, T.E. *Inorg. Chem*. **1996**, *15*, 1497.

[112] Kaim, W.; Schwederski, B.; Dogan, A.; Fiedler, J.; Kuehl, C.J.; Stang, P.J. *Inorg. Chem.,* **2002**, *41*, 4025-4028.

[113] Scott, D. J.; Puddephatt, R. J. *Organometallics*, **1986**, *5*, 1538-1544.

[114] (a) Fujita, M.; Yakazi, J.; Ogura, K. *J. Am. Chem. Soc*. **1990**, *112,* 5645. (b) Fujita, M.; Nagao, S.; Iida, M.; Ogata, K.; Ogura, K. *J. Am. Chem*. Soc. **1993**, *115*, 1574. (c) Fujita, M.; Yakazi, J.; Ogura, K *Tetrahedron Lett*. **1991**, *32*, 5589. (d) Fujita, M.; Yakazi, J.; Ogura, K *Chem. Lett*. **1991**, 1031. (e) Fujita, M.; Sasaki, O.; Mitsuhashi, T.; Fujita, T.; Yazaki, J.; Yamaguchi, K.; Ogura, K. *Chem Commun*. **1996**, 1535.

[115] Benkstein, K. D.; Hupp, J. T.; Stern, C. L. *J. Am. Chem. Soc.*, **1998**, *120*, 12982-12983.

[116] Gudat, D.; Dogan, A.; Kaim, W.; Klein, A. *Magn. Reson. Chem.* **2004***, 42*, 781-787.

[117] Bruns, W.; Kaim, W.; Waldhör, E.; Krejcik, M. *Inorg. chem*. **1995**, *34*, 4, 663

[118] Kaim, W.; Bruns, W.; Kohlmann, S.; Krejcik, M. *Inorg. Chim. Acta* **1995**, *229*, 143.

[119] Baranski, A.S.; Fawcett, W.R.; Gilbert, C.M. *Anal. Chem*. **1985,** *57*, 166.

[120] Vlcek, A.A. *Coord. Chem. Rev*. **1982**, *43*, 39.

[121] Tapolsky, G.; Duesing, R.; Meyer, T. J. *Inorg. Chem.* **1990**, *29*, 2285.

[122] Tapolsky, G.; Duesing, R.; Meyer, T. J. *J. Phys. Chem.* **1991**, *95*, 1105.

[123] (a) Tapolsky, G.; Duesing, R.; Meyer, T. J. *J. Phys. Chem.* **1989**, *93*, 3885. (b) Woessner, S.M.; Helms, J.B.; Shen, Y.; Sullivan, B.P. *Inorg. Chem.*, **1998,** *37 (21), 5406*

[124] Klein, A.; Kaim, W.; Hornung, F., M.; Fiedler, J.; Zalis, S. *Inorg. Chim. Acta* **1997**, *264*, 269-278.

[125] Shida, T. *Electronic Absorption Spectra of Radical Ions*; Elsevier, Amsterdam, **1988**; p:198

[126] (a) Braterman, P. S.; Song, J.-I.; Kohlmann, S.; Vogler, C.; Kaim, W. *J. Organomet. Chem*. **1991**, *411*, 207 (b) Krejcik, M.; Zalis, S.; Ladwig, M.; Matheis, W.; Kaim, W. *J. Chem. Soc., Perkins Trans*. *2* **1992**, 2007

[127] Matheis, W. *Ph.D. Thesis*, Universität Stuttgart, **1994**

[128] Braterman, P.S.; Song, J.I.; Wimmer, F.M.; Wimmer, S.; Kaim, W.; Klein, A.; Peacock, R.D. *Inorg. Chem*. **1992**, *31 (24),* 5084-5088.

[129] Kaim, W.; Moscherosch, M. *Coord. Chem. Reviews,* **1994**, *129*, 157-193

[130] M. Konno, T. Ishii and Y. Saito, *Acta Crystallogr. Sect. B*, **1977**, *31* 163

[131] L. Shields, *J. Chem. Sot. Faraday Trans. 2*, **1985**, *81*, 1.

[132] M. Pasquali, C. Floriani, A. Chiesi-Villa and C. Guastini, *Inorg. Chem*. **1981**, *20* 349.

[133] Flamini A.; Poli, N. *Inorg. Chim. Acta*, **1988**, *150*, 149.

[134] Baukova,T.V.; Ellert, O.G.; Kuzmina, L.G.; Dvortsova, N.V.; Lemenovskii, D.A.; Rubezhov, A.Z.; *Mendeleev Commun*. **1991,** 22.

[135] J.S. Miller, J.C. Calabrese, R.S. McLean and A.J. Epstein, *Adv. Mater.,* **1992**, *4,* 498.

[136] (a) J. Baumgarten, C. Bessenbacher, W. Kaim and T. Stahl, *J. Am. Chem. Soc.,* 1989, *111,* 2126, 5017.(b) H. Masai, K. Sonogashira and N. Hagihara, *J. Organomet. Chem.* **1972**, *34,* 397.

[137](a) V.F. Traven and R. West, *J. Am. Chem. Soc.* **1973**, *95,* 6824. (b) H. Sakurai, M. Kira and T. Uchida, *J. Am. Chem. Soc.* **1973**, *95,* 6825. (c) H. Watanabe, T. Muraoka, M. Kageyama, K. Yoshizumi and Y. Nagai, *Organometallics,* **1984**, *3,* 141.

[138] D.A. Dixon and J.S. Miller, *J. Am. Chem. Soc.* **1987**, *109,* 3656.

[139] Hartmann, H.R. *Ph.D. Thesis*, Universität Stuttgart, **2003**

[140] Hartmann, H.; Kaim, W.; Wanner, M.; Klein, A.; Frantz, S.; Duboc-Toia, C.; Fiedler, J.; Záliš, S*. Inorg. Chem*. **2003**, *42*, 7018-7025

[141] Maity, A. N*. Ph.D. Thesis*, Universität Stuttgart, **2007**

[142] (a) Skotheim, T. A., Elsenbaumer, R. L., Reynolds, J. R., Eds. *Handbook of Conducting Polymers*, *2nd ed.*; Marcel Dekker: New York, **1998**. (b) Ishiguro, T.; Yamaji, K.; Sato, G. *Organic Superconductors*; Springer: New York, **1998**. (c) Potember, R. S.; Poehler, T. O.; Cowan, D. O. *Appl. Phys. Lett.* **1979**, *34*, 405.

[143] Braun-Sand, S. B.; Wiest, O. *J. Phys. Chem. A* **2003**, *107*, 285.

[144] (a) Miller, J. S.; Epstein, A. J. *Angew. Chem.* **1994**, *106*, 399; *Angew. Chem., Int. Ed. Engl.* **1994**, *33*, 385. (b) Miller, J. S. *Interface* **2002**, *11*, 22. (c) Yee, G. T.; Manriquez, J. M.; Dixon, D. A.; McLean, R. S.; Groski, D. M.; Flippen, R. B.; Narayan, K. S.; Epstein, A. J.; Miller, J. S. *Ad*V*. Mater.* **1991**, *3*, 30. (d) Manriquez, J. M.; Yee, G. T.; McLean, R. S.; Epstein, A. J.; Miller, J. S. *Science* **1991**, *252*, 1415.
(e) Pokhodnya, K. I.; Epstein, A. J.; Miller, J. S. *Ad*V*. Mater.* **2000**, *12*, 410. (f) Wang, G.; Zhu, H.; Fan, J.; Siebodnick, C.; Yee, G. T. *Inorg. Chem.* **2006**, *45*, 1406

[145] (a) Taliaferro, M. L.; Thorum, M. S.; Miller, J. S. *Angew. Chem.* **2006**, *118*, 5452; *Angew. Chem., Int. Ed.* **2006**, *45*, 5326. (b) Vickers, E. B.; Selby, T. D.; Thorum, M. S.; Taliaferro, M. L.; Miller, J. S. *Inorg. Chem.* **2004**, *43*, 6414. (c) Cle´rac, R.; O'Kane, S.; Cowen, J.; Ouyang, X.; Heintz, R.; Zhao, H.; Bazile, M. J.,

Jr.; Dunbar, K. R. *Chem. Mater.* **2003**, *15*, 1840. (d) Miyasaka, H.; Izawa, T.; Takahashi, N.; Yamashita, M.; Dunbar, K. R. *J. Am. Chem. Soc.* **2006**, *128*, 11358.
[146] (a) Zhao, H.; Heintz, R. A.; Dunbar, K. R.; Rogers, R. D. *J. Am.Chem. Soc.* **1996**, *118*, 12844–12845. (b) Zhao, H.; Heintz, R. A.; Ouyang, X.; Dunbar, K. R.; Campana, C. F.; Rogers, R. D. *Chem. Mater.* **1999**, *11*, 736–746. (c) Carlucci, L.; Ciani, G.; van Gudenberg, D. W.; Proserpio, D. M. *New J. Chem.* **1999**, *23*, 397–401.

[147] Berger, S.; Hartmann H.; Wanner M.; Fiedler, J.; Kaim, W. *Inorg. Chim. Acta*, **2001**, *314*, 22–26.

[148] Leirer, M.; Knör, G.; Vogler, A. *Inorg. Chem. Commun*. **1999**, *2*, 110.

[149] Kaim, W.; Ernst, S.; Kasack, V. *J. Am. Chem. Soc.* **1990**, *112*, 173.

[150] Scott, J.D.; Puddephatt, R.J. *Organometallics,***1983**, *2*, 1643-1648.

[151] G. M. Sheldrick, *Programme SHELXS*: Göttingen, **1997.**

[152] G. M. Sheldrick, *Programme SHELXL*: Göttingen, **1997.**

[153] W. Herrendorf and H. Bärnighausen, *Programme HABITUS*: Gießen, Karlsruhe, **1993**, Gießen, **1996**.

[154] CRYSTAL IMPACT *Programme DIAMOND, Version 3.2b*: Bonn, **2009**.

Abbreviations

a	Hyperfine coupling constant
a_0	isotropic hyperfine constant
α	Alpha
A	ampere
Å	ångström
abb.	Abbildung
abpy	2,2´-azobispyridine
ADF/BP	Amsterdam-Density-Functional/Becke-Perdew
ax	axial
B	magnetic field
big	bis(1-methylimidazol-2-yl)glyoxal
bik	bis-(1-methyl-2-imidazolyl)ketone
bmiq	2,3-bis(1-methylimidazol-2-yl)quinoxaline
bmptz	3,6-bis(2-(4-methylpyridyl))-1,2,4,5-tetrazine
bp	4,4´-bipyridine
bpy	2,2´-bipyridine
bpym	2,2´-bipyrimidine
bptz	3,6-bis(2-pyridyl)-1,2,4,5-tetrazine
Br	Bromo
BuLi	butyllithium
Bu_4NPF_6	tetrabutylammonium hexafluorophosphate
ca	circa
CHN	Carbon-Hydrogen-Nitrogen
cm	centimetre
Cl	chloro
d	doublet / bond length
dd	doublet of a doublet
δ	chemical shift
Δ	difference
DCM	dichloromethane
DEE	diethylether

dibmiq	2,3-bis(1-methylimidazol-2-yl)7,8-dimethylquinoxaline
dm	doublet of multiplet
DMF	dimethylformamide
dmso	dimethylsulfoxide
DPV	Differential Pulse Voltammetry
E_{pa}	anodic peak potential
E_{pc}	cathodic peak potential
$E_{1/2}$	half wave potential
ε	molar extinction coefficient
EPR	electron paramagnetic resonance
ESI	electrospray ionization
etc	Et cetera
eq	equatorial
exp	experimental
eV	electronvolt
fac	facial
$FeCp_2^{0/+}$	ferrocene / ferrocenium
Fig	figure
g	gram
GHz	gigahertz
Hal	halogen
HCl	hydrochloric acid
HOMO	highest occupied molecular orbital
Hz	hertz
I	Iodo
I	nuclear spin
IL	intra-ligand
im	imidazole
IR	infrared
irr	irreversible
iso	isotropic
J	NMR coupling constant
K	kelvin

L	ligand
λ	wavelength
LLCT	ligand to ligand charge transfer
LMCT	ligand to metal charge transfer
LUMO	lowest unoccupied molecular orbital
M	molar / metal
m	multiplet
max	maximum
Me	methyl
MeLi	methyllithium
MeOH	methanol
MHz	megahertz
ml	mililitre
MLCT	metal to ligand charge transfer
mm	milimeter
mmol	milimole
MO	molecular orbital
mol	mole
mT	militesla
mV	milivolt
μ	mu
ν	wavenumbers
N	nitrogen
nat	natural
NIR	near infrared
nm	nanometer
NMR	nuclear magnetic resonance
η	hapticity
°	degree
°C	degree centigrade
o	ortho
OTTLE cell	optically Transparent Thin Layer Electrochemical cell
OTf	triflate

ph	phenyl
ppm	parts per million
red	reduction
RT	room temperature
s	strong (IR band) / singlet
S	electron spin
SBLCT	sigma bond to ligand charge transfer
sec	second
sh	shoulder
SOMO	singly occupied molecular orbital
σ	sigma
t	triplet
T	temperature / Tesla
TCNB	1,2,4,5-tetracyanobenzene
TCNE	tetracyanoethene
TCNQ	7,7,8,8-tetracyano-*p*-quinodimethane
thf	tetrahydrofuran
TD-DFT	Time Dependent Density Functional Theory
UV	ultra violet
V	volt
vs.	versus
vis	visible
Z	atomic number

Curriculum Vitae

Name: Cüneyt KAVAKLI

Date and place of birth: 04.07.1980 in Eskisehir (Turkey)

Gender: Male

Nationality: Turkish

Schooling

1987 – 1992 Elementary School, Düzce, Turkey

1992 – 1995 Secondary School, Düzce, Turkey

1995 – 1998 High School, Ankara Cankaya Atatürk High School, Ankara, Turkey

Studies

1999 – 2003 ***Bachelor of Science in Chemistry:*** Middle East Technical University, Faculty of Arts and Science, Chemistry Department, Ankara

2003 – 2005 ***Master of Science in Chemistry:*** Middle East Technical University, Chemistry Department, Ankara Under the guidance of Prof. Dr. S. Özkar Specialization: Inorganic Chemistry,
Title of thesis: "Synthesis and Characterization of Carbonyl-Tungsten Complexes of N, N'- bis(ferrocenylmethylene)ethylenediamine"

2005 - 2009 ***Doctoral work:*** Institut für Anorganische Chemie der Universität Stuttgart, under the guidance of Prof. Dr. W. Kaim.
Title of thesis: "Spectroscopic, Electrochemical and Structural Investigation of Platinum(IV) Complexes with Nitrogen-Rich Chelate Ligands"

Positions held

August 2005-December 2009 : Teaching Assistantship at the Institut für Anorganische Chemie der Universität Stuttgart